2020-01-01

Development Of A Framework For The Calibration Of RPAS, A 3D Finite Element Analysis Tool For Rigid Pavements

Abbasali Taghavighalesari
University of Texas at El Paso

Recommended Citation

Taghavighalesari, Abbasali, "Development Of A Framework For The Calibration Of RPAS, A 3D Finite Element Analysis Tool For Rigid Pavements" (2020). *Open Access Theses & Dissertations*. 3045.
https://scholarworks.utep.edu/open_etd/3045

DEVELOPMENT OF A FRAMEWORK FOR THE CALIBRATION OF RPAS A 3D FINITE ELEMENT ANALYSIS TOOL FOR RIGID PAVEMENTS

ABBASALI TAGHAVIGHALESARI

Doctoral Program in Civil Engineering

APPROVED:

Cesar J. Carrasco, Ph.D., Chair

Soheil Nazarian, Ph.D., Co-Chair

Cesar Tirado, Ph.D.

Calvin M. Stewart, Ph.D.

Richard Rogers, P.E.

Saurav Kumar, Ph.D.

Stephen L. Crites, Jr., Ph.D.
Dean of the Graduate School

Dedication

To My Love
Setare

To My Parents
Hosseinali And Rahimeh

And To MMERFF

DEVELOPMENT OF A FRAMEWORK FOR THE CALIBRATION OF RPAS A 3D FINITE ELEMENT ANALYSIS TOOL FOR RIGID PAVEMENTS

by

ABBASALI TAGHAVIGHALESARI, M.Sc.

DISSERTATION

Presented to the Faculty of the Graduate School of
The University of Texas at El Paso
in Partial Fulfillment
of the Requirements
for the Degree of

DOCTOR OF PHILOSOPHY

Department of Civil Engineering
THE UNIVERSITY OF TEXAS AT EL PASO
May 2020

Acknowledgements

I would first like to express my sincere gratitude and appreciation to my advisor, Dr. Cesar Carrasco, whose in-depth knowledge, guidance, support and encouragement were the major source of motivation in my studies.

I would like to extend my gratitude to Dr. Soheil Nazarian for providing me with the opportunity to work as a Research Assistant at the Center for Transportation Infrastructure System (CTIS) at The University of Texas at El Paso.

I wish to thank my dissertation committee members, Mr. Richard B. Rogers, Dr. Cesar Tirado, Dr. Calvin M. Stewart, and Dr. Saurav Kumar. I highly appreciate their great ideas and invaluable comments and feedbacks throughout this research.

I would like to recognize Southern Plain Transportation Center (SPTC) for funding part of my research through project SPTC14.1-94. I am very thankful for the help from Mr. Benjamin Worel, Dr. Michael Vrtis, and Dr. Bernard Izevbekhai at Minnesota Department of Transportation for their continuous support in providing MnROAD test data, and Dr. Navneet Garg and Mr. Ryan Rutter at FAA William J. Hughes Technical Center for their assistance in collecting test data at NAPTF.

I would like to thank all the graduate and undergraduate students and staff at CTIS, who not only helped me in the completion my research work but also contributed to the having great quality time through extracurricular activities.

I would like to specially thank my wife, Setare Ghahri Saremi, for her love, patience, support, understanding, and contribution to this research. Last but not least, I am grateful for the support from my wonderful parents, Hosseinali and Rahimeh, and my great brother and sisters.

Abbasali TaghaviGhalesari

May 2020

Abstract

The accurate analysis of rigid pavements requires a reliable modeling procedure based on integrating mechanistic analysis methods (i.e. closed-form solutions or numerical methods) and empirical observations (i.e. field measurements and laboratory test results). The use of the finite element method to model the response of rigid pavements has increased in recent decades due to its capability to incorporate the complexity of material behavior, traffic information, and environmental condition. Researchers from the University of Texas at El Paso developed the software Rigid Pavement Analysis System (RPAS) to comprehensively analyze the response of concrete pavements under different geometric configurations, foundation models, temperature gradient profiles and traffic loads by using the finite element method. Despite a few comparative studies that have been carried out during the development of this program, the implemented models and approaches may need improvement through a well-established calibration process. Therefore, this research aims to calibrate RPAS through a comparison with analytical solutions and field measurements. At the early stage of this study, a pre-validation was conducted in which field pavement critical responses and laboratory tests were compared with the responses predicted by RPAS. While a reasonable agreement between the responses was observed, it is the goal of the work presented here to develop and implement a calibration process that reduces the existing discrepancies. To this end, a series of studies that included verification and validation were conducted on a variety of pavement sections under different loading conditions. The calibration process of RPAS utilizes a multi-objective optimization algorithm that produces a list of calibration factors that are applied to the foundation moduli which was found, through a sensitivity study, to have a significant impact on pavement responses and also large variability. The calibration factors obtained ranged from 0.75 to 1.60 with most being close to 1.00 which, given the high variability in the foundation moduli, confirms the capability of RPAS in predicting the pavement responses with a good accuracy. The accuracy of RPAS after applying the calibration factors was assessed using a reliability metric that indicates a successful calibration process that

brings the results produced by RPAS to within engineering expected thresholds. Ultimately, this research provides transportation agencies and pavement design engineers with a more reliable tool for the analysis of concrete pavements in comparison with the existing analysis tools.

Graphical Abstract

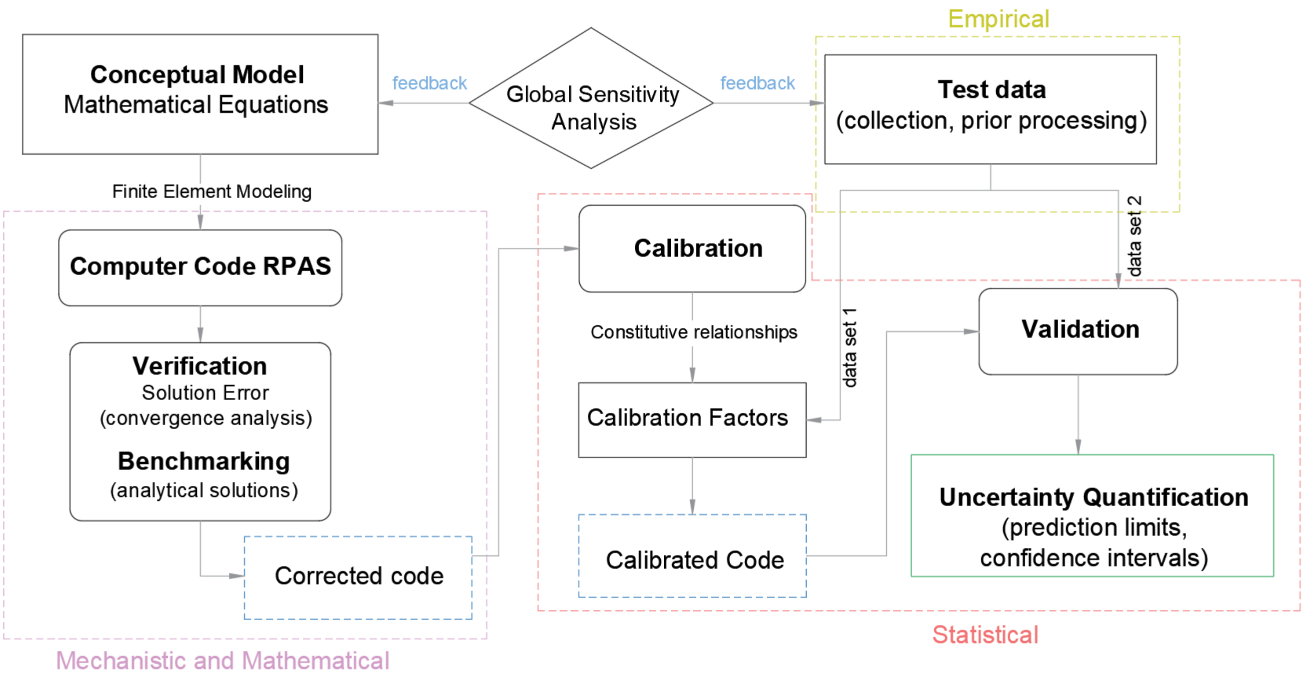

Table of Contents

List of Tables

List of Figures

1. Introduction

Since 1891 when the first Portland cement concrete pavement (PCCP) was placed in Ohio, different types of rigid pavements are utilized that are classified into four main categories: jointed plain concrete pavement (JPCP), continuous reinforced concrete pavement (CRCP), jointed reinforced concrete pavement (JRCP), and pre-stressed concrete pavement (PCP) (Rao et al. 2013). The focus of most rigid pavement analysis tools is on the capability to analyze the response of JPCP and CRCP because they are the commonly used types of rigid pavements. The mechanistic-empirical pavement design guide (MEPDG) identifies the JPCP as a concrete pavement with transverse joints with or without load transfer devices (dowels), no distributed steel, and with tied or untied longitudinal joints, over one or more unbound or stabilized foundation layers. CRCP, on the other hand, is defined as concrete pavement with longitudinal joints, longitudinal reinforcement at or above mid-depth, and with or without transverse construction joints. Although joints serve to minimize transverse cracking from temperature gradient, to relief drying gradient shrinkage stresses and to hold shrinkage cracks tightly closed, they may be critical sections as the distress (e.g., spalling, joint faulting, fatigue damage, poor load transfer, punchout) typically occurs near the slab edge closest to the applied repeated heavy axle loads (Zollinger and Barenberg 1989, Grater and McCullough 1994, NCHRP 1-37A). To attain the accurate prediction of pavement thermo-mechanical responses, it is necessary to consider the combined effect of material properties of PCC slab and the underlying layers (i.e., subbase, base and subgrade) as well as the environmental and traffic loads in the M-E design procedure. Hence, the investigation on durability properties of concrete pavement in terms of abrasion resistance as well as changing temperature gradient (warping and curling, freeze-thaw resistance) and moisture conditions over time through the depth of the PCC slab was conducted by several researchers (Gjorv et al. 1990, Ioannides and Khazanovich 1998, Hiller and Roesler 2009, Li et al. 2011, Huang et al. 2017).

While a considerable amount of research has been devoted to the development of the analysis tools and methods for PCC pavements (Tabatabaie and Barenberg 1980, Tayabji and

Colley 1986, Khazanovich 1994, Kim et al. 2001, Carrasco et al. 2011), further studies are still needed to present a reliable tool that is properly calibrated and provide accurate results.

1.1. Problem Statement

A brief review of the specifications of the state DOTs indicate that most of the rigid pavement design methods are still based on the 1993 AASHTO Guide for Design of Pavement Structures, which utilizes empirical design methods and has led to designs that are not necessarily effective in terms of performance, and consequently, on their construction and maintenance costs. There is also no uniform approach among the states that have implemented mechanistic procedures (Bordelon 2009). However, mechanistic-empirical (M-E) design method is being increasingly adopted by highway agencies to enhance the design effectiveness. TxDOT, just as other state DOTs, implemented M-E procedure for the design of CRCPs through the program CRCP-ME (Ha et al. 2011) and have identified the M-E design for JPCP in an ongoing research project.

To achieve a reliable and efficient pavement design, the development of an analysis tool capable of accurately predicting the pavement critical responses is of primary importance. This tool must be capable of predicting the pavement's mechanical response for varied types of materials and traffic and environmental loads. Another important aspect of PCC pavement analysis is associated with the contact conditions along the slab-foundation interface, which may significantly impact the mechanical behavior of the pavement. It is important not only due to the influence of traffic loading characteristics on the slab response but also because of the thermal loading that may induce bending stress (from curling and thus separation of slab from the soil), as wells as compressive or tensile stress (due to expansion or contraction as a result of sliding friction at the interface) within the slab. To address these issues, a number of rigid pavement analysis tools have been developed since 1979, namely ILLI-SLAB, ISLAB, JSLAB, EVERFE, CRCP-10, which will be discussed in the next chapter. To overcome the limitations of the aforementioned tools to take advantage of the modern finite element (FE) programming tools and to avoid the complexity of implementation by pavement design engineers, NYSLAB was developed at The

University of Texas at El Paso, which is capable of comprehensively analyze jointed plain concrete pavements' (JPCPs) responses for different geometric configurations (no limit on the number of slab and soil layers), foundation models (accounting for normal and shear stiffness), linear/non-linear temperature gradient profiles and traffic load configurations. All complications related to appropriate discretization and modeling are handled internally by the software. In the most recent version of this software renamed RPAS, the capacity of the program was expanded to predict the stresses and strains in CRCP, taking into account the complex interaction between the reinforcement steel and concrete as well as the slab-foundation interaction. Hexahedron solid elements were employed to model the foundation layers to determine the critical responses throughout the depth of the pavement layers without dealing with the problems associated with the calculation of modulus of subgrade reaction. However, the software has not yet been calibrated through a comparison with the existing analytical solutions and field measurement data.

1.2. Objectives of Research

A thorough investigation of the literature indicates that most of the pavement design specifications such as MEPDG rely on some type of analysis program (i.e. a model based on finite element method, elastic layer theory, etc.) to calculate critical pavement responses (deflections, stresses, and strains) and then to establish performance prediction models. Thus, it is essential to develop an accurate and reliable pavement analysis program to realistically predict the behavior of a given pavement under any possible traffic and environmental loads. Hence, the primary purpose of this research is to calibrate the PCC pavement analysis tool developed at The University of Texas at El Paso, called RPAS. The field calibration of the program requires data on pavement responses such as maximum concrete stresses, steel stresses, base deformations and subgrade strains within a critical section. In addition, the field investigations should provide important input information (e.g., material properties, loading information, environmental condition, etc.) to undertake the calibration. To have a comprehensive framework with no limitation, the calibration process will be defined based on the assumption that enough data would available. The main objectives of this research can be summarized as,

1. *Review and document the capabilities of the RPAS software, main features, advantages and limitations*: As mentioned earlier, this software was developed to address the limitations of the existing rigid pavement analysis tools. Thus, one of the objectives of this study is to investigate the structure and basic components of the program as well as the supplementary features provided to improve the analysis procedure for calibration purposes.
2. *Defining a comprehensive methodology for identifying the main influencing factors on the response of concrete pavement*: One of the limitations of the existing literature to explore the important parameters in modeling is that they are mainly based on a local sensitivity analysis (one-at-a-time technique), which tests the sensitivity of outputs for a certain input by keeping the rest of inputs constant. To avoid the possible errors caused by employing this technique due to interdependence of different parameters, a procedure will be developed based on a global sensitivity analysis.
3. *Establishment of a calibration framework*: The most significant contribution of this study to the existing literature is to develop a framework for the calibration of the program. A brief review of the literature indicates that most of the analysis tools are either verified against analytical solutions or validated against laboratory data, which cannot be considered as the predictive capability of the software to analyze an arbitrary problem. However, this research attempts to establish and implement the calibration algorithm(s) in a way that the reliability level of the results and a range of data on which the software is calibrated can be determined.
4. *Implementing the capability of re-calibration for new sets of data and site condition*: One of the main concerns in the calibration process is the applicability of the suggested framework for an unseen set of data, which obviously is not feasible for a comparison of the observed data and predicted values. This feature will be considered as a part of the calibration algorithm(s) to address the mentioned issue.

1.3. Significance of Study

The contribution of this research to the field of pavement engineering is to provide transportation agencies and pavement design engineers with a more representative method for the analysis of PCC pavement. At the early stage of the research, a sensitivity analysis by simulating cases with the typical pavement characteristics and critical loading condition will be conducted to find the most influencing factors, and consequently, to collect the most appropriate data from field measurements and laboratory tests. The databases will cover a wide variety of designs and regions (site conditions). As a prerequisite of calibration, a computational verification and cross-model validation will be performed to compare the results among different models for similar analyses. Then, instead of using a calibration coefficient that may lead to the corresponding uncertainties in the analysis procedure, a framework will be established to find a range of data on which the software is calibrated. The established framework can be continuously implemented as new information and more high quality field test data becomes available. A validity study will be performed to identify the level of reliability for each category. Therefore, in addition to the advantages of RPAS software in finding the critical response of pavement in any section and predicting the critical sections where the distress (e.g., faulting, transverse and longitudinal cracking) can occur, this research contributes to determining the significant factors that affect the behavior of rigid pavements and defining a promising methodology for the field calibration of pavement analysis programs.

1.4. Structure of Dissertation

Chapter 2 provides a thorough review on the modeling techniques and computer programs that are available for the analysis of rigid pavements. The methods that have been previously employed for the validation of analysis tools as well as the recommended procedure in this study were presented. An overview of the optimization methods is given that can be used to minimize the resulting errors in the calibration and validation process. Chapter 3 discusses the technical details of the formulation of rigid pavement, foundation layers, interaction of the pavement layers, and modeling the thermal loading that were implemented in RPAS. Chapter 4 describes the two major sources of collecting pavement field data for the purpose of validation: MnROAD and NAPTF. Different pavement structures (thickness and number of layers), loading condition (truck loading, environmental loading, accelerated loading), pavement material properties (different concrete mixtures, bound and unbound base, natural and stabilized subgrade) as the main factors affecting the design of rigid pavements are considered. A preliminary study is performed to evaluate the performance of RPAS prior to calibration and validation. Chapter 5 presents the verification process through a convergence study and bench-marking. A review of the existing analytical solutions for the analysis of rigid pavements and the comparison of responses predicted using these methods with those from RPAS are presented. Chapter 6 explains the calibration process proposed in this study and the implementation of sensitivity analysis in this process. After calibration, a set of calibration factors is processed and applied to RPAS calibration parameters. Chapter 7 provides an overview of the existing validation and reliability assessment metrics and demonstrates the performance of RPAS in identifying the pavement critical responses after applying the appropriate calibration factors. Chapter 8 presents a summary and conclusion of this study and provides practical application of the proposed calibration process. It also states the limitations of the study and provides recommendations for future studies.

2. Theoretical Background

This chapter contains an overview of the current methods and techniques used in the analysis of concrete pavements. Since most of these methods are based on the numerical simulation, the procedure available for the evaluation of the developed tool and minimization of the error in the results are reviewed.

2.1. Rigid Pavement System

Rigid pavement systems consist of a number of Portland cement concrete (PCC) slabs placed over one or more foundation layer(s) (base, subbase, and subgrade). In a rigid pavement system, the concrete slab is the stiffest structural element that provides major bearing capacity against the applied loads. Pavement slabs can be composed of layers with different material properties and thicknesses, with the interface between them considered either bonded or unbonded.

The slab layers are usually placed over an unstabilized or stabilized base course. Unstabilized or unbound base courses may be composed of densely graded or open-graded granular materials. Stabilized bases are usually composed of granular materials bounded with cement, asphalt, lime or fly ash blend, or other agents. Base layers can also contribute to the load resistance system. However, their main roles (as defined in some design guides) are to provide a uniform platform for pavement slabs, contribute to the subgrade drainage and frost protection, reduce shrinkage and swelling potential of subgrade, and prevent subgrade pumping (Hammons and Ioannides 1997).

One or more subbase layer may also be used in the pavement foundation system. Subbases are usually made with lesser quality granular materials to replace soft and compressible soils. Like base layer, subbase layers can be bonded or unbonded. In addition, they can provide strength to the pavement system and offer frost and swelling protection.

The last layer in a rigid pavement system is subgrade, which is either natural or compacted soil. The subgrade strength property is represented by resilient modulus, which is a function of soil classification, compaction and moisture content.

There are three conventional types of concrete pavements: jointed plain concrete pavement (JPCP), (see Figures 2-1a and 2-1b), jointed reinforced concrete pavement (JRCP), (see Figure 1c), and continuously reinforced concrete pavement (CRCP), (see Figure 1d). For all conventional rigid pavement types, a concrete slab is usually poured directly on a subgrade, base, or subbase. All the three common rigid pavements carry traffic loading through flexural strength of the concrete. However, they differ in the slab dimensions, joint details, and the type and amount of reinforcement they use. In addition to the conventional rigid pavements, two other types of rigid pavements are being used: precast and prestressed concrete pavement (PCP) and roller-compacted concrete pavement (RCCP). Prestressed concrete pavements make use of preapplication of compressive stress to the concrete to reduce the tensile crack potential. PCPs can be installed quickly on separate lanes with the minimum impact on the traffic as a durable long-lasting repair. Roller-compacted concrete pavement is a type of non-reinforced concrete pavement placed with high-density paving equipment and compacted with vibratory rollers. RCCPs are mainly used in industrial facilities and highway pavements with speed limits of 45 mph (unless diamond grinding is utilized) and are utilized when strength, speed of construction, durability, and economy are primary needs.

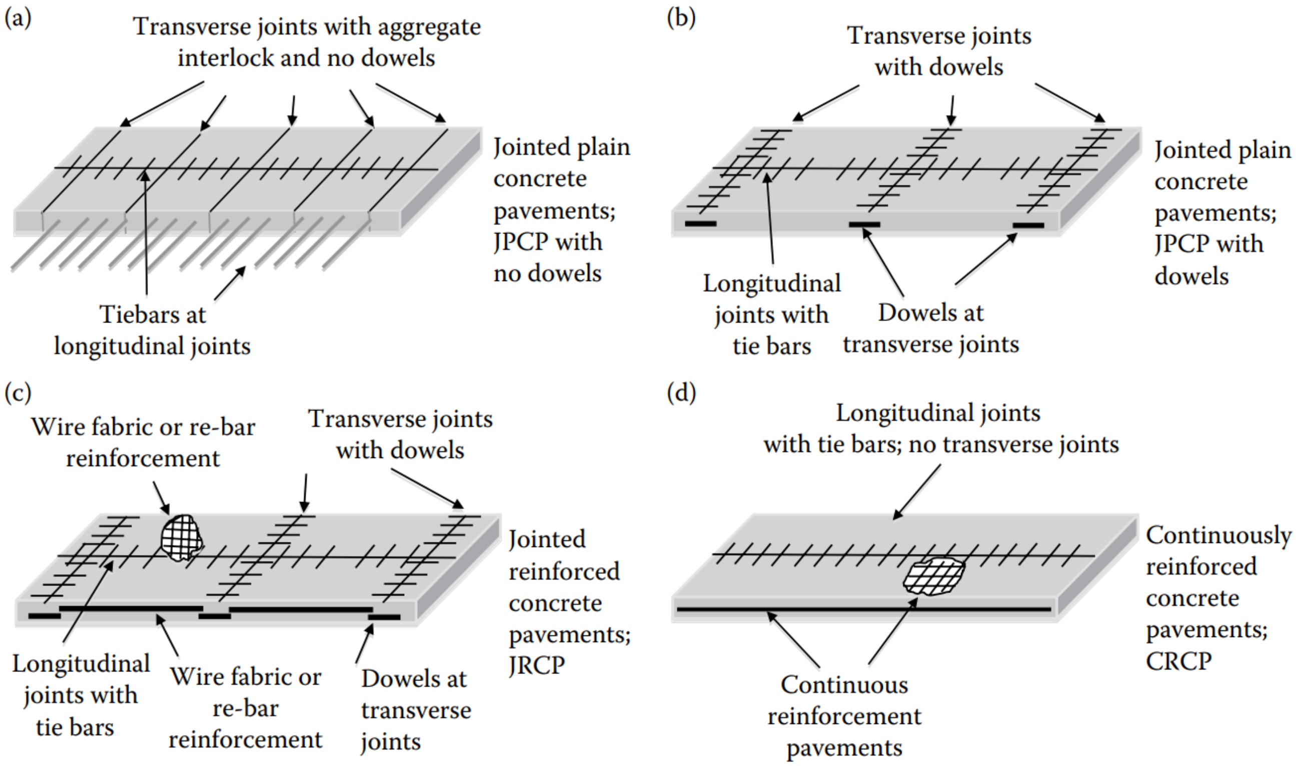

Figure 2-1. (a) Jointed Plain Concrete Pavement (JPCP) With Tie-Bars and No Dowels, (b) JPCP With Tie-Bars and Dowels, (c) Jointed Reinforced Concrete Pavements (JRCP) With Tie-Bars and Dowels, (d) Continuously Reinforced Concrete Pavements (CRCP) (Mallick and El-Korchi 2018)

Most of the rigid pavement analysis tools were designed to calculate the critical responses of either JPCP or CRCP because they are the most common types of rigid pavements. JPCPs are a more common type of rigid pavements than CRCP due to their low cost and simplicity. Contraction joints in JPCPs are typically constructed every 10-15 ft apart to control mid-slab cracking. In JPCP, no slab reinforcement is used except for dowel bars placed at transverse joints and tie-bars at longitudinal joints. Dowels are used for load transfer across transverse joints and allow the joints to move along the-longitudinal axis of the dowel. Conversely, tie-bars keep the longitudinal joints held tightly together. If dowels are not used, then load transfer across the joint can be achieved through aggregate shear interlock. Aggregate interlock is developed once a joint is cut in the young concrete pavement and a crack develops along the depth of the slab. Aggregate interlock is effective as long as the joint widths (a function of drying shrinkage and temperature effects) remain narrow. Repeated heavy loads across the transverse joint can cause the aggregate bond to wear down along the crack wall, rendering the aggregate shear bond ineffective, resulting in faulting, a bumpy ride, and, in poor support conditions, to joint failure.

CRCPs are heavily reinforced concrete slabs with no contraction joints. The characteristic cracking pattern consists of cracks typically spaced every 2.0–8.0 ft. They are held tightly together by reinforcing steel, allowing for aggregate interlock and shear transfer. If this aggregate shear interlock is not maintained and compromised, then punchout failure at the pavement edge occurs (especially if tied shoulders or stabilized foundation are not utilized), which is a typical distress in CRCP. The amount of reinforcing steel used in the longitudinal direction is typically 0.6%–0.8% of the cross–sectional area of the concrete, with less being used as temperature steel and support of longitudinal steel in the transverse direction. The cost of CRCP is much higher than that of JPCP or JRCP because of the heavy reinforcing steel used. However, CRCPs may prove cost-effective in high-traffic-volume roadways due to their better long-term performance compared to the other types of concrete pavements (Mallick and El-Korchi 2018).

Structural analysis and design of pavements is based on the concept of estimating and limiting stresses and deformations to prevent excessive damage and deterioration of pavements. Overstressed rigid pavements due to traffic loads and environmental effects will result in pavement distress such as fatigue cracking, faulting, pumping, punchouts, and curling and warping. The objective of pavement design is to recommend a pavement structure and configuration, including slab thickness, slab length, mix design, reinforcement requirements, joint details, and foundation support.

2.2. Rigid Pavement Analysis Techniques and Tools

Traditionally, for analysis of stresses and deflections in rigid pavements, a simplified idealization of the concrete pavement as a rigid slab resting on a spring-like foundation was employed. The slab is much stiffer than the supporting base or foundation material, and therefore carries a significant portion of induced stresses. The load-carrying mechanism in concrete pavement is similar to beam action, although a concrete slab is much wider than the beam and should be considered as a plate. The supporting layers of rigid pavement slabs are typically simplified as a Winkler or liquid foundation, which is a conceptual model that considers the foundation as a series of closely-spaced, isolated vertical springs. In recent decades, finite element method (FEM) facilitated analyzing complex concrete pavement structures (including joints, load transfer devices, voids, non-homogeneous materials) and producing accurate and more reliable solutions over shorter period of time.

CONCRETE SLAB

The first idealization of a rigid pavement system was introduced by Westergaard in the 1920's. He represented it as a case of slab-on-grade (Westergaard 1926). In that case, the rigid pavement was modeled as a thin plate resting on an infinite number of independent springs. The stiffness of those independent springs, with constant value, characterized the subgrade rigidity in Westergaard's model. The magnitude of spring stiffness was represented as the modulus of subgrade reaction with the unit of force per area per unit deflection. When the slab is loaded vertically down, the springs tend to push back; when the environment-related loads are pulling up on the slab, the springs tend to pull down toward the foundation. This behavior will result in tensile (or compressive) bending stress at the bottom (or top) of the concrete slab. This induced stress will be controlled in design by a number of factors such as restrained temperature and moisture deformation, externally applied loads, volume changes of the supporting material and frost action, continuity of subgrade support through plastic deformation, or materials loss due to pumping action.

Simple and approximate closed-form solutions and analytical models have been developed through making simplification assumptions. With the assumption of modeling the concrete slab by an infinite thin plate resting on an elastic foundation (a set of axial springs), the moment due to bending in x and y directions is given by the following equation:

$$M_{xx} = \frac{Eh^3}{12(1-\nu^2)}\left(\frac{\partial^2\omega}{\partial x^2} + \nu\frac{\partial^2\omega}{\partial y^2}\right) \tag{2-1}$$

where E, ν, and h are the elastic modulus, Poisson's ratio, and thickness of the slab, respectively, and ω denotes the deflection of the springs.

The stiffness term in Eq. (2-1) was used by Westergaard (1927) to derive the radius of relative stiffness ℓ, which is used in many of the stress and deflection equations of rigid pavements.

$$\ell = \sqrt[4]{\frac{Eh^3}{12(1-\nu^2)k}} \tag{2-2}$$

where k is the modulus of subgrade reaction.

By utilizing the parameter ℓ in the analytical solution, the relationships for the calculation of stress and deflection in slabs due to traffic and temperature loading have been developed, that are discussed in more details in Chapter 5.

Westergaard's initial analytical modeling had been adopted as a promising method for reliable design and was used as a design basis for new analysis tools. Westergaard extended his procedure to calculate stresses and deflections in rigid pavements due to interior, edge and corner loads. Although Westergaard's procedure had reached a certain level of maturity in idealization of rigid pavements, thereafter, several investigations were conducted to improve its model. The poor assumption regarding the modeling of thin slab layer and foundation as well as the restricted capabilities in considering tire loading position, thermal loads, and modeling load transfer devices were the main drawbacks of the Westergaard's method. Furthermore, using the *k*-value does not allow the engineer to analyze the impact of heavy loads or weak soils on the stresses and strains in the foundation layers.

JOINTS

Joints are often served to relief stresses and control cracking. In JPCP, load transfer devices (dowels, tie-bars) or mechanisms (aggregate interlock) are used in both the longitudinal joints and transverse joints to facilitate movements and transfer load caused by traffic and environmental effect from one slab to adjacent slab. In JRCP, dowels are used at the transverse contraction joints and the reinforcement controls the cracks caused by temperature and moisture effects. The subsequent benefit of using load transfer devices are to prevent faulting, reduce slab deflections, control mid-slab cracking, reduce pumping and bending stresses in slabs due to loss of base support and finally provide a smooth, safe and comfortable ride.

Figure 2-2 shows the application of tie-bars and dowels as well as the mechanism of developing stress in dowels under applied load. Top estimate the stress in dowels, an analytical solution was proposed by Friberg (1940). This solution uses the original solution by Timoshenko because it assumes the dowel to be a beam and the concrete to be a Winkler foundation. The maximum deformation of concrete under the dowel shown by y_0 in Figure 2-2, can be expressed as:

$$y_0 = \frac{P_t(2+\beta z)}{4\beta^3 E_d I_d} \tag{2-3}$$

where P_t is the load applied on the dowel, β is the relative stiffness of the dowel embedded in concrete, z is the joint width, E_d and I_d are the Young's modulus and moment of inertia of the dowel, respectively. I_d and β are defined as follows:

$$I_d = \frac{1}{64}\pi d^4 \tag{2-4}$$

$$\beta = \sqrt[4]{\frac{Kd}{4E_d I_d}} \tag{2-5}$$

where K is the modulus of dowel support, and d is the diameter of the dowel.

Therefore, the bearing stress on a dowel can be calculated as:

$$\sigma_b = Ky_0 = \frac{KP_t(2+\beta z)}{4\beta^3 E_d I_d} \tag{2-6}$$

The finite element expressions of the load transfer device modeling are presented in Chapter 3.

Tie-bars Dowels

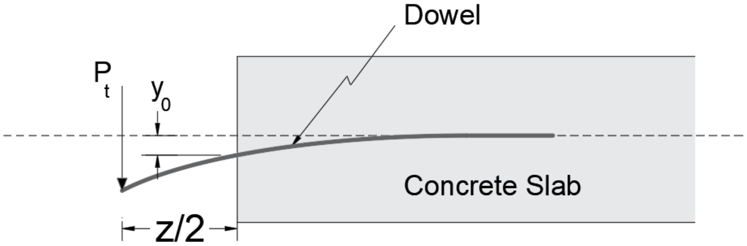

Figure 2-2. Application of Dowels and Tie-Bars, Dowel Deformation Under Load (pavementinteractive.org)

SUPPORTING LAYERS

The idealization of concrete pavement supporting layers was performed using different foundation models such as Winkler, Boussinesq, Vlasov, Kerr, Pasternak, and ZSS foundation (Tayabji and Colley 1986), Khazanovich et al. 2000, Huang 2004, Carrasco et al. 2011). Winkler model or dense liquid foundation considers the foundation layer as vertical springs independent of the displacement or pressure produced by the neighboring nodes. The vertical pressure produced on the Winkler foundation surface, $q(x, y)$ is proportional to the vertical deflection $w(x, y)$ with a constant of spring axial stiffness (K):

$$q(x, y) = \mathrm{K}\, w(x, y) \tag{2-7}$$

where $K = Ak$ in which k is the Winkler parameter and A is the associated surface area.

As the actual soil is continuous, it is capable of providing shear interaction. Winkler's idealization of subgrade does not have any mechanism to provide an interaction between adjacent springs or the so-called shear-interaction. This deficiency of the Winkler idealization is improved by modeling the subgrade as a two-parameter medium, such as Vlasov model, which provides shear interaction between individual spring elements. The parameters in Vlasov model to characterize the normal and shear stiffnesses are obtained from soil elastic properties and layer dimensions. However, an iterative procedure is required to estimate these parameters (Vallabhan and Das 1989).

Elastic solid foundations are better representations of the soil behavior compared to spring foundations because it considers a continuous surface deflection. Boussinesq model is one of the well-known solid foundations for which the following solution was developed for the deflection of point j due to a point load applied P_i at i, w_{ij} (Pickett et al. 1952):

$$w_{ij} = \frac{P_i(1-\nu_s^2)}{\pi E_s r_{i,j}} \tag{2-8}$$

where E_s and ν_s are the Young's modulus and Poisson's ratio of the soil and $r_{i,j}$ is the distance between points i and j.

The most recent types of foundation models are the three-dimensional solid elements that have been recently implemented in several numerical analysis as well as in RPAS program.

TRAFFIC LOADING

The load applied on the pavement surface due to traffic is considered in the design using truck load distribution in terms of factors such as average annual daily traffic (AADT), growth factor, lane distribution, and directional distribution. In AASHTO 1993, equivalent single-axle load (ESAL) was used as an indicator of traffic flow. MEPDG considers the actual traffic load spectra that will be projected over the period of service life of pavement.

For analysis purposes, the tire load is modeled from a simplified single circular tire print to the full tire configurations with a rectangular tire print. The latter is used in RPAS. Although the scanning of tire pressure and tire prints showed a higher pressure at the center of tire and a combined shape of circle and rectangle, a uniform distribution of each tire pressure is assumed in numerical modeling.

ENVIRONMENTAL LOADING

The major factors considered as the environmental load on pavements are the thermal effects due to air temperature (and convection) and the moisture intrusion. The former causes thermal curling while the latter induces warping. These two types of deformation in slab produce bending stresses due to internal and external restraints. Several researchers (Westergaard 1927, Bradbury 1938, Choubane and Tia 1992, Mohamed and Hansen 1996) investigated the effect of temperature on the pavement responses. However, the actual modeling of thermal curling requires taking a non-linear temperature profile within the slab and the concrete built-in curling into account (Rao and Roesler, 2005, Hansen et al. 2006). Further explanations on the theoretical solutions and the procedure of taking environmental loads into account for pavement analysis are given in Chapter 3.

In general, mathematical modeling of the stress state of a concrete slab on a supporting foundation layer system is very complex due to variation in materials, non-linear behavior, changing moisture and temperature conditions, changing support conditions, and complex interactions between components. Several computer modeling tools have been developed that will incorporate one or more of the above components. A list of these computer programs and their advantages or disadvantages will be presented later in this section.

FINITE ELEMENT MODELING

Traditional available analytical solutions may not realistically account for complex loads, mixed boundary conditions, and arbitrary geometry. The advance of computer algorithms led to the development of rigid pavement analysis software that consider more complexities in the modeling procedure. Given the complexity of all the parameters that influence the state of stress in a rigid pavement, finite element methods are being used to determine the response of rigid pavements such as stresses, strains, and deflections using a mechanistic approach. Extensive research has been devoted to the development of FE-based analysis tool to predict the behavior of rigid pavements. A number of these tools were generally developed to analyze the stiffness of the slabs on liquid or solid elastic foundation (Cheung and Zinkiewicz 1965), while others are being particularly applied to the analysis of jointed slabs on elastic solids, listed in the following sections. although general-purpose finite element packages, such as ABAQUS and ANSYS, have powerful ability to handle with complex problems, they can be difficult to learn and use effectively, model generation can be time-consuming, simulation times can be long in the case of 3D analysis, and extracting results of interest can be difficult.

Some of the programs developed specifically for rigid pavements using finite element method include ILLI-SLAB (Tabatabie and Barenberg 1980), WESLIQID (Chou 1981), JSLAB (Tayabji and Colley 1986), KOLA (Kok 1990), FEACONS-IV (Choubane and Tia 1992), KENSLAB (Huang 1993), ISLAB (Khazanovich et al. 2000), and EVERFE (Davids et al., 1998). Most of these programs can analyze multi-wheel loading of one- or two-layered medium thick plates resting on a Winkler or liquid foundation or an elastic solid. Some of the listed programs in this section were used for bench-marking purposes and will be discussed in further detail in Chapter 5.

WESLIQUID

Huang and Wang (1974) used the FE method for the analysis of jointed slabs on liquid foundations, later extended by Huang for solid foundations. This research resulted in the development of the WESLIQUD program by Chou (1981) that facilitated calculating stresses and deflections in PCC slab and the subgrade with or without joints and cracks.

ILLI-SLAB

Firstly developed at the University of Illinois (Tabatabaie and Barenberg 1980), ILLI-SLAB was an FE program written in FORTRAN® for the analysis of rigid pavement slabs discretized into rectangular four-node elements with three degrees of freedom (DOF) per node. PCC layer was modeled based on classical medium-thick elastic plate theory. Winkler foundation, modeled as vertical spring elements, was the initial form of modeling underlying layers in ILLI-SLAB and then elastic solid foundation has been added. ILLI-SLAB is capable of the analysis of PCC layers as classical medium-thick elastic plates, taking into consideration a temperature difference between the top and the bottom of the slab, mechanical load transfer through aggregate interlock, dowels, or a combination of them at the joints between slabs, and bonded or unbonded base condition (by assuming strain compatibility and neglecting shear stress at the interface, respectively).

ISLAB

To eliminate some of the limitations of ILLI-SLAB by introducing semi-infinite elements in horizontal dimensions, Khazanovich (1994) developed ILSL2 that was capable of considering the effects of subgrade deformation under slab edges using Totsky model. This program offered a variety of subgrade model options such as the Pasternak model, Kerr model and ZSS model (Khazanovich and Ioannides 1994). Khazanovich et al. (2000) at the ERES Division of Applied Research Associates improved ILSL2 by development of ISLAB2000 to overcome finite element modeling limitations, enable curling analysis of slabs (and allowing slab and subgrade separation), and obtain the pavement responses due to temperature, traffic, and construction loading.

JSLAB

First version of JSLAB was developed by Tayabji and Colley (1986) based on an early version of ILLI-SLAB incorporating the Portland Cement Association’s (PCA’s) thickness design procedure to compute the critical stresses and deflections in JPCP, JRCP, and CRCP under different loading conditions. Several limitations of this program such as neglecting the self-weights, two-execution stage for thermal analysis, limited number of slabs for curling analysis, not finding the location and value of the maximum stress, and incapability to calculate the subgrade stress have been eliminated in JSLAB92 by verification of the program by conducting a comparison with other numerical and theoretical solutions (e.g., BISAR, FAA's H5l). However, the program has been revised in JSLAB 2004 to incorporate six subgrade models (spring, Winkler, Boussinesq, Vlasov, Kerr, and ZSS foundation), partial contact in slab/base interface, nonuniformly spaced circular or noncircular dowels in joints, warping effects due to moisture, a linear temperature and moisture distribution within a single layer pavement system, and perform the time history analysis under moving loads at specified locations.

EVERFE

This 3D finite element analysis tool was developed by the collaboration of University of Washington and WSDOT to present a program capable of capturing detailed local response, on which 2D programs are limited. The program is also capable of modeling multiple slabs (up to nine slabs), extended shoulder, dowels (including mislocation or looseness) and tie-bars, load configurations, linear or non-linear aggregate interlock shear transfer at the skewed or normal joints, the contact between the slab and up to three bonded and/or unbonded base layers, and non-linear modeling of thermal gradient (Davids et al. 1998). Even though the utilized modeling has been experimentally verified and was improved in later versions (Davids et al. 2003), it has still limitations on the subgrade modeling by a dense liquid (Winkler) model and axle loading within the slab length.

2.3. Model Validation Process

Once the best computer program for the analysis of rigid pavement has been developed, the validation process of this tool will be initiated. However, two major steps preceding the model validation are verification and calibration.

Verification is defined as “the process of determining that a computational model accurately represents the underlying mathematical model and its solution” (Schwer 2006). Verification consists of bench-marking (or code verification) and calculation verification. Bench-marking is defined as establishing confidence that the mathematical model and solution algorithms are working correctly. Comparison of computer code outputs with analytical solutions is the most popular bench-marking technique, which requires manufactured solutions to expand the number and complexity of analytical solutions and even comparing the results with the existing modeling tools. Calculation verification is associated with establishing confidence that the discrete solution of the mathematical model is accurate. It includes estimating the errors in the numerical solution due to discretization, comparing numerical solutions at more meshes with increasing mesh resolution to determine the rate of solution convergence.

Calibration (or model parameter estimation) is defined as "the process of adjusting physical modeling parameters in the computational model to improve agreement with experimental data" (Schwer 2006, Kennedy and O'Hagan 2001). A computer model will have a number of context-specific inputs that define a particular situation in which the model is to be used. When the values of one or more of these context-specific inputs are unknown, experimentation is used to learn about them. In current practice, model calibration consists of searching for a set of values of the unknown inputs such that the measured data fit as closely as possible to the corresponding outputs of the model. These values are considered as estimates of the context-specific inputs, and the model is then used to estimate the behavior of the process in this context by setting these inputs to their estimates. To achieve the highest possible agreement between the results of experimentations and those from simulations, a multi-objective optimization process will be implemented to minimize the errors while adjusting the inputs.

Generally, computer (or mathematical) model validation is defined as the "process of determining the degree to which a computer model is an accurate representation (within some tolerance) of the real world from the perspective of the intended model applications." (U.S. DOE 2000, AIAA 1998). This validation is accomplished through the comparison of estimation from a model to experimental results. The main reasons of model validation include the need to replace experimentation with model predictions with some degree of accuracy, necessity to prove the reliability of a structure under a broad range of operating conditions or environments (which is very expensive to be done in the field), and to assure that the design modifications yield acceptable system behavior.

Before a well-structured validation comparison can be performed, there are several decisions that must be made and some criteria that must be defined:

1. *Specify the model use and purpose*: Comparison of the current model relative to the ultimate system of interest (the physical system and its associated environment) to a particular level of accuracy.
2. *Specify the conceptual model*: The conceptual model of the physical system is the set of assumptions and descriptions of physical processes representing the behavior of the system of interest, and from which the mathematical model and the pre-validation experiments can be constructed.
3. *Specify pre-validation experiments*: These experiments must be specified early in the planning process in order to develop the details of the computational model, which contains the appropriate components to be considered.
4. *Specify the mathematical model* (mathematical equations, boundary conditions, excitations, initial conditions, etc.).
5. *Specify the computational model* (the numerical implementation of the mathematical model in the form of numerical discretization, solution algorithm, and convergence criteria): To assure that the features of the mathematical model are captured with sufficient accuracy to guarantee positive validation results.
6. *Specify the physical system response measures of interest*: The response measures of interest are the quantities that are functions of system behavior or response to be used in the comparison of model predictions to experimental system predictions, which can be inferred from excitations and responses of the experiment and the model.
7. *Specify validation metrics*: The precise mathematical means for comparing model predicted response measures to response measures computed from experimental responses (e.g., statistical parameters such as RMSE).
8. *Specify the domain of comparison*: The region of environment space and model and physical system parameter space within which experiment responses will be measured and model predictions will be made. The results of the comparison are normally specified

only for that domain unless a careful extrapolation implies that the results are useful over an extended domain.

9. *Specify adequacy or accuracy criteria* (validation requirements): Adequacy and accuracy criteria define the values that validation metrics must assume in order for the model to be judged valid.

After the validation is performed, two actions can be taken regarding the use of the computer model. If the model is valid, it can be used as the basis for development of the model in the next step of the hierarchy (in modular programming of the computer code) or it can be used to make predictions of structural response within the domain of comparison. If the mode is not valid, the source of errors can be found in the following categories:

- Additional, un-modeled sources of randomness exist: Identify the additional sources of randomness, perform calibration testing, specify the probability models for the additional sources of randomness, re-validate.
- Insufficient physics included in the model: Augment the model physics (such as non-linear behavior in structural response), perform calibration testing to identify the parameters of the physics model, re-validate.
- Inadequate data were collected during calibration and/or validation experiments (Sensitivity of the validation conclusion to the amount of data): Collection of additional data and improvement of model parameters, followed by revalidation.
- Form of the response measure of interest may be too difficult for the model to predict correctly: Modify the response measures and re-validate (not simply change from one response measure to another).
- The adequacy or accuracy criteria used during the validation comparisons are too stringent for the model to satisfy (modelers, experimentalists, and validation analysts may have been too optimistic about the potential for model accuracy): Modify the adequacy criteria and re-validate.

2.4. Optimization Techniques

To minimize the error in the predictions from a computer model with respect to the experimental data for verification, calibration and validation purposes, several mathematical optimization techniques are available. In mathematics, conventional optimization problems are usually stated in terms of minimization. An optimization (minimization) problem can be represented in the following way:

Given a function $f : A \rightarrow \mathbb{R}$ (from some set A to real numbers), find an element $\mathbf{x}_0 \in A$ such that $f(\mathbf{x}_0) \leq \mathrm{f}(\mathbf{x})$ for all $\mathbf{x} \in A$.

Typically, *A* is some subset of the Euclidean space $\mathbb{R}^n$, often specified by a set of constraints, equalities or inequalities that the members of *A* have to satisfy. The domain *A* of *f* is called the search space or the choice set, while the elements of *A* are called candidate solutions or feasible solutions. The function *f* is called an objective function (or loss function, cost function energy function. A feasible solution that minimizes (or maximizes) the objective function is called an optimal solution. In Machine Learning, it is always necessary to continuously evaluate the quality of a data model by using a cost function where a minimum implies a set of possibly optimal parameters with an optimal (lowest) error (Miettinen 2012, Hwang and Masud 2012).

MULTI-OBJECTIVE OPTIMIZATION

Many real-world practical engineering and scientific application problems involve simultaneous optimization of several competing objectives. To these problems, there is often no single optimal solution, but rather a set of alternative solutions. These solutions are considered to be the best because no other solutions in the decision space (feasible solution space) are superior to them when considering all the target objectives. One objective is improved always at the expense of other objectives at the same time for these multi-objective optimization problems.

As such, a multi-objective optimization problem (MOOP) is an optimization problem that involves multiple objective functions. Adding more than one objective to an optimization problem adds complexity. For example, to optimize a structural design, one would desire a design that is both light and rigid. When two objectives conflict, a trade-off must be created. There may be one lightest design, one stiffest design, and an infinite number of designs that are some compromise of weight and rigidity.

To avoid long computational time, stochastic approaches seem to be particularly suitable in solving MOOPs. Evolutionary algorithms (EAs), which are the meta-stochastic methods that simulate the process of natural biological evolution, have been verified to be an effective and efficient tool for MOOPs as they have the capability to process a set of solutions in parallel and explore big search space in a reasonable time. Among the biological-inspired EAs, the most known approaches are the genetic algorithms (GAs), and recently, one of the most popular pioneering work with respect to the GAs for solving MOOPs is Pareto optimal front genetic algorithms.

OVERVIEW OF MOOPS

Generally, MOOPs contain several objectives to be minimized. Without the loss of generality, we assume that the optimization can be described as a minimization problem with m objectives and n variables, which in mathematical terms can be expressed as follows:

$$\begin{aligned} &\text{Minimize:} \quad \mathrm{F(x)} = (f_1(\mathrm{X}), f_2(\mathrm{X}), \ldots, f_m(\mathrm{X}))^T \\ &\text{s.t.} \quad \begin{cases} g_i(X) \le 0, & i = 1, 2, \ldots, k \\ h_j(X) = 0, & j = 1, 2, \ldots, l \end{cases} \end{aligned} \tag{2-9}$$

where $X = (x_1, x_2, \ldots, x_n) \in \Omega$ is a solution vector, Ω is the decision space, $g_i(X)$ and $h_j(X)$ are the optional inequality and equality constraints, respectively. The aim is to find a solution vector subject to the constraints, which minimizes the objective values. However, since the characters of these functions $f_1(\mathrm{X}), f_2(\mathrm{X}), \ldots, f_m(\mathrm{X})$ are usually in conflict with each other, when multi-objectives reach the optimal simultaneously, the result of which is a set of compromise solutions, i.e. the so-called Pareto optimal set.

PARETO OPTIMAL SOLUTION

As previously stated, in multi-objective optimization, there does not typically exist a feasible solution that minimizes all objective functions simultaneously. Therefore, attention is paid to Pareto optimal solutions; that is, solutions that cannot be improved in any of the objectives without degrading at least one of the other objectives (see Figure 2-3).

Pareto solutions are also called nondominated solutions, Pareto efficient solutions, or noninferior solutions. To better understand this concept, the following terms must be defined:

Pareto dominate: A vector $x^{(1)} = (x_1^{(1)}, x_2^{(1)}, ..., x_n^{(1)})$ is said to dominate another vector $x^{(2)} = (x_1^{(2)}, x_2^{(2)}, ..., x_n^{(2)})$, note as $x^{(1)} \prec x^{(2)}$ if and only if:

$$(\forall i \in \{1, 2, ..., k\}, f_i(x^{(1)}) \leq f_i(x^{(2)})) \wedge (\exists i \in \{1, 2, ..., m\}, f_i(x^{(1)}) < f_i(x^{(2)})) .$$

Pareto optimal: For a given multi-objective problem, a solution $x^{(1)} \in \Omega$ is the Pareto optimal if and only if:

$$\neg \exists x^{(2)} \in \Omega : x^{(1)} \prec x^{(2)} .$$

Pareto optimal set: The set *P* in the decision variable space consisting of all Pareto optimality vectors:

$$P = \left\{ x^{(1)} \in \Omega \mid \neg \exists x^{(2)} \in \Omega : x^{(2)} \prec x^{(1)} \right\} .$$

Pareto optimal front: The plot of a set *PF* which includes the values of all objective functions corresponding to the solution in *P* (Yuan et al. 2015):

$$PF = \left\{ F(x) = (f_1(x), f_2(x), .., f_m(x))^T \mid x \in P \right\} .$$

A solution is said to be Pareto-optimal if it is not dominated by any other solutions in Ω. As can be seen in Figure 2-3, each of the boxed points, including points A and B, represent Pareto optimal solutions and a set of these points is called Pareto optimal set. However, point C is not a Pareto optimal solution because it was dominated by both points A and B. The red line connecting the Pareto optimal solutions shows the Pareto optimal front *PF*.

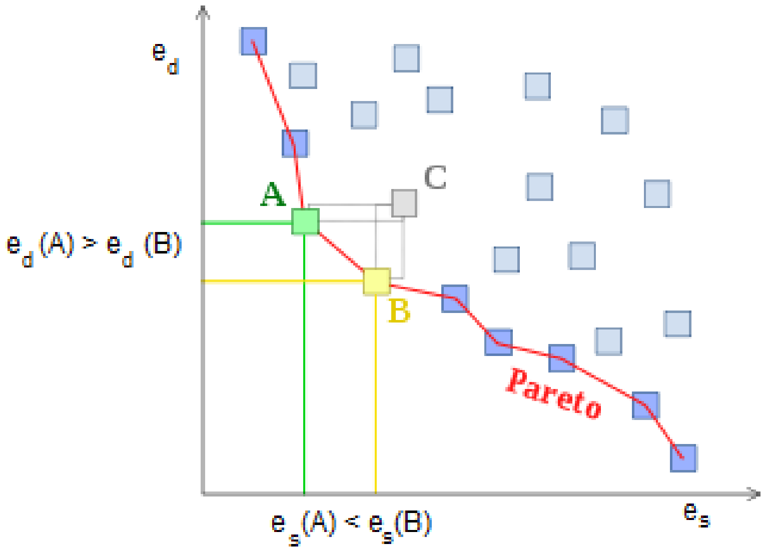

Figure 2-3. Schematic View of a Pareto Optimal Front

The goal of multi-objective intelligence algorithms is to find a uniformly distributed front PF_{known} from multi-objective EAs that approximates the real Pareto-optimal front PF_{true} (Van Veldhuizen and Lamont 2000).

3. Rigid Pavement Analysis System (RPAS)

Researchers from the University of Texas at El Paso developed the Rigid Pavement Analysis System (RPAS) as a tool for evaluating responses of jointed concrete pavement systems under environmental and vehicle loadings. By improving several features of the previous version of this pavement analysis tool, namely NYSLAB (Carrasco et al. 2009), RPAS makes use of the FE method coded in MATLAB® and was developed with the purpose of calculating pavement responses due to any arbitrary vehicle loading configuration and temperature profile using different foundation models.

3.1. Modeling Pavement Slab

There is no explicit limit in the number of concrete and foundation layers that can be modeled in RPAS and no limit in the number of jointed slabs that can be included in the analysis. Pavement slab layers are modeled as plate elements that account for the shear deformation as they become significant for relatively thick plates. When two or more pavement slab layers are modeled, the interface between them can be considered either bonded or unbonded. In bonded slabs, shear stresses can be transferred through their interface and no sliding or separation can occur between them. On the other hand, unbonded slabs can separate and move relative to each other and shear tractions, due to friction, can be produced in their interface. To model the contact between two unbonded slabs, in addition to an isoparametric 18-node interface element (Zokaei-Ashtiani et al. 2014), a new non-linear contact and friction model was introduced which will be explained below.

Bonded pavement slabs are modeled as composite laminated plates in RPAS using the first order shear deformation theory (FSDT) or laminated plate theory. The laminated domain is discretized using nine-node isoparametric quadrilateral elements (Figure 1a), each element having five degrees of freedom (DOF) per node: two in-plane displacements in the *x* and *y* directions (U_x , U_y), vertical deflection in *z* (U_z), and two rotations about *y* and *x* axes (ϕ_x , ϕ_y) (Figure

1b). These dependent variables (U_x, U_y, U_z, ϕ_x, ϕ_y) are approximated using the Lagrange interpolation function (Zokaei-Ashtiani et al. 2014).

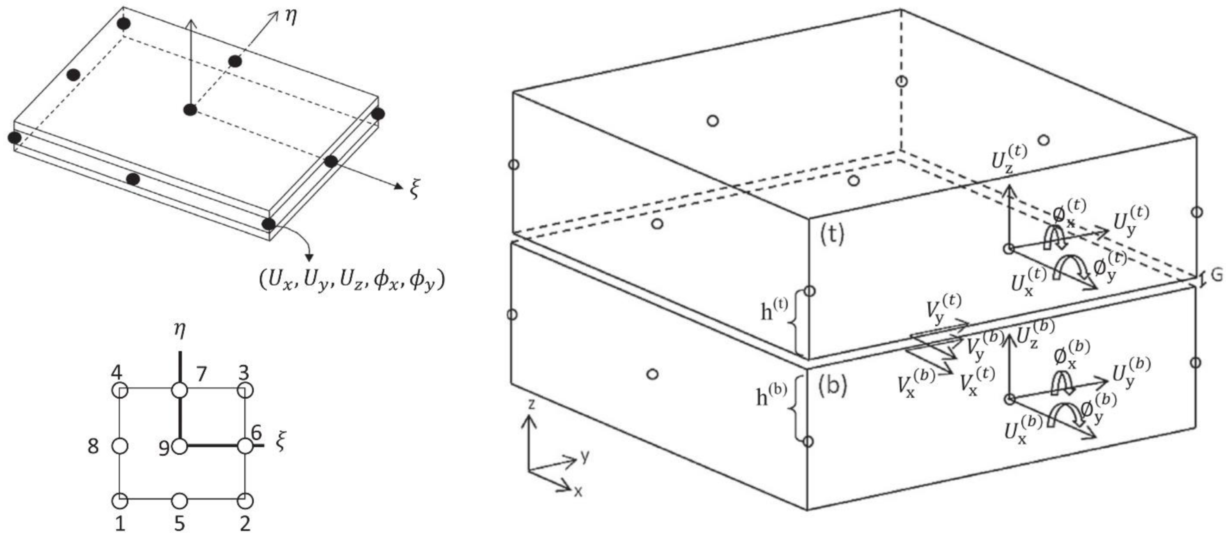

(a) **(b)**

Figure 3-1. (a) Five Degrees of Freedom in the 9-Node Quadrilateral Element Used to Model Bonded Pavements (b) Kinematics of Two Plates in Contact* (Zokaei-Ashtiani et al. 2014)

* U_x, U_y, U_z, ϕ_x, ϕ_y are the five degrees of freedom, ξ and η are the local coordinates, V_x and V_y are the relative displacement vectors, *G* is the gap between the plates caused by deformation under traffic or thermal loading, superscripts (*t*) and (*b*) represent the top and the bottom surface of the interface elements, respectively.

FINITE ELEMENT MODELING OF THE SLAB

The first order shear deformation theory (FSDT) or Mindlin laminated plate theory as an extension of the Mindlin plate theory to composite laminates was used in RPAS to model the slabs. This model is capable of capturing shear deformations, which are important in the modeling of thick slabs. Considering a laminated plate with total thickness of *h* composed of *N* orthotropic layer which are completely bonded together (Figure 3-1), the position (*u,v,w*) of each arbitrary point in the laminate after deformation can be expressed as

$$u(x,y,z) = u_0(x,y) + z\phi_x(x,y)$$

$$v(x,y,z) = v_0(x,y) + z\phi_y(x,y) \quad (3\text{-}1)$$
$$w(x,y,z) = w_0(x,y)$$

where u_0, v_0, w_0 are the displacements of that arbitrary point in the laminate mid-plane (z =0), and ϕ_x, ϕ_y are the rotations about the y and x axes, respectively. Therefore, the strain tensor can be expressed as (Reddy 2004):

$$\begin{bmatrix} \epsilon_{xx} \\ \epsilon_{yy} \\ \gamma_{xy} \end{bmatrix} = \begin{bmatrix} {\epsilon^0}_{xx} \\ {\epsilon^0}_{yy} \\ {\gamma^0}_{xy} \end{bmatrix} + \begin{bmatrix} {\epsilon^1}_{xx} \\ {\epsilon^1}_{yy} \\ {\gamma^1}_{xy} \end{bmatrix} = \begin{bmatrix} \dfrac{\partial u_0}{\partial x} \\ \dfrac{\partial v_0}{\partial y} \\ \dfrac{\partial u_0}{\partial y} + \dfrac{\partial v_0}{\partial x} \end{bmatrix} + z \begin{bmatrix} \dfrac{\partial \emptyset_x}{\partial x} \\ \dfrac{\partial \emptyset_y}{\partial y} \\ \dfrac{\partial \emptyset_x}{\partial y} + \dfrac{\partial \emptyset_y}{\partial x} \end{bmatrix} \quad (3\text{-}2)$$

$$\begin{bmatrix} \gamma_{yz} \\ \gamma_{xz} \end{bmatrix} = \begin{bmatrix} \dfrac{\partial w_0}{\partial y} + \emptyset_y \\ \dfrac{\partial w_0}{\partial x} + \emptyset_x \end{bmatrix} \quad (3\text{-}3)$$

where ε_{xx}, ε_{yy}, γ_{xy} are the in-plane strains which are linear through the laminate thickness, and γ_{yz}, γ_{xz} are out of plane shear strains which are constant through the thickness.

By applying the principle of virtual displacement into the governing equation of FSDT, the equilibrium equations can be derived as follows:

$$\frac{\partial N_{xx}}{\partial x} + \frac{\partial N_{xy}}{\partial y} = 0 \quad (3\text{-}3)$$

$$\frac{\partial N_{xy}}{\partial x} + \frac{\partial N_{yy}}{\partial y} = 0 \quad (3\text{-}4)$$

$$\frac{\partial V_x}{\partial x} + \frac{\partial V_y}{\partial y} + q = 0 \quad (3\text{-}5)$$

$$-V_x + \frac{\partial M_{xx}}{\partial x} + \frac{\partial M_{xy}}{\partial y} = 0 \quad (3\text{-}6)$$

$$-V_y + \frac{\partial M_{xy}}{\partial x} + \frac{\partial M_{yy}}{\partial y} = 0 \quad (3\text{-}7)$$

where, N_{xx}, N_{yy}, N_{xy} denote in-plane force resultants, M_{xx}, M_{yy}, *and* M_{xy} denote Moment resultants, V_x, V_y are out-of-plane shear force resultants in the laminate, and q is the distributed load applied to the laminate.

Using laminate constitutive equation for *N*-layer of lamina with orthotropic material and using Hooke's law, the resultant forces and moments in a matrix form can be expressed as the following constitutive equations:

$$\begin{bmatrix} N_{xx} \\ N_{yy} \\ N_{xy} \end{bmatrix} = \begin{bmatrix} A_{11} & A_{12} & A_{13} \\ A_{12} & A_{22} & A_{23} \\ A_{13} & A_{23} & A_{33} \end{bmatrix} \begin{bmatrix} \varepsilon^0{}_{xx} \\ \varepsilon^0{}_{yy} \\ \gamma^0{}_{xy} \end{bmatrix} + \begin{bmatrix} B_{11} & B_{12} & B_{13} \\ B_{12} & B_{22} & B_{23} \\ B_{13} & B_{23} & B_{33} \end{bmatrix} \begin{bmatrix} \varepsilon^1{}_{xx} \\ \varepsilon^1{}_{yy} \\ \gamma^1{}_{xy} \end{bmatrix} \tag{3-8}$$

$$\begin{bmatrix} M_{xx} \\ M_{yy} \\ M_{xy} \end{bmatrix} = \begin{bmatrix} B_{11} & B_{12} & B_{13} \\ B_{12} & B_{22} & B_{23} \\ B_{13} & B_{23} & B_{33} \end{bmatrix} \begin{bmatrix} \varepsilon^0{}_{xx} \\ \varepsilon^0{}_{yy} \\ \gamma^0{}_{xy} \end{bmatrix} + \begin{bmatrix} D_{11} & D_{12} & D_{13} \\ D_{12} & D_{22} & D_{23} \\ D_{13} & D_{23} & D_{33} \end{bmatrix} \begin{bmatrix} \varepsilon^1{}_{xx} \\ \varepsilon^1{}_{yy} \\ \gamma^1{}_{xy} \end{bmatrix} \tag{3-9}$$

$$\begin{bmatrix} V_x \\ V_y \end{bmatrix} = k \begin{bmatrix} As_{11} & As_{12} \\ As_{21} & As_{22} \end{bmatrix} \begin{bmatrix} \gamma_{xz} \\ \gamma_{yz} \end{bmatrix} \tag{3-10}$$

where, A_{ij} are called extensional stiffness, D_{ij} are bending stiffness, B_{ij} are bending-extensional coupling stiffness, and As_{ij} are shear stiffness, which are defined in terms of stiffness and thickness of each layer.

By applying the principle of virtual displacement and expanding the equilibrium equations, the finite element model of the first-order shear deformation theory for linear and static case will be obtained as:

$[K^e]\{U^e\} = \{F^e\}$

$$\begin{bmatrix} [K^{11}] & [K^{12}] & [K^{13}] & [K^{14}] & [K^{15}] \\ [K^{12}]^T & [K^{22}] & [K^{23}] & [K^{24}] & [K^{25}] \\ [K^{13}]^T & [K^{23}]^T & [K^{33}] & [K^{34}] & [K^{35}] \\ [K^{14}]^T & [K^{24}]^T & [K^{11}]^T & [K^{44}] & [K^{45}] \\ [K^{15}]^T & [K^{25}]^T & [K^{35}]^T & [K^{45}]^T & [K^{55}] \end{bmatrix} \begin{Bmatrix} u^e \\ v^e \\ w^e \\ {\phi_x}^e \\ {\phi_x}^e \end{Bmatrix} = \begin{Bmatrix} F^1 - {F_T}^1 \\ F^2 - {F_T}^2 \\ F^3 \\ F^4 - {F_T}^4 \\ F^5 - {F_T}^5 \end{Bmatrix} \tag{3-11}$$

where the elements of the sub-matrices $[K^{\alpha\beta}]$ for $\alpha = 1, 2, \ldots, 5$ and their numerical integral expressions are defined using the Gauss quadrature method (Zokaei-Ashtiani 2014). These elements are expressed as a function of extensional stiffness, bending stiffness, and bending-extensional coupling stiffness as defined above.

3.2. Modeling Temperature in the Slab

Uniform temperature-change, within the depth of the pavement slabs during daily temperature variation, can cause thermal expansion and contraction in concrete slabs. In RPAS, the impact of horizontal interaction between adjacent jointed slabs, due to thermal expansion in producing additional compressive stress, is considered in the mathematical model. RPAS can simulate a non-linear temperature profile throughout the slab thickness, allowing for the modeling of partial contact between the slab and foundation due to curling (Zokaei-Ashtiani et al. 2014). The pavement temperature measured at various depths (z =depth from mid-plane of the slab) and times of day can be curve-fitted to a three-dimensional polynomial as follows:

$$\Delta T = a_0 + a_1 z + a_2 z^2 + a_3 z^3 \qquad (3\text{-}12)$$

where a_0 contributes to the expansion or contraction of the neutral plane of the concrete slab, a_1 is associated with the linear temperature difference between the top and bottom of slab, a_2 and a_3 affect the non-linear temperature profile that produce internal stresses in the PCC slab regardless of its external constraints.

However, an accurate modeling of the effect of thermal loads on the concrete pavement requires considering the non-linear built-in (set) temperature profile $T_{Set}(z)$ (also called the zero-stress temperature profile in AASHTO MEPDG) in addition to the non-uniform temperature profile due to temperature change $T(z)$ (Mohamed and Hansen 1997, Chen et al. 2014). Built-in temperature profile is developed in the newly constructed slabs during concrete setting and its magnitude depends on the time of placement, curing quality, the ambient conditions and the mixture properties. Thus, the effective temperature profile should be defined as $\Delta T = T(z) - T_{Set}(z)$. This effective temperature profile will also be non-linear and thus in addition to the stress caused by the linear component of temperature profile, $(\sigma_{Th})_{linear}$, a residual thermal stress distribution, $(\sigma_{Th})_{res}$ must be calculated. RPAS uses the finite element formulation to calculate this residual stress; however, an analytical solution can be obtained using Eq. (3-13). To derive this analytical solution, the slab was modeled as a plate with linear elastic and isotropic material behavior that is assumed to be totally restrained against deformation. By applying Hooke's law and considering the stress state in two dimensions, Eq. (3-13) can be obtained:

$$(\sigma_{Th})_{res} = \frac{E}{1-\nu}\left[-\varepsilon(z) + \frac{12M_T}{h^3}(z) + \frac{N_T}{h}\right] \tag{3-13}$$

where E , ν , and h are Young's modulus, Poisson's ratio, and thickness of the slab, respectively, z is the distance from slab mid-depth, and the effect of built-in temperature ($T_{Set}(z)$) is taken into account in the calculation of $\varepsilon(z) = \alpha\ \Delta T$ (α =concrete's coefficient of thermal expansion) as well as in the calculation of M_T and N_T, which are the constants corresponding to bending moment and normal force at the slab mid-depth.

FINITE ELEMENT MODELING OF THE THERMAL LOADS

The truck load in RPAS is modeled as equivalent series of point loads. However, the resultant thermal forces and thermal moments for each laminated plate (bonded pavement slabs) can be expressed as:

$$N_T = \sum_{k=1}^{N} \int_{Z_k}^{Z_{k+1}} Q^{(k)} \alpha^{(k)} \Delta T \, dz \tag{3-14}$$

$$M_T = \sum_{k=1}^{N} \int_{Z_k}^{Z_{k+1}} Q^{(k)} \alpha^{(k)} \Delta T \, z \, dz \tag{3-15}$$

where Q is the stiffness components which is the function of modulus of elasticity and Poisson's ratio and α is the coefficient of thermal expansion for each layer in the N-layer laminate,

$$Q_{ij}^{k} = \frac{E^{(k)}}{1-\nu^{(k)2}}\begin{bmatrix} 1 & \nu^{(k)} & 0 \\ \nu^{(k)} & 1 & 0 \\ 0 & 0 & \frac{1-\nu^{(k)}}{2} \end{bmatrix} \tag{3-16}$$

$$\alpha^{(k)} = \begin{bmatrix} \alpha \\ \alpha \\ 0 \end{bmatrix} \tag{3-17}$$

The total laminate constitutive equations become,

$$\begin{Bmatrix} \{N\} \\ \{M\} \end{Bmatrix} = \begin{bmatrix} [A] & [B] \\ [B] & [D] \end{bmatrix} \begin{Bmatrix} \{\varepsilon^0\} \\ \{\varepsilon^1\} \end{Bmatrix} - \begin{Bmatrix} \{N_T\} \\ \{M_T\} \end{Bmatrix} \tag{3-18}$$

where, the matrices N and M are the total resultant force and moment in the laminate defined by Zokaei-Ashtiani (2014). In the finite element model of the laminate, the contribution of thermal loads is added to the force vector (Eq. 3-11) as,

$$F_T^1 = \int_s \frac{\partial N_i}{\partial x} N_T dxdy \tag{3-19}$$

$$F_T^2 = \int_s \frac{\partial N_i}{\partial y} N_T dxdy \tag{3-20}$$

$$F_T^4 = \int_s \frac{\partial N_i}{\partial x} M_T dxdy \tag{3-21}$$

$$F_T^5 = \int_s \frac{\partial N_i}{\partial y} M_T dxdy \tag{3-22}$$

where, N_i is the interpolation function (Zokaei-Ashtiani 2014).

3.3. Modeling Load Transfer Devices

Adjacent slabs in a jointed concrete pavement system in RPAS can be connected with dowels, tie-bars and aggregate or key interlock, or a combination of those load transfer devices through their joints. Dowels and tie-bars are used in the transverse and longitudinal joints, respectively, and can be placed in uniform or non-uniform intervals.

FINITE ELEMENT MODELING OF THE DOWELS AND TIE-BARS

Beam elements were used to model dowels and tie-bars in RPAS. For this reason, a Timoshenko beam is used for the modeling of short-beam (thick- beam) elements. Thus, the stiffness matrix of dowels and tie-bars account for two degrees of freedom. However, the total stiffness matrix of those elements should include the components corresponding to all the degrees of freedom considered in the modeling of pavement slabs. Therefore, the total stiffness matrix for dowels and tie-bars considering five degrees of freedom per node of a beam element are derived as:

$$[K_{dowel}] = \begin{array}{cc} \begin{bmatrix} 0 & 0 & 0 & 0 & 0 & 0 & 0 & 0 & 0 & 0 \\ 0 & D & 0 & 0 & 0 & 0 & -D & 0 & 0 & 0 \\ 0 & 0 & D & 6LC & 0 & 0 & 0 & -D & 6LC & 0 \\ 0 & 0 & 6LC & (4+\emptyset)CL^2 & 0 & 0 & 0 & -6LC & (2-\emptyset)CL^2 & 0 \\ 0 & 0 & 0 & 0 & 0 & 0 & 0 & 0 & 0 & 0 \\ 0 & 0 & 0 & 0 & 0 & 0 & 0 & 0 & 0 & 0 \\ 0 & -D & 0 & 0 & 0 & 0 & D & 0 & 0 & 0 \\ 0 & 0 & -D & -6LC & 0 & 0 & 0 & D & -6LC & 0 \\ 0 & 0 & 6LC & (2-\emptyset)CL^2 & 0 & 0 & 0 & -6LC & (4+\emptyset)CL^2 & 0 \\ 0 & 0 & 0 & 0 & 0 & 0 & 0 & 0 & 0 & 0 \end{bmatrix} & \begin{array}{c} (u)_L \\ (v)_L \\ (w)_L \\ (\emptyset_x)_L \\ (\emptyset_y)_L \\ (u)_R \\ (v)_R \\ (w)_R \\ (\emptyset_x)_R \\ (\emptyset_y)_R \end{array} \end{array} \qquad (3\text{-}23)$$

$$[K_{tie}] = \begin{array}{cc} \begin{bmatrix} D & 0 & 0 & 0 & 0 & -D & 0 & 0 & 0 & 0 \\ 0 & A_tE_t/L & 0 & 0 & 0 & 0 & -A_tE_t/L & 0 & 0 & 0 \\ 0 & 0 & D & -6LC & 0 & 0 & 0 & -D & -6LC & 0 \\ 0 & 0 & -6LC & (4+\emptyset)CL^2 & 0 & 0 & 0 & 6LC & (2-\emptyset)CL^2 & 0 \\ 0 & 0 & 0 & 0 & 0 & 0 & 0 & 0 & 0 & 0 \\ -D & 0 & 0 & 0 & 0 & D & 0 & 0 & 0 & 0 \\ 0 & -A_tE_t/L & 0 & 0 & 0 & 0 & A_tE_t/L & 0 & 0 & 0 \\ 0 & 0 & -D & 6LC & 0 & 0 & 0 & D & 6LC & 0 \\ 0 & 0 & -6LC & (2-\emptyset)CL^2 & 0 & 0 & 0 & 6LC & (4+\emptyset)CL^2 & 0 \\ 0 & 0 & 0 & 0 & 0 & 0 & 0 & 0 & 0 & 0 \end{bmatrix} & \begin{matrix} (u)_L \\ (v)_L \\ (w)_L \\ (\emptyset_x)_L \\ (\emptyset_y)_L \\ (u)_R \\ (v)_R \\ (w)_R \\ (\emptyset_x)_R \\ (\emptyset_y)_R \end{matrix} \end{array}$$

(3-24)

where L is the joint spacing, $C = \dfrac{E_{LTD} I_{LTD}}{L^3(1+\phi)}$ (E_{LTD}, I_{LTD} = the elastic modulus and moment of inertia of the load transfer devices (dowel or tie bar), respectively), and $\phi = \dfrac{24 I_{LTD}(1+\nu_{LTD})}{A_{LTD} L^2}$ (ν_{LTD} =Poisson's ratio of the load transfer devices, A_{LTD} =effective cross-section of the load transfer devices), $D = \dfrac{1}{\dfrac{1}{DCI} + \dfrac{1}{12C}}$ (DCI =dowel-concrete interaction parameter, equal to 1.5×10^6 psi/in for practical purposes), E_t and A_t are the elastic modulus and cross-section area of tie bars, u, v, w are the displacements of load transfer devices in longitudinal (x), transverse (y) and vertical (z) directions, respectively, ϕ_x and ϕ_y denote the rotation of the load transfer devices in x and y directions, and the subscripts R and L show the degree of freedom on right and left end of the load transfer devices.

3.4. Modeling the Contact between Pavement Layers

The mechanical behavior of pavement is significantly influenced by the contact properties as well as frictional characteristics of pavement layers. Thus, an appropriate constitutive relationship for the slab-foundation interface needs to be defined. In addition to the existing gap element (to model the contact) and 2-D interface elements (to model both contact and friction)

(Carrasco et al. 2011, Zokaei-Ahtianai 2014), a new model has been implemented that associates the normal and frictional properties of each point of contact to the relative displacement of the corresponding nodes in two contacting surfaces (Bhatti 2006). As indicated in Figure 3-2a, the constitutive behavior for the normal contact must satisfy consistency condition, that is the contact force exists only if the gap between two contacting surfaces is closed i.e., either gap g or force F_n must be zero.

Therefore, the normal constraint function can be approximated by the following equation:

$$\phi(g,F_n)=\frac{g+F_n}{2}-\sqrt{\left(\frac{g-F_n}{2}\right)^2+\varepsilon}=0 \tag{3-25}$$

where ε is a small positive number, controlling the smoothness of the friction function in Figure 3-2b, which leads to a more efficient numerical convergence of the contact-friction solution as opposed to the linear or bilinear functions such as Coulomb model.

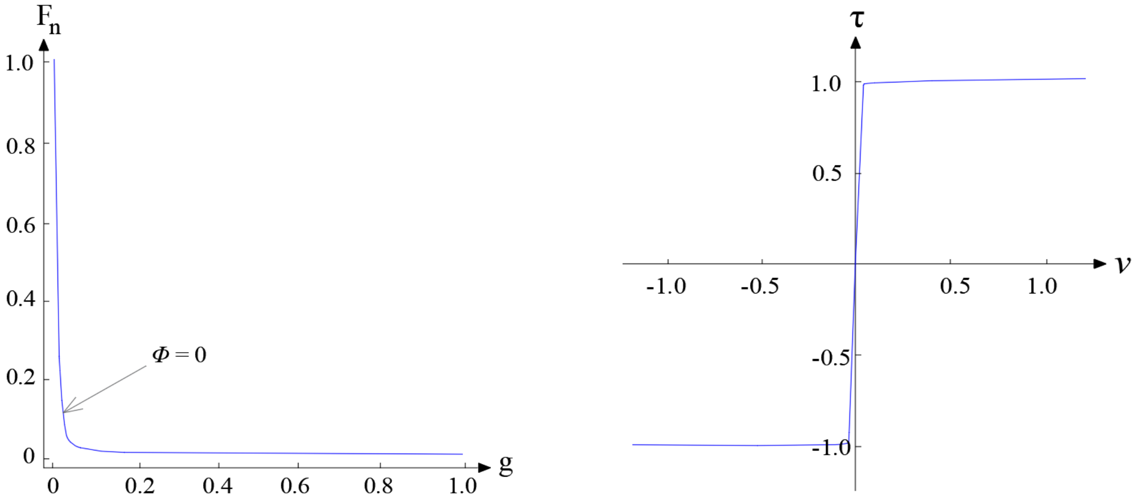

(a) **(b)**

Figure 3-2. Constitutive Contact-Friction Relationship (a) Normal Contact Function (b) Frictional Constraint Function (Bhatti 2006)

Regarding the tangential component of contact force, the frictional properties of the surfaces and the physical condition (i.e., sticking or sliding) play important role. The frictional constitutive equation in the tangential direction, which correlates the frictional tractions F_t to the tangential relative displacements v, is expressed as follows (see Figure 3-2b):

$$\psi(v,\tau) = \frac{F_t}{\mu F_n} - \frac{2}{\pi}\arctan\left(\frac{v}{\varepsilon}\right) \tag{3-26}$$

where μ is the coefficient of friction between the two surfaces.

The use of this non-linear model, as opposed to the commonly used 1D spring connections between contacting nodes, allows for the proper distribution of the normal and tangential stiffness and tractional forces for non-uniform meshes and, as a consequence, allows the for the friction and separation between layers due to slab curling to be realistically represented.

3.5. Modeling Supporting Layers

Three different foundation models are included in RPAS to idealize the behavior of the foundation system: Winkler, Vlasov and 3-D solid foundation (Carrasco et al. 2011, Aguirre 2020). Both the Winkler and Vlasov foundation models consider the slab supporting layers as an infinite set of linear elastic springs. These foundation models have been commonly used by different modeling programs for the purpose of modeling JCP, such as ILLI-SLAB (Tabatabaie and Barenberg 1980) and JSLAB (Tayabji and Colley 1986). To improve on the models, a 3-D solid foundation model was developed and incorporated into RPAS. In this model, the soil is discretized using 27-node hexahedron elements for each slab supporting layer (Figure 3-3). Compared to the standard 8-node hexahedron element, second order elements have demonstrated to require fewer elements for a given accuracy. This comparison will be made in the next section.

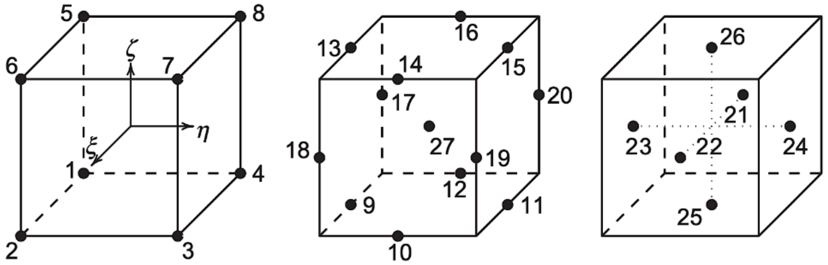

Figure 3-3. Numbering of the Developed Second-order 27-Node Hexahedron Element (node 27 at the Origin of ξ, η, ζ Coordinates) (Aguirre 2020)

The 3-D modeling of the foundation layer, in comparison to the use of subgrade reaction *k*, uses the moduli (modulus of elasticity and Poisson's ratio) for each supporting layer. Furthermore, this method allows for the calculation of responses at any given depth for each foundation layer. An extension of the foundation layers beyond the edge of the slabs was also developed to more realistically model the edge deflections and stresses close to the pavement edge.

FINITE ELEMENT MODELING OF THE FOUNDATION ELEMENTS

The finite element expression of the Winkler and Vlasov foundation models are well documented in Zokaei-Ashtiani (2014). This section describes the finite element modeling of the 3D foundation (Aguirre 2020). In this model, each foundation layer is discretized using 27-node hexahedron elements. Compared to the standard 8-node hexahedron element, second order elements have demonstrated to require fewer elements for a given accuracy. For the 27-node element shown in Figure 3-3, there are 81 element degrees of freedom (DOF), i.e., three DOFs for horizontal (longitudinal and transverse) and vertical translations associated with the 27 integration points.

After defining the shape functions and arranging the terms by their DOFs, the 27-node element strain vector can be computed by appropriate differentiation as follows:

$$\boldsymbol{\varepsilon} = \begin{pmatrix} \frac{\partial N_1}{\partial x} & 0 & 0 & 0 & 0 & \frac{\partial N_2}{\partial x} & 0 & 0 & \cdots \\ 0 & \frac{\partial N_1}{\partial y} & 0 & 0 & 0 & 0 & \frac{\partial N_2}{\partial y} & 0 & \cdots \\ 0 & 0 & \frac{\partial N_1}{\partial z} & 0 & 0 & 0 & 0 & \frac{\partial N_2}{\partial z} & \cdots \\ \frac{\partial N_1}{\partial y} & \frac{\partial N_1}{\partial x} & 0 & 0 & 0 & \frac{\partial N_2}{\partial y} & \frac{\partial N_2}{\partial x} & 0 & \cdots \\ 0 & \frac{\partial N_1}{\partial x} & \frac{\partial N_1}{\partial y} & 0 & 0 & 0 & \frac{\partial N_2}{\partial z} & \frac{\partial N_2}{\partial x} & \cdots \\ \frac{\partial N_1}{\partial z} & 0 & \frac{\partial N_1}{\partial x} & 0 & 0 & \frac{\partial N_2}{\partial z} & 0 & \frac{\partial N_2}{\partial x} & \cdots \end{pmatrix} \begin{pmatrix} u_1 \\ v_1 \\ w_1 \\ \theta_{x1} \\ \theta_{y1} \\ u_2 \\ v_2 \\ \vdots \end{pmatrix} = \boldsymbol{B}^T \boldsymbol{d} \tag{3-27}$$

Finally, the element stiffness matrix can be obtained by

$$\boldsymbol{k} = \int_V \boldsymbol{BDB^T} \,\mathrm{dV} \tag{3-28}$$

where $\boldsymbol{D}$ is the material property matrix and is written as follows:

$$\boldsymbol{D} = \frac{E}{(1+\nu)(1\text{-}2\nu)} \begin{bmatrix} 1-\nu & \nu & \nu & 0 & 0 & 0 \\ \nu & 1\text{-}\nu & \nu & 0 & 0 & 0 \\ \nu & \nu & 1\text{-}\nu & 0 & 0 & 0 \\ 0 & 0 & 0 & \frac{1\text{-}2\nu}{2} & 0 & 0 \\ 0 & 0 & 0 & 0 & \frac{1\text{-}2\nu}{2} & 0 \\ 0 & 0 & 0 & 0 & 0 & \frac{1\text{-}2\nu}{2} \end{bmatrix} \tag{3-29}$$

where E is the Young's modulus and ν is the Poisson's ratio. As will be discussed in Chapter 6, the moduli of foundation layer will be targeted to apply the calibration factors.

4. Field Test Data Collection and Pre-Validation

This chapter provides an introduction of the data collected on the pavement test sections in MnROAD and National Airfield Pavement Test Facility (NAPTF). The data processing method was explained for different types of tests (accelerated pavement testing, truck loading, FWD and HWD testing). A preliminary comparison of RPAS predictions of the pavement responses with the measured responses (pre-validation) has been performed.

4.1. MnROAD

Minnesota Road Research Project (MnROAD) is a cold region pavement research facility owned and operated by the Minnesota Department of Transportation (MnDOT). The facility is located on westbound I-94, northwest of the Twin Cities metropolitan area, was initially constructed between 1990 and 1993 and opened to traffic in 1994.

MNROAD DESCRIPTION

Thus far, MnROAD has four separate experimental roadway segments (Van Deusen et al. 2018):

- A 2.7-mile, two-lane, westbound I-94 Mainline (Figure 4-1a) with average traffic of 26,500 vehicles per day (13% trucks) providing approximately 750,000 flexible and 1,000,000 rigid ESALs per year.
- A 2.5-mile, two-lane closed loop Low-Volume Road (LVR) (Figure 4-1b) with the traffic provided by an 80-kip, 5-axle, tractor/trailer combination. This traffic loading is applied approximately 70 laps a day to the inside lane, whereas the outer lane is preserved for the study of environmental effects.
- A 1000-foot long, two-lane roadway in the MnROAD stockpile area that is being utilized for testing the impact of implements of husbandry (farm implements, towed vehicles to transport agricultural machinery, tools and chemicals) on low-volume roads. This area is used by contractors to test placement methods before proceeding to test sections.

- A 2.7-mile newly constructed segment (originally constructed in 1973), a series of asphalt overlay and partial-depth spall repair test sections on the original westbound concrete pavement lanes of I-94. This segment is used seven days per month when the traffic is diverted from the MnROAD mainline for monitoring or construction and thus receives about one-third cumulative ESALs of that that mainline I-94 experiences.

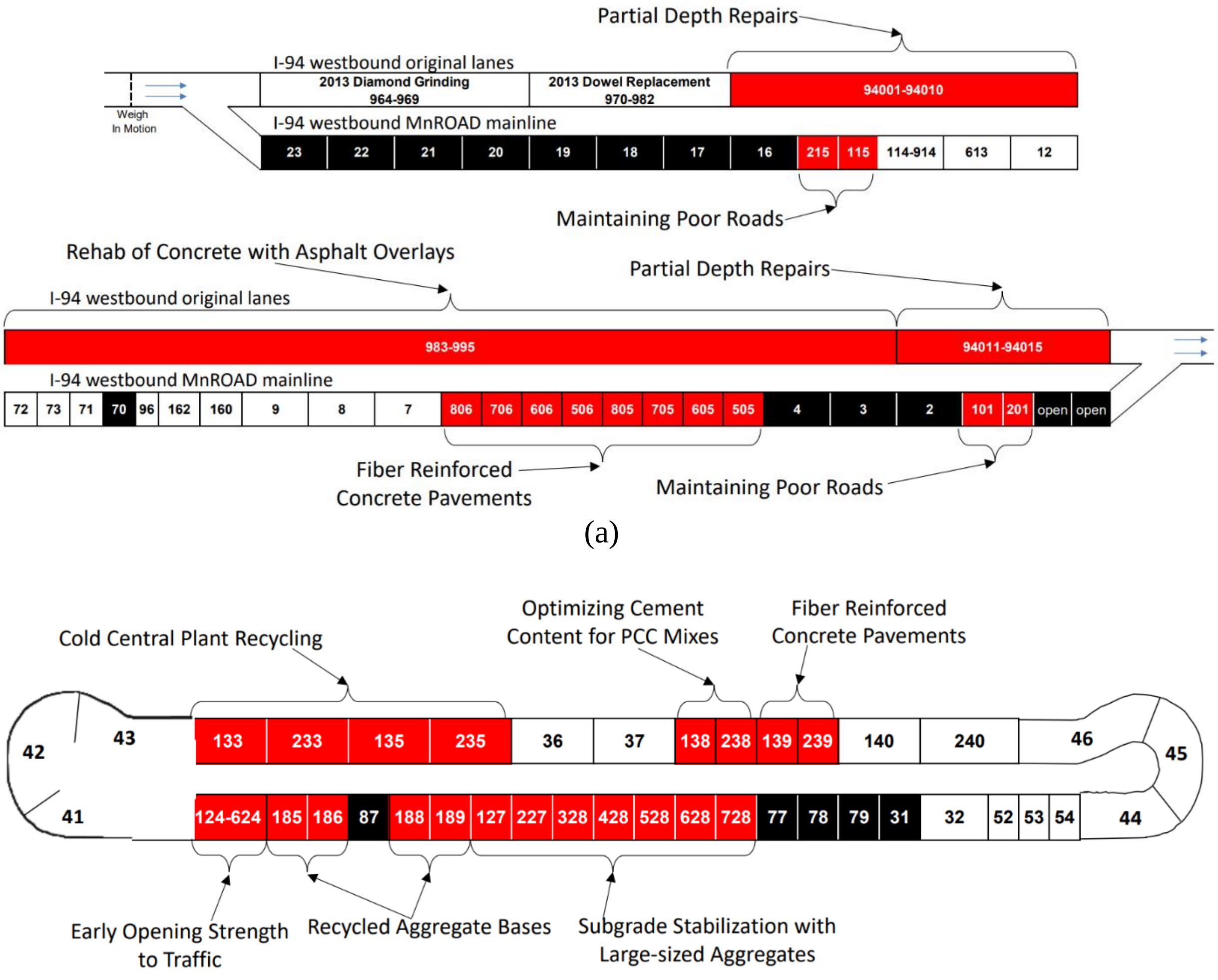

(a)

(b)

Figure 4-1. MnROAD NRRA Sections (a) I-94 Westbound Original and Mainline (b) Low Volume Road (LVR) (Van Deusen et al. 2018)

Since its initial construction in 1993, MnROAD has progressed through three phases. Phase-I (1994-2007) primarily investigated concrete and asphalt structural (thickness) designs. Phase-II (2008-2015) focused on partnerships with government, academia, and industry, led by

MnDOT through the former Transportation Engineering and Road Research Alliance. Phase-III (2016-current) has begun with the construction of eight flexible pavement sections as part of a National Cracking Performance Test experiment with a partnership with the National Center for Asphalt Technology (NCAT). During 2017 construction season, 35 new and unique test sections were added to address National Road Research Alliance (NRRA) high-priority research topics, conceived and planned by NRRA Rigid, Flexible, Preventive Maintenance, and Geotechnical team members.

In general, MnROAD enables researchers to evaluate pavement performance under real, physical conditions (traffic and environment), examine the interaction between factors such as moisture, frost, traffic loading, construction, and materials through use of an extensive instrumentation network, design customized experiments supporting specific research needs, and develop tools and methods based on actual performance data to improve design, construction, and maintenance of pavements.

MNROAD DATABASE

Pavement performance in MnROAD was being monitored since the initial opening to traffic in 1994 through laboratory testing (inspection, sampling, and testing of subgrade, bound/unbound base materials, concrete, and asphalt surface materials), static and dynamic sensor response (for environmental measurements and load response measurements, respectively), and field monitoring (e.g. stiffness, strength, distress measurements) over the life of each test cell. MnROAD monitoring begins with initial measurements after construction and follows pavement performance throughout its life. Forensic investigations are completed after each research project's conclusion. MnROAD database allows researchers to accurately record methodology and pertinent information for research and design purposes (MnROAD Data Library 2019).

STATIC SENSOR RESPONSE

Static or environmental measurements in MnROAD are usually made continuously for the life of the sensor or the cell. The time periods for data collection are most commonly 15 minutes.

Environmental measurements include temperature, moisture content, relative humidity, soil pressure, pore water pressure, strain, electrical resistivity. As one of the important factors in the analysis of stresses in concrete pavements, temperature profile data should be collected within the slabs and combined with the effect of repeated wheel loading. Temperature sensing at MnROAD is predominately accomplished with thermocouples but thermistors are also integrated into other instruments. To record the temperature data within the depth of the pavement, thermocouple arrays (trees) of varying lengths and numbers of sensors were constructed and installed in a drilled hole at the final base grade (just prior to paving) (see Figure 4-2). Thermocouple leads are connected to the data logger where the temperature is calculated by an internal function and stored in degrees Celsius.

Figure 4-2. Building and Installation of Temperature Sensing Arrays (Tree) At MnROAD

DYNAMIC SENSOR RESPONSE

Dynamic or load response measurements at MnROAD consist of collecting data seasonally from pavement sensors in response to dynamic loads applied using the test vehicle to provide uniform pavement loading. The test cells are closed to public traffic during scheduled data collections and load response is acquired in real time. Load response measurements may include stress, strain, displacement, pore water pressure, and accelerometer data. Dynamic strain measurements were taken as the 18-wheel, 5-axle, tractor trailer (weighed a total of 80,000 lb or 102,000 lb) to provide a known dynamic load to test the dynamic sensor instrumentation. The truck traveled slowly (at a speed of approximately 5 mph) forward and backward, systematically moved laterally across the instrumented slabs containing the embedded dynamic strain sensors. This slow speed should allow valid application of the data in future studies comparing measured load response to static load finite element models. To monitor the location of the tires with respect to the test slabs, a special video camera was mounted over the leading drive axle of the truck (passenger side). Measuring strips were painted on the instrumented slabs such that the camera captured the lateral location of the tire in the lane as it passed.

Truck driver operates the vehicle around 6 hours of driving or 80 laps a day and truck is tracked using Real Time Kinematic (RTK) GPS-based vehicle tracking system for accurate recording of the truck location as well as a GPS-based vehicle tracking system (VTS) to track the location of a vehicle’s tires during load response testing. Throughout the test period, different vehicles of heavy (102 kips) load configuration (1994-2008) in the outside lane and Minnesota highway legal 80 kips loading configuration (1994-current) were utilized. Therefore, depending on the year of the test, the type of the vehicle must be considered in the modeling.

Navistar Tractor with Fruehauf Trailer was used for loading during 1997 to 2011. The weights of this tractor are depicted in Figure 4-3 and the description and trailer configuration were similar to the Mack tractor-trailer. It has also been operated in legal and heavy load configurations. This truck uses Michelin XDA 11R24.5 for drive tires and Michelin XZA1+ LRG 11R24.5 for steer tires with tire pressure set to 100 psi.

Mack Tractor with Fruehauf Trailer was used for dynamic loading during 1994 to 2011 and the weights and description of this tractor and trailer configuration used at MnROAD are depicted in Figure 4-4. This truck was operated in two forms of legal (gross weight of 80 kips) and heavy (gross weight of 102 kips) load configurations in inside and outside lanes, respectively. It runs with Michelin XDA 11R24.5 MS drive tires and XZA 11R24.5 steer tires with the tire pressure of 100 psi.

For the sections tested under truck loading after 2012, a WorkStar Tractor with Towmaster trailer was used. This truck uses Michelin XDN2 11R22.5 drive tires and Continental 11.4R22.5 HSU steer tires with tire pressure set to 100 psi. Figure 4-5 shows the weights and description of this tractor and trailer configuration used at MnROAD.

Timeframe	Total Weight (lbs)	Steering Axle	Front axle Tractor tandem	Back axle Tractor tandem	Front axle Trailer Tandem	Back axle Trailer Tandem
June 15, 1994 Present	102,400	12,400	21,400	23,400	22,100	23,100
			44,800		45,200	

Figure 4-3. Weight Distribution and Axle Configuration of the 102 kips Navistar Tractor with Fruehauf Trailer Used at MnROAD (1994-current) As Heavy Load Configuration (MnROAD Data Library 2019)

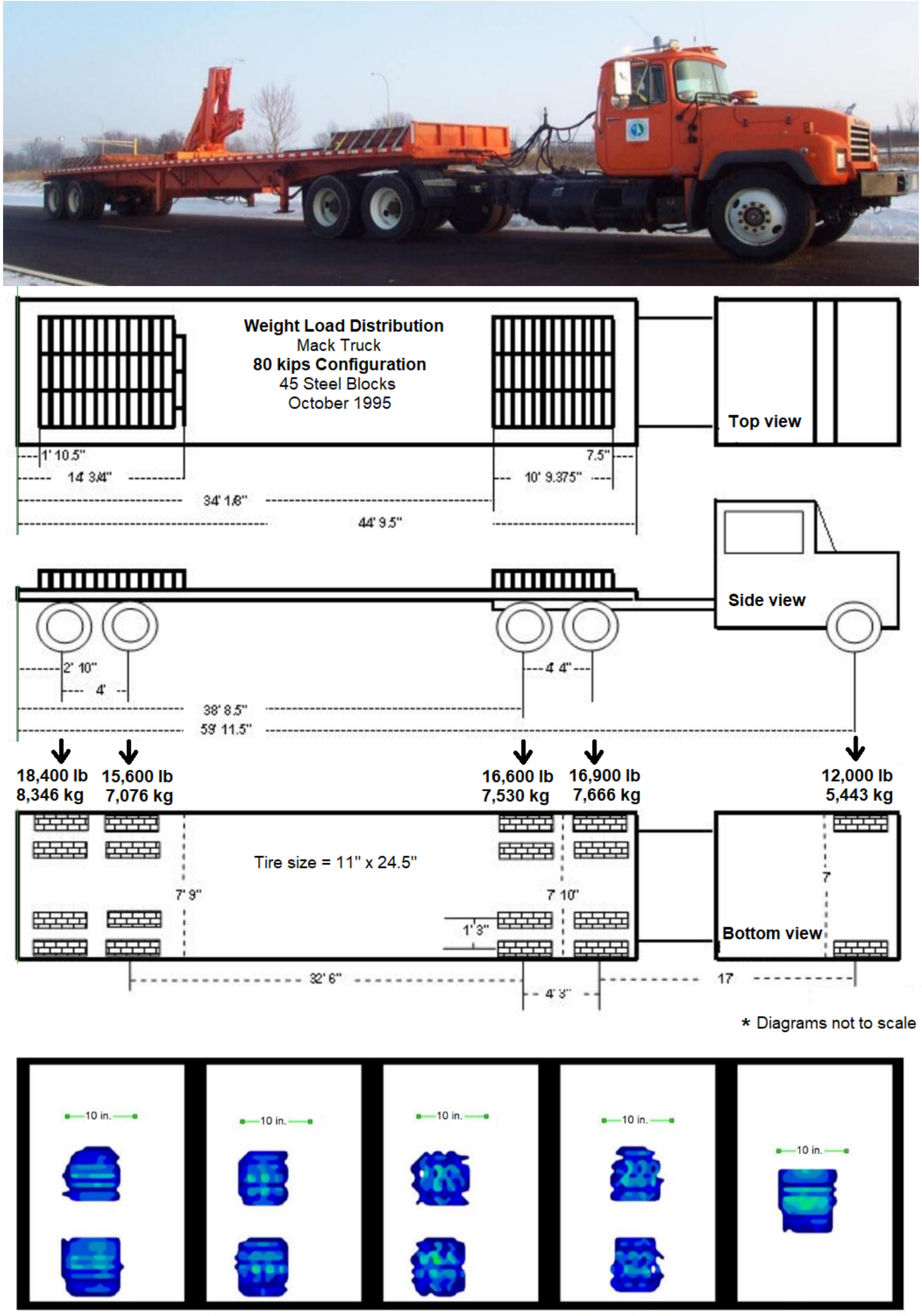

Tire size and pressure measurements using TECHSCAN system

Figure 4-4. Weight Distribution, Axle Configuration and Tire Size Measurements of the 80 kips Mack Tractor with Fruehauf Trailer Used at MnROAD (1994-current) As Legal Load Configuration (MnROAD Data Library 2019)

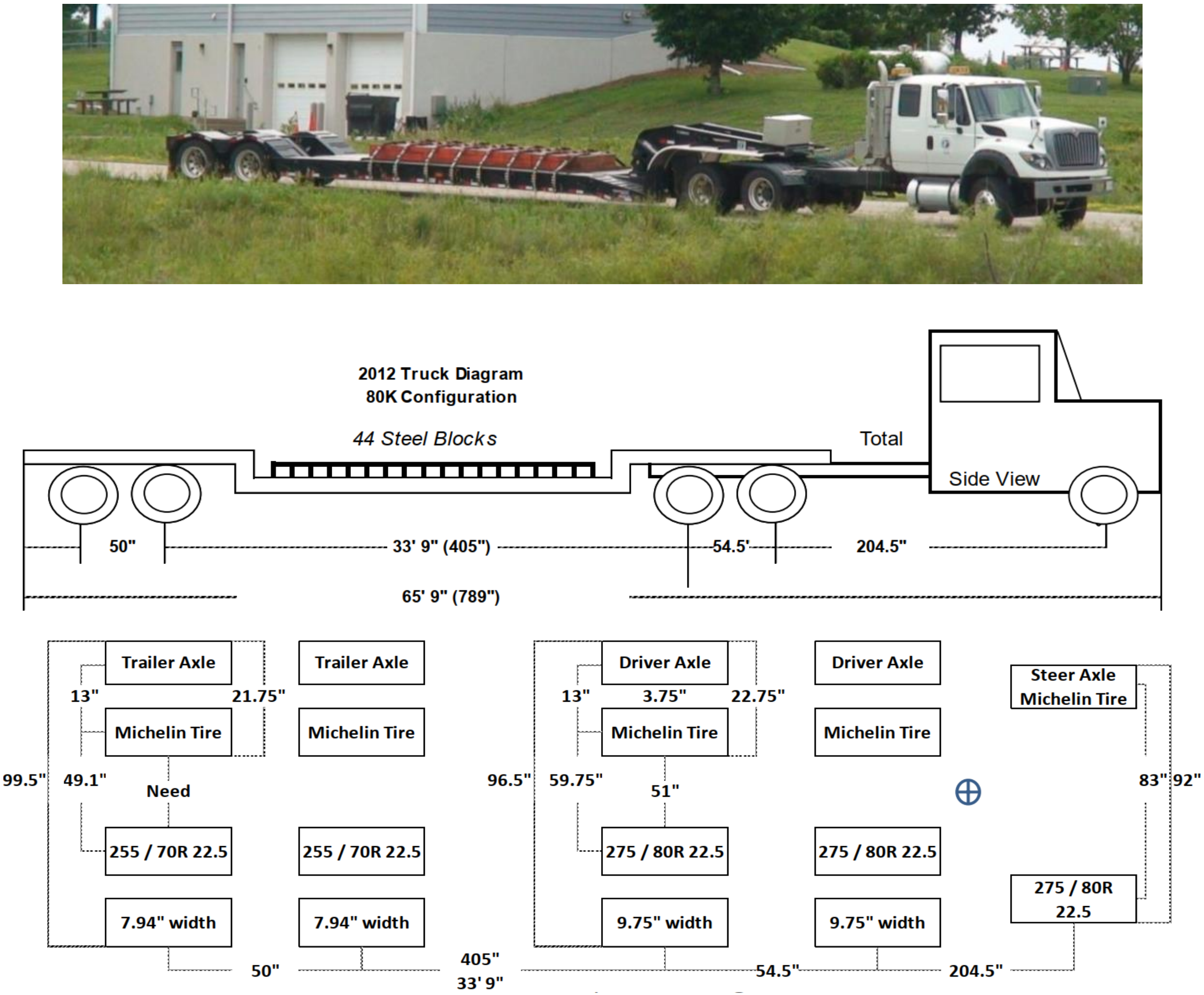

Timeframe	Total Weight (lbs)	Steering Axle	Front axle Tractor tandem	Back axle Tractor tandem	Front axle Trailer Tandem	Back axle Trailer Tandem
June 15, 2012 Present	79,700	11,700	17,650	16,450	16,800	17,100
			34,100		33,900	

Figure 4-5. Weight Distribution and Axle Configuration of the 80 kips Workstar Tractor with Towmaster Trailer Used at MnROAD (2012-current) As Legal Load Configuration (MnROAD Data Library 2019)

PCC strain response due to dynamic loads are recorded using concrete embedment strain gauges (CE, MM, etc.) that are embedded into the concrete surface layer near the top and bottom of the slab at various locations throughout a particular panel. Peak responses were selected from a dynamic strain versus time plot for each forward pass of the truck. Since the sensors are embedded in the slab, and thus are not located at the surface or very bottom of the slab, their measured values had to be linearly extrapolated to the surfaces using plane strain theory. Although as-built survey measurements were taken following the construction of test sections, local variations in the thickness of the slab only allow an estimate of the accurate depth of the sensors. Therefore, the values used in this analysis are only close approximations of the true dynamic strain response. Once load test data acquisition is complete (using either Optim Electronics MEGADAC units or National Instruments units), the resulting output are fed into data processing software to automatically select peak sensor response (peak-picking) and eliminate the noise. For this purpose, the spectrogram of the raw sensor waveform was plotted and the cutoff frequency that most of the signal energy is concentrated on was determined. This frequency for MnROAD was 30 Hz. Thus, a low-pass filtering with a cutoff at 30 Hz was employed to denoise the dynamic sensor data so that the processed data are in a format comparable to the modeling outputs (Burnham et al. 2007).

FIELD MONITORING

The data collected through field monitoring at MnROAD includes strength (falling weight deflectometer FWD, lightweight deflectometer LWD) strength (dynamic cone penetrometer DCP, nuclear density, moisture content), ride (lightweight profiler), distress (crack survey, PCC joint faulting, lane/shoulder dropoff, rutting), texture (sand patch, friction tester, circular texture meter), noise (on-board sound intensity, sound absorption). However, for the purpose of validating the analysis tool, FWD test data on concrete pavements were considered. MnROAD uses Dynatest Model 8000 device with the geophone sensor spacing shown in Table 4-1 for measure the response of a pavement layer system to a dynamic (impulse) load in order to evaluate the structural capacity of the system as well as to back-calculate the modulus of the underlying layers. In this table, sensor number 10 was utilized to conduct load transfer efficiency testing of PCC transverse joints.

Table 4-1. FWD sensor Spacing at MnROAD

Sensor number	1	2	3	4	5	6	7	8	9	10
Distance from center of loading plate (in.)	0	8	12	18	24	36	48	60	72	-12

Since 1998, FWD testing has been conducted with the trailer facing in the direction of traffic loading for all PCC test cells to consider the impact of traffic loading direction on the development of transverse joint faulting. Prior to 2008, the deflections at each test point were collected for three drops at each load level of 6000, 9000, and 15000 lb and after 2008 the deflections only one drop per load level were recorded. Figure -6 illustrates the typical test pattern concrete pavements, representing five distinct locations on the PCC slabs: center, midedge, corner, joint after, and joint before.

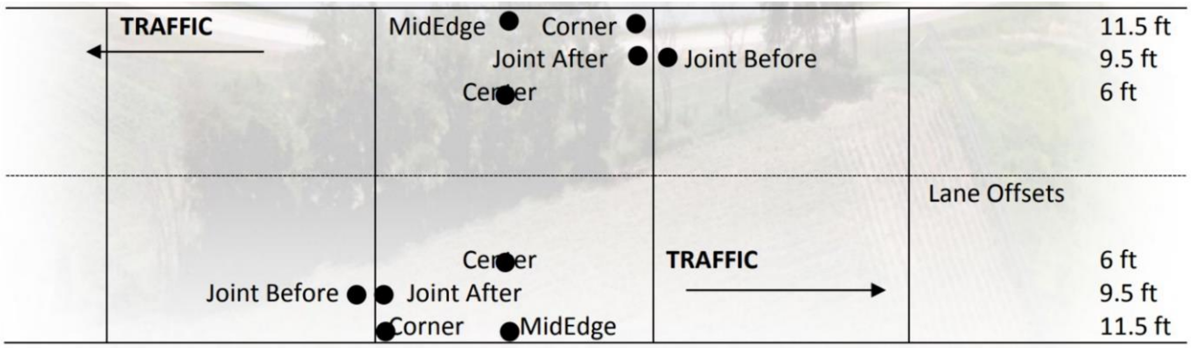

Figure 4-6. FWD Test Locations for Each Testing Panel in Every LVR Or Mainline Cell (MnROAD Data Library 2019)

MnROAD Cell 32

Cell 32 is located on the low-volume loop at MnROAD, which is a closed-access portion of MnROAD that is loaded by a single MnDOT tractor-trailer that drives laps around the loop. Figure 4-7 illustrates the pavement structure and the pavement cross-section with the cell layout and instrumentation locations. Panels were 12 ft. wide with undoweled joints every 10 ft.

Various types of instrumentation were installed during construction of Cell 32. Particularly relevant to this study, dynamic strain gauges (Tokyo Sokki Kenkyujo model PML-60) and thermocouples (fabricated by MnROAD staff) cast into pavement at various depths were utilized. Figure 4-7 shows the depths and locations of these sensors. Dynamic strain sensors only collect data when they were activated during MnROAD dynamic load testing under the known loading from the MnROAD truck. For truck loading, the (80 kips) Mack tractor with Fruehauf trailer was used in Cell 32. More details on sensor installation and data collection can be found in MnROAD Data Library (2019).

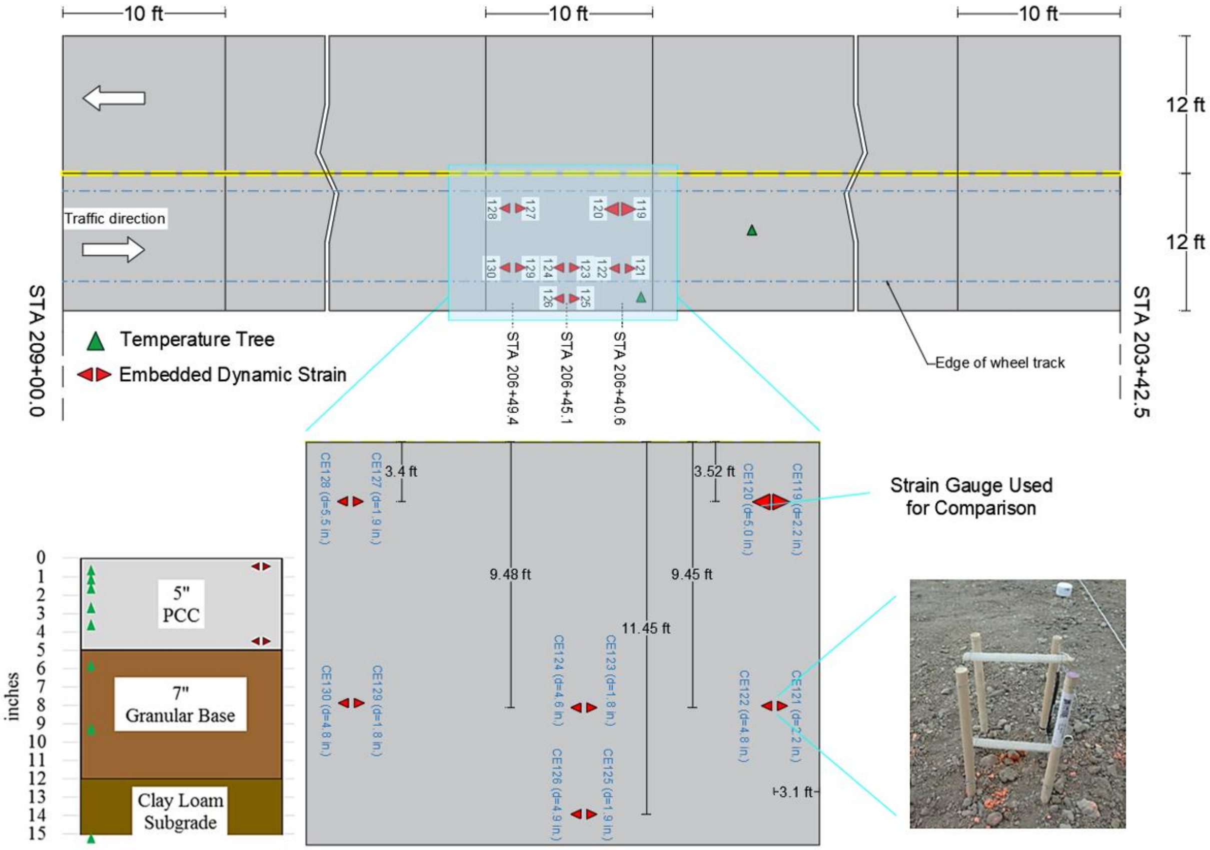

Figure 4-7. MnROAD Cell 32 section and sensor layout (modified from Burnham 2002).

Falling weight deflectometer (FWD) data were also used for comparison against RPAS in this study. FWD testing was routinely conducted as part of MnROAD's normal data collection activities. The deflections at each test point were collected for three drops at each load levels of 6000, 9000, and 15000 lb. Five distinct locations on the PCC slabs namely slab center, midedge (0.5 ft. from slab edge), corner, joint before (2.5 ft. from slab edge), and joint after (mirrored joint before with respect to the transverse joint) were selected for FWD testing. The MnROAD Cell 32 data, based on testing from field cores and laboratory specimens, are summarized in Table 4-2. The data set on the truck loading and FWD tests collected on July 18, 2000 was considered for this study.

Table 4-2. Summary of Material Properties of MnROAD Cell 32 from Experimental and Field Testing (MnROAD Data Library 2019)

Pavement layer	**Property**	**Value**			**Unit**	**#Observations**	**CV %**
		Min.	**Avg.**	**Max.**			
Concrete slab (10×12 ft) Astro turf	**$(E_{28})_{avg}$**[*] From cores:	3,378	3,567	3,700	ksi	3	15.0
	From cylinder specimens:	4,333	4,495	4,702	ksi	3	4.2
	Poisson's ratio, $(\nu_c)_{avg}$ From cores:	0.11	0.12	0.13	-	3	3.0
	From cylinder specimens:	0.11	0.155	0.16	-	3	4.5
	Unit weight, $(\gamma_c)_{avg}$	145	149	152	pcf	10	0.4
	Thickness, t_c From cores:	5.3	5.4	5.6	in.	12	13.0
	From design:	-	5.0	-	in.	-	-
	CTE[†] From cylinder specimens:	4.8	5.3	5.4	$\mu\varepsilon/^{\circ}F$	6	1.2
Gravel base (Class 1f)	**$(M_r)_{b,avg}$**[‡]	9,040	12,400	19,300	psi	12	9.0
	Poisson's ratio, $(\nu_b)_{avg}$	-	0.30	-		-	-
	Unit weight, $(\gamma_{wet})_{b,avg}$	131	147	151	pcf	16	2.5
	Thickness, t_b From design:	-	6.0	-	in.	-	-
Subgrade (Clay: R=12)	**$(M_r)_{SG,avg}$**[‡]	2,800	9,400	18,500	psi	15	31.4
	Poisson's ratio, $(\nu_{SG})_{avg}$	-	0.45	-		-	-
	Unit weight, $(\gamma_{wet})_{SG,avg}$	108	127	129	pcf	15	1.4

- subscripts c, b, and SG show material property corresponding to concrete, base and subgrade layers, respectively.

[*] E_{28} = 28-day Elastic modulus

[†] CTE = Coefficient of thermal expansion

[‡] M_r = Resilient modulus

As indicated in Table 4-2, there is a significant variation in the modulus of the pavement layers as measured in laboratory tests. As a rational alternative to using laboratory test results, FWD tests were carried out at the locations where sensors were installed, and material properties were back-calculated using BAKFAA program (developed by FAA) based on layered elastic theory.

The pavement temperature measured on the test day at various depths and times of day were curve-fitted to a three-dimensional polynomial and are plotted in Figure 4-8a. Since most of the FWD and dynamic testing at MnROAD were conducted after 11:00 a.m., an average curve related to afternoon measurement (2:00 p.m.) was selected as a representative temperature throughout the slab depth. As discussed earlier, the non-linear built-in (set) temperature profile $T_{Set}(z)$ was considered in addition to the non-uniform temperature profile due to temperature change $T(z)$ (see Figure 4-8b). A target value of 1 °F/in. of slab depth was suggested as built-in temperature gradient in previous studies in order to minimize JCP cracking (Mohamed and Hansen 1997, Beckemeyer et al. 2002, Joshaghani and Zollinger 2019). Thus, a three-dimensional polynomial below was fitted to the MnROAD data and used in RPAS to consider the temperature differences throughout the depth of the slab:

$$\Delta T_{Model}(z) = 75.515 - 0.606z - 0.079z^2 - 0.188z^3 \tag{4-1}$$

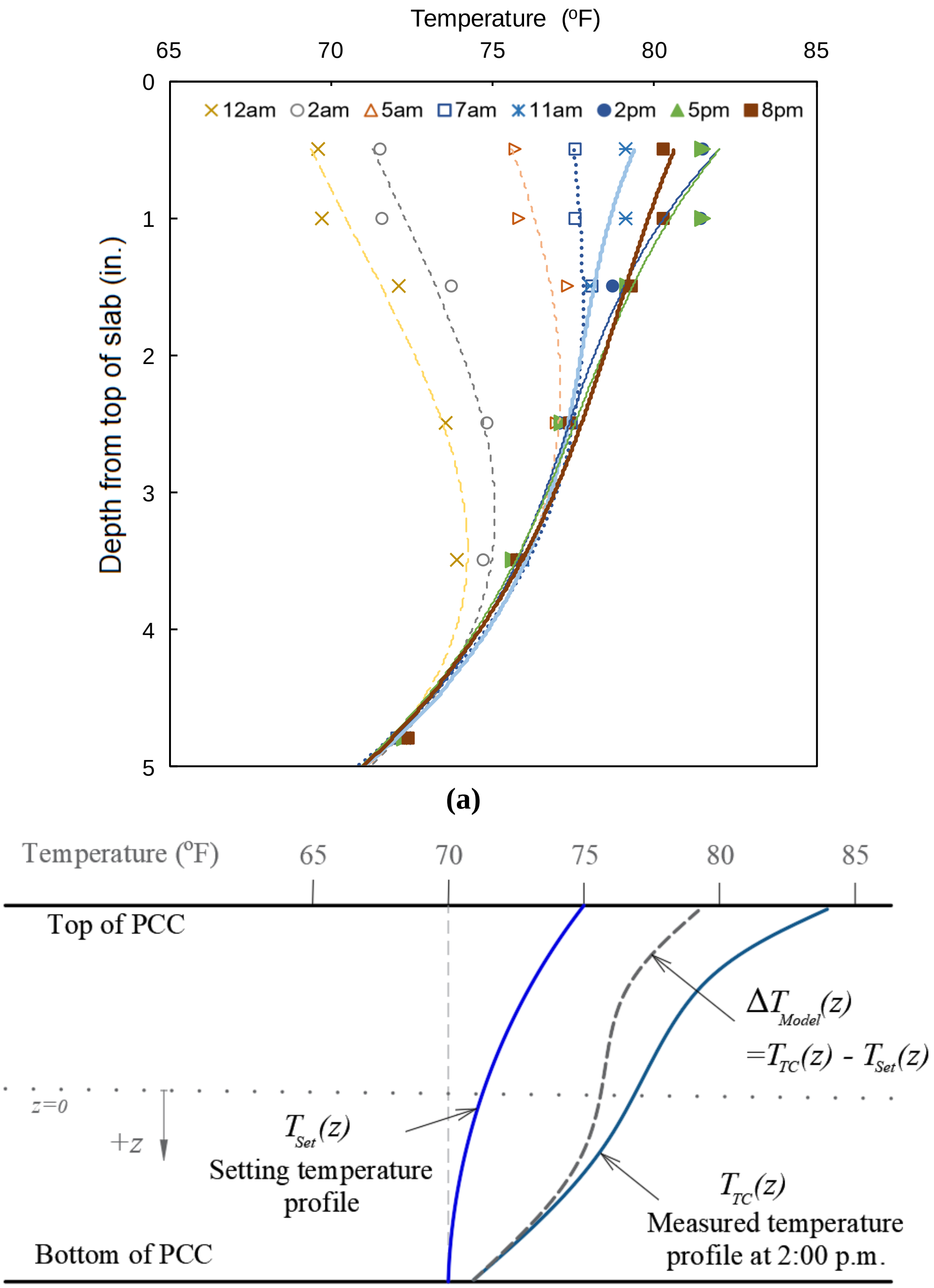

(a)

(b)

Figure 4-8. (a) Actual Temperature Distribution Measured at Different Time Intervals on The Test Day at MnROAD Cell 32 (b) Non-Linear Temperature Profile Used for MnROAD Sections After Considering Built-in Temperature Profile.

Comparison of FWD Test Responses

FWD deflections recorded at MnROAD vary at each test sequence with the coefficient of variation (CV) of 10 to 15%. It should be noted that although FWD loading system produces a transient impulse load to the pavement surface, neglecting this dynamic effect introduces a very small error to the to the predicted responses, particularly for concrete pavements (Ong et al. 1991, Hamim et al. 2018). Figure 4-9 shows the comparison between the deflection measured during FWD testing of MnROAD Cell 32 and those calculated using RPAS. In most cases, the deflections calculated using RPAS are in well agreement with those from the FWD measurements. A pre-validation through comparison of the deflections in Figure 4-9 shows that all the deflections are within ±20% limit. Taking into consideration all the responses from testing and modeling, they reasonably agree with the adjusted-R^2=0.85.

To better describe the difference between the modeling results in RPAS and FWD test results, the Nash-Sutcliffe Efficiency (NSE) coefficient was used (Nash and Sutcliffe 1970). This statistical metric is recommended when several observations slightly vary under the same condition, but the simulation can only produce a single response.

$$NSE = 1 - \frac{\sum_{i=1}^{n} (Y_i^{obs} - Y_i^{sim})^2}{\sum_{i=1}^{n} (Y_i^{obs} - Y^{mean})^2} \tag{4-2}$$

where Y_i^{obs} denotes the observed responses, Y_i^{sim} is the simulated or modeled response(s), and Y^{mean} is the average of the observed responses. *NSE* ranges $-\infty < NSE < 1$, where *NSE* = 1 corresponds to a perfect match of model to the observation and *NSE* = 0 indicates that model predictions are as accurate as the mean of the observed data. The values of *NSE* shown in Figure 4-9 indicate that, except for the case of center loading, a good agreement between the responses can be observed. A plausible explanation for the larger difference in the center loading can be the uncertainties involved in the field testing conditions. As shown below in the full-scale testing under more controlled conditions (NAPTF comparison), a much better agreement between the results of FWD in center loading was observed.

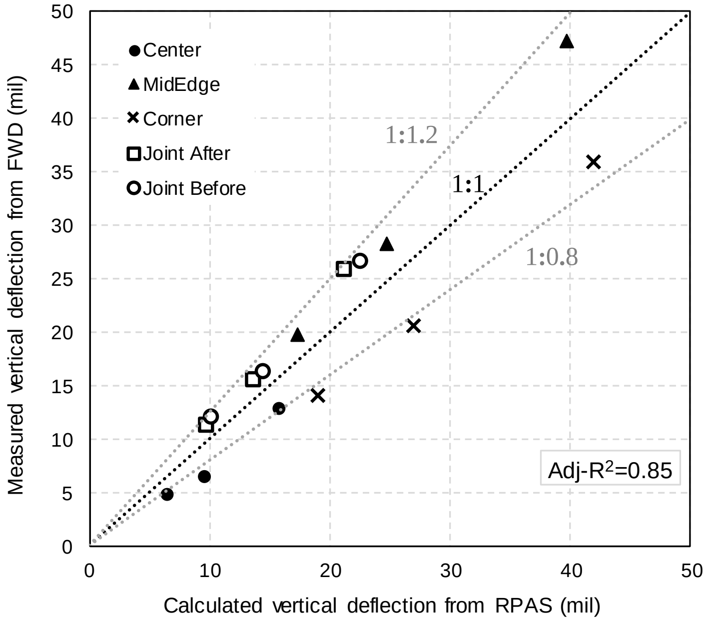

Nash-Sutcliffe Efficiency (NSE)

Center		
6 kips	9 kips	15 kips
-30.1	*-52.5*	*-17.9*

MidEdge		
6 kips	9 kips	15 kips
-0.5	*-0.7*	*-1.8*

Corner		
6 kips	9 kips	15 kips
-9.8	*-8.2*	*-3.5*

Joint After		
6 kips	9 kips	15 kips
-0.9	-0.7	-1.8

Joint Before		
6 kips	9 kips	15 kips
-1.9	*-1.3*	*-2.4*

Figure 4-9. Maximum Basin Deflection from FWD Tests Versus the Deflections from RPAS Analyses and The NSE Between Simulated and Observed Deflections in Cell 32.

Comparison of Truck Loading Responses

The results of RPAS analyses for a range of material properties (Table 4-2) were compared against dynamic strain measurement at MnROAD Cell 32 for pre-validation. The strain response was taken from the measurements in sensor 120 as shown in Figure 4-7. Figure 4-10a shows the strain at the bottom of the slab calculated by RPAS using the lower bound (minimum) resilient modulus of the foundation layers LB_M_r, upper bound (maximum) resilient modulus UB_M_r, and average resilient modulus as measured from laboratory testing of several samples at each test cell (see Table 4-2) as well as using back-calculated resilient modulus, BC_M_r. To obtain the strain response with respect to time, the movement of truck along the traffic direction was simulated by using the truck speed (ranging from 4.5 to 5.7 mph) and the tire configuration. Again, it should be noted that the measured strains from embedded strain gauges have been extrapolated to the surfaces using linear extrapolation.

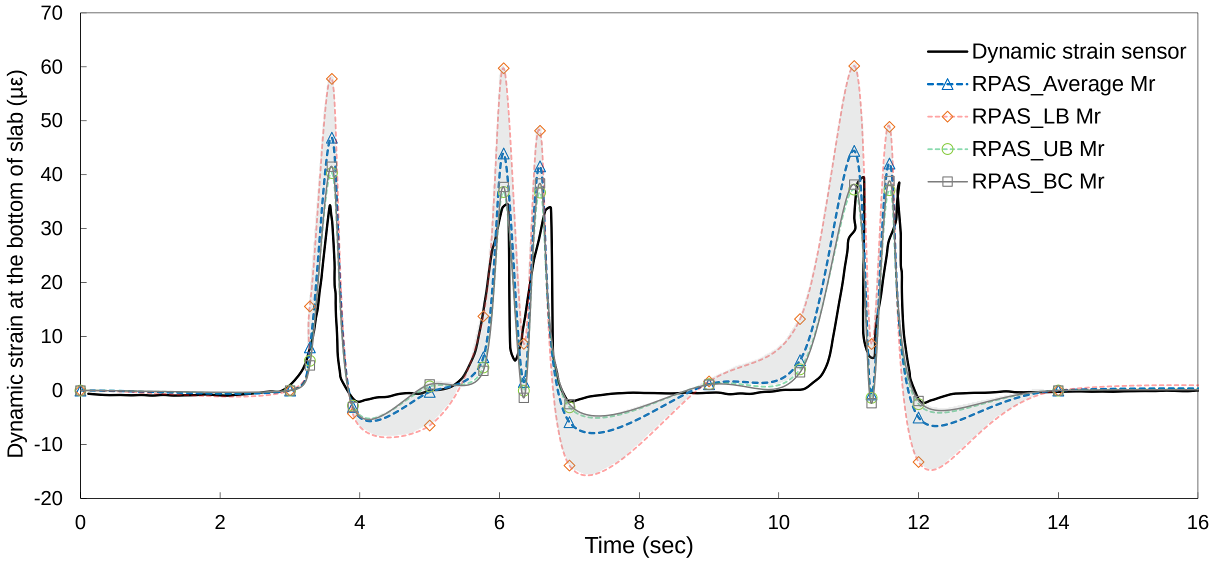

(a)

Incorporated Modulus	1st axle	2nd axle	3rd axle	4th axle	5th axle
Measured	34.1	34.4	33.8	39.3	38.5
LB-M$_r$	57.8	59.7	48.1	60.1	48.9
UB-M$_r$	40.3	36.8	36.7	37.2	37.2
Average-M$_r$	46.8	43.9	41.6	44.4	42.1
BC-M$_r$	41.5	37.7	38.3	38.1	38.8

Unit: Microstrain

(b)

Incorporated modulus	Peaks	Troughs	Peaks and Troughs	
	RMSE ($\mu\varepsilon$)	RMSE ($\mu\varepsilon$)	Adj-R^2	RMSE ($\mu\varepsilon$)
LB-M$_r$	19.73	7.50	0.93	12.95
UB-M$_r$	3.43	6.17	0.92	4.94
Average-M$_r$	8.39	5.82	0.93	6.41
BC-M$_r$	4.19	6.90	0.91	5.50

(c)

Figure 4-10. (a) Comparison of Measured Dynamic Strain Sensor Responses at Cell 32 with Those Obtained Using RPAS For Different Material Properties (b) The Comparison of Peak Values of Dynamic Strains by Utilizing Different Moduli (c) Numerical Evaluation of The Goodness of Calculated Responses Using RPAS.

As can be seen in Figure 4-10a, there is a difference of up to 60% between the peaks and troughs of the curves associated with the use of the upper and lower bounds of the resilient modulus and the field data does not fall close to the RPAS results when using the average modulus. When using the back-calculated modulus, the results are more consistent with the measured responses. To identify the goodness of each prediction the R^2 and root mean squared error (RMSE) were calculated. As shown in Figure 4-10b, using the minimum values of layer moduli leads to large errors in the estimation of pavement responses. However, utilizing the maximum M_r from laboratory tests yields very consistent results with those using back-calculated moduli and significantly reduces the discrepancy between the field and RPAS calculated responses. Since M_r varies as a function of moisture content and stress level, this consistency between the maximum and back-calculated moduli indicates that even though the soil may not maintain the optimum moisture content in the field, the maximum applied deviatoric stress in the tests were almost the same as those in the field. The difference between the measured strain and the simulated response can also partially be attributed to the filtering of the noise induced during dynamic strain measurements. It should also be noted that although the difference between the responses incorporating different modulus of pavement layers are obvious by considering RMSE, adjusted-R^2 shows no sensitivity to different responses.

MnROAD Cell 52

MnROAD test section 52 was built to replicate one of the thinner interstate highway designs (Mainline test cell 6) for a curl-and-warp study. Cell 52 was constructed with 7.5 inches of jointed plain concrete over a 5 in. thick layer of gravel base. Total length of the cell 52 is 285 ft, and lane widths are 13 ft (eastbound lane) and 14 ft (westbound lane). The slabs are 15 ft long and the transverse joints are doweled and cut perpendicular to the centerline of the road. The dowel bars in the test area are 1 in. diameter epoxy coated steel, 15 in. in length. The subgrade layer is a silty-clay material and the shoulders are constructed of gravel.

The test section instrumentation and the testing procedure of Cell 52 was the same as those for Cell 32. More detailed information on sensor installation and data collection can be found in MnROAD Data Library (2019). Instrumentation includes strain gages (to measure dynamic and environmental loads), thermocouples, moisture sensors, and under-slab pressure plates. The data analyzed in this study came from dynamic strain sensors and thermocouples. For truck loading, the (102 kips) Navistar tractor with Fruehauf trailer was used in Cell 52. Figure 4-11 shows the depths and locations of these sensors in test section 52.

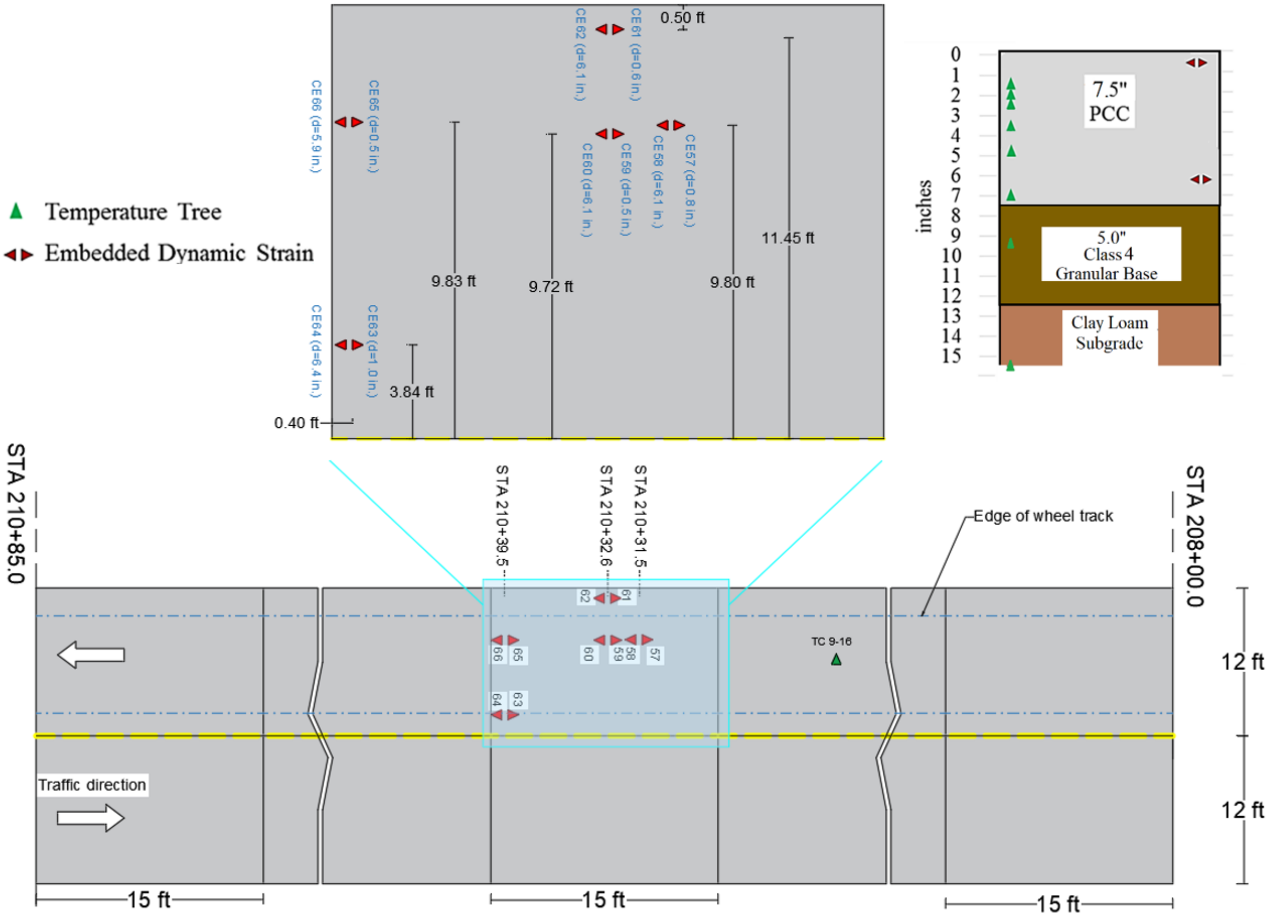

Figure 4-11. MnROAD Cell 52 Section and Sensor Layout

Figure 4-12 shows the non-linear temperature variation throughout the concrete slab in July 26, 2000, that was used for the analysis. As explained for Cell 32, the temperature profile measured at 2:00 p.m. was used for modeling FWD and truck loading tests. The three-dimensional polynomial below fitted to the Cell 52 temperature data and used in RPAS to consider the temperature differences throughout the depth of the slab was as follows:

$$\Delta T_{Model}(z) = 86.527 - 2.635z + 0.116z^2 + 0.0004z^3 \tag{4-3}$$

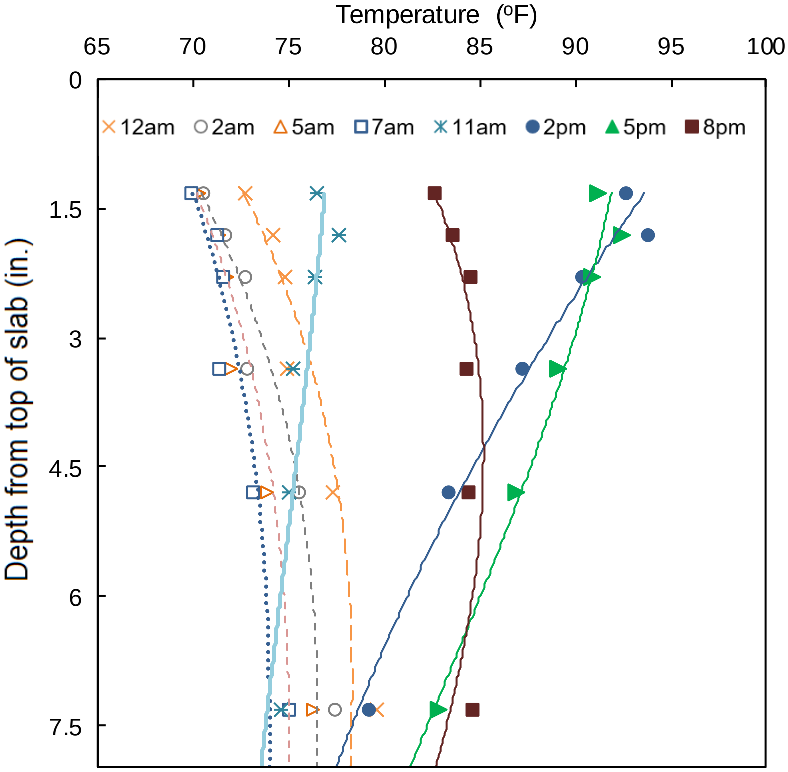

Figure 4-12. Temperature distribution measured at different times on the test day at MnROAD Cell 52

The MnROAD Cell 52 data, based on testing from field cores and laboratory specimens, are summarized in Table 4-3. The data set on FWD test collected on July 26, 2000 and the truck loading test data collected on July 18, 2001 were considered for this study.

Table 4-3. Summary of Material Properties of MnROAD Cell 52 from Experimental and Field Testing (MnROAD Data Library 2019)

Pavement layer	**Property**	**Value**			**Unit**	**#Observations**	**CV %**
		Min.	**Avg.**	**Max.**			
Concrete slab (15×12 ft) Astro Turf 1.0” Dowel	**$(E_{28})_{avg}$*** From cores: From cylinder specimens:	3,400 3,925	4,410 4,370	4,745 5,030	ksi ksi	5 6	12.0 8.3
	Poisson’s ratio, $(\nu_c)_{avg}$ From cores: From cylinder specimens:	0.10 0.12	0.11 0.13	0.13 0.14	- -	3 3	8.7 13.0
	Unit weight, $(\gamma_c)_{avg}$	145	149	151	pcf	4	1.9
	Thickness, t_c From cores: From design:	7.5 -	7.8 7.5	8.2 -	in. in.	3 -	4.2 -
	CTE† From cylinder specimens:	5.3	5.3	5.3	$\mu\varepsilon/^{\circ}$ F	2	0
Gravel base (Class 4)	**$(M_r)_{b,avg}$**‡	17,700	27,560	46,600	psi	18	34.4
	Poisson’s ratio, $(\nu_b)_{avg}$	-	0.30	-		-	-
	Unit weight, $(\gamma_{wet})_{b,avg}$	136	143	148	pcf	18	3.5
	Thickness, t_b From design:	-	5.0	-	in.	-	-
Subgrade (Clay: R=12)	**$(M_r)_{SG,avg}$**‡	16,950	27,000	47,020	psi	30	26.8
	Poisson’s ratio, $(\nu_{SG})_{avg}$	-	0.40	-		-	-
	Unit weight, $(\gamma_{wet})_{SG,avg}$	134	136	137	pcf	10	1.2

- subscripts c, b, and SG show material property corresponding to concrete, base and subgrade layers, respectively.

* E_{28} = 28-day Elastic modulus

† CTE = Coefficient of thermal expansion

‡ M_r = Resilient modulus

As seen in Table 4-3, similar to Cell 32, the moduli of the pavement foundation layers from laboratory tests show a considerable variation as compared to the concrete slab. Therefore, the back-calculated moduli of supporting layers from FWD test data were utilized in the rest of analyses. The results of pre-validation for FWD testing shown in Figure 4-13 indicates a good agreement.

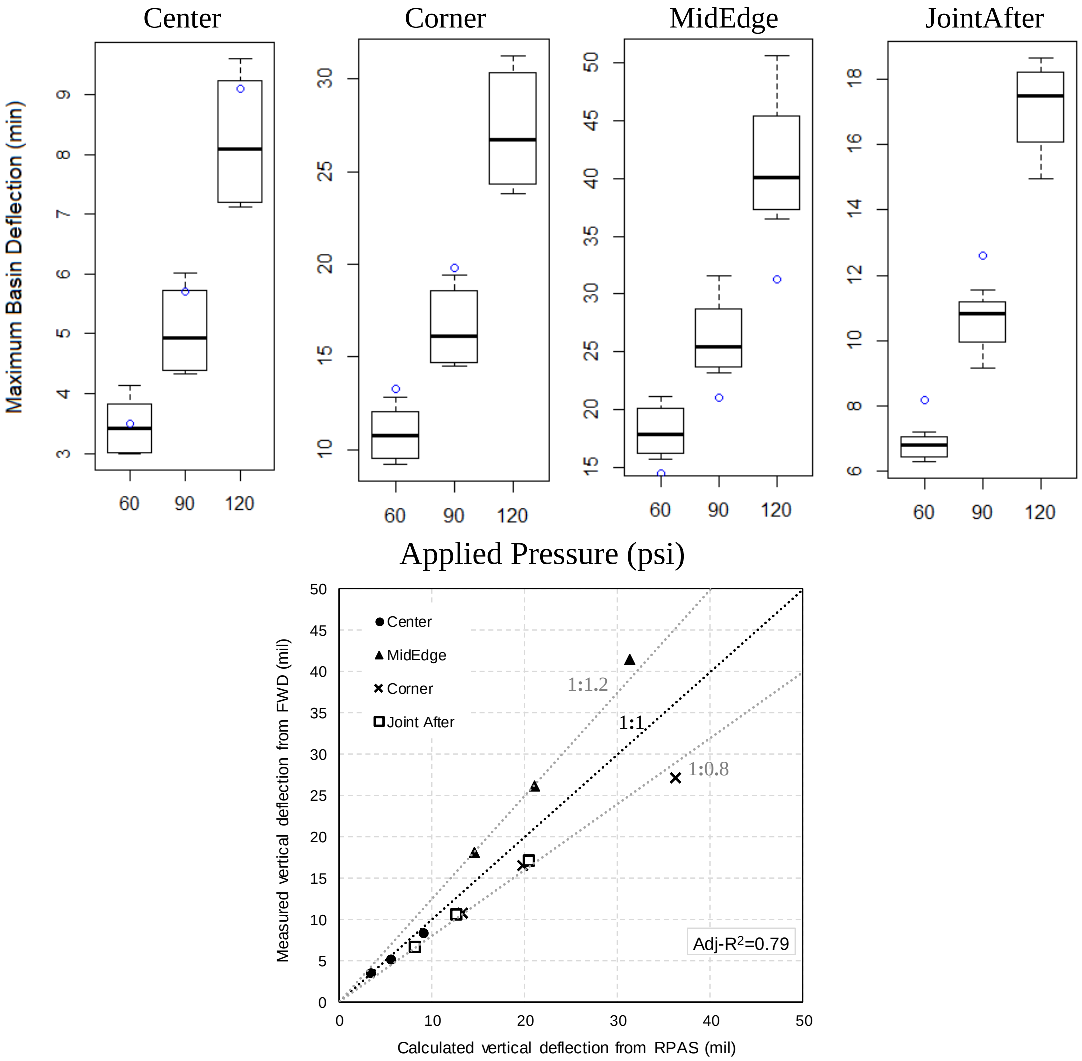

NSE values:

	Center	MidEdge	Corner	JointAfter
Load 1	-0.02	-3.12	-3.34	-18.01
Load 2	-0.85	-2.98	-2.52	-5.64
Load 3	-0.69	-4.17	-8.73	-5.85

Figure 4-13. Maximum Basin Deflection from FWD Tests Versus the Deflections from RPAS Analyses and The NSE Between Simulated and Observed Deflections in Cell 52.

For truck loading, a Navistar tractor with Fruehauf trailer with the weight of 102 kips was used in Cell 52. As can be seen in Figure 4-13, as opposed to Cell 32, the truck loading in outside lane was used for comparison in this study. Table 4-4 summarizes the peak values of dynamic strain measured at Cell 52 in July 18, 2001 compared to those from RPAS analysis using average and back-calculated moduli of foundation layer. As shown, peak strains calculated utilizing resilient modulus from laboratory testing and back-calculation yield higher calculated responses compared to the measured ones but the peak strains obtained using back-calculated moduli are in better agreement with the measured strains, where the maximum difference changes from 68% using average M_r to 33% with the back-calculated moduli.

Table 4-4. Comparison of Peak Values of Strain Under Truck Loading Measured at MnRAOD Cell 52 and Calculated Using RPAS

Source of utilized Moduli	Location of record under truck load				
	1st Axle	2nd Axle	3rd Axle	4th Axle	5th Axle
Measured	12	28	22	22	27
Average Mr	19	34	37	36	39
Back-calculation	16	28	29	27	33

All the values above show the dynamic strain under truck loading in microstrain.

MnROAD Cell 613

Cell 613 is intended to be a model for sustainable concrete pavement design. Ideally, it would be preferable to reuse the in-place pavement materials in the newly constructed test cell. In this case, however, recycled material came from the contractor’s stockpile in Maple Grove, MN. This concrete was verified to come from previous pavements produced under MnDOT specifications. Recycled concrete was crushed to a controlled maximum size of 1.5 inch and minimal material passing the No. 200 sieve. Project special provisions further required that there be less than 5% passing the No. 4 sieve. The final mix design included 75% replacement of the coarse aggregate with recycled concrete aggregate. Pavement design consisted of 7.5-inch-thick slabs with 15 ft long by 12 ft wide panels. Transverse joints included 1-inch diameter epoxy coated steel dowels, and longitudinal joints were tied with 0.5-inch diameter, 30-inch long rebars. The original research plan included studying two different narrow width neoprene preformed seals. However, saw cut widths were incompatible with the very narrow seals, so only the wider (0.25-inch wide) seals were installed in the joints.

Figure 4-14 and Table 4-5 show the properties of pavement section Cell 613 as well as the arrangement of static and dynamic sensors. The pavement temperature was measured on the test day at various depths and times of day were curve-fitted to a three-dimensional polynomial, as illustrated in Figure 4-15. As explained above, the temperature profile measured at 2:00 p.m. was used for modeling FWD and truck loading tests. The three-dimensional polynomial below fitted to the Cell 613 temperature data and used in RPAS to consider the temperature differences throughout the depth of the slab was as follows:

$$\Delta T_{Model}(z) = 92.000 - 4.253z + 0.144z^2 + 0.155z^3 \tag{4-4}$$

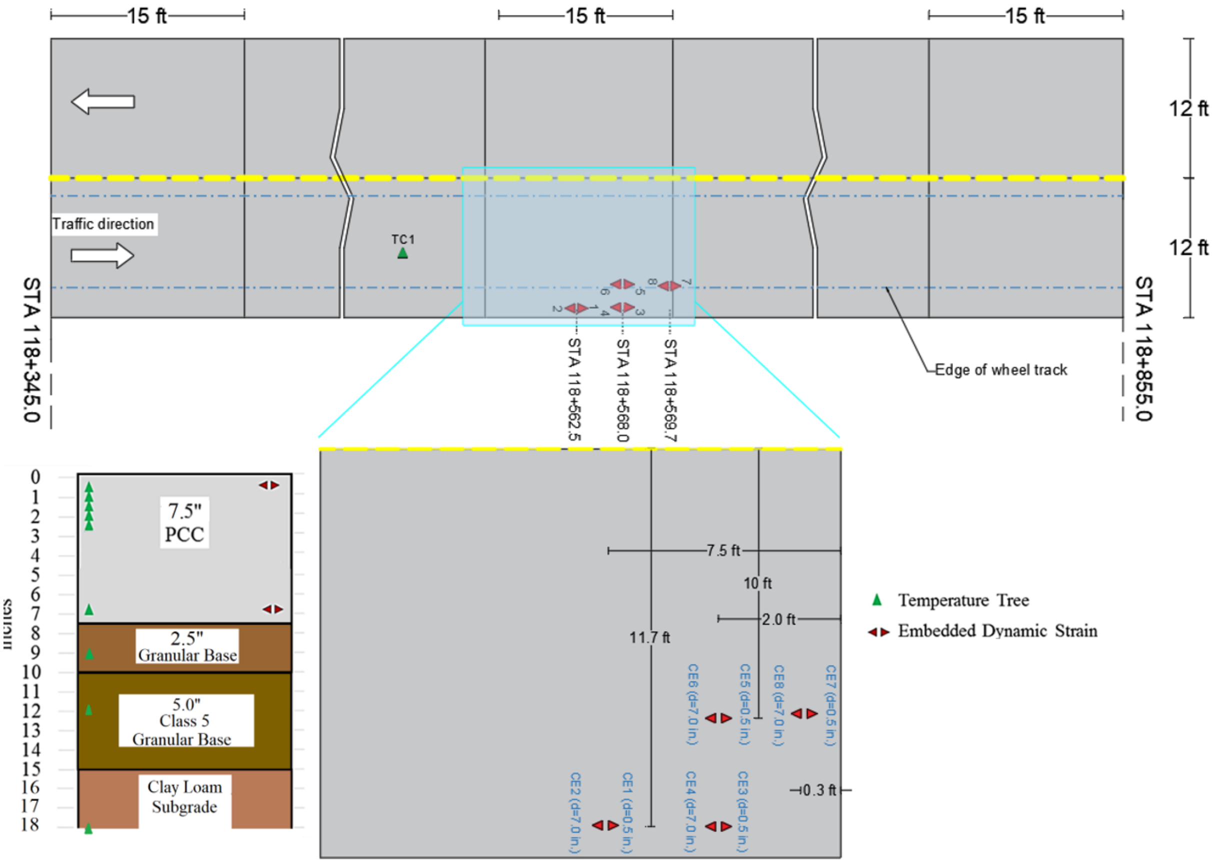

Figure 4-14. MnROAD Cell 613 Section and Sensor Layout.

Table 4-5. Summary of Material Properties of MnROAD Cell 613 from Experimental and Field Testing (MnROAD Data Library 2019)

Pavement layer	**Property**	**Value**			**Unit**	**#Observations**	**CV %**
		Min.	**Avg.**	**Max.**			
Concrete slab (15×12 ft) (75% RCA) 1.0” Dowel	**$(E_{28})_{avg}^{*}$** From cores: From cylinder specimens:	 4,050 3,978	 5,152 4,045	 5,435 4,130	 ksi ksi	 5 4	 12.0 3.6
	Poisson’s ratio, $(\nu_c)_{avg}$ From cores: From cylinder specimens:	 0.14 0.11	 0.24 0.14	 0.28 0.16	 - -	 3 3	 8.7 13.0
	Unit weight, $(\gamma_c)_{avg}$	146	147	149	pcf	4	1.9
	Thickness, t_c From cores: From design:	 -	 7.9 7.5	 -	 in. in.	 3 -	 4.2 -
	CTE† From cores:	 4.8	 4.9	 5.0	 $\mu\varepsilon/^{\circ}$ F	 3	 0
Gravel base (Class 1)	**$(M_r)_{b1,avg}$**‡	17,920	20,040	29,500	psi	18	34.4
	Poisson’s ratio, $(\nu_{b1})_{avg}$	-	0.30	-	-	-	-
	Unit weight, $(\gamma_{wet})_{b1,avg}$	141	157	159	pcf	18	3.5
	Thickness, t_{b1} From design:	 -	 2.5	 -	 in.	 -	 -
Gravel base (Class 5)	**$(M_r)_{b2,avg}$**‡	16,650	20,580	31,790	psi	12	22.6
	Poisson’s ratio, $(\nu_{b2})_{avg}$	-	0.35	-	-	-	-
	Unit weight, $(\gamma_{wet})_{b2,avg}$	132	144	147	pcf	12	2.1
	Thickness, t_{b2} From design:	-	5.0	-	in.	-	-
Subgrade (Clay: R=12)	**$(M_r)_{SG,avg}$**‡	7,955	16,860	24,030	psi	30	24.9
	Poisson’s ratio, $(\nu_{SG})_{avg}$	-	0.45	-	-	-	-
	Unit weight, $(\gamma_{wet})_{SG,avg}$	115	120	127	pcf	30	3.3

- subscripts c, b, and SG show material property corresponding to concrete, base and subgrade layers, respectively.

* E_{28} = 28-day Elastic modulus, ‡ M_r = Resilient modulus

† CTE = Coefficient of thermal expansion

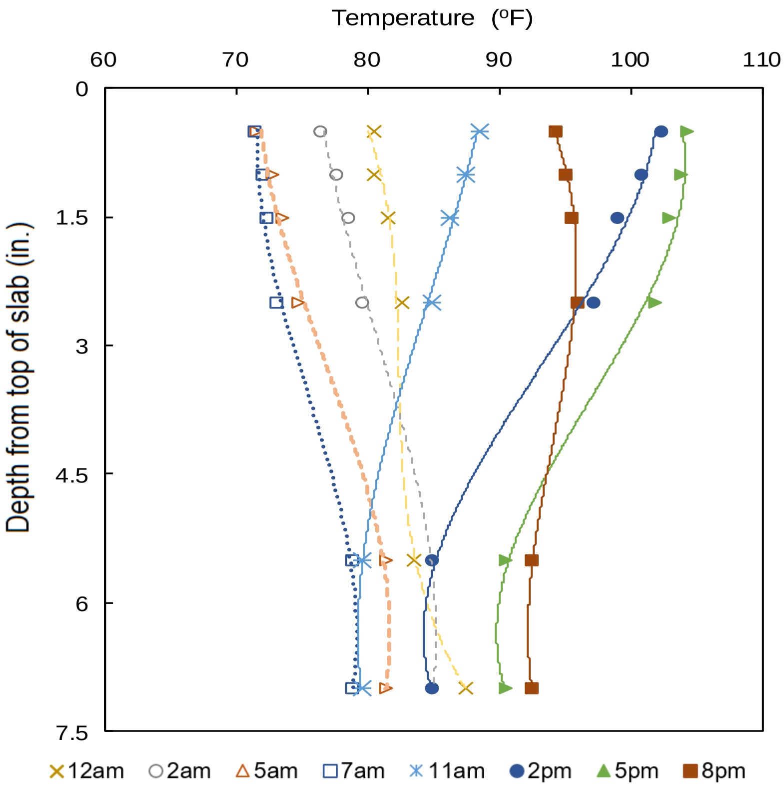

Figure 4-15. (a) Actual Temperature Distribution Measured at Different Time Intervals on The Test Day in MnROAD Cell 613

As in previous sections, the relatively high variation of the moduli of the foundation layers made the use of back-calculated moduli a more accurate alternative than laboratory derived moduli for modeling purpose. The results of RPAS analyses based on the material properties (Table 4-5) were compared against FWD test results as well as dynamic strain measurement at MnROAD Cell 613, which are shown in Figures 4-16 and 4-17. For truck loading, a WorkStar Tractor with Towmaster trailer was used in Cell 613. As can be seen, the calculated deflections from RPAS are in a reasonable agreement (NSE_{max}=-2.5, Adj-R^2=0.95) with the measured deflections. In terms of strain at the slab (Figure 4-17), as in Cell 32 and 52, utilizing back-calculated moduli (BC_Mr) of the foundation layers results in a better agreement between the responses.

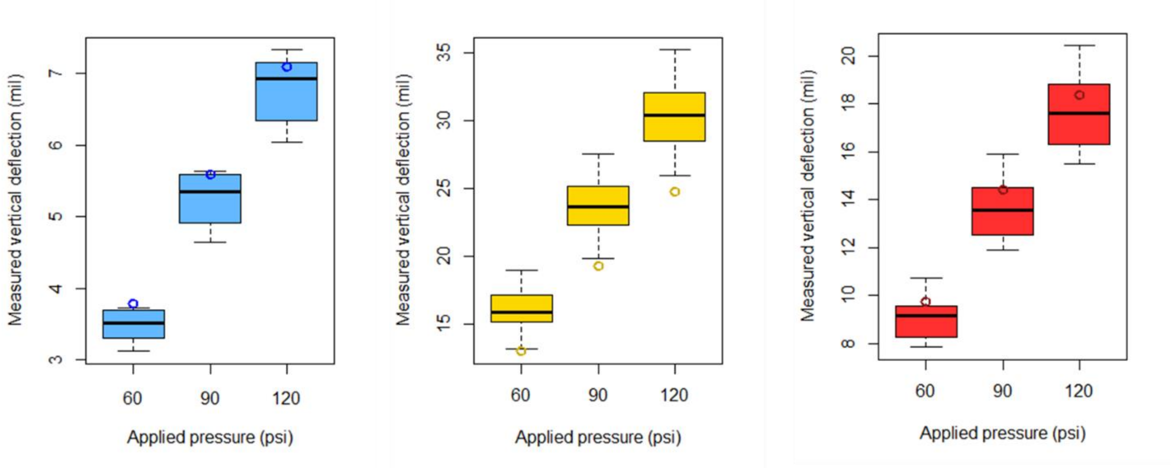

Center Corner MidEdge

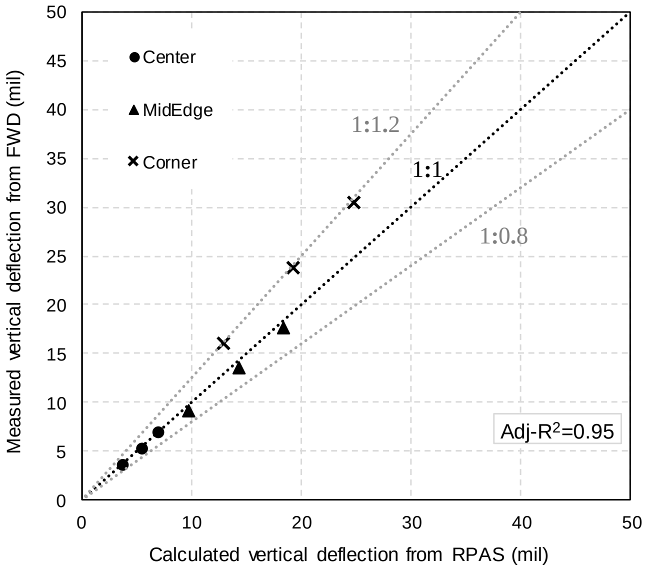

NSE values:

	Center	MidEdge	Corner
Load 1	-0.3	-0.3	-2.2
Load 2	-0.9	-1.1	-2.5
Load 3	0.9	0.9	0.5

Figure 4-16. Maximum Basin Deflection from FWD Tests versus the Deflections from RPAS Analyses and the NSE Between Simulated and Observed Deflections in Cell 613.

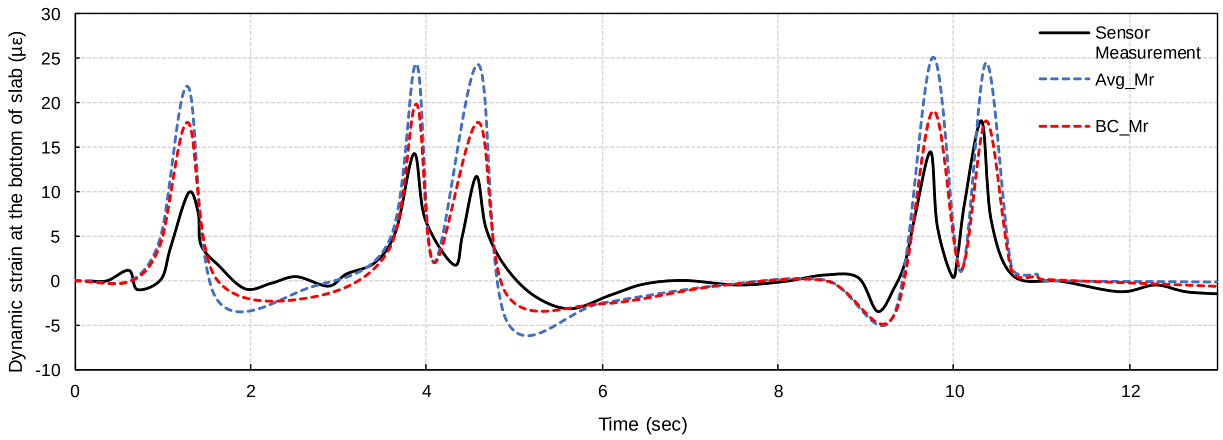

Note: Avg_Mr is for the average moduli and BC_Mr is for the back-calculated moduli

Figure 4-17. Comparison of Measured Dynamic Strain Sensor Responses with Those Obtained Using RPAS For Different Material Properties

4.2. National Airport Pavement Test Facility (NAPTF)

Federal Aviation Administration (FAA) operates a full-scale accelerated airport pavement test facility known as the National Airport Pavement Test Facility (NAPTF) located at the William J. Hughes Technical Center near Atlantic City, New Jersey, USA. The primary objective of the NAPTF is to generate full-scale pavement response and performance data for development and verification of airport pavement design criteria. Since completing the construction of NAPTF in 1999, FAA has conducted eight construction cycles for various purposes. Each construction cycle (CC) includes pavement construction, instrumentation installation, traffic testing to failure, post traffic testing, and demolition of the test item. The testing facility consists of a fully enclosed instrumented test pavement track (900 ft long by 60 ft wide). The rail-based test vehicle is capable of simulating aircraft weighing up to 1.3 million pounds with up to 20 test wheels configured to represent two complete landing gear trucks, wheel loads independently adjustable up to 75,000 lb. per wheel, controlled aircraft wander simulation, and fully automated computerized data acquisition system (see Figure 4-18). The test track is divided into independent test items on three subgrade classifications: low strength, medium strength, and high strength. In the first four construction cycles, each pavement test item is designated by its construction cycle (CC) number and three characters. The first character denotes the subgrade strength (L-low, M-medium, and H-high). The second character denotes the type of pavement (F-flexible or R-rigid). The third character denotes the type base (S-stabilized, C-conventional, or G-grade). At NAPTF, a variety of embedded (static or dynamic) sensors are used in each CC to capture instrumentation data based on the testing objectives. Static sensors collect temperature, moisture, and crack data on an hourly basis. Dynamic sensors are triggered by the vehicle operation to measure the pavement responses such as strain and deflection during traffic loading.

Construction cycles can be categorized as rigid or flexible test pavement (odd numbers indicate flexible pavement testing and even numbers show rigid pavement testing), except for CC-1 that includes testing both pavement types. Table 4-6 shows a list of construction cycles for testing rigid pavements and the purpose of each test.

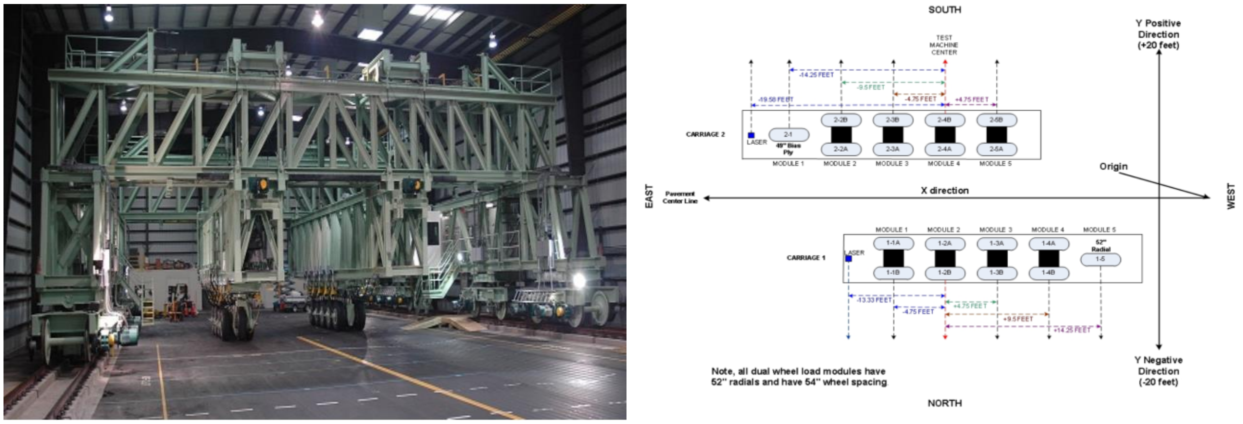

Figure 4-18. National Airport Pavement Test Facility (NAPTF Database 2019).

Table 4-6. Construction Cycles for Testing of Rigid Pavements at NAPTF

Construction Cycle	**Purpose**
Construction Cycle 1	To provide full-scale test data to: • support the new computer-based design procedures that were under development by FAA • be used in airplane landing gear design and configuration studies
Construction Cycle 2	The main experiment was intended to compare the performance of three types of rigid pavements: concrete slabs on stabilized bases (MRS), concrete slabs on aggregate bases (MRC), and concrete slabs placed directly on subgrade (MRG). Other components include: Test Strip – to study the effects of slab size and mix design on pavement curling during the early age of the concrete. Single Slab – to provide experience for the design, placement, and monitoring of the actual PCC test items. Twin Slab – to compare the behavior of the slab with no fly ash content vs. slab with high fly ash content.
Construction Cycle 4	To improve the understanding of the influence of design parameters on unbonded concrete overlays of rigid airfield pavements
Construction Cycle 6	To determine the effect of concrete flexural strength on rigid pavement structural life.
Construction Cycle 8	Phase 1 Overload: The primary objective of Phase 1 was to develop rational overload criteria for rigid pavements. Phase 2 Overlay: The primary object of Phase 2 was to test the performance of a PCC overlay on an existing PCC with Structural Condition Index (SCI) in the 50-80 range. Phase 3 Joint Comparison: The primary objective of Phase 3 was to compare the performance of Type E (doweled construction) and nonstandard sinusoidal keyed longitudinal joints. Phase 4 Strength & Fatigue: The primary objective of Phase 4 was to obtain slab strength (rupture strength) for full-scale slabs under a monotonically increasing aircraft gear load, as well as the fatigue strength of rigid pavement slabs under non-wandered traffic.

CONSTRUCTION CYCLE 2

The primary objectives of the CC-2 tests were to evaluate the pavement performance with different supporting layer properties, to study the influence of 4-wheel and 6-wheel gear traffic on the pavement life, and to assess pavement performance using structural condition index (SCI) versus traffic repetitions. The interior and edge stresses under gear loads as well as shrinkage and curling measurement were other objectives of this construction cycle tests.

The CC-2 consisted of three test items of 75 ft. long by 60 ft. wide, separated by 25 ft. long rigid transitions. Each 75-ft test section comprised of 4 transverse slabs by 5 longitudinal slabs (see Figure 4-19). In main test items, a 12-in. concrete slab with the nominal dimensions of 15 ft. by 15 ft. was placed on medium-strength subgrade (CBR=7~8) area replaced from CC-1. The slab size was selected of based on the results of a previous experiment conducted at the NAPTF, which led to the reduction of corner cracking due to curling when using a smaller size slab. A high amount of (50%) of Class-C fly ash was used in the cementitious mix of concrete to provide a thicker curl resistant slab.

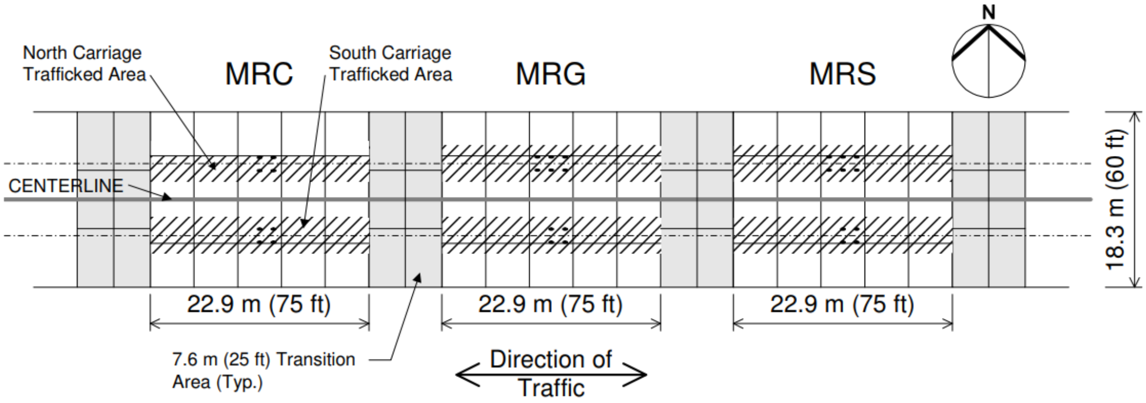

Figure 4-19. Layout of CC-2 Test Items at NAPTF (Brill et al. 2005)

As mentioned in Table 4-7, three configurations of concrete slabs on stabilized (Econocrete) base (MRS), concrete slabs on conventional granular base (MRC), and concrete slabs on grade (MRG) were tested. Figure 4-20 shows the pavement structure for CC-2 test items.

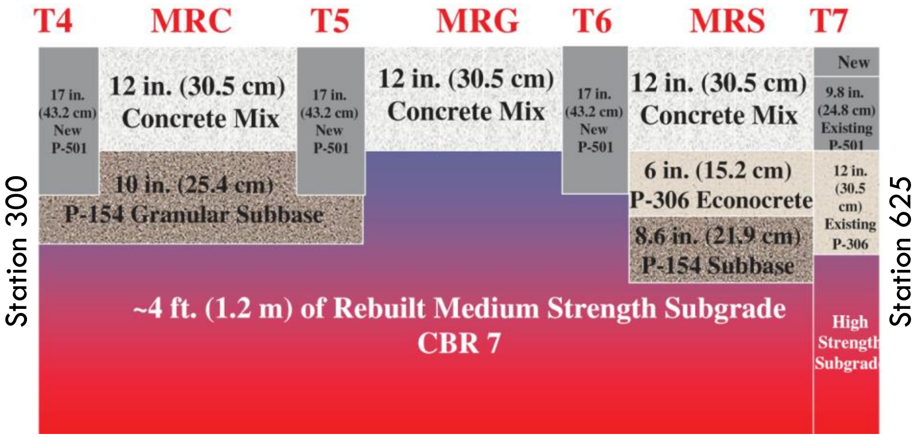

Figure 4-20. Structural Design Data For CC-2 Test Items (Ricalde and Daiutolo 2005)

Target elastic moduli for CC-2 pavement layers were 4,000,000 psi for the concrete slab (P-501), 700,000 psi for the stabilized base layer (P-306), 10,500 psi for Subgrade (Clay CH) layer and the modulus of the granular base (P-154) was variable. To monitor meeting these target values, almost three cylinders and four beams from each slab were taken for laboratory testing of concrete and more than 150 CBR tests and several plate load tests were carried out, with at least one CBR test on each lift during construction to determine the material properties of the base and subgrade layers. CBR tests were conducted on randomly selected locations, preferably within the wheel tracks mirrored on both south and north sides and the acceptable range of the average CBR was set to 5.5 to 8.0. According to the NAPTF database and existing reports on CC-2, the unit weight of the slabs, granular base, stabilized, and subgrade were considered as 149 pcf, 145 pcf, 147 pcf, and 140 pcf, respectively. Poisson's ratio of the slabs, granular base, stabilized, and subgrade were also assumed as 0.15, 0.35, 0.20, 0.45.

Table 4-7 summarizes the layer configurations in MRC, MRG, and MRS test items, results of testing field cured samples, and material properties of the supporting pavement layers. Other material properties such as unit weight and Poisson's ratio were extracted from the NAPTF database and existing reports on CC-2.

Table 4-7. Correlated Modulus of CC-2 Main Test Sections from Field Testing (NAPTF Data Library 2019)

MRC		**MRG**		**MRS**	
Pavement layer	**Modulus (psi)**	**Pavement layer**	**Modulus (psi)**	**Pavement layer**	**Modulus (psi)**
Concrete slab – 12 in.	3,422,000†	Concrete slab – 12 in.	3,336,000†	Concrete slab – 12 in.	3,450,000†
Granular Subbase (P-154) – 10 in.	16,500‡			Econocrete (P-306) – 6 in.	72,000‡
Subgrade	13,500‡	Subgrade	13,500‡	Granular Subbase (P-154) – 8.6 in.	16,500‡
				Subgrade	13,500‡

† Correlated from compressive strength of field cured samples at 28 days using ACI 318 correlation

‡ Correlated from CBR values using correlation $M_r = 1500CBR$

As mentioned earlier, the tire loads in NAPTF are adjustable independently so that the effect of different tire configurations can be evaluated. As one of the objectives of CC-2 testing, the influence of 4-wheel and 6-wheel gear traffic on the pavement life was evaluated. Gear load configuration shown in Figure 4-21a was used in CC-2 traffic testing and the lateral wander of the traffic follows the pattern illustrated in Figure 4-21b. As shown, the pavement was trafficked by a 6-wheel gear configuration on the north side and a 4-wheel gear configuration on the south. The selected load was 55,000 lb. per wheel at 210 psi tire pressure.

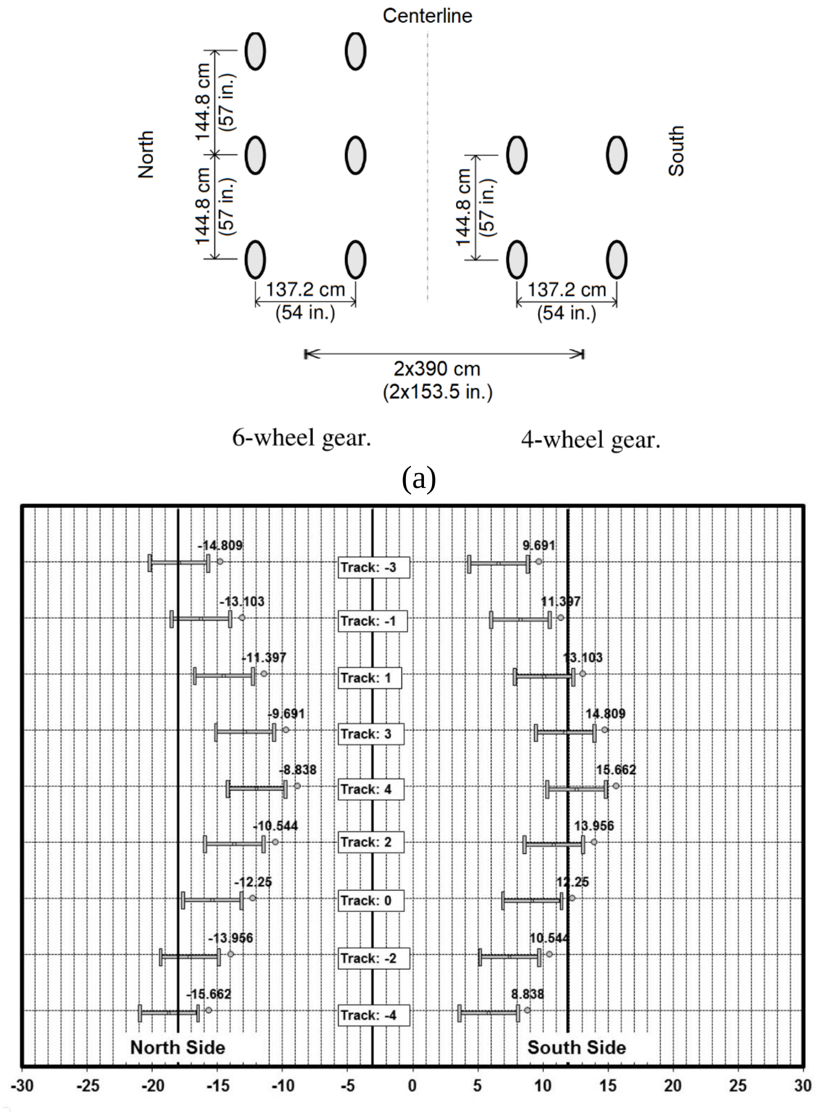

(a)

(b)

Figure 4-21. (a) Gear Load Configuration and (b) Traffic Wander Pattern for CC-2 Traffic Tests (Brill et al. 2005)

Temperature and moisture information were measured using static sensors (e.g. thermistors, vibrating wire strain gauges) embedded at different locations of the test pavement. Dynamic strain sensors were installed at 1.5 in. from the top of slab to capture the critical strains due to reverse slab bending away from the landing gear in order to analyze top-down cracking. Another set of dynamic strain sensors were installed at 1.5 in. from the bottom of slab to record the critical strains under aircraft loading gear, which are associated with the bottom-up cracking of the concrete slab. The coordinates of the load location on the test area change with the traffic wander for each track according to the pattern illustrated in Figure 4-21.

Comparison of HWD Responses

FAA standard configuration (12-in. diameter plate, three impact loads of 12-kips, 24, kips, and 36-kips after seating) was used in HWD testing using Kuab Model 240. HWD tests were performed on the slab centers (to verify pavement uniformity and study the effect of support condition) and on both sides of the outboard longitudinal joints opposite the slab centers (to check the load transfer efficiency at joints) (Ricalde and Daiutolo 2005) at intervals of 15 test vehicle wanders. Figure 4-22a demonstrates the comparison of maximum basin deflection at MRC, MRG and MRS with those obtained from RPAS analysis. A very good agreement between the results of HWD tests and RPAS can be inferred from the figure and the statistical metric *NSE* is close to unity, which confirms this close agreement.

Comparison of Accelerated Loading Responses

To validate the performance of RPAS in modeling heavy aircraft loads on JCPs, the longitudinal and transverse strain responses from 4-wheel gear loading on the south side of the pavement section with different supporting conditions were compared against the responses from RPAS. In each case, two sensors at the inbound of longitudinal joints (S04 and S10 for MRC, S32 and S42 for MRG and S48 and S62 for MRS) and two sensors at the inbound of transverse joints (S02 and S08 for MRC, S24 and S30 for MRG and S46 and S52 for MRS) were selected for comparison. Figure 4-22b demonstrates the comparison of the measured longitudinal strains near the longitudinal joints and those calculated by RPAS (with the maximum RMSE of 18.3 $\mu\varepsilon$) indicate a good agreement (upper three subplots). The biggest difference appears on the MRS case although there is also significant difference between the S48 and S62 sensors with the results of RPAS falling right on the average of the two. For the transverse joint (lower three subplots) the biggest RMSE is 19.1με appearing in the MRS case. It is important to note that, just in the case of the S48 and S62 sensors above, the sensors in the MRC and MRS in these transverse joint strains also show significant differences. It is only in the MRG case that the two sensors show consistent measurements and RPAS under predicts the strain by 20% which will require further analysis to identify the source of the difference.

Similar to the cases from the HWD testing comparison, the program yields the best prediction for cases with conventional pavement section, MRC at longitudinal joints. There are larger errors in strain responses at transverse joints which may occur due to different load transfer mechanism. Some of the sources of errors in the predictions include the dynamic effect of accelerated loading and non-uniformity of in-place pavement properties.

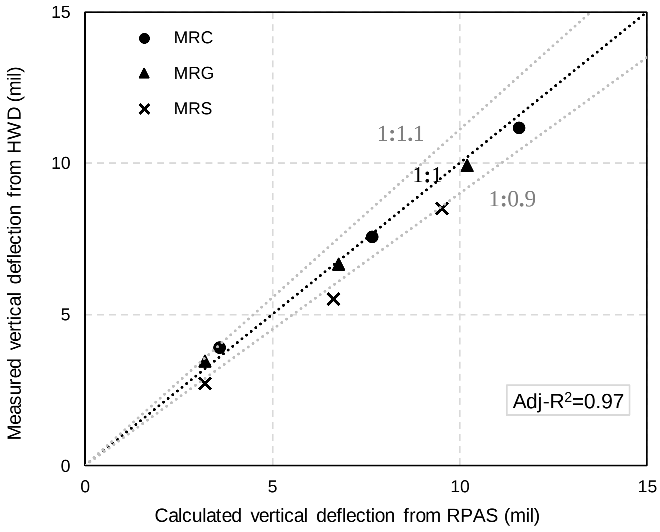

Nash-Sutcliffe Efficiency (NSE)

MRC		
12 kips	24 kips	36 kips
0.997	*0.999*	*0.999*

MRG		
12 kips	24 kips	36 kips
0.996	*0.998*	*0.997*

MRS		
12 kips	24 kips	36 kips
0.969	*0.929*	*0.936*

(a)

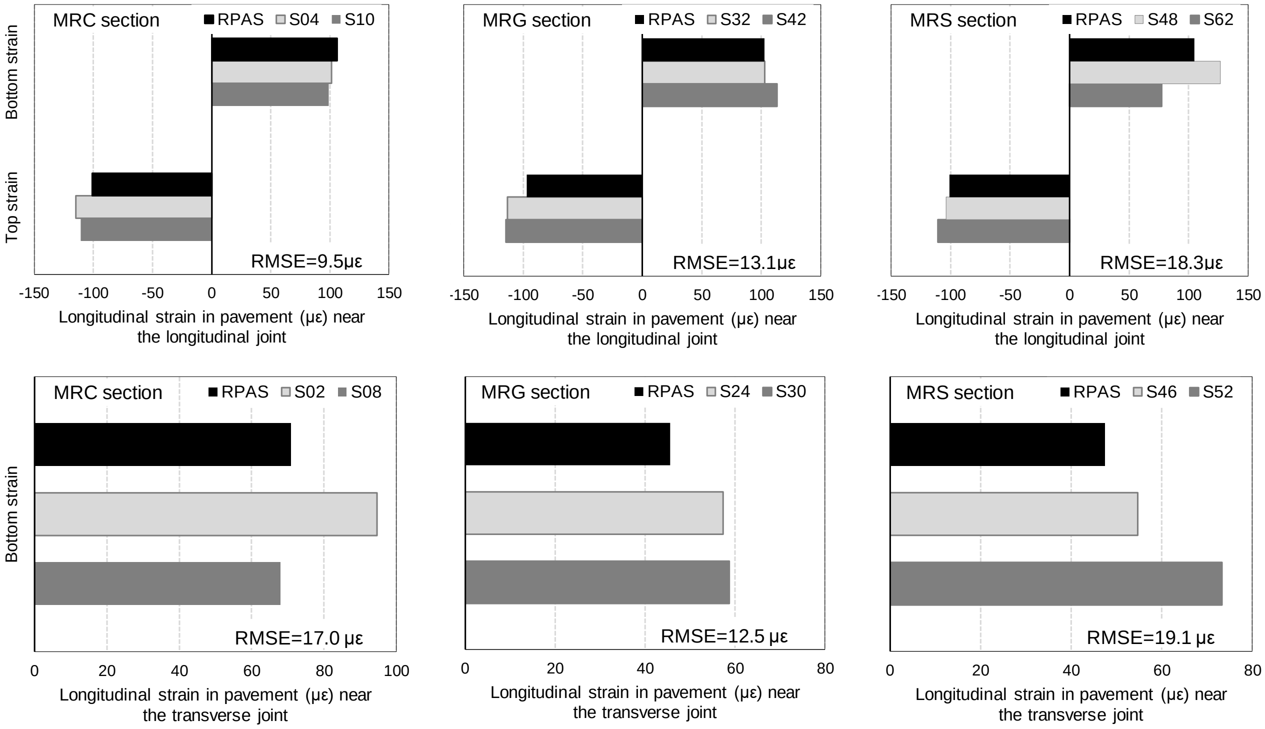

(b)

Figure 4-22. (a) Maximum Basin Deflection at the Center Of Slab From HWD Tests In CC-2 NAPTF versus The Deflections Calculated From RPAS Analyses (b) Comparison of Strain Responses at the Top and Bottom of Concrete Slab From Two Consecutive Sensors Along The Longitudinal/Transverse Joints of Different Sections From Accelerated Testing and The RPAS Strain Responses.

CONSTRUCTION CYCLE 4

The primary objectives of the CC-4 tests were to enhance the knowledge about the influence of design parameters on unbonded concrete overlays of airfield pavements and thus enabling improvement of design methodologies. CC-4 consisted of two separate components: baseline tests on new rigid pavements, and validation test on damaged rigid pavements. verifying failure mechanisms, formulating overall life prediction, and determining effects of discontinuities (mismatched joints and cracks) on stresses and deflections are the objectives of the baseline tests. As in CC-2, the performance of pavements was evaluated under different support conditions, subjected to 4-wheel and 6-wheel gear traffic loading, and using structural condition index (SCI). The present study will only consider baseline tests on new pavements.

CC-4 consisted of a 300-foot test pavement that had three structural cross-sections and was constructed on the medium-strength (CBR=6~9) subgrade. The baseline experiment consists of six test items, in three structural sections of varying thicknesses constructed on the medium-strength subgrade, separated by transition slabs in both the longitudinal and transverse directions. As shown in Figure 4-23, each test item consists of 12 slabs of 12.5×12.5 ft, that is, 12.5-ft wide lanes, with a 10-ft transition slab between the test items. Overlay slabs were dowelled in longitudinal and transverse directions but not to the transition slabs, whereas the underlay slabs were designed to be undoweled to provide greater discontinuities in support. The concrete mix was designed to be identical to that in CC-2. The design thickness of overlay and underlay concrete pavements are shown in the pavement structure diagram in Figure 4-23b.

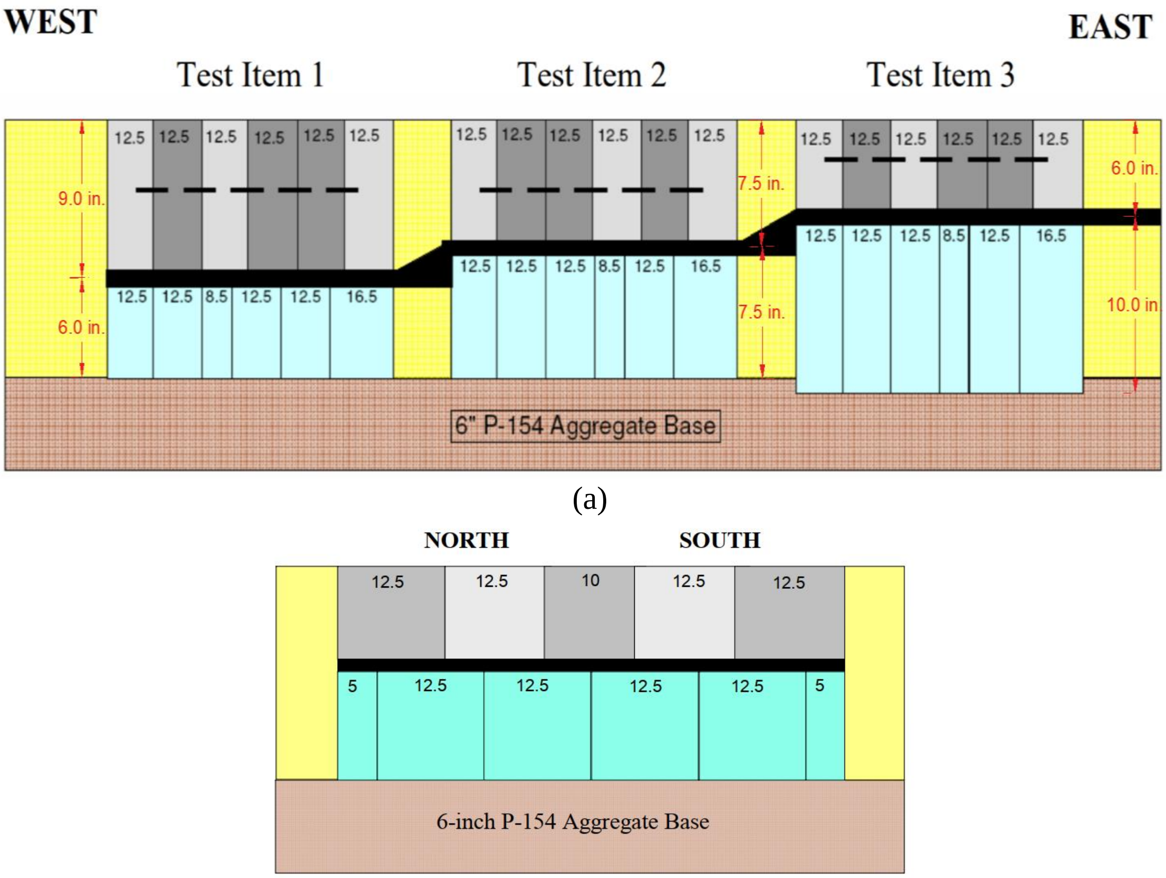

(a)

(b)

Figure 4-23. Layout of CC-4 Test Items at NAPTF (a) Longitudinal Cross-Section Showing Transverse Joints (b) Transverse Cross-Section Showing Longitudinal Joints (Stoffels et al. 2008)

Target elastic moduli for CC-4 pavement layers was 4,000,000 psi for the concrete slab (P-501) and the modulus of the granular base (P-154) was variable. CBR tests were conducted on randomly selected locations, preferably within the wheel tracks mirrored on both south and north sides and the acceptable range of the average CBR was set to 6 to 9. Table 4-8 summarizes the results of testing lab/field cured samples in CC-4 test items.

As mentioned by Stoffels et al. (2008), results from strength testing of underlay and overlay concrete pavements were fairly consistent. Thus, for modeling purposes in the present study, the correlated elastic moduli of 90-day flexural strength of field cured concrete specimens equal to 503 psi for underlay and 560 psi for overlay were used. The numbers shown for the thickness of pavement layers are the average of the thicknesses measured on a 10 by 10 ft grid. However, based on the coordinates of the section being modeled, the actual measured thickness was used.

As indicated in Table 4-8, the resilient modulus of base and subgrade layers were correlated with the reported CBR values and have been confirmed with the *k*-values of 143 psi/in. on the north side and 146 psi/in. on the south side, averaged from several plate load tests.

According to the NAPTF database and existing reports on CC-4, the unit weight of the overlay slab, underlay slab, granular base and subgrade were considered as 155 pcf, 152 pcf, 147 pcf, and 140 pcf, respectively. Poisson's ratio of the slabs, granular base, and subgrade were assumed as 0.15, 0.35, and 0.45.

Table 4-8. Material Properties Used for Modeling CC-4, Extracted from Field and Laboratory Testing

Pavement layer		**Test item**	**Modulus (psi)**	**Poisson's ratio**	**Thickness (in.)**[*]	**Unit weight (pcf)**
Concrete slab	OL[**]	1	3,840,000†	0.15	8.7	155
		2			7.4	
		3			5.7	
	UL[**]	1	4,276,000†		6.3	152
		2			7.5	
		3			9.9	
Granular Subbase (P-154)		1	16,200‡	0.35	5.7	147
		2	15,800‡		5.6	
		3	16,250‡		4.7	
Subgrade		1	11,700‡	0.45	-	140
		2	11,325‡			
		3	12,900‡			

* As-built thicknesses, measured on a $10' \times 10'$ grid

** OL=overlay, UL=underlay

† Correlated from flexural strength of field cured samples at 90 days using ACI 318 correlation $E_c = 7635 f_r$

‡ Correlated from CBR values using correlation $M_r = 1500CBR$

As in CC-2 testing, the influence of 4-wheel and 6-wheel gear traffic on the pavement life was evaluated in CC-4. Gear load configuration shown in Figure 4-24a was used in CC-4 traffic testing and the lateral wander of the traffic follows the pattern illustrated in Figure 4-24b. As shown, the pavement was trafficked by a 6-wheel gear configuration on the north side and a 4-wheel gear configuration on the south. The applied load was 45,000 lb. to 65,000 lb. per wheel at an inflated tire pressure of 230 psi. For modeling purposes, depending on the date and time of the test, the exact magnitude of each tire load and pressure were used, as reported in the CC-4 database.

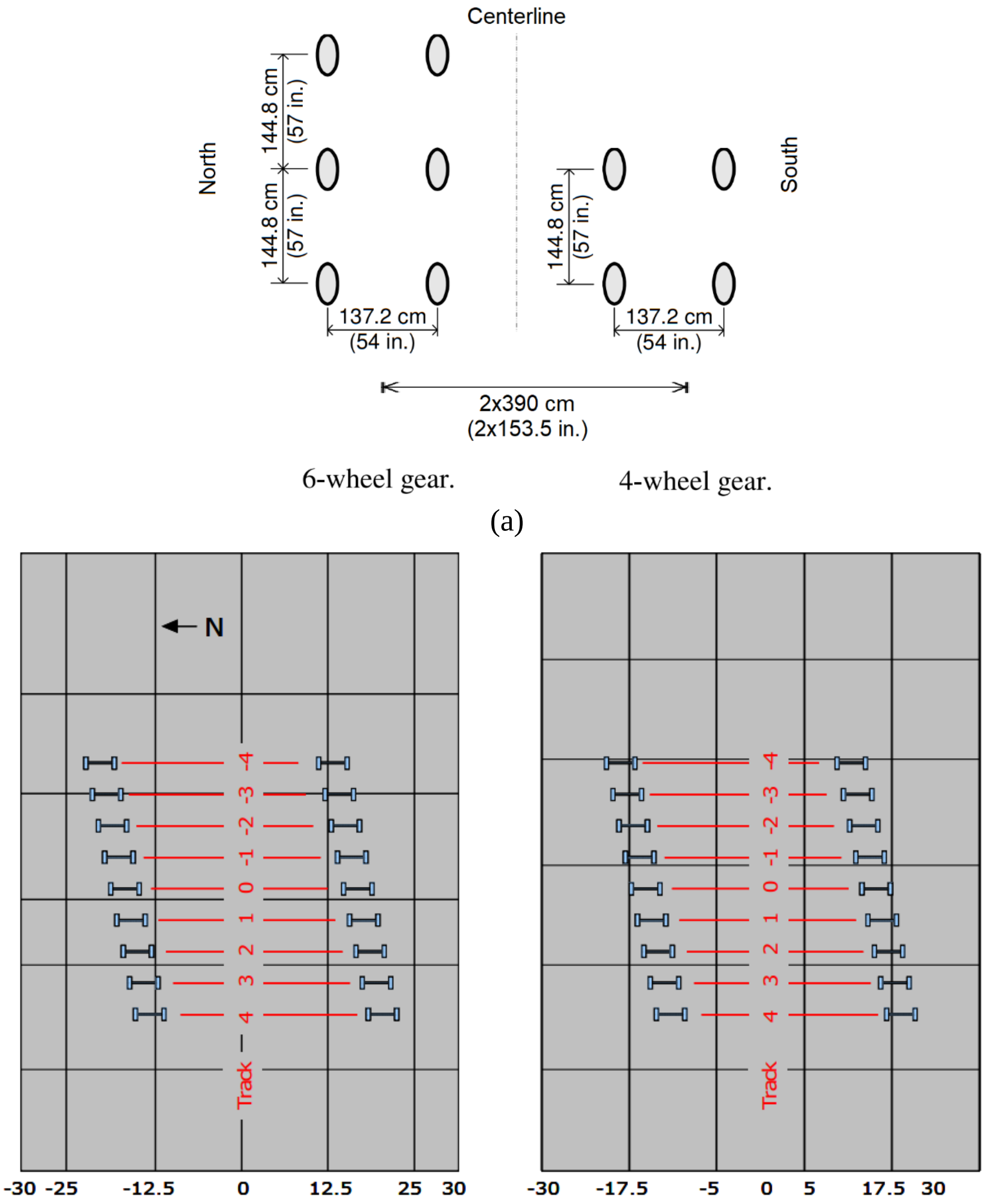

(a)

(b)

Figure 4-24. (a) Gear Load Configuration and (b) Traffic Wander Pattern for CC-4 traffic tests

Temperature and moisture information were measured using static sensors (e.g. thermistors, vibrating wire strain gauges) embedded at different locations of the test pavement. Dynamic strain sensors were installed at 1.5 in. from the top of slab to capture the critical strains due to reverse slab bending away from the landing gear in order to analyze top-down cracking. Another set of dynamic strain sensors were installed at 1.5 in. from the bottom of slab to record the critical strains under aircraft loading gear, which are associated with the bottom-up cracking of the concrete slab. The coordinates of the load location on the test area change with the traffic wander for each track according to the pattern illustrated in Figure 4-24.

Figure 4-25 illustrates the overlay and underlay joint arrangements and the modeled section of the pavement. The results of RPAS modeling of this accelerated loading compared to those of field measurements are shown in Figure 4-26. As can be seen, there is reasonable agreement between the measured strain responses and those calculated using RPAS in both overlay and underlay. The maximum dynamic strain percent differences occur at points 2 and 4 which is expected since it is at these points that the absolute strains are the lowest. The maximum difference at a peak strain points is of 59% and it is expected that the calibration process will reduce it.

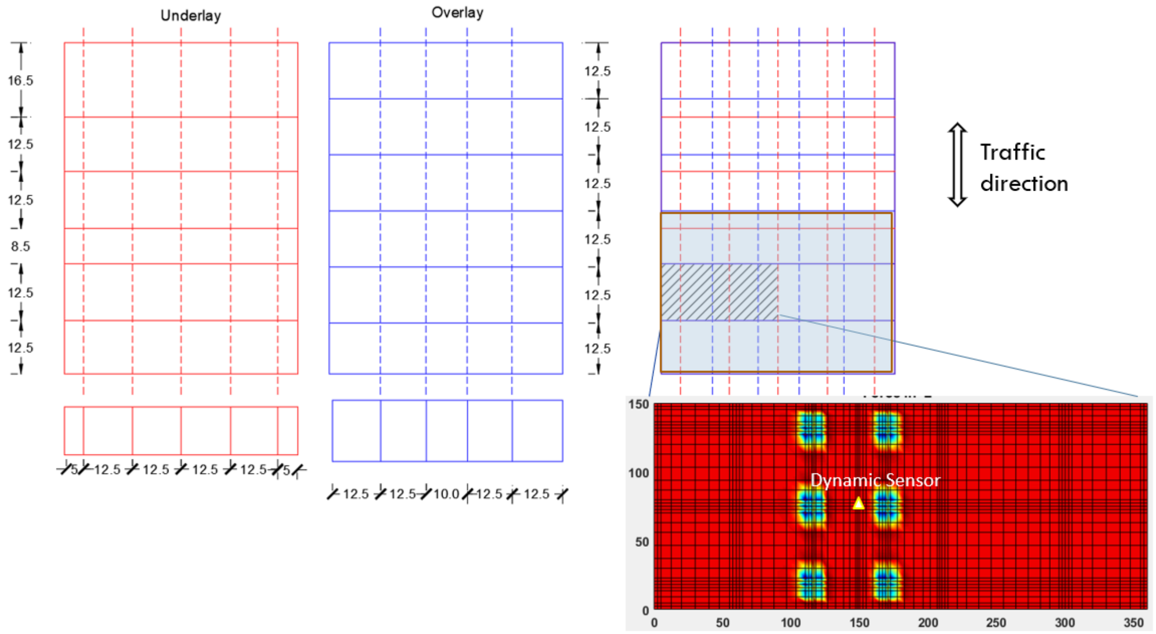

Figure 4-25. Overlay and Underlay Joint Arrangements and The Modeled Section of The Pavement

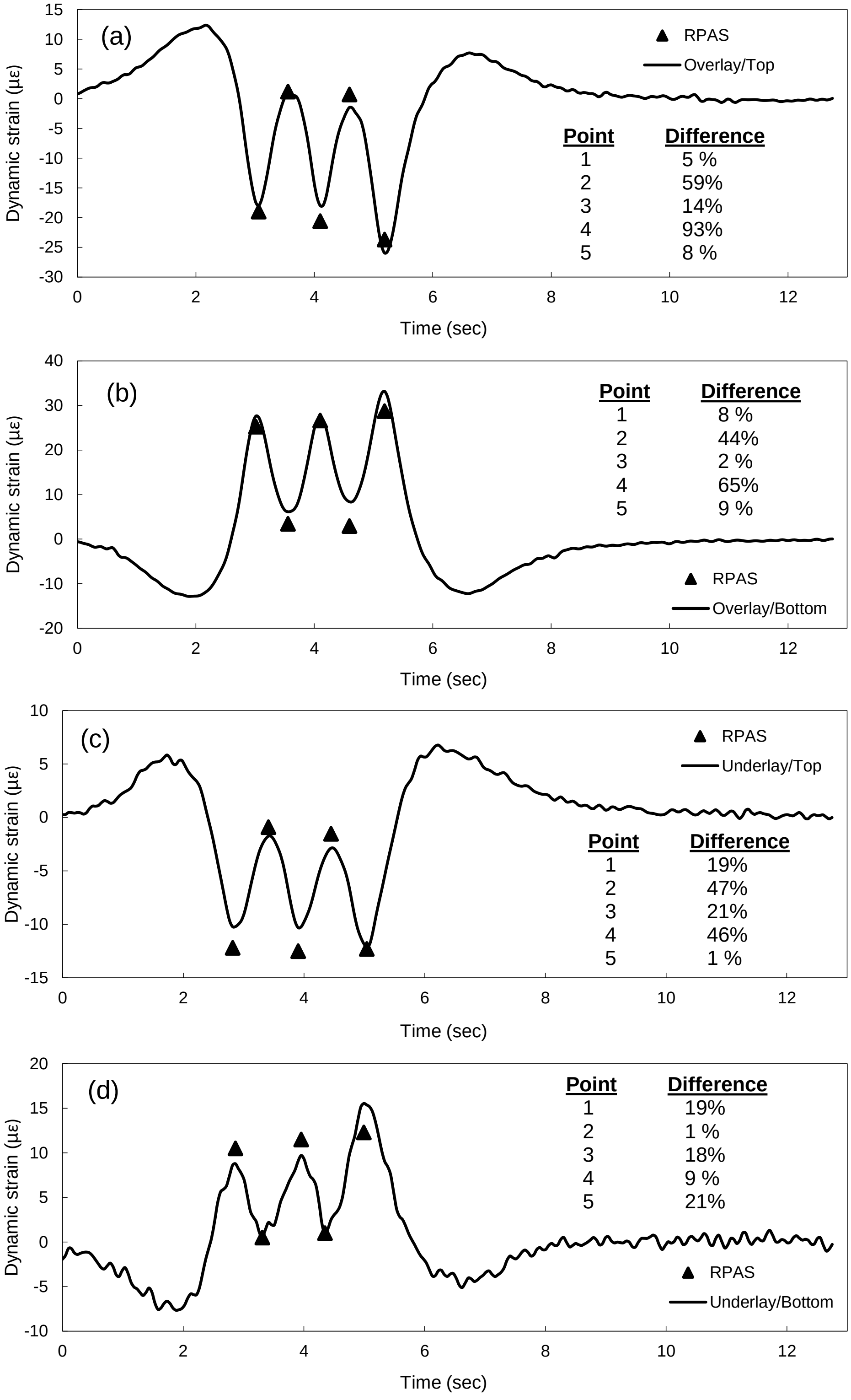

Figure 4-26. Comparison of Dynamic Strain Responses Developed in Overlay and Underlay from RPAS Analyses and Field Measurements

CONSTRUCTION CYCLE 6

The primary objective of the CC-6 tests was to determine the effect of concrete flexural strength on rigid pavement structural life. For this purpose, three test items of rigid pavement with similar cross sections and varying concrete flexural strength were designed. Comparison of the influence of different stabilized base materials (hot-mix asphalt and Econocrete) on the rigid pavement performance was another objective of this study. Two types of isolation joints, thickened edge and steel-reinforced, have also been compared. All the test items were designed on the medium-strength subgrade. The performance of the pavements was evaluated by applying a 4-wheel gear traffic loading on both north and south sides.

CC-6 consisted of a 300 ft long by 60 ft wide test pavement that had three test items of MRS-1, MRS-2, and MRS-3, having the concrete 28-day target flexural strength of 500, 750, and 1000 psi, respectively (see Figure 4-27a). Each test item consisted of 10 slabs of 15×15 ft by 12-in. thick with a 10-ft transition slab between the test items. The slabs were doweled on all sides, except for slab edges abutting the shoulder and the isolation joints located in the transition areas. The 6-in. stabilized base layer was HMA P-403 on the north side and Econocrete P-306 on the south side. A 10-in. granular subbase layer was placed below this stabilized base layer and the pavement was constructed on the medium-strength (average CBR=8) subgrade (Figure 4-27b).

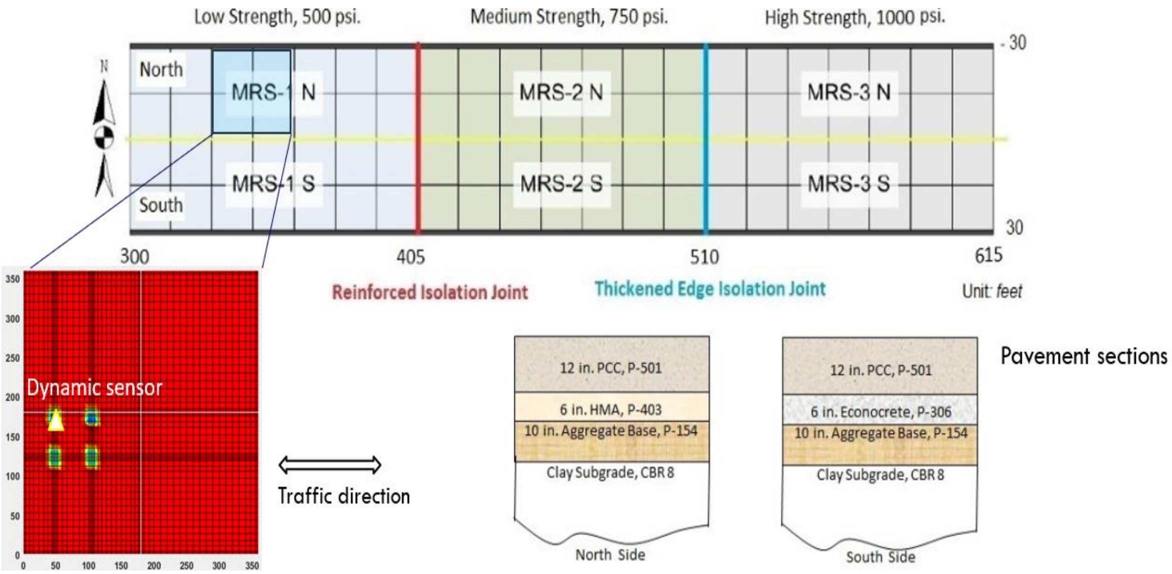

Figure 4-27. Layout of CC-6 Test Items at NAPTF Pavement Plan Showing Three Test Items and Transverse Cross-Section Showing Pavement Structure (McQueen and Hayhoe 2014)

The target strengths indicated in Figure 4-27 might not necessarily be achieved during construction and thus the material characterization and testing was carried out to assess the pavement uniformity using both destructive and nondestructive (e.g. FFRC, PSPA, GPR, HWD) testing.

In CC-6, the strength of concrete layer was evaluated using compressive and flexural strength tests on core samples and laboratory casted specimens as well as nondestructive (e.g. FFRC, PSPA) testing. The average 28-day compressive strength was estimated as 4,012 psi on the north side and 4,386 psi on the south side. The average flexural strength of concrete layer was generally above the target values. For instance, the average flexural strength of concrete in MRS-1 on the north side was 650 psi, which is higher than the target value of 500 psi. However, for modeling purposes, the target values were used for comparison with other tests to derive modulus of concrete layers in order to consider a more conservative design. Table 4-9 summarizes the results of testing lab or field cured samples in CC-6 test items and the average values of each parameter.

CBR and plate load tests were conducted after the construction of each pavement layer at certain stations before and after trafficking. These tests have been conducted at the offset of 15 ft from the centerline, mirrored on north and south sides of the test section. The results of these tests were compared to verify that the obtained modulus of each pavement layer from the existing correlations match within a reasonable tolerance. For the purpose of this study, the as-built material properties prior to trafficking were utilized. From the results of plate load tests, the average *k*-values of subgrade, subbase, and base layers were 132, 205, 416 psi/in. on the north side (HMA base) and 139, 214, 850 psi/in. on the south side (Econocrete base), respectively. The CBR values of subgrade were 6.5 on the north side and 7.2 on the south side. The results of resilient modulus tests has shown an average resilient modulus of 11,600 psi for the north side and 12,300 psi for the south side, which confirms the validity of using the correlation $M_r = 1500CBR$. Even though the average material properties for the pavement layers on the north and south side have been reported here, the values from laboratory or field measurements at each test item were used for modeling. The unit weight of the concrete slab, stabilized base (HMA/Econ), granular subbase, and subgrade were considered as 148 pcf, 143/146 pcf, 149 pcf, and 155 pcf, respectively, according to the NAPTF database and existing reports on CC-6. Poisson’s ratio of the slab, stabilized base (HMA/Econ), granular subbase, and subgrade were assumed as 0.15, 0.30/0.25, 0.35, and 0.45 (see Table 4-9).

Table 4-9. Material Properties Used for Modeling CC-6, Extracted from Field and Laboratory Testing

Pavement layer		Test item*	Modulus (psi)	Poisson's ratio	Thickness (in.)	Unit weight (pcf)
Concrete Slab (P-501)		N S	3,610,000† 3,775,000†	0.15	12	148
Stabilized Base	HMA (P-403)	N	60,000‡	0.30	6	143
	Econ (P-306)	S	1,432,000†	0.25		146
Granular Subbase (P-154)		N S	24,200‡ 25,500‡	0.35	10	149
Subgrade		N S	11,600‡ 12,300‡	0.45	-	155

* N=North side, S=South side

† From correlation with compressive strength of field cured samples using ACI 318 correlation, confirmed with fracture testing by Stoffels et al. (2014)

‡ Correlated from CBR values using correlation $M_r = 1500CBR$, confirmed with *k*-values

In CC-6 testing, the influence of airplane gear loading on the pavement performance was evaluated. As opposed to CC-2 and CC-4, gear load configuration consists of two identical 4-wheel gears on both north side and south side of the test pavement (see Figure 4-28a). Wheel loads varied in three levels of 45,000, 52,000, and 70,000 lb. per wheel at different testing periods. MRS-1 was only trafficked with the first load level that was sufficient to cause failure in this low-strength concrete test item. The nominal inflated tire pressure was 250 psi, although the actual tire pressures were reported in CC-6 database and have been used for modeling. The wander pattern used for the traffic testing was designed in a way that it simulates a normal distribution of aircraft traffic (Figure 4-28b). For modeling, 50,000 lb load and the pressure of 230 psi were used.

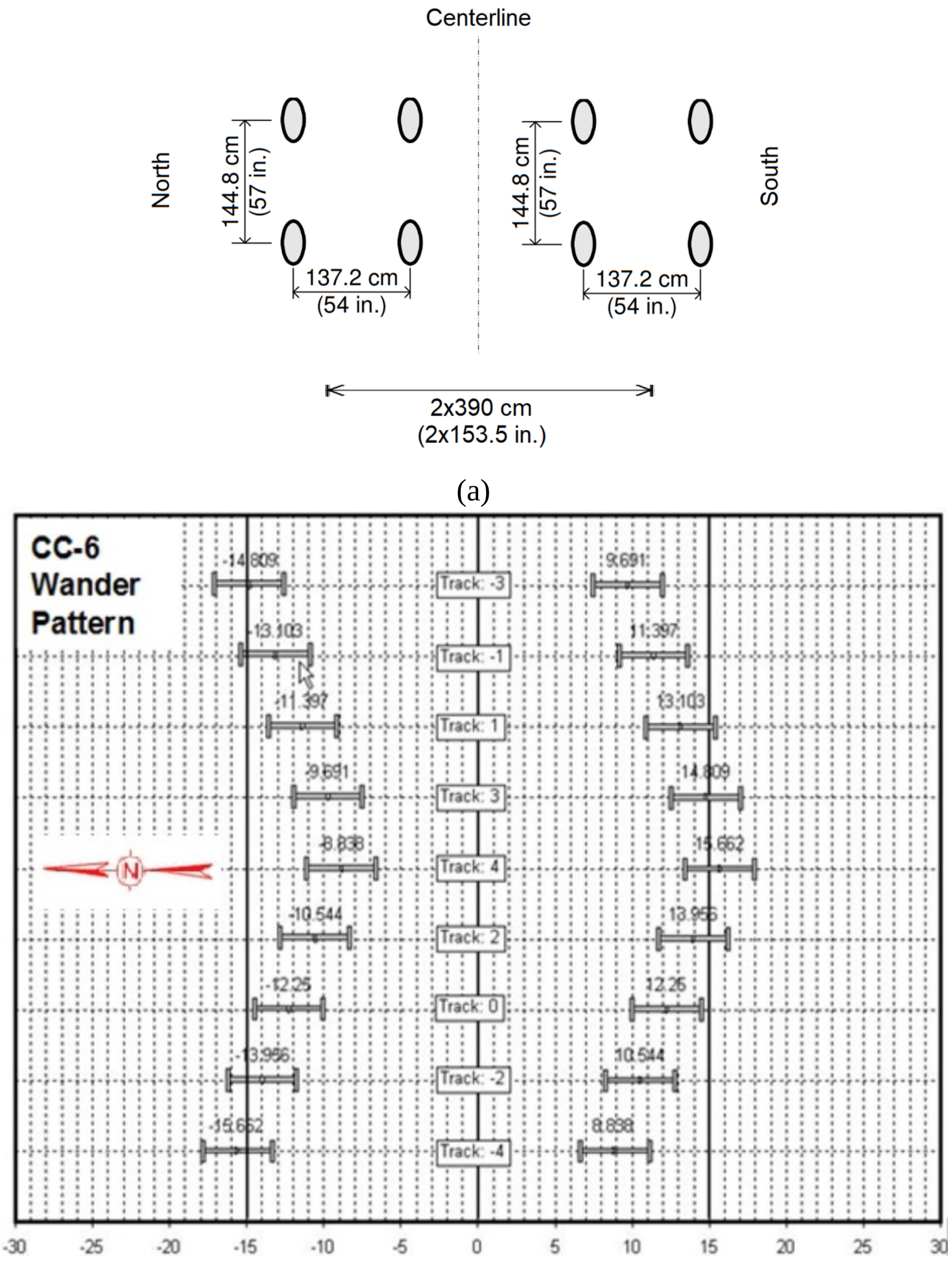

(a)

(b)

Figure 4-28. (a) Gear load configuration and (b) traffic wander pattern for CC-6 traffic tests

The hourly temperature and moisture information were measured using static sensors (e.g. thermistors, vibrating wire strain gauges) embedded at different locations of the test pavement. Dynamic strain sensors were installed at 1.0 in. from the top of and bottom of the slabs to capture top-down and bottom-up cracking potential. These sensors are triggered by movements of the load vehicle. The coordinates of the load location on the test area change with the traffic wander for each track according to the pattern illustrated in Figure 4-28.

A comparison of the dynamic strain responses of pavement from RPAS and field measurement at CC-6 is made in Figure 4-29. As can be seen, there is a reasonable agreement in the variation of the measured and calculated pavement responses. The maximum differences at peak strain points is of 23% and it is expected that the calibration process will reduce it.

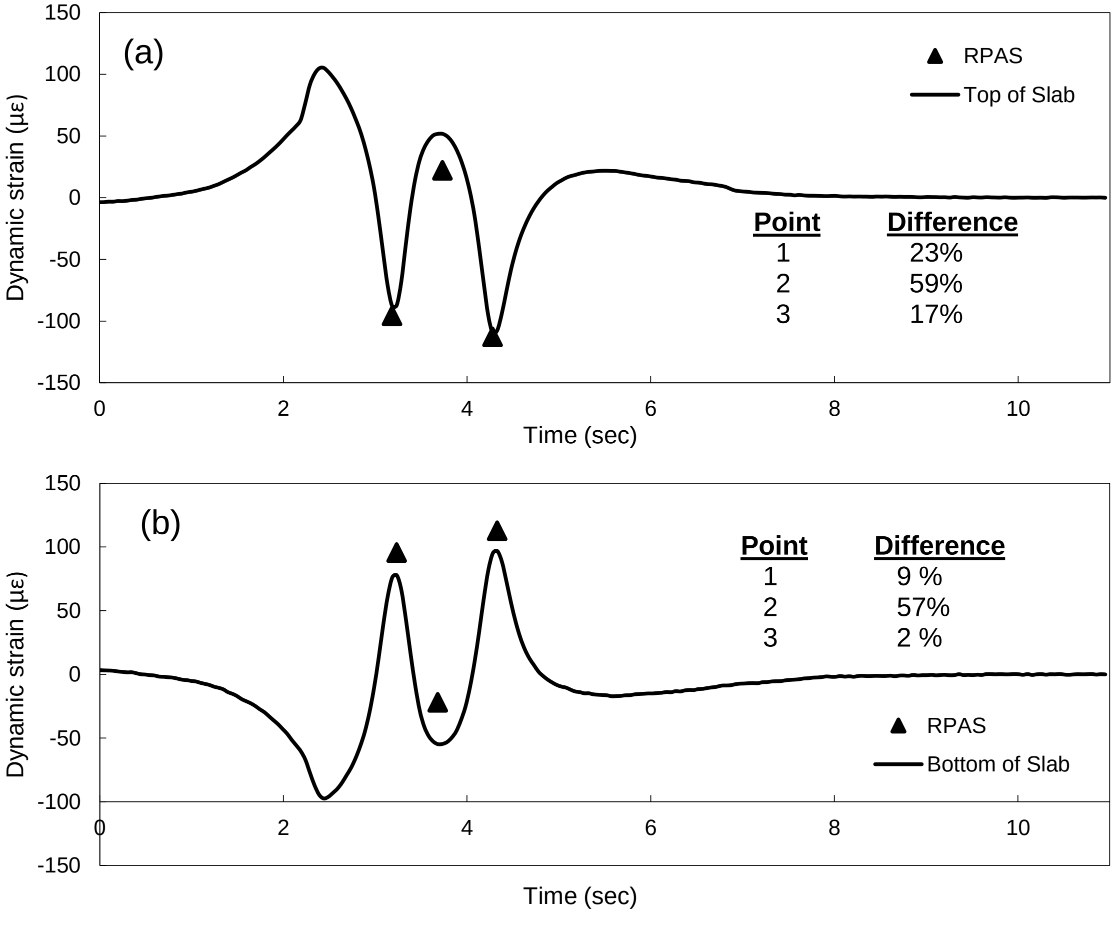

Figure 4-29. Comparison of the dynamic strain responses of pavement from RPAS and field measurement at CC-6

5. Verification

This chapter discusses the verification process that includes the calculation verification and bench-marking of RPAS against existing analytical solutions and numerical analyses. The purpose of verification is to check how close the code outputs are to the closed-form or numerical solution of the problem and attempt to minimize the generated error.

5.1. Calculation Verification

Calculation verification is associated with establishing confidence that the discrete solution of the mathematical model is accurate, which includes estimating the errors in the numerical solution due to discretization. This discretization error (ε_h), that is also called solution approximation error, is used to quantify the uncertainty in the predictions. Several methods are available in the literature (Babuška and Rheinboldt 1978, Rangavajhala et al. 2011) to estimate discretization error in finite element analysis. The Richardson extrapolation (RE) method has been commonly applied to quantifying the solution approximation error (Sankararaman and Mahadevan 2015). In this method, the finite element analysis is repeated for three different mesh sizes ($h_1 < h_2 < h_3$) and the corresponding finite element solutions ($y_{FE}(\mathrm{h}_1) = \theta_1$, $y_{FE}(\mathrm{h}_2) = \theta_2$, $y_{FE}(\mathrm{h}_3) = \theta_3$) are recorded. If a relationship for the calculation of the true solution is available, the obtained three equations could have been solved simultaneously to estimate the solution approximation error, ε_h. However, in most cases of finite element analysis, by considering the assumption of constant mesh size ratio (i.e., $r = h_3 / h_2 = h_2 / h_1$), the following closed-form solution can be used to estimate ε_h, and, correspondingly, the real solution y (Sankararaman and Mahadevan 2015):

$$y = \theta_1 - \varepsilon_h \tag{5-1}$$

$$\theta_2 - \theta_1 = \varepsilon_h (r^p - 1) \tag{5-2}$$

where y is the real solution, θ_1, θ_2, θ_3 are the finite element solution for different mesh sizes, r is the mesh size ratio, and p is a variable that is a function of r and the solutions θ_1, θ_2, θ_3 .

The above process based on Richardson extrapolation method has been used in this study that will be discussed later in this chapter. However, the study in the following section was performed to determine the range of mesh sizes to be used in the RE method.

MESH SIZE IN RPAS

RPAS has the capability of generating uniform and non-uniform meshes with any level of refinement in the horizontal plane, as shown in Figure 5-1. The non-uniform mesh is automatically generated in the model by increasing the number of elements in the region close to the point of application of the vehicle loads and on the edges of the slabs when more than one concrete slab is modeled. To identify the element size that results in the convergence of solutions, Carrasco et al. (2011) developed a single slab with a single-tire load model. The control parameters used to characterize convergence were the pavement maximum deflection and normal bending stress. Based on their results, for a uniform mesh, an element size of no more than 12 in. in each direction is required. The non-uniform mesh beneath the tires and at the slab edges was obtained by subdividing each element in these regions into at least four elements (see Figure 5-1).

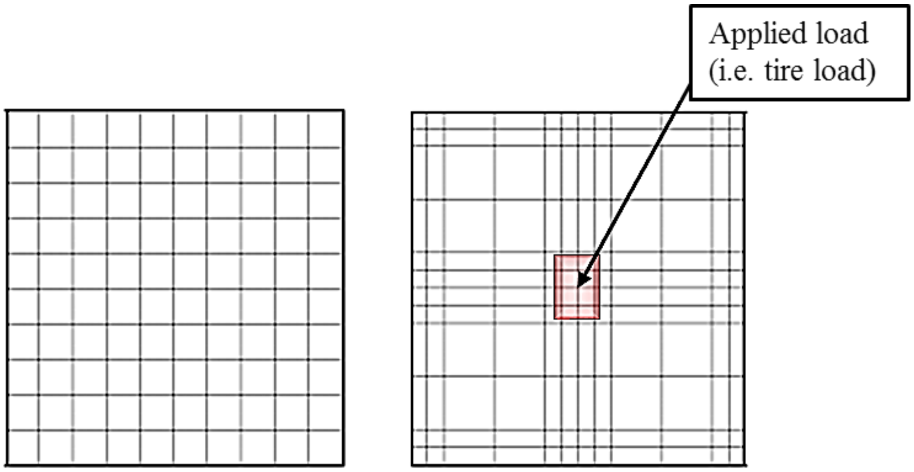

(a) Uniform Mesh **(b) Non-Uniform Mesh**

Figure 5-1. Configuration of Uniform and Non-uniform Mesh

Upon the incorporation of the 3-D solid foundation, a new convergence study is developed to determine the number of elements required throughout the depth of each foundation layer. A single slab (150 in. by 100 in.) under a single tire load of 9 kips and a single-axle load of 18 kips with a pressure of 120 psi was applied at the center of the slab. Three different pavement structures were analyzed for this purpose: slab on subgrade (G), conventional pavement, i.e. slab on a base layer over subgrade (C), and slab on the stabilized base, granular base, and subgrade (S). Table 5- 1 shows the analysis cases used to determine the number of elements required for each soil thickness and pavement structure; a total of 128 cases.

Table 5-1. Input Variables to Determine Mesh Convergence

On Grade (G)		**Conventional (C)**		**Stabilized (S)**	
Pavement layer	**Modulus (ksi)**	**Pavement layer**	**Modulus (ksi)**	**Pavement layer**	**Modulus (ksi)**
Concrete slab – t = 10 in.	5,000	Concrete slab – t =10 in.	5,000	Concrete slab – 10 in.	5,000
		Granular Base – t = 2,4,8,12 in.	100	Stabilized Base – t = 2,4,6,10 in.	500
Subgrade – t = 6,10,20,30 in.	30	Subgrade – t = 8,20,30 in.	30	Granular Base – t = 2,4,8,12 in.	100
				Subgrade – t = 12,20,30 in.	30

- Concrete slab was modeled as plate element and all soil layers were modeled using the solid 27-node element.
- All cases were analyzed under both single tire and axle loading.

The maximum horizontal (longitudinal and transverse) stresses underneath the tire load at the surface of the soil layer were the control parameter used to characterize convergence. The horizontal stress was normalized with respect to the stress obtained from the number of elements that provided less than one percent difference from the previous recorded stress. Figure 5-2a provides the normalized stress converge results for soil thicknesses, *t* = 6, 10 and 20 in. on (G) cases. The rest of the cases were analyzed similarly. It is assumed that the maximum element size in each layer is primarily dependent on its thickness. To confirm this assumption, the correlation between layer thickness and the number of elements for convergence of the horizontal stress was plotted in Figure 5-2b. As can be seen, there is almost a one-to-one relationship between the layer thickness (in inch) and the number of elements.

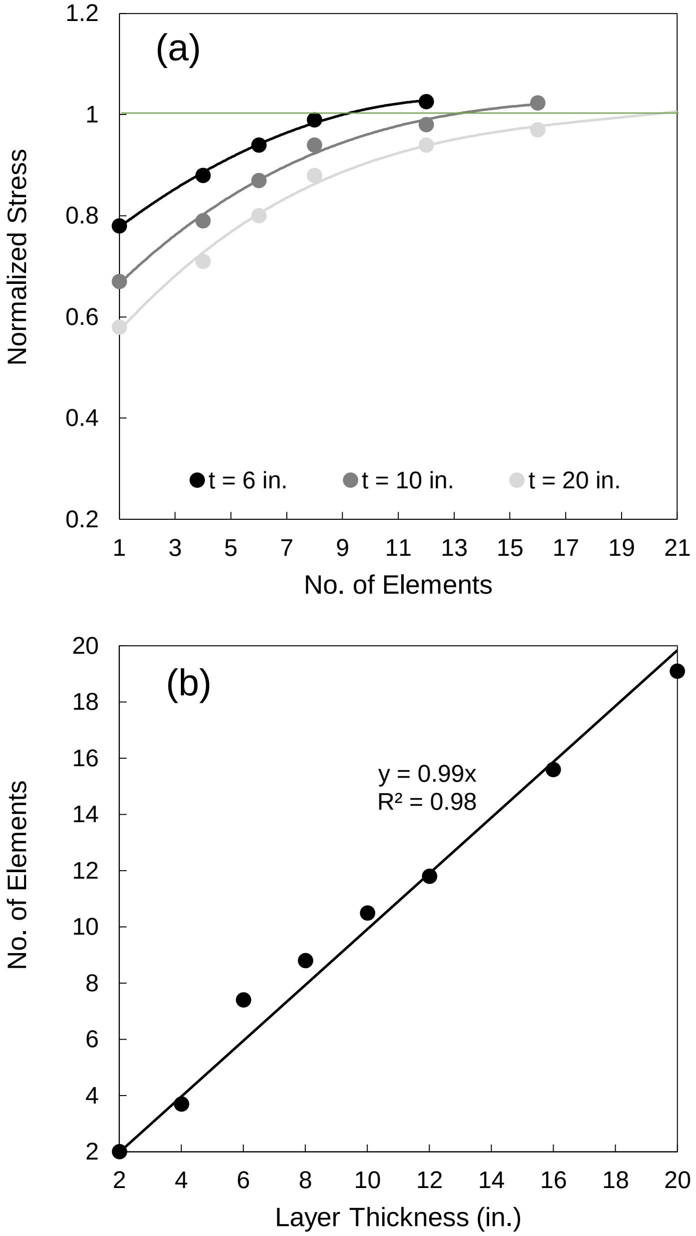

Figure 5-2. (a) Horizontal Stress Convergence for Varied Soil Thicknesses (b) Correlation between the Layer Thickness and number of elements required to reach convergence.

Based on the results, the maximum element size that allows the stress to converge was achieved when the slab on the stabilized layer (S) under single tire load was analyzed. This can be due to low variation of stress within the pavement depth as a result of high stiffness. In this case, the maximum element size of slightly over 2 in. for the first layer and two vertical elements in the subsequent layers were determined. On the other hand, the minimum necessary thickness to reach the convergence was observed when the slab was placed directly on the subgrade layer (G), which was almost 1 in. for the first layer and three vertical elements for the subsequent layers. Therefore, to ensure that the stress in the foundation layers converge based on the criterion of maximum one percent difference, it is recommended that the first foundation below the slab to be discretized in 1-in. thick elements and the rest of the layers to be divided into more than three vertical elements. Although this recommendation addresses the possible convergence issues, it is necessary to quantify the solution approximation error due to discretization and incorporate it in the finite element analysis of concrete pavement system.

DETERMINATION OF SOLUTION APPROXIMATION ERROR

As discussed earlier, the pavement model in RPAS is discretized in horizontal plane based on the location of tire loads and slab edges. In vertical direction, once the decision on the element size or number of elements is made, the solution approximation error (ε_h) can be estimated. To demonstrate the process, an example from the analyses in the previous section is presented here. Let's consider the pavement with the 10-in. concrete slab over a 4-in. stabilized base, an 8-in. granular base, and a 20-in. subgrade (S case) in Table 5-1 subjected to single tire load of 9 kips. Three element size of 0.5, 1, and 2 in. were considered for the stabilized base layer and the magnitude of horizontal stress at the top of this layer were recorded for each mesh size, i.e. 11.2, 11.0, and 10.7 psi, respectively. The reason for this small difference in the magnitude of stresses is the considered narrow range of element size that have been determined based on the convergence analysis in the previous section. Using equations (5-1) through (5-2), we obtain:

$$\varepsilon_h = \frac{11.0 - 11.2}{(2^{0.585} - 1)} = -0.40 \tag{5-3}$$

Therefore, the solution approximation error in this case will be equal to -0.40 psi, which is less than 4% error and can be utilized to correct the finite element solution of stresses. It is recommended that this process to be incorporated before the calibration process of RPAS (or any other finite element analysis tool) is initiated to integrate the verification with the calibration and validation process.

5.2. Bench-Marking

The failure of a numerical code to reproduce an analytical solution is a critical issue. As discussed in Chapter 2, the practice of comparing numerical and analytical solutions is referred to as bench-marking (Oreskes et al. 1994). This term that is commonly used in geodetic practice denotes the reference of the solution (obtained from numerical code) to an accepted standard (analytical solution) whose absolute value can never be known. Therefore, bench-marking is a multi-level process in which a complex engineering system is divided into multiple subsystems. For instance, the slab under a point load is initially analyzed and compared with the close-form solutions and, subsequently, the foundation layers and then the temperature loading are considered to perform next levels of bench-marking. The range of the input parameters used for bench-marking were selected based on recommended values in design specifications, that are specified in Chapter 6.

PAVEMENT RESPONSE DUE TO TIRE LOADING

As discussed in the previous section, verification begins with the comparison of the developed code with the analytical solution for a simplified system (with restricted features, physics, etc.) and then will be expanded to more advanced comparisons. Thus, as the first level of bench-marking, RPAS results under traffic loading were compared with the Westergaard's solution (Westergaard 1926) for the pavement over a single layer foundation and Burmister's solution (Burmister 1943) based on multi-layered elastic theory (MLET) employing BISAR program (De Jong et al. 1973). Then, a series of finite element analysis using EVERFE (Davids et al. 1998) was performed in which the slab was modeled using 3D elements. Finally, the all-purpose 3D finite element program ABAQUS was utilized to compare the results of RPAS against fully 3D analysis of multi-layered pavement with several slabs.

Westergaard's solution

The study of the stresses and deflections due to applied loading and temperature curling made by Westergaard (1926, 1927, 1939) is considered as the earliest and more extensive theoretical research in this field. The analytical expression of the deflection and stress at the bottom of concrete pavement was presented based on the static equilibrium between a homogeneous, isotropic, and linear elastic concrete pavement slab of semi-infinite length and an elastic foundation (subgrade), assuming the frictionless contact between the slab and the subgrade. The slab was modeled as a thin plate on a soil represented by a set of axial force springs. Therefore, the reactive force between the pavement and the subgrade at any given point was assumed to be normal to the surface of the subgrade and proportional to the deflection of the slab at that point, independent of the deflections at other points. A single wheel load is modeled as a distributed load on a circular, semicircular, elliptical, or semielliptical contact area at the center of an infinite slab. The tensile stress at the bottom of the slab and the surface deflection under a uniform circular load od radius a at the center of the slab can be calculated as (Westergaard 1926, 1939):

$$\sigma_l = \frac{3(1+\nu)P}{2\pi h^2}[\ln(\frac{\ell}{b}) + 0.6159] \tag{5-4}$$

$$\omega_0 = \frac{P}{8k\ell^2}\left\{1 + \frac{1}{2\pi}\left[\ln\left(\frac{a}{2\ell}\right) - 0.673\right]\left(\frac{a}{\ell}\right)^2\right\} \tag{5-5}$$

where P is the equivalent applied load, ν and h are the Poisson's ratio and the thickness of the slab, respectively, ℓ is the radius of relative stiffness $\ell = [Eh^3/12(1-\nu^2)k]^{0.25}$ in which P is the elastic modulus of the slab and k is the modulus of subgrade reaction, and b is defined as:

$$b = \begin{cases} a & \text{when } a \geq 1.724h \\ \sqrt{1.6a^2 + h^2} - 0.675h & \text{when } a < 1.724h \end{cases} \tag{5-6}$$

where a is the radius of the circular loaded area. As can be seen, the self-weight of the slab and the geostatic stress caused by the weight of the foundations layers is neglected in the calculations.

To ensure that the numerical modeling of balance and constitutive equations in RPAS are performed correctly and to verify the capability of RPAS to calculate the stress and deflection of pavement under uniform circular loading, an analysis factorial of 5,292 cases were conducted. These analyses were performed using a simple model of pavement (using plate elements) with a Winkler foundation. The analysis factorial consists of E_{Slab} =3,500-6,000 ksi (500 ksi increment), t_{Slab} =6-14 in. (one inch increment), $k-value$=25-300 pci (50 pci increment), total load of P =4.5-30 kips with the radius of a=4-8 in. Although assuming the finite dimensions for the slab is in contrast with the Westergaard's assumption, a stress convergence study was performed to ensure that the assumed width and length of the slab of 300 in. are sufficient for the decay of the responses away from the loaded region and elimination of the effect of boundaries. Figure 5-3 illustrates a comparison of the tensile stress of the slab and the surface deflection calculated from Eq. (5-4) through (5-5) and RPAS program. The residuals (difference between the predicted and calculated stresses) were quantified using the root mean square error ($RMSE$). As shown, in terms of the stress due to internal circular loading in Figure 5-3a, it can be generally said that the calculated stresses from RPAS are consistent with those from Westergaard's solution. It was observed that RPAS tends to predict higher stresses than those from Westergaard's solution by approximately 5%. The $RMSE$ value (25.7 psi) and the intercept of the line fitted to the data points (3.915) is negligible in the scale of the predicted-calculated space. The comparison of surface deflections Westergaard's solution and RPAS program in Figure 5-3b shows that the deflections from RPAS are almost 10% higher than those from Westergaard's solution. The $RMSE$ value of 0.002 in. in this scale of responses (ranging from 0 to 0.1 in.) indicates the good agreement of the results. In addition to the influence of infinite layer assumption in Westergaard's method, different formulations of the two methods are the reasons of the small discrepancies observed in Figure 5- 3.

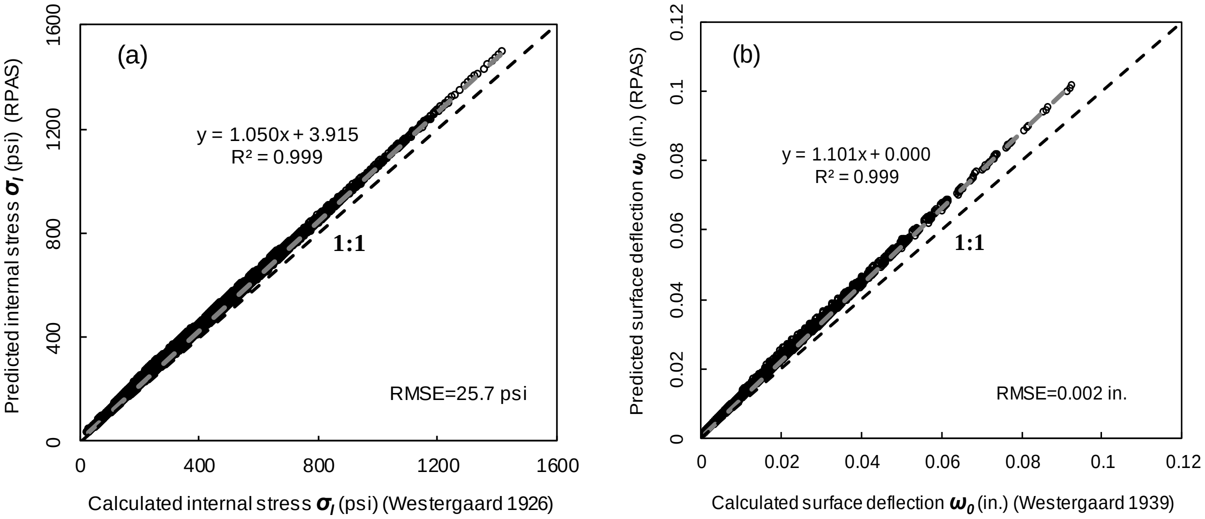

Figure 5-3. Comparison of Pavement Responses from Westergaard's Solution and RPAS with Winkler Foundation (a) Tensile Stress of Slab (b) Surface Deflection

As another level comparison, the 3D 27-node solid elements were utilized for modeling the foundation and the non-linear contact model was implemented to model the slab-foundation interface. Since the analysis of pavement using 3D foundation requires more computational time, 36 representative cases from the aforementioned ranges were selected with the constant E_{Slab} =4,500 ksi and a =6 in. The variable parameters included t_{Slab} =6-12 in. (with 3-inch increments), k=25, 100, 250 pci, total load of P =4.5-30 kips. To find the modulus of the foundation layer equivalent to the listed k-values, the area method was used. The equivalent moduli for k-values of 25, 100, and 250 pci were determined to be 10,285, 41,140, and 102,850 psi. As shown in Figure 5-4, both the stresses and deflections predicted with RPAS by implementing 3D foundation are smaller than those from Westergaard's solution, which utilizes the liquid (Winkler) foundation. The difference in the calculated and predicted deflections (identified by the slope of the fitted line equal to 0.260) is more pronounced than the difference in the stresses (identified by the slope of the fitted line equal to 0.713). This might be due to the higher influence of the k value in the calculation of surface deflection using Eq. (5-5) than in the calculation of stress using Eq. (5-4), where the k-value is only incorporated in the calculation of ℓ. The critical loads on pavements are usually greater than 9 kips, as defined in equivalent single-axle load, ESAL. However, if only the responses associated with the applied load of equal or less than 9 kips are considered in Figure 5-4, the differences between the calculated and predicted responses would be smaller with the *RMSE* of 43.8 psi and 0.007 in. for the stress and deflection.

A plausible explanation for the large differences observed in Figure 5-4 is the limitation of the procedure for estimating the *k*-values of different pavement layer configurations. Since all the supporting layers are represented by a single value, it is highly probable that two layer configurations of various thickness and elastic properties of layers yield the same *k*-value (due to the same deflection under the same applied load) although they are totally different in terms of the load transfer and interaction between the layers and the responses contributing to the development of pavement deformations and stresses. It should also be noted that the *k*-value does not consider the shear stiffness while 3D foundation includes the interaction of the surrounding points and thus yields more accurate responses. A more detailed investigation of the effect of foundation models on the pavement responses and the need to incorporate 3D foundation models in the analysis and design of concrete pavements was studied by authors (TaghaviGhalesari et al. 2020a and 2020b).

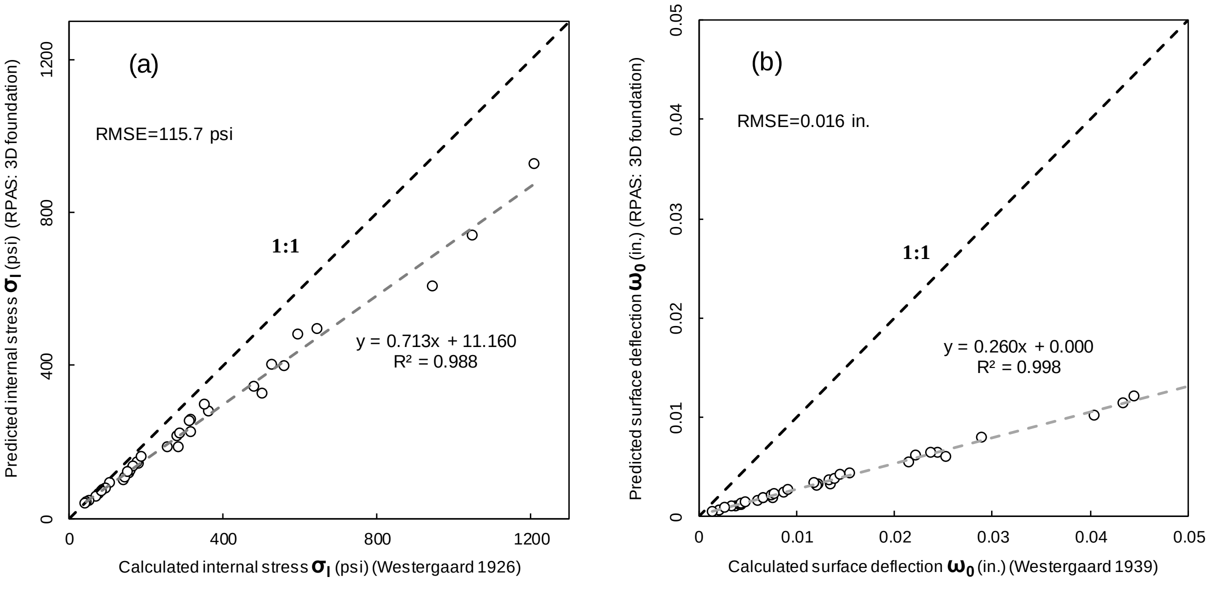

Figure 5-4. Comparison of Pavement Responses from Westergaard's Solution and RPAS with 3D Foundation (a) Tensile Stress of Slab (b) Surface Deflection

Multi-layered elastic theory

Layered elastic theory (LET) was first developed by Burmister (1943) by using strain continuity equations at the layer interface for a two-layer system and was later extended for three-layer (Burmister 1945) and multi-layer systems (Huang 1967). This analytical solution was based on the assumption that all materials are homogeneous, isotropic, and linear elastic of finite thickness (except for the lowest layer) and infinite areal extent. The weight of all the materials is also ignored. The wheel load is applied as a circular uniformly loaded area. Like Westergaard's solutions, the influence of wheel load applied close to cracks or joints as well as the actual contact area shape with loading cannot be captured in LET due to the assumption of infinite layer area dimensions and uniform loading. To determine the longitudinal stresses and deflections in a multi-layer system under a vertical load, the following equations can be used (Huang 1967):

$$(\sigma_l)^*_i = \left[mJ_0(m\rho) - \frac{J_1(m\rho)}{\rho} \right]\{[A_i + C_i(1+m\lambda)]e^{-m(\lambda_i-\lambda)} + [B_i - D_i(1-m\lambda)]\times e^{-m(\lambda-\lambda_{i-1})}\} \\ +2\nu_i mJ_0(m\rho)[C_i e^{-m(\lambda_i-\lambda)} - D_i e^{-m(\lambda-\lambda_{i-1})}] \tag{5-7}$$

$$(\omega_0)^*_i = -\frac{1+\nu}{E_i} J_0(m\rho)\{[A_i - C_i(2-4\nu_i - m\lambda)]e^{-m(\lambda_i-\lambda)} - [B_i + D_i(2-4\nu_i + m\lambda)]e^{-m(\lambda-\lambda_{i-1})} \tag{5-8}$$

where m is a parameter, J_0 and J_1 are the Bessel functions of first kind order 0 and order one, respectively, $\rho = d / D$ (d =horizontal distance from the load centerline, D =distance from surface to upper boundary of the lowest layer), $\lambda = z / D$ (z is the depth from the surface), subscript i denotes that the quantity corresponds to i th pavement layer, A, B, C, D are constants of integration to be determined from boundary and continuity (layer bonding) conditions. The superscript * indicates that the above equations estimate stress and deflection of the pavement under a vertical load of $mJ_0(m\rho)$, therefore, the Hankel transform can be used to obtain these stresses and deflections under a uniformly distributed circular area with the radius and the magnitude of q:

$$R = q\alpha \int_0^\infty \frac{R^*}{m} J_1(m\alpha) dm \tag{5-9}$$

in which $\alpha = a / D$ and R^* is the stress/deflection due to the load $mJ_0(m\rho)$.

The multi-layer elastic theory (MLET) that has been incorporated in this study uses the BISAR software. In BISAR, in addition to modeling each layer using their elastic properties (E , ν) and thicknesses, different loading condition and layer bonding by considering the slip and interlayer shear transfer can be modeled. The loading condition is identified by magnitude of load and contact radius/pressure as well as load configuration. The bonding condition can be considered as (fully bonded or partially bonded layers.

To compare the pavement responses from RPAS with 3D foundation with those from MLET, a total of 216 pavement sections was established. The modulus of the slab was fixed at E_{Slab} =4,500 ksi and the radius of the applied load was set to a =6 in. The variable parameters comprised of t_{Slab} =6-12 in. (with 3-inch increments), E_{Base} = 50, 150, 500 ksi, t_{Base} =4, 6, 10 in., $E_{Subgrade}$ =8 and 18 ksi, total load of P =4.5, 9, 16, 30 kips. The result of the comparison between the tensile stress in the slab, pavement surface deflection, and the compressive strain at the top of subgrade, as the key parameters influencing the fatigue and rutting of the pavement, are plotted in Figure 5-5. As can be seen, the responses from MLET and RPAS compare very well for all three metrics. The highest discrepancy between the two models was observed in the deflections (see Figure 5-5b), where the slope of the fitted line was 0.827. This difference can be due to different formulations and assumptions of the MLET and finite element analysis, such as the limitation of MLET in assuming the concrete layer as infinite. The highest agreement was observed between the compressive strain at the top of subgrade from the two models, where the slope of the fitted line was 1.020 (see Figure 5-5c). This better agreement could occur because subgrade layer is more similar to an infinite medium. The discrepancy of the strain data with the $RMSE$ of 29.3 $\mu\varepsilon$ was observed, which is due to different formulations implemented in two models. It should be noted that the $RMSE$ values plotted on graphs in each figure must be evaluated relative to the scale of data. For instance, the $RMSE$ value of 29.3 $\mu\varepsilon$ still shows small percentage of the data that range from 0 to 650 $\mu\varepsilon$.

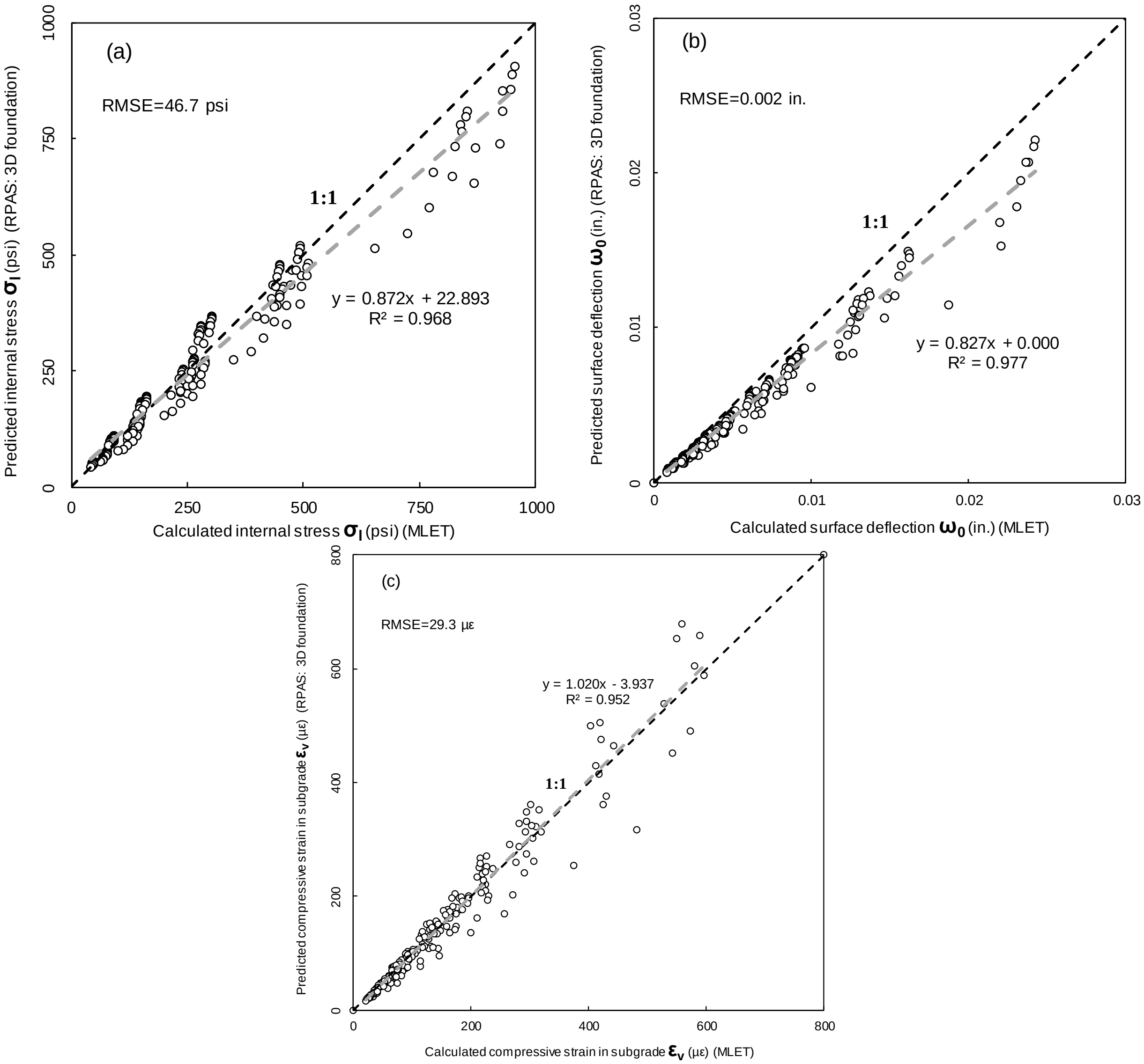

Figure 5-5. Comparison of Pavement Responses from Multi-Layer Elastic Theory (MLET) and RPAS with 3D Foundation (a) Tensile Stress of Slab (b) Surface Deflection (c) Compressive Strain at The Top of Subgrade

Finite element analysis

As mentioned earlier, one of the limitations of the Westergaard's solution is that it uses a liquid (Winkler) foundation to model all the underlying layers, which is not only incapable of transferring the shear loads but also requires the estimation of the support of all foundation layers' stiffnesses by a single number k-value. Although the costly plate load test is used for determining this parameter in the field, no direct laboratory procedure was developed for this purpose and there is a debate on this value among researchers. On the other hand, even though MLET incorporates the elastic properties (E, ν) of each layer in the calculations, it has certain limitations in considering the effect of boundary conditions on the responses. Thus, the aforementioned methods of the analysis of the stress, strain and deflection at different layers are limited when dealing with the load transfer across the pavement edge or slab joints. Finite element method enables addressing these limitations. This study makes use of two three-dimensional finite element tools, EVERFE and ABAQUS, for verification purposes.

EVERFE

This 3D finite element analysis tool was developed by the collaboration of University of Washington and WSDOT to present a program capable of capturing detailed local response, on which 2D programs are limited. The program is also capable of modeling multiple slabs (up to nine slabs), extended shoulder, dowels (including mislocation or looseness) and tie-bars, load configurations, linear or non-linear aggregate interlock shear transfer at the skewed or normal joints, the contact between the slab and up to three bonded and/or unbonded base layers, and non-linear modeling of thermal gradient (Davids et al. 1998). Even though the utilized modeling has been experimentally verified and was improved in later versions (Davids et al. 2003), it has still limitations on the subgrade modeling by a dense liquid (Winkler) model and axle loading within the slab length.

To compare the pavement responses from EverFE with those from RPAS, a total of 72 pavement sections was established. The modulus of the slab was fixed at E_{Slab}=4,500 ksi and the radius of the applied load was set to a=6 in. The variable parameters comprised of t_{Slab}=6-12 in. (with 3-inch increments), E_{Base}= 50, 500 ksi, t_{Base}=4, 10 in., $E_{Subgrade}$=8 and 18 ksi, total load of P=4.5, 9, 16 kips. A few of these cases were repeated for pavement under axle loading. Figure 5-6 shows the comparison of the stress in the slab and the pavement surface deflections from EVERFE and RPAS from the same factorials used in previous section.

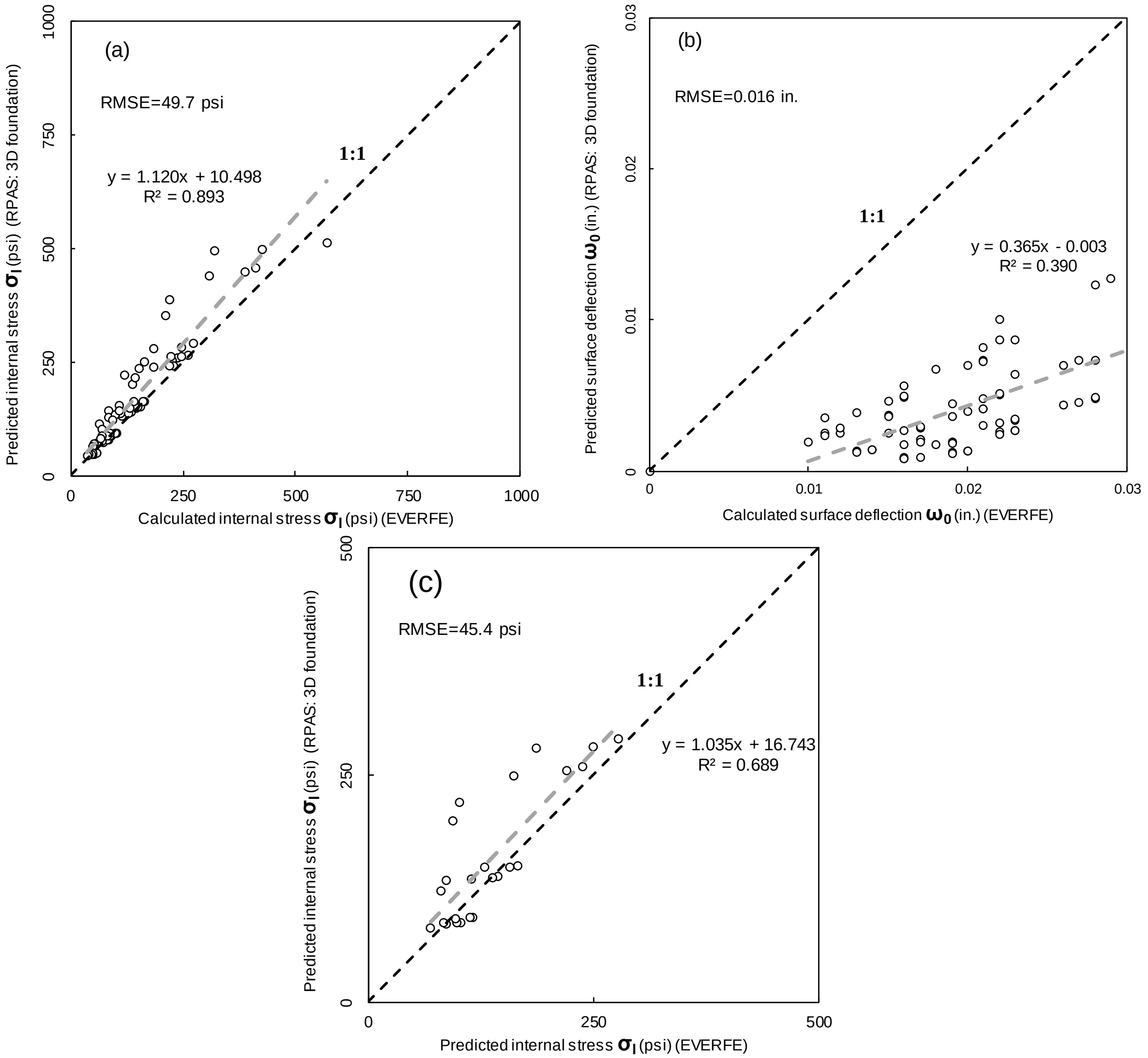

Figure 5-6. Comparison of Pavement Responses from EVERFE Program and RPAS with 3D Foundation (a) Tensile Stress of Slab Under Single Tire Loading (b) Surface Deflection (c) Tensile Stress of Slab Under Axle Loading

As indicated in Figure 5-6, the results of the stress comparisons for both single tire load and axle loading agree well, with the slope of 1.120 and 1.035, respectively. The *RMSE* values of 49.7 and 45.4 psi obtained for single and axle loading are very small compared to the range of the values that range from 0 to 600 or 300 psi, respectively. However, the deflections from EVERFE program are greatly higher (slope of the fitted line is 0.365) than those from RPAS. The reason for this high difference is the use of Winkler foundation for the subgrade layer in EVERFE.

As it was observed in several studies by authors (Aguirre et al. 2019 and 2020, TaghaviGhalesari et al. 2020a), the deflections predicted by Winkler foundation are higher than the deflections measured in the field. It must be noted that the reason of the agreement in the stress is that the stress is mainly caused by the bending of the slab that will be developed after the slab settled even more than reality.

ABAQUS

This all-purpose finite element analysis tool has been widely used and verified for pavement analysis in 2D and 3D calculations (such as Uddin et al. 1995, Aure and Ioannides 2010, Gamez et al. 2018). The capabilities of ABAQUS in solving pavement engineering problems include various material models (linear and non-linear elastic, viscoelastic, and elasto-plastic), solid and shell element to model the slab, static and harmonic/transient dynamic loading simulation, interface modeling with friction, cracking propagation modeling, and temperature change analysis (SIMULIA 2016).

The example considered to compare the results of RPAS against ABAQUS is a conventional pavement section (i.e., consisting of a slab, a base, and a subgrade layer) constructed at National Airport Pavement Testing Facility (NAPTF) construction cycle 2 (CC-2). This section was selected to ensure that the pavement response predictions from both programs are consistent with the field measurements. The conventional pavement section at NAPTF CC-2 consisted of a 12-inch concrete slab placed on a 10-inch gravel base and a clay subgrade (R=12), having the modulus of 3,422, 16.5, and 13.5 ksi, respectively. The concrete slabs were 15 ft long and 15 ft wide. This section was instrumented with static sensors (vibrating wire sensors and thermocouples) measuring the moisture and temperature distribution within the pavement depth as well as dynamic sensors measuring the responses under a 6-wheel gear traffic loading and heavy weight deflectometer (HWD) tests. The applied load for gear traffic was 55,000 lb. per wheel at 210 psi tire pressure and the HWD loads were 12, 24, and 36 kips. Further details on the pavement testing facility, instrumentation and measurement techniques, and test database can be found in NAPTF Data Library (2019) and TaghaviGhalesari (2020a).

The modeling of this pavement section in ABAQUS uses plate elements for the concrete slabs and beam elements for the dowels. The soil foundation was modeled using 20-node solid elements and were expanded beyond the slab edges (as in RPAS) to accurately model the field condition. The contact between the slab and foundation layer was modeled using the tangential and hard contact interactions. The loading was applied as a uniformly distributed pressure at the surface of the pavement.

Figure 5-7 compares the pavement responses in terms of surface deflection as well as the dynamic strain at the top and bottom of the concrete slab (near the longitudinal joints) from RPAS, ABAQUS, and field measurements. As can be seen, a good agreement between the results of predictions from FE tools and field measurements was observed. RPAS predictions generally show less deviations from the field measurements. For instance, the maximum difference of deflections and strain between RPAS predictions and measurements are 3.8 and 8.7%, respectively; whereas these values for ABAQUS are 12.8 and 7.6%, respectively.

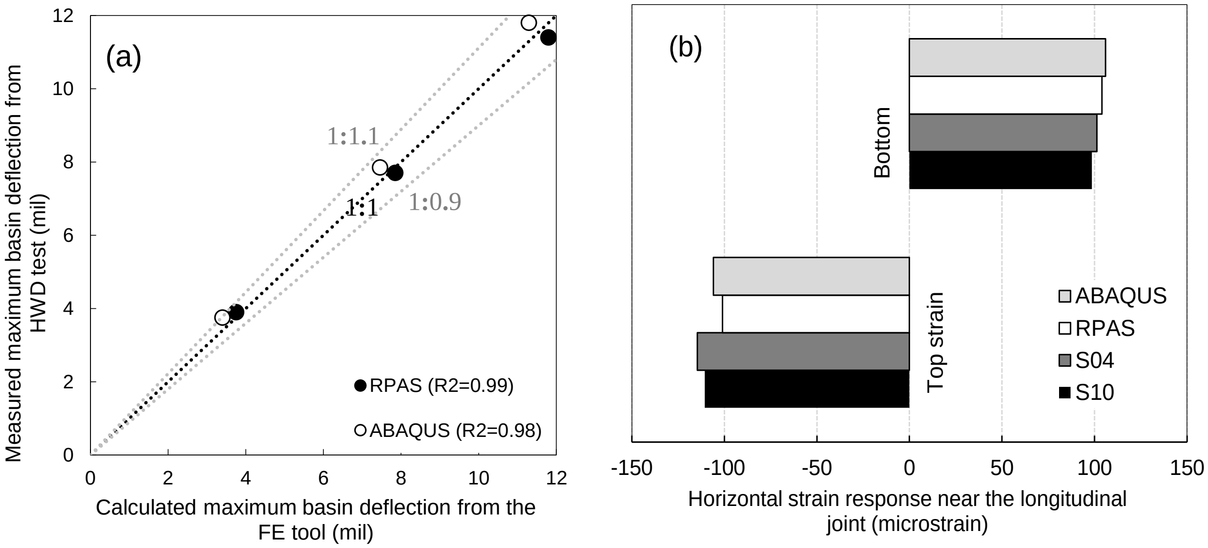

Figure 5-7. Comparison of The Pavement Responses From RPAS, ABAQUS and Field Measurements at NAPTF CC-2 In Term Of (A) Maximum Basin Deflection from HWD Test (B) Dynamic Strain at The Top and Bottom of Concrete Slab Near the Longitudinal Joint

* S04 and S10 show sensor measurements at two consecutive slabs

Another example was also solved using ABAQUS and RPAS model composed of 27-noded elements in RPAS, a single slab on top of a single-layered foundation model. Table 5-2 lists the properties of the pavement layers considered.

Table 5-2. Input Variables Used for Verification

Property	**Concrete slab***	**Subgrade**
Modulus (ksi)	4,000	30
Poisson's ratio	0.15	0.35
Thickness (in.)	10	40

* dimension of the slab is 15 by 12 ft

The contact between the two layers was represented by the non-linear contact function available in RPAS. A similar model with the same material properties was also created in the all-purpose FE computer program, ABAQUS. Similar to the model developed in RPAS, the concrete slab was discretized using plate elements and soil layer was modeled using 8-node solid elements. The normal contact between the two layers was defined using the hard contact interaction option in ABAQUS. Friction between the concrete and soil layer was neglected in both models. The load dimensions were chosen after performing a mesh convergence study to fit a uniform mesh in RPAS with an element size of 12 in. in the longitudinal and transverse direction and 8 in. in the vertical direction. The size of the 8-node elements in ABAQUS was 3 in. in both longitudinal and transverse directions and 2 in. in the vertical direction. The pressure load applied to both models consisted of 100 psi with rectangular dimensions of 24 in. in length and 24 in. in width; 4 loaded elements were required in RPAS and 64 loaded elements were required in ABAQUS to cover the total load area due to the refinement of the mesh.

As part of the evaluation of the developed computer code (RPAS), verification is performed to ensure that the relevant numerical algorithms and mathematical equations were accurately and consistently implemented in the code. Figure 5-8 illustrates the pavement responses for the cases mentioned above through the depth of the longitudinal cross-sectional area of the soil layer at the center of the load obtained from RPAS. The maximum responses were extracted and compared against the corresponding response from ABAQUS. As shown, there is a small difference (less than 9%) between the responses obtained from the two models. This difference may be associated with the different element formulation and contact constitutive relationship in the models. Based on the comparison between maximum responses, it can be concluded that the 3-D solid foundation model in RPAS adequately simulates the supporting layers.

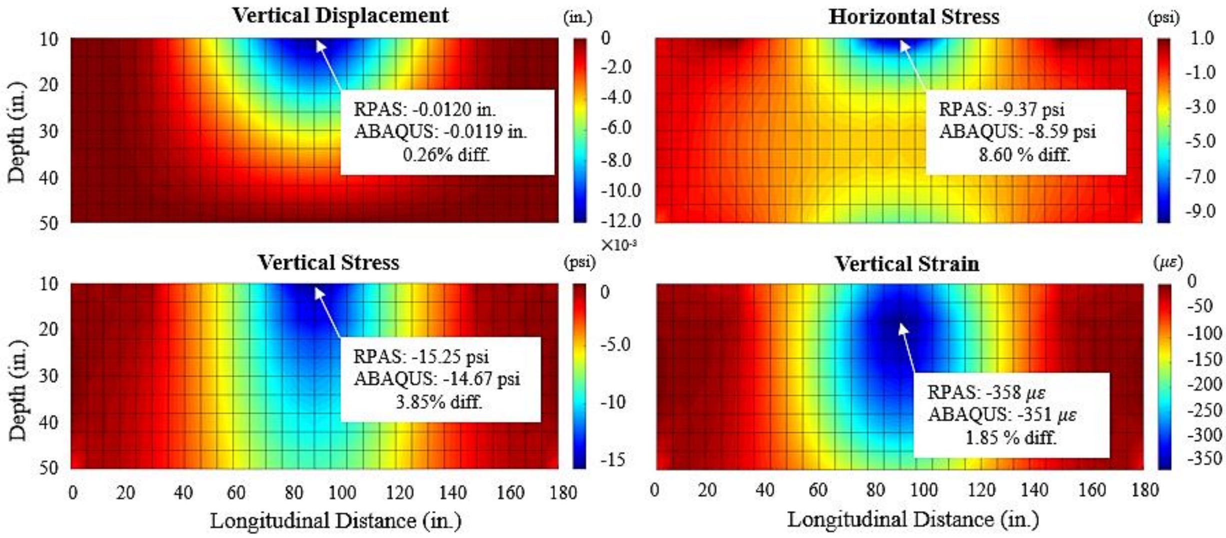

Figure 5-8. Comparison of Maximum Responses in RPAS and ABAQUS

THERMAL LOAD BENCH-MARKING

This section discusses the bench-marking of the temperature modeling in RPAS with respect to analytical solutions. The multi-level bench-marking of the temperature modeling in RPAS includes verifying a plate under linear temperature gradient (Westergaard 1927, Bradbury 1938), as well as a plate under non-linear temperature profile (Vinson 1999). For this study, a 300 × 300 in. slab with thickness varied from 6 to 12 in. and elastic modulus from 3,500 to 6,000 ksi. A simple support condition was modeled at the edges of the slab and the bottom of the model was fixed against translational degrees of freedom. The coefficient of thermal expansion (CTE) has been varied from $\alpha_T = 4.5\times10^{-6}$ in./in./°F to $\alpha_T = 5.5\times10^{-6}$ in./in./°F. The temperature difference between the top and the bottom of the slab was varied from $\Delta T_{Nighttime}$ =-40 to -10 °F (10 °F increment) for the night time and $\Delta T_{Daytime}$ =10 to 40 °F (10 °F increment) for the daytime, which are the highest and lowest typical values measured in the field and implemented in the previous studies.

Plate under linear temperature gradient

The curling analysis of a plate without a tire load is not sensitive to the positive or negative temperature gradient because both will result in the same curling stresses that are only different in their signs. Thus, the curling analyses of the plates in this study were conducted using the daytime temperature profiles and the nighttime analyses were performed to confirm this conclusion but they are not presented here for the brevity.

The bending analysis of a plate under a linear temperature gradient will lead to the following equation to calculate the curling stress:

$$\sigma_{T,Linear} = \frac{E\alpha_T \Delta T}{2(1-\nu)} \tag{5-10}$$

To correct for the finite length (and width) of the slab, based on the solution proposed by Westergaard (1927), Bradbury (1938) developed a chart to determine the stress correction factors C_x and C_y to be implemented as follows:

$$\sigma_T = \frac{E\alpha_T \Delta T}{2(1-\nu^2)}(C_y + \nu C_x) \tag{5-11}$$

Although in the first glance, it appears that Eq. (5-11) is independent of the thickness of the slab, the effect of the thickness is considered in the calculation of the correction factors C_x and C_y. As seen the non-linear variation of the temperature throughout the depth is not considered in this solution and the curling stress only depends on the temperature at the top and the bottom of the slab assuming a linear temperature profile. However, the necessity of non-linear modeling of the temperature profile, which is a more representative of the field condition, will be discussed later.

Figure 5-9 compares the maximum curling stress in the slab from Westergaard's solution with considering the length correction factor with the maximum curling stress from RPAS. As shown, the predicted curling stresses from RPAS are consistent with the calculated curling stresses from Westergaard's solution with a good level of accuracy, where the slope of the fitted line is 0.946 and $RMSE$ is 19.9 psi. This slight difference can be attributed to the differences in assumptions made by the two models.

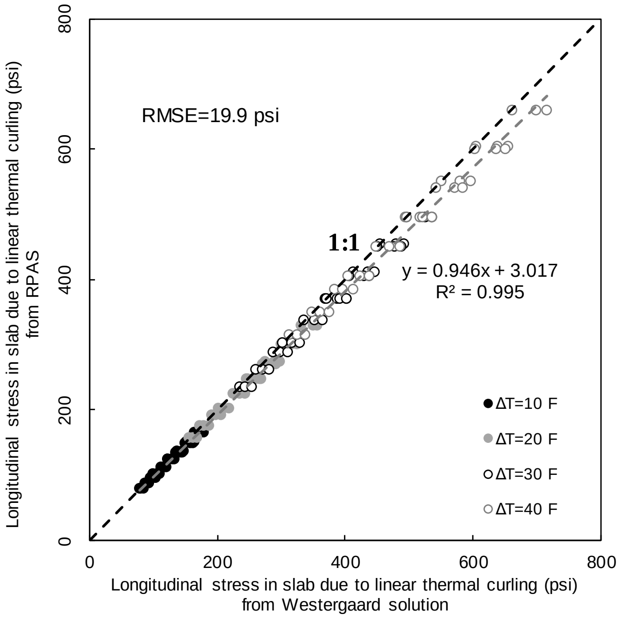

Figure 5-9. Comparison of The Thermal Curling Stress in A Plate Due to The Linear Temperature Profile from RPAS And Westergaard's Solution with Applying Bradbury's Correction Factors for Finite Length

Plate under non-linear temperature profile

It is now well established that the temperature throughout the depth of concrete slab in a pavement system varies as a non-linear function and thus merely taking the temperature at the top and bottom of the slab in the calculation of the curling stress may lead to the errors that can be significant in thick slabs. This non-linear temperature variation can be expressed with three components: a uniform temperature that causes expansion or contraction, a linear gradient that causes the bending of slab, and a non-linear component that is equivalent to the difference between the total temperature change and the first two components. The first component is typically ignored as it will not induce any stresses to jointed concrete pavements. The third (non-linear) is not accounted for in conventional concrete pavement analysis since it is difficult to be predicted as a representation of the field condition (Hiller et al. 2010). Therefore, an accurate prediction of the curling stresses in the slab requires taking two components of linear (Eq. 5-11) and non-linear component in Eq. (5-12) (Mohamed and Hansen 1997, Vinson 1999), i.e.

$$\sigma_T = \sigma_{T,Linear} + \sigma_{T,Nonlinear} \tag{5-12}$$

$$\sigma_{T,Nonlinear} = \frac{E}{1-\nu}\left[-\varepsilon(z) + \frac{12M^*}{h^3}(z) + \frac{N^*}{h}\right] \tag{5-13}$$

where E, ν, and h are elastic modulus, Poisson's ratio, and thickness of the slab, respectively, z is the distance from slab mid-depth, $\varepsilon(z) = \alpha_T\ \Delta T$, in which $\Delta T(z) = T(z) - T_{Set}(z)$, $T(z)$ is the temperature variation function and $T_{set}(z)$ is built-in temperature profile, M^* and N^* are the constants corresponding to bending moment and normal force at the slab mid-depth. $\Delta T(z)$ can be expressed as a cubic function that can be defined by fitting to the temperature at four different depth throughout the depth of the slab:

$$T(z) = a_0 + a_1 z + a_2 z^2 + a_3 z^3 \tag{5-14}$$

The contribution of each coefficient a_0, a_1, a_2, a_3 to the Eq. (5-14) was explained by Zokaei-Ashtiani et al. (2014). Note that the weight of the slab was not taken into account in the development of these solutions.

To verify the capability of RPAS to take into account the non-linear temperature profile, a total of 288 cases were analyzed in which t_{Slab}=6-12 in. (three inches increment) E_{Slab}=3,500-6,000 ksi, ν_{Slab}=0.15, $\alpha_T = 4.5\times10^{-6}$ to 5.5×10^{-6} in./in./°F. The temperature profiles were considered as listed in Table 5-3 and shown in Figure 5-10, according to Zokaei-Ashtiani (2014) Zokaei-Ashtiani et al. (2014). As mentioned earlier, for a plate that is only subjected to temperature change profile treats positive or negative temperature loading in almost the same way. Therefore, the results of the comparison between the analytical solution and RPAS will be presented using positive temperature profiles for brevity.

Table 5-3. Coefficients for temperature change profiles

Profile	ΔT	Deviation	a_0	a_1	a_2	a_3
N1	-15	Low	-16.3	-1.5000	-0.0476	0.000
N2	-15	High	-15.0	-1.5720	-0.1008	0.003
N3	-20	Low	-23.0	-2.0000	-0.0800	0.000
N4	-20	High	-20.5	-2.1457	-0.1780	-0.006
P1	15	Low	16.3	1.5000	0.0476	0.000
P2	15	High	15.0	1.5720	0.1008	-0.003
P3	20	Low	23.0	2.0000	0.0800	0.000
P4	20	High	20.5	2.1457	0.1780	0.006

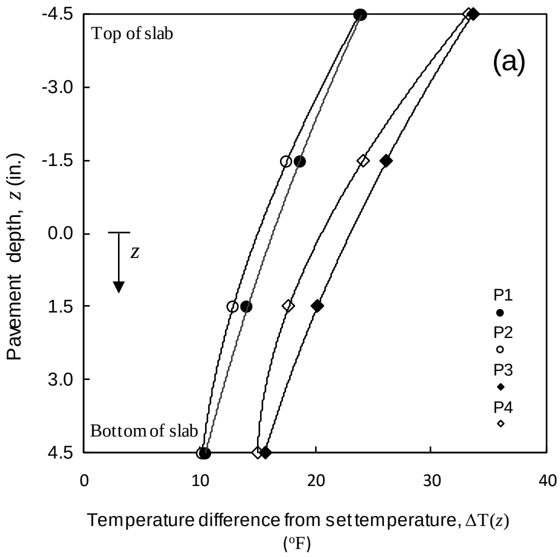

Figure 5-10. Non-linear Temperature Profiles Considered for Verification

Figure 5-11 shows a comparison between the stresses and strains at the top and bottom of the plate under non-linear temperature profile calculated by the Eq (5-13) and analyzed using RPAS. As shown, the stresses predicted by RPAS are slightly (in average, less than 3% for the stress at the top of plate and 6% at the bottom of the plate) larger than those calculated using the analytical solution. This small difference was expected due to different calculations methodologies and does not have to be symmetric for the responses at the top and bottom of the plate. Moreover, a very good agreement between RPAS and analytical solution for the strain responses at the top and bottom of the plate was observed.

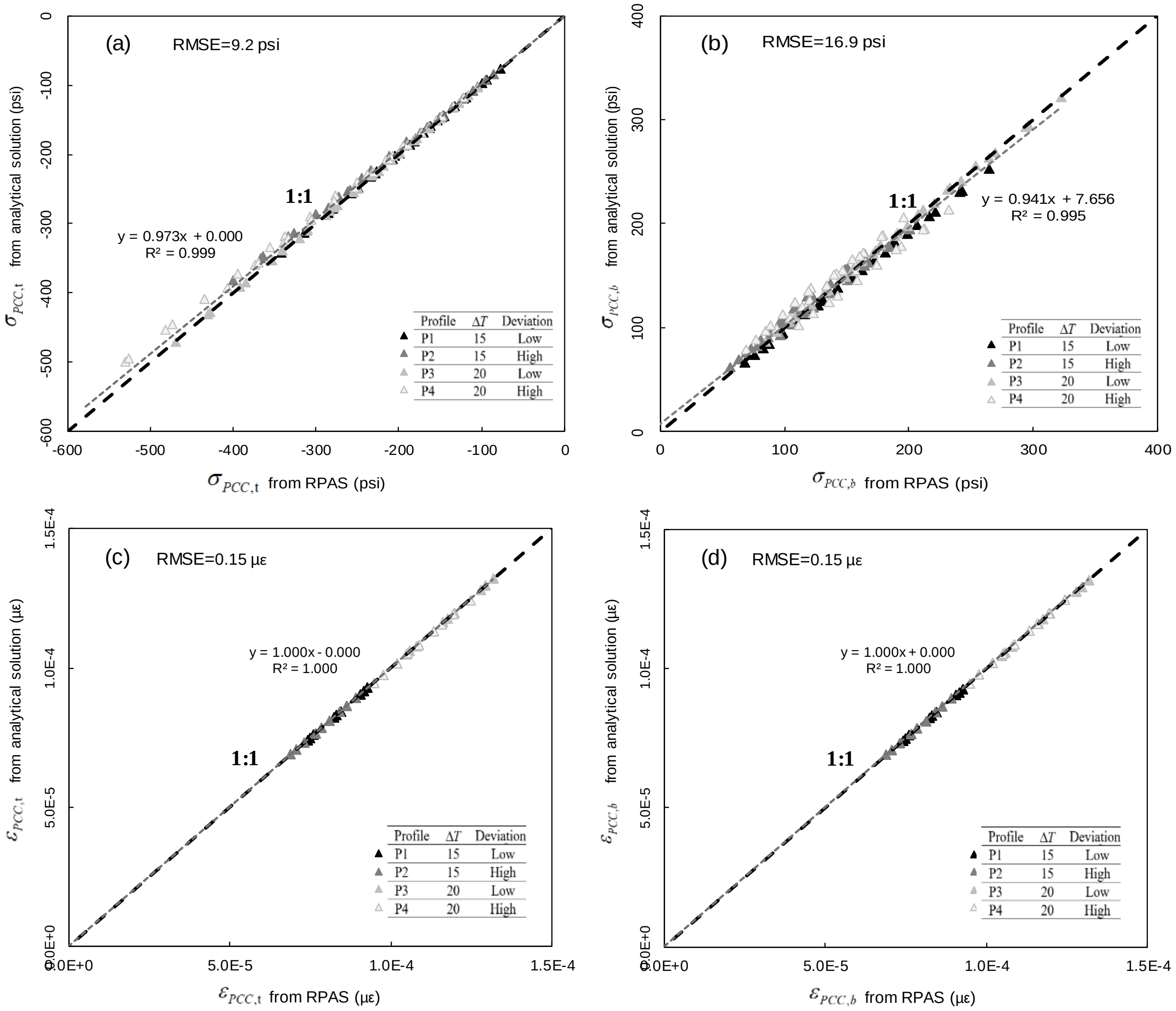

Figure 5-11. Comparison of The Pavement Responses from RPAS and Analytical Solution (Vinson 1999) In Terms of (a) Stress at The Top of The Slab (b) Stress at The Bottom of The Slab (c) Strain at The Top of The Slab (d) Strain at The Bottom of The Slab

COMBINED TIRE AND THERMAL LOAD BENCH-MARKING

Bench-marking of RPAS for the modeling of a slab under linear temperature gradient as the first step in multi-level bench-marking have verified the performance of this program; however, the distresses in the pavements are mainly developed as a result of a combined temperature and tire loading. As opposed to the curling of a plate, investigation of the combined effect of thermal and tire loading on the pavement requires studying both positive and negative temperature profiles because the tire load always exerts upward curling to the slab while the curling caused by temperature loading varies during the day (downward curling due to positive temperature change) and night (upward curling due to negative temperature change).

Furthermore, as discussed by TaghaviGhalesari et al. (2020b), considering the contribution of the underlying pavement layers is a key factor in the prediction of the future damages induced to the pavement. Therefore, the support condition was modified in this section by varying the k-value or equivalent modulus of the foundation layer.

The bench-marking in this section consists of comparing the responses of a pavement simulated in RPAS with a spring foundation against Westergaard's solution or with a 3D foundation against EVERFE software. The thickness of the slab was t_{Slab} =6-12 in. (three inches increment) and the applied tire load was P =4.5, 9, 16, 30 kips. The parameters that were constant in all the analyses include E_{Slab} =4,500 ksi, ν_{Slab} =0.15, $\alpha_T = 5\times10^{-6}\ 1/{}^{\circ}F$, and a =6 in. The positive and negative temperature changed were similar to those considered in the previous section. The modulus of the foundation layer was based on the k-values of 25 to 250 pci to be implemented in the Westergaard's model or the equivalent modulus of the foundation layer estimated using the area method for 3D foundation modeling. Thus, the total of 144 cases were studied.

A realistic way to incorporate the thermal effect in the analysis of a concrete pavement under tire loading is to run the analysis for a pavement subjected to only temperature loading and use the obtained curling stresses as the initial conditions for the analysis of the slab under tire loading. This procedure was also tested in this study; nevertheless, the effect of this two-step analysis as compared to applying the temperature and tire loading simultaneously was negligible.

Pavement with liquid foundation under combined loading

Figure 5-12 illustrates a comparison between the maximum stress developed in the slab due to the combined curling and tire loading from Westergaard's solution and RPAS analyses.

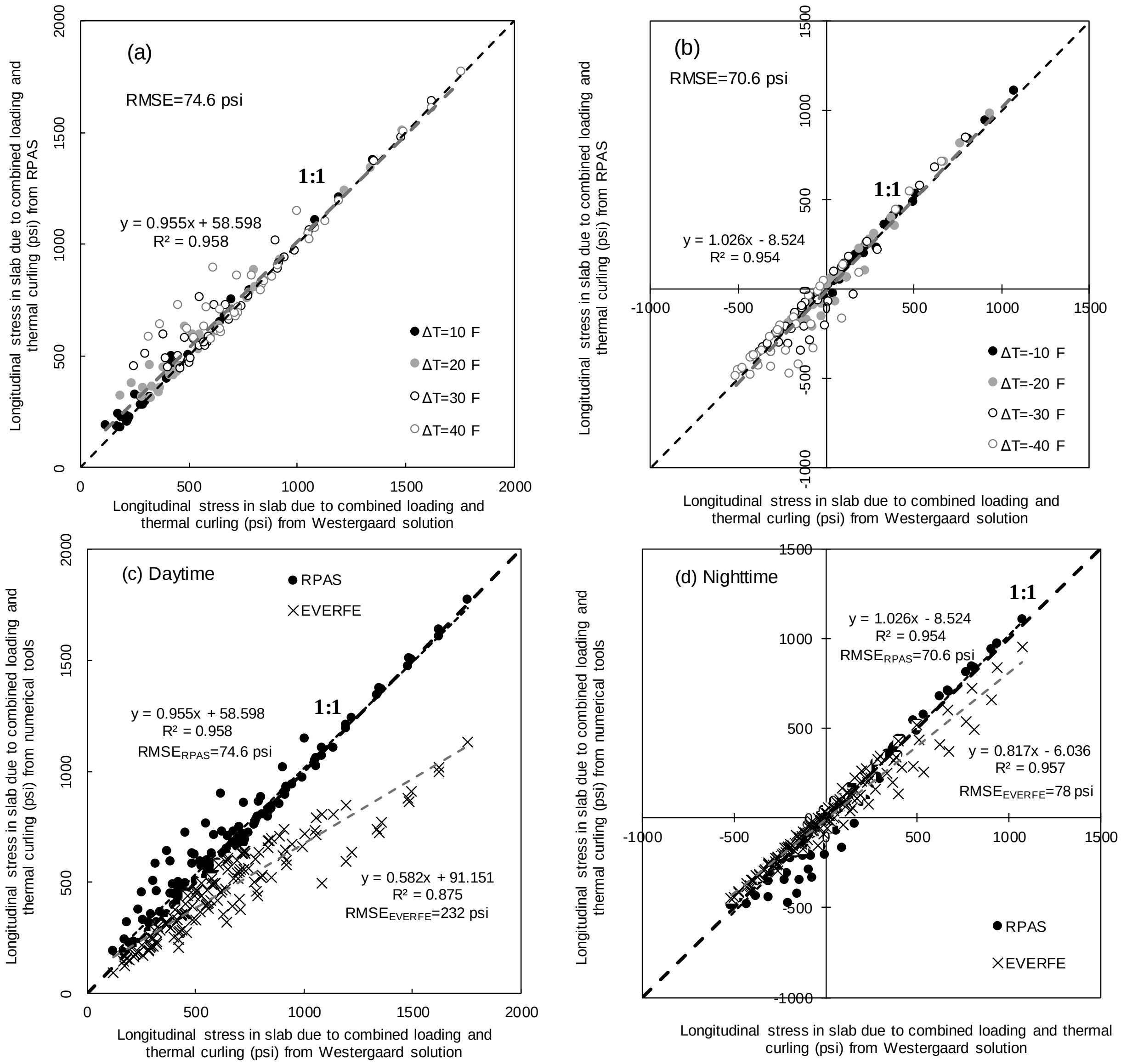

Figure 5-12. Comparison of The Maximum Stresses Caused by The Combined Curling and Tire Loading From RPAS and Westergaard's Solution (With Applying Bradbury's Correction Factors) for The Pavement with a Liquid Foundation (a) Daytime (Positive) Temperature Profile (b) Nighttime (Negative) Temperature Profile (c) RPAS And EVERFE versus Westergaard In Daytime (d) RPAS and EVERFE versus Westergaard In Nighttime

As shown in Figure 5-12, the difference between predicted and calculated stresses are very small in the ranges of the responses, showing the *RMSE* of 74.6 psi and 70.6 psi for positive and negative temperature profiles, respectively. In average, the predicted stresses are approximately less than 5% different from the calculated stresses. The higher discrepancy of the data in the high temperature change occurred with the large thickness of t_{Slab} =12 in., which can be attributed to the slightly different distribution of thermal stresses in two models.

The same analyses were repeated using EVERFE program and the results were plotted in Figures 5-12c and 5-12d regardless of the temperature change.

It can be seen in Figure 5-12, the difference between the results from EVERFE program and Westergaard's solution (slope of the fitted line equal to 0.582 and 0.817 and $RMSE$ of 232 psi and 78 psi for daytime and nighttime, respectively) is larger than those between RPAS and Westergaard's solution, particularly for the daytime. The reason for this large deviation might be different formulation of modeling the slab with 3D elements in EVERFE as compared to plate modeling in Westergaard's solution.

Pavement with 3D foundation under combined loading

Similar cases as in the previous section were analyzed using RPAS implementing the 3D solid foundation and the result of this comparison was plotted in Figure 5-13. As shown and was expected from the analysis of pavement with 3D foundation under tire only loading, the stresses from Westergaard's method (liquid foundation) are quite higher than those from RPAS predictions. A better agreement of the data was observed between the responses in daytime than in the nighttime. By forcing the intercept of the fitted line to the origin, the slope of this line will increase from 0.654 to 0.828. However, in the nighttime, a different pattern for the stress responses was observed. This difference occurs not only in terms of the magnitude but also in terms of the sign, i.e. tensile or compressive stress. Most of the stresses from RPAS range between 0 and 500 psi whereas the stresses from Westergaard's method vary from -500 to 500 psi. This high difference will result in two pavement designs that are highly different. The largest difference occurred in the cases with high load level (30,000 kips) where RPAS predicts a higher contribution of the tire loading than the temperature loading, which contradicts the Westergaard's solution. This was discussed by Ioannides et al. (1999), where they explained that the complex interaction among the governing variables under nighttime condition cannot be captured using Westergaard's solution.

Therefore, it is essential to employ a more accurate solution for the prediction of the combined load and curling stresses in the pavements (TaghaviGhalesaeri et al. 2020d). The aim of the verification and bench-marking analyses in this study is to minimize this error and correct the developed tool RPAS that can consider all the influencing variables on the behavior of the pavement by modeling 3D foundation and the interaction between the layers using the non-linear contact model.

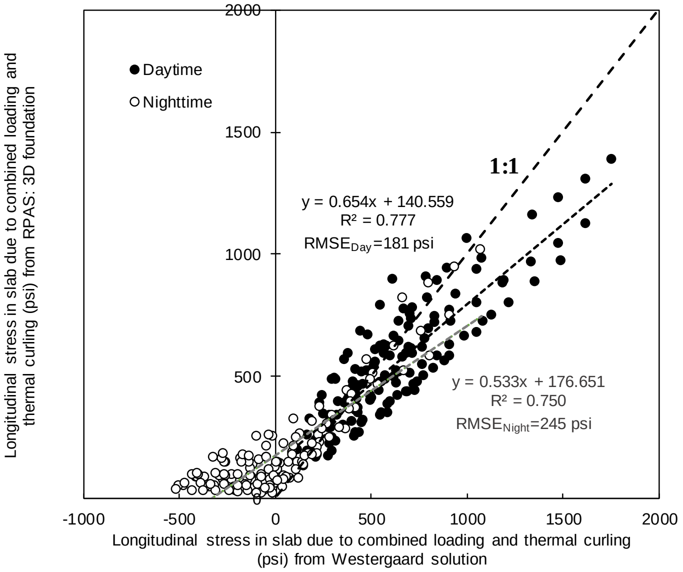

Figure 5-13. Comparison of The Maximum Stresses Caused by The Combined Curling and Tire Loading from RPAS with 3D Foundation and Westergaard (Liquid Foundation)

DYNAMIC EFFECTS OF HEAVY TRAFFIC LOADING

When pavement is subjected to heavy traffic loads, the dynamic effects resulting from the vertical motion of the tire load must be taken into account in the calculation of pavement responses. This dynamic impact is caused by the excitation of the suspension of the vehicles by the irregularities at the road surface or pavement roughness. One way of accounting for the dynamic effects is to model the full interaction between the vehicle and the pavement by simulating the actual or random road surface profile (Han et al. 2017). This type of detailed, time-consuming analysis is necessary when a sudden irregularity on the road surface was developed due to construction errors (e.g. at approach slab of bridges) or pavement damage. Further, this analysis is usually conducted for a short time period at a certain pavement section involving a small number of vehicles (Eymard et al. 1990). An alternative is to use a dynamic load coefficient (DLC) to modify the static load. The latter method is justifiable because the full interaction analysis is only necessary when the natural period of the suspension system of the vehicle is comparable with the natural period of the pavement system. However, the previous studies indicated that the natural period of the conventional vehicles and trucks range from 2.5 to 6.5 seconds (Barbosa 2011), whereas the natural period of a layered soil system (according to the equation $4H/(2n-1)V_s$, H=soil depth above the bedrock, n=mode number, V_s=shear wave velocity, presented by Kramer 1996) and the pavement system ranges between 0.1 and 0.6 seconds (Ye et al. 2018, Prażnowski and Mamala 2016). These values indicate that in most cases, modeling of the dynamic effects of the traffic loading does not require considering the full vehicle-pavement interaction. Thus, a study conducted at the University of Texas at El Paso on the estimation of the DLC based on the type (leaf spring system) and properties (stiffness, damping, sprung/unsprung mass, pitch inertia) of the truck suspension system, tire stiffness and configuration, as well as road roughness (IRI) is recommended for the readers' reference (Misaghi 2011).

6. Calibration

This chapter provides the results of a sensitivity analysis performed on a conventional pavement structure of varying characteristics in order to identify the most important factors influencing a rigid pavement response. A calibration process was proposed that uses multi-objective optimization to minimize the differences between field data and simulation results.

6.1. Sensitivity Analysis

Numerical models implemented in computer codes are generally designed in a way that they can be implemented in a wide range of applications. However, prior to using these models for practical applications, they must be calibrated by utilizing good-quality experimental data from calibrated sensors. Although the computer models provide deterministic responses that may not represent the real behavior of a system as good as the field tests, they can be used as a fast and affordable tool to reproduce the field conditions if calibrated at the desired level of accuracy (Kennedy and O'Hagan 2001). As an integral part of the calibration procedure, a sensitivity analysis is defined as the study of how uncertainty (or variability) in the output of a model can be apportioned to different sources of uncertainty (or variability) in the model input (Saltelli et al. 2008). Sensitivity analysis helps to identify a candidate set of important factors influencing the results by simulating cases with the typical characteristics as well as critical conditions. Sensitivity analysis methods are categorized into two main groups of local sensitivity analysis (LSA) and global sensitivity analysis (GSA). Most of the sensitivity analyses described in the literature are based on the derivative of an output Y_j with respect to an input X_i, $\partial Y_j / \partial X_i$, which are categorized as LSA. Although the derivative-based approaches (or LSAs) have the attraction of being very efficient in computer time, they have limitations when the inputs are stochastic and when the problem is non-linear. Furthermore, LSA is largely applied using one-at-time (OAT) method, where only one parameter changes values independently between consecutive simulations and the rest of parameters are kept constant. This makes the predictions prone to a type of error where an important factor or a critical combination of input factors is neglected (type II error in statistical context) (Hastie et al. 2017). GSA, however, explores all the input factors and assesses the sensitivity by varying all the parameters simultaneously, which is far more effective and informative than estimating derivatives at a single data point.

Several authors have implemented similar approaches to the sensitivity analysis of pavement modeling tools. Hall and Beam (2005) performed a sensitivity analysis on the input parameters of mechanistic-empirical (M-E) design guide and assessed their influence on the distress models in jointed concrete pavements, that is, cracking, faulting, and roughness. They stated the main limitation of their study to be not considering the interaction of input parameters due to the OAT procedure employed in the analysis. Guclu et al. (2009) studied the sensitivity of the distress models of jointed and continuous concrete pavements in M-E design software to the input variables, focusing on the Iowa condition and concluded that discrepancy of the results with the field data can be reduced through a local calibration of the software for each area. Ceylan et al. (2013) conducted a series of sensitivity analysis on the M-E design software using multivariate linear regressions (MVLR) and artificial neural networks (ANN) and concluded that, under a certain traffic and weather condition, concrete layer properties are the most important factor on the jointed concrete pavement response and the properties of the subgrade can affect the smoothness of pavements.

Generally, most of the previous studies are limited to LSA. To avoid the possible errors caused by employing this technique due to the interdependence of various parameters, the calibration procedure of RPAS will be based on a GSA by modeling cases with typical pavement characteristics and critical loading conditions. This will also lead to efficient and cost-effective data collection from field measurements and laboratory testing while including a wide variety of designs and site conditions as well as reducing the number of processes to be modeled and the number of parameters to be estimated. For this purpose, Random Decision Forest (RDF) and the variable importance score (*VIS*) of each input parameter was utilized for various pavement performance indicators of interest. To find the variable importance score (*VIS*), the values of each input variable is permuted among the data and the out-of-bag (OOB) error is again computed. VIS is thus calculated by finding the differences between the OOB errors before and after permutation and by normalizing them with respect to standard deviation of the differences. The GSA process used in this study was discussed in detail by Breiman (2001), Hastie et al. (2017), Loh and Shih (1997), and TaghaviGhalesari et al. (2020a, 2020c). This GSA method has several advantages over other methods such as considering the inter-dependence of variables, capability of incorporating fast classification algorithms, eliminating common errors in the predictors in the fitting process.

GSA FACTORIAL

The sensitivity analysis in this paper was conducted by varying key input variables including moduli and thickness of concrete (PCC) slab, base, and subgrade layers. The pavement performance outputs used in GSA were the pavement surface deflection, longitudinal stress at the bottom of concrete layer, longitudinal stress at the mid-depth of base layer, vertical strain at the top of subgrade layer, and deflection-based load transfer efficiency at joints as the critical pavement responses (Rogers et al. 2017). A set of cases developed to cover the ranges of commonly encountered pavement material properties and layer configuration from existing specification and recommendations is presented in Table 6-1.

Based on the values listed in Table 6-1 a sensitivity analysis factorial was developed and is listed in Table 6-2. The chosen factorial resulted in 4,860 simulations. It must be noted that not all combinations of the listed inputs are practically plausible. For example, at a low loading level, a thick concrete pavement on a stiff, stabilized base layer cannot be considered as a realistic design scenario. Thus, GSA was conducted over all model inputs (set I) as well as the cases with practical combinations of input values (set II) separately.

The concrete pavement considered in the sensitivity analysis consisted of four jointed plain concrete slabs, each of length and width of 15 ft, loaded near one joint with a 18,000 lb load representing an equivalent single axle load (ESAL), that is commonly used to evaluate traffic impact on pavement performance and design. The effect of temperature gradient on the pavement responses was not included in this sensitivity analysis because of (1) the problem becomes very nonlinear due to separation of concrete slab from soil and will skew the results (2) there will be numerous variations of temperature profiles (degree of nonlinearity, shape and magnitude of the profile) that will make the quantification of the results highly difficult. The joints are dowelled with diameter of dowels ranging from 1.0 to 1.5 in. depending on the thickness of the slab and the distance between them is set to 12 in.

Table 6-1. Common Range of GSA Input Parameters Recommended in Design Specifications.

Pavement layer	**Property**	**Unit**	**Range**	**Source**
Concrete slab	Elastic modulus	ksi	3,000-4,000	MEPDG
			3,000-6,000	FHWA[*]
			5,000	TxDOT[**]
	Poisson's ratio	-	0.20	MEPDG
			0.15-0.20	FHWA
			0.15	TxDOT
	Thickness	in.	JPCP: min=6 CRCP: min=7	MEPDG
			JPCP: 7-14 CRCP: 6-10	FHWA
			JPCP: 6-12 CRCP: 7-13	TxDOT
Base	Elastic modulus	ksi	45-2,000 (GB/SB[†])	MEPDG
			20-40 (only GB[†])	FHWA
			50-2,000 (GB/SB[†])	TxDOT
	Poisson's ratio	-	[‡]	MEPDG
			‡	FHWA
			0.25-0.30	TxDOT
	Thickness	in.	‡	MEPDG
			‡	FHWA
			2-6	TxDOT
Subgrade	Elastic modulus	ksi	8-18	MEPDG
			5-10	FHWA
			8-45	TxDOT
	Poisson's ratio		0.35-0.40	MEPDG
			‡	FHWA
			0.35-0.40	TxDOT
	Thickness	in.	12-18 ft	Other

* Adapted from Rao et al. (2012)

** Adapted from Texas Pavement Manual (2019)

† GB: granular base, SB: stabilized base

‡ No recommended value(s)

Table 6-2. Input Variables Used for Sensitivity Analysis.

Property	**Concrete slab**	**Base**	**Subgrade**
Modulus (ksi)	3,000-5,000-6,000	20-50 (15 ksi increment) 100-500-2,000	5-8-10-13-18
Thickness (in.)	6-14 (1-inch increment)	2-12 (2 inches increment)	50
Number of cases	27	36	5
Total number of cases:	$27 \times 36 \times 5 = 4,860$		

RESULTS OF GSA

Since most pavements are constructed on local material, the practical GSA factorial was based on three different cases of poor subgrade (E_{SG} = 5-8 ksi), fair subgrade (E_{SG} = 10 ksi), and good subgrade (E_{SG} = 13-18 ksi), corresponding to the default values in MEPDG. Concrete slabs with high thickness range (t_{PCC} = 10-12 in.) over stiff or stabilized (E_{Base} = 100-2000 ksi), thin base layers (t_{Base} = 2-6 in.) were considered for the poor subgrade cases; however, concrete slabs of low thickness (t_{PCC} = 6-10 in.) over soft or granular base layers (E_{Base} =20-50 ksi) of high thickness (t_{Base} =8-12 in.) were utilized in good subgrade condition. A lower number of cases were modeled with fair subgrade condition having the intermediate values.

Table 6-3 shows the variable importance scores of each input parameter produced by the global sensitivity analysis performed using random decision forests, where $w_{\max}$ is the pavement surface deflection under the tire, σ_{PCC} is the tensile stress developed at the bottom of concrete layer, $\sigma_{mid,Base}$ is the longitudinal stress at the mid-depth of base layer, $\varepsilon_{V,SG}$ is the compressive strain at the top of the subgrade layer, and *LTE* is the deflection-based joint load transfer efficiency.

Table 6-3. Variable Importance of Input Parameters Obtained from GSA

Property	**Variable importance score (VIS)**									
	All Cases (set I)					**Practical Cases (set II)**				
	$w_{\max}$	σ_{PCC}	$\sigma_{mid,Base}$	$\varepsilon_{V,SG}$	LTE	$w_{\max}$	σ_{PCC}	$\sigma_{mid,Base}$	$\varepsilon_{V,SG}$	LTE
E_{PCC}	-6.67	5.32	5.14	-6.77	2.63	-2.34	0.23	0.56	-2.25	0.91
t_{PCC}	-3.67	-10.25	-3.27	-3.68	7.75	-0.57	-3.09	-0.59	-1.37	2.53
E_{Base}	-8.11	-2.39	8.61	-8.11	-1.64	-0.96	-0.53	3.09	-2.65	-0.61
t_{Base}	-1.80	-3.23	-1.66	-2.95	-0.99	-0.96	-1.51	-1.36	-1.19	-0.36
E_{SG}	-18.48	-3.02	-2.79	-12.23	-3.20	-3.72	-0.51	-0.32	-3.72	-1.15

E_{PCC}, E_{Base}, E_{SG} : the elastic modulus of the concrete slab, base, and subgrade layers

t_{PCC}, t_{Base} : the thickness of the concrete slab and the base layer

$w_{\max}$: pavement surface deflection under the tire

σ_{PCC} : tensile stress at the bottom of concrete layer under the tire

$\sigma_{mid,Base}$: longitudinal stress at the mid-depth of base layer

$\varepsilon_{V,SG}$: vertical (compressive) strain at the top of subgrade

LTE: load transfer efficiency

Since VIS is a standard metric for comparing the importance of each parameter in the model, it can be easily interpreted. Note that VIS values from set I should not be compared with those in set II due to different normalization algorithms in GSA. A positive value of VIS shows a direct relationship whereas a negative value denotes an inverse relationship. In this section, the results of GSA on set I is initially analyzed and after finding the most important factors from this analysis, they are compared with the important factors obtained from GSA on set II.

As shown in Table 6-3, the pavement surface deflection under the tire is mainly affected by the subgrade modulus, which was discussed on previous studies (Kannekanti and Harvey 2005). The base modulus E_{Base} was found to be the second most important factor influencing the pavement surface deflection which contradicts previous studies (Zhou 2013).

The σ_{PCC}, which is considered the main factor contributing to the development of bottom-up fatigue cracking, is inversely affected by the t_{PCC} (and, correspondingly, the diameter of dowels). This conclusion can be confirmed by considering the Westergaard's solution for edge loading where the slab bending stress has an inverse relationship with the square of slab thickness. It should be noted that this statement is true in the absence of temperature loading, which was neglected in the GSA. E_{PCC} is the second most influential factor that has a direct relationship to σ_{PCC}. It is worth mentioning that unlike what has been done elsewhere using LSA and reported in the literature, t_{PCC} and E_{PCC} cannot be considered independet parameters in the design process and in our study this dependance was cosidered when defining what we call the practical cases. The results descibed above indicate that the contribution of the supporting layers is not small and cannot be neglected in the analysis and design of concrete pavement. Slab dimension could have been considered as another important factor in the calculation of σ_{PCC} but since the typical range of 10 to 15 ft. is implemented in practice (FHWA 2019) and is fixed throughout a pavement section, its effect has not been considered in this study.

One of the advantages of RPAS is its capability to capture the pavement responses throughout its depth, including the foundation. This enables studying the $\sigma_{mid,Base}$, which is an indicator of the stress distribution in thick base layers. The results in Table 6-3 also show that $\sigma_{mid,Base}$ is highly and positively affected by the modulus of this layer (E_{Base}), followed by E_{PCC}. This agrees with the high percentage cracks observed in the field when using a stabilized base layer underneath the concrete slab. A thin stress-relieving layer between the pavement layers can be added to relax the stresses in these cases. The beneficial contribution of the modulus of subgrade layer (E_{SG}) to the $\sigma_{mid,Base}$ implies the possiblity of using low-strength material for base layer when there is a good subgrade, which has been considered in set II of the analyses.

The $\varepsilon_{V,SG}$ is also an important factor in the design of pavements with the goal of preventing permanent deformations. As can be seen in Table 6-3, $\varepsilon_{V,SG}$ is highly dependent on the modulus of the subgrade layer followed by the moduli of base and the concrete slab. As expected, this finding agrees with the results observed in pavement surface deflection and indicates the significance of the foundation layer properties in the pavement performance. As the thickness of the concrete slab increases, load transfer efficiency (*LTE*) of the joints prominently increases, which may also correspond to the increase of the diameter of dowels. As expected, another important factor influencing *LTE* is the modulus of the subgrade layer.

By comparing the practical combinations of pavement parameters (set II) with the analysis of all cases (set I) considered in GSA, it is seen that the overall behavior of both sets is the very similar; however, in some cases and as expected, the range of VIS values is lower for the reduced practical set II. The parameters E_{SG} and E_{PCC} are the most influential factors on the pavement surface deflection but the contribution of E_{Base} has decreased in set II compared to the cases in set I. This is due to the fact that several nonpractical pavement structures (e.g. thick base layer under a thick slab or strong base over the good subgrade condition) that overemphasizing the role of base layer in pavement deflection were eliminated. Furthermore, a lower influence of the slab modulus on the stress developed in base and concrete slab was observed in the practical cases compared to the analysis of set I. Thus, E_{Base} and t_{Base} are the main factors affecting the $\sigma_{mid,Base}$, which is a more reasonable conclusion as observed in engineering practice. Other conclusions made based on the analysis of set I are still valid for practical combinations of pavement structure.

The findings from the sensitivity analysis demonstrates that RPAS predicts pavement responses that agree with the general understanding of pavement mechanics and field observations. More importantly, it indicated the significance of considering the contribution of the supporting layers to the response of JCPs, which are not always included in the mechanistic-empirical designs.

6.2. Calibration Test Dataset

To ensure the efficiency and robustness of a calibration process, the calibration experimental dataset must contain a wide range of pavement material properties (e.g., concrete mixture, stabilized foundation layer), pavement structure (e.g., thickness, configuration of layers), slab configurations (e.g., bonded or unbonded, slab dimensions, load transfer devices), and loading condition (e.g., truck loading, impact loading). Therefore, one of the aims of data collection was to take into consideration the variety of measurements. Furthermore, the data were collected from field tests were measured at different locations on the slab (e.g., center, corner, edge). A summary of the considered pavement tests sections is given here, and the details of pavement properties and testing condition can be found in Chapter 4.

To establish a test dataset that is as comprehensive as possible, three test cells at MnROAD pavement test facility were selected. Cell 32 was a conventional pavement designed to assess the performance of undoweled thin concrete slab for highways. Cell 52 was a conventional doweled pavement with larger slabs that was designed for curl-and-warp study. Cell 613 consisted of a doweled slab over two base layers and a subgrade, a sustainable pavement design where 75% recycled concrete aggregate was used in the concrete mixture. In addition to the environmental loading, the traffic loading at MnROAD facility was applied through FWD test device as well as 80-kip or 102-kip semi-truck trailers with different tire configurations at different tests sections.

Furthermore, the data from three construction cycles CC-2, CC-4, and CC-6 at NAPTF were collected. CC-2 consisted of a constant-thickness slab on three different pavement foundation configurations: concrete slab on the subgrade, conventional concrete pavement, and the slab on the stabilized base. CC-4 consisted of three combinations of bonded (overlay, asphalt interlayer, underlay) slabs with different thicknesses. CC-6 consisted of the concrete slab over two types of stabilized base: asphalt treated base and cement stabilized base. The environmental loading at NAPTF was controlled to the small variation of temperature throughout the pavement depth. The traffic loading was applied by HWD test device as well as accelerated pavement test facility at different magnitudes, pressures, and tire configurations.

As mentioned in Chapter 4, the first set of available data at each section were utilized to eliminate the possibility of analyzing the pavement with deteriorated properties, particularly in the case of accelerated loading. The collected data were categorized into three groups of two-layer pavement (2L), three-layer pavement (3L), and four-layer pavement (4L) to be fed into the calibration and validation analyses. For 2L, the total 16 FWD tests data and 6 dynamic strain data were used. For 3L, the total 340 FWD/HWD tests data and 16 dynamic strain data were utilized. For 4L, the total 138 FWD/HWD tests data and 15 dynamic strain data were used in this study.

It should be noted that uniform pseudorandom number generator was used to divide the dataset into two sets of D_C (70% of the entire data) for calibration and D_V (30% of the entire data) for validation purposes.

6.3. Calibration Process

The process of fitting a model (or computer code) to experimental data by adjusting the input parameters is known as calibration and it seeks to reduce the model prediction errors. The sources of this error or uncertainty in computer modeling are classified as parameter uncertainty, model inadequacy, residual variability, parametric variability, observation error, and code uncertainty (Kennedy and O'Hagan 2001).

After collecting the data for calibration, they are processed to be used in calibration process. In general, to conduct the calibration process, two groups of model input parameters need to be identified. First, those parameters that are not considered to be significant contributors to the difference between the model and experimental results because they have low variability such as the thickness of the PCC slab. These parameters will be identified as the vector $\mathbf{x} = (x_1, \ldots, \mathrm{x}_n)$ which does not need to be calibrated. Second, those parameters that are known to significantly impact the discrepancies because they have a large variability such as the foundation moduli. They will be identified as the vector $\mathbf{t} = (t_1, \ldots, t_n)$ and are the ones that will be calibrated to minimize the discrepancies. Given these two groups of parameters, the calibration process will generate a vector of calibration factors $\mathbf{CF}(\mathbf{x}, \mathbf{t})$ that will then be applied to the parameters **t** to produce a calibrated model.

The calibration of RPAS in this study is based on the Pareto front multi-objective constrained optimization algorithm as explained in Chapter 2. The objective functions are the differences between model outputs and the field test data for the pavement deflection, $\mathbf{d}_{RPAS}(\mathbf{x}, \mathbf{t})$ and $\mathbf{d}_{field}$ as well as the strain in slab $\boldsymbol{\varepsilon}_{s,RPAS}(\mathbf{x}, \mathbf{t})$ and $\boldsymbol{\varepsilon}_{field}$. To characterize the properties of the supporting layers, their constitutive relation must be taken into consideration. Since concrete pavements response under conventional loads are characterized through linear elastic analysis, their constitutive equation will be based on the stress-strain relationship (Hooke's law). That is, for the study presented here, only the moduli of the foundation layers were selected for calibration. This results in the re-definition of the deflections and strains produce by RPAS as $\mathbf{d}_{RPAS}(\mathbf{x},\mathbf{E}^*)$ and $\boldsymbol{\varepsilon}_{s,RPAS}(\mathbf{x},\mathbf{E}^*)$, where $\mathbf{E}^*$ are the moduli of the foundation layers. Therefore, the optimization (minimization) problem can be expressed as finding the vector: $\mathbf{E}^* = [E_1^*, E_2^*, \ldots, E_m^*]^T$ that minimizes the discrepancies between modeled and field responses as:

$$\min \left\{\mathbf{e}_d, \mathbf{e}_s\right\} \text{ such that } \begin{cases} \mathbf{e}_d = \dfrac{[\mathbf{d}_{RPAS}(\mathbf{x},\mathbf{E}^*) - \mathbf{d}_{field}]^2}{\mathbf{d}_{field}} \ll \varepsilon_c \\ \\ \mathbf{e}_s = \dfrac{[\boldsymbol{\varepsilon}_{s,RPAS}(\mathbf{x},\mathbf{E}^*) - (\boldsymbol{\varepsilon}_s)_{field}]^2}{(\boldsymbol{\varepsilon}_s)_{field}} \ll \varepsilon_c \\ E_{ll} \le \mathbf{E}_i^* \le E_{ul} \qquad i = 1, 2, \ldots, \mathrm{m} \end{cases} \tag{6-1}$$

where *m* is the number of soil layers, E_{ll} and E_{ul} are positive values denoting the lower limit and upper limit of the moduli based on typical soil properties, and ε_c is a small number denoting the calibration accuracy requirement.

Now that both the calibration inputs $\mathbf{E}$ ($\mathbf{t}$ in the above statement) and calibration output $\mathbf{E}^*$ are known, the vector of calibration factors $\mathbf{CF}$ can be extracted from:

$$\mathbf{E}^* = (\mathbf{CF})(\mathbf{E}) \tag{6-2}$$

The diagram in Figure 6-1 shows how the calibration factors are generated utilizing data from different sources, MnROAD and NAPTF. As can be seen, for each pavement tested, the calibration process was performed in two levels: (a) using a single objective function (SOF) that minimizes the difference between measured deflection and predicted deflection using RPAS ($\mathbf{e}_d$), and (b) using a multiple objective function (MOF) that simultaneously minimizes the difference between the pavement maximum deflection ($\mathbf{e}_d$) and strain in the slab ($\mathbf{e}_s$) from measurement and predicted by RPAS. Since 70% of the data are randomly selected for calibration, the dataset used in SOF may be different from those in MOF. Although MOF is more comprehensive, SOF can be used when the deflection of pavement is of greater importance to the designer and it can reduce the computational cost.

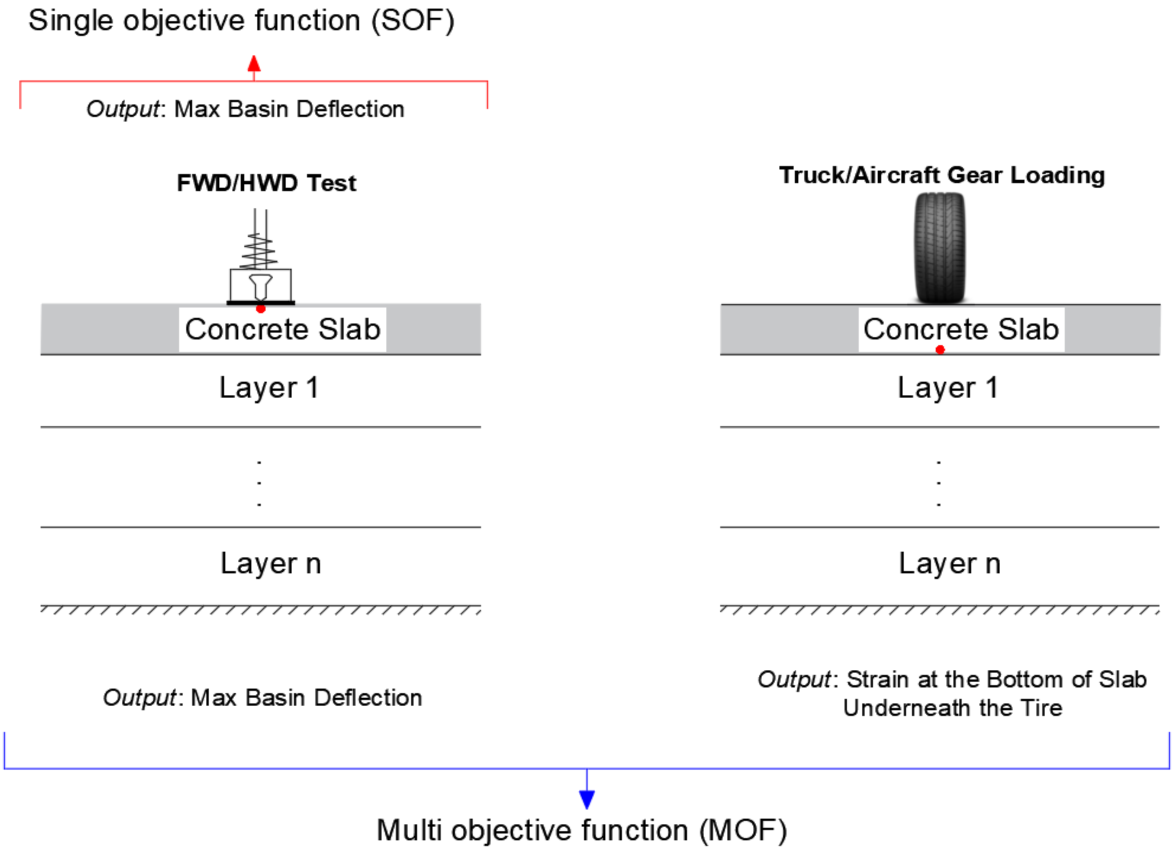

Figure 6-1. The procedure of generating calibration factors using single or multiple objective function(s)

The 3D foundation was used to model pavement underlying layers unless otherwise stated, as in section 6.4. In those cases, Eq. (6-2) will be changed to $\mathbf{k}^* = (\mathbf{CF})(\mathbf{k})$, where $\mathbf{k}$ is the vector of *k*-values of the foundation layer(s). Further explanations on the selecting the correct calibration factors $\mathbf{CF}$ and their incorporation in the validation process are given in the following section and next chapter.

6.4. Analysis of Generated Calibration Factors

By having the vector of calibration factors, $\mathbf{CF}$, the calibration factor to be applied to each case can be obtained using deterministic or stochastic method. To determine the calibration factors using the deterministic method, the average (or median) of their absolute values can be taken into account. Another approach would be to plot the calibration factors against the impact stiffness (P/D_0) (P=FWD load, D_0=maximum basin deflection) and/or strain in the slab (ε_c) and develop an equation to calculate the calibration factor for a pavement structure. In the stochastic method to estimate the calibration factor, the probability distribution function of $\mathbf{CF}$ can be plotted and according to a limit λ (set by the user, depending on the skewness of data), the $\mathbf{CF}$ corresponding to can be determined as the constant calibration factor to be applied to an arbitrary pavement structure. However, the deterministic method using the median of **CF** was used in the following section for different pavement structures.

Figure 6-2 and Tables 6-4 and 6-5 show an example of the outputs of the calibration process for the 2-layer pavement using single- and multi objective function. Using the data in Table 6-5, Figure 6-2a shows the plot of load-deflection of the 2-layer pavement (11 randomly selected test data as 70% of the total of 16 FWD tests) and the corresponding calibration factors against the load-deflection ratio (P/D_0) or impact stiffness. Note that 12-36 kips are the target loads to be applied in FWD tests and are slightly different from P. As can be seen, the measured deflections at higher applied loads show a wider range of variation compared to those for lower load level. The corresponding calibration factor graph indicates that a higher calibration factor (typically greater than the average of 1.0967) must be utilized when the applied load increases. In other words, at higher loads, RPAS slightly overpredicts the deflections that need higher calibration factor to correct for this error. Furthermore, aside from the average value of calibration factor, the developed correlation between the impact stiffness and calibration factor can be used for future predictions.

Figure 6-2b illustrates the data in Table 6-5 on the generation of calibration factors for the two-layer pavement system at NAPTF CC-2 by integrating the FWD and dynamic strain data in the process. This figure indicates that the load-deflection behavior remained the same, although another set of random data were selected. Even though the accelerated pavement loading data are not displayed in this plot, their effect can be seen as the higher discrepancy in the calibration factors. This behavior was expected because calibration factors are not necessarily in direct relationship with the values of impact stiffness, as opposed to CF in Figure 6-2a. Although the fitted line changed in the slope to some extent, the average calibration factor remained almost the same, which can be due to the uniformity of data that were collected on the same test site. This behavior was not observed in the rest of analysis shown in the appendix A.

Table 6-4. The Generated Calibration Factors for the Deflection (SOF) of Two-Layer Pavements at NAPTF CC-2

FWD Load, P (lb)	**Max. Deflection, D_0 (mil)**	**Given Modulus of Soil[†] (psi)**	**Calibrated Modulus of Soil (psi)**	**Calibration Factor, CF[‡]**
36,317	10.9	13,467	12,638	0.9385
36,475	9.3	13,467	17,262	1.2818
24,189	6.5	13,467	15,596	1.1581
24,262	6.3	13,467	16,664	1.2374
24,214	7.0	13,467	13,557	1.0067
36,341	10.5	13,467	13,578	1.0082
24,303	6.3	13,467	16,717	1.2414
36,438	9.3	13,467	17,228	1.2792
12,037	3.7	13,467	11,978	0.8894
24,149	7.2	13,467	12,779	0.9489
12,207	3.4	13,467	14,472	1.0746
			Median:	1.0857

† Correlated from CBR values, as described in Chapter 4.
‡ The ratio of calibrated modulus of soil to the correlated one.

Table 6-5. The Data of Deflection and (b) Strain at the Bottom of Slab Used for Generating the Calibration Factors using MOF for Two-Layer Pavements at NAPTF CC-2

(a)

FWD Load, P (lb)	**Max. Deflection, D_0 (mil)**	**Given Modulus of Soil (psi)**	**Calibrated Modulus of Soil (psi)**	**Calibration Factor, CF**
24,149	7.2	13,467	14,400	1.0693
36,438	9.3	13,467	16,386	1.2167
36,341	10.5	13,467	14,262	1.0590
36,414	9.6	13,467	16,578	1.2310
12,130	3.6	13,467	12,817	0.9517
12,235	3.3	13,467	14,952	1.1102
24,303	6.3	13,467	16,664	1.2374
24,262	6.3	13,467	15,892	1.1801
12,037	3.7	13,467	12,278	0.9117
12,086	3.3	13,467	14,661	1.0887
36,317	10.9	13,467	13,596	1.0096
	Median:			1.0928

(b)

APT[†] Load (kips)	**Strain in Slab ($\mu\varepsilon$)[‡]**
55.0	L1:-113.3 L2:102.7 L3:-114.7 L4:113.5 T1:57.3 T2:58.7

† Accelerated Pavement Testing

‡ Dynamic strain due to accelerated gear loading measured near longitudinal (L) and transverse (T) joints

Therefore, to develop a consistent procedure to determine the best calibration factor for different pavement structures, the deterministic method explained in Section 6.3 by utilizing the median of calibration factors was used. Using the median calibration factor eliminates the effect of outliers in **CF**. For example, from Figure 6-3a corresponding to the deflection data using SOF, a calibration factor of CF =1.0857 was obtained and from Figure 6-3b that is associated with the deflection and strain data using MOF, a calibration factor of CF =1.0928 was calculated.

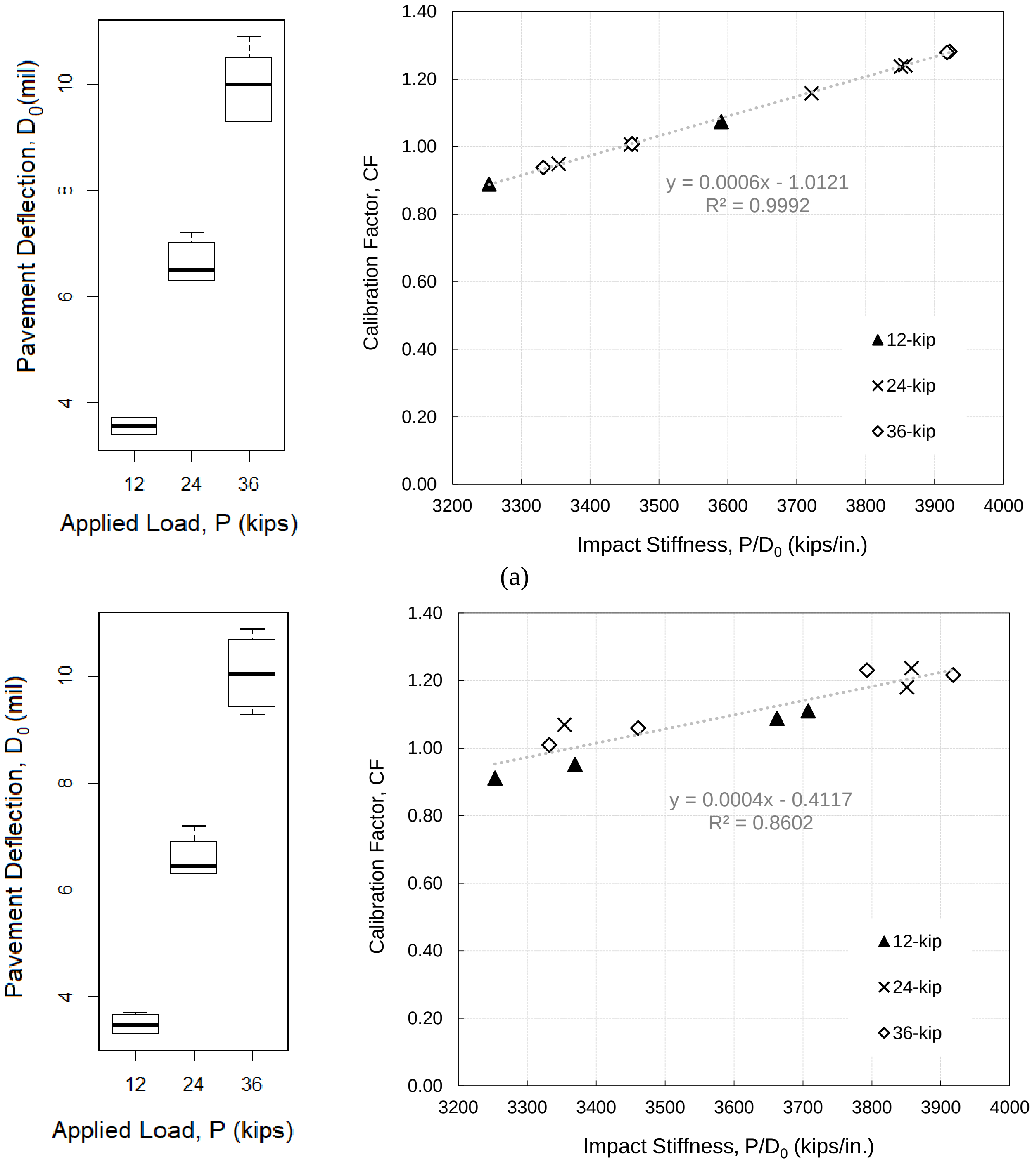

(a)

(b)

Figure 6-2. Load-Deflection Relationship and Generated Calibration Factors for The Two-Layer Pavement (a) Using SOF (By Incorporating FWD Data) (b) Using MOF (By Incorporating FWD and Dynamic Strain Data) (Refer to Tables 6-4 and 6-5, Respectively)

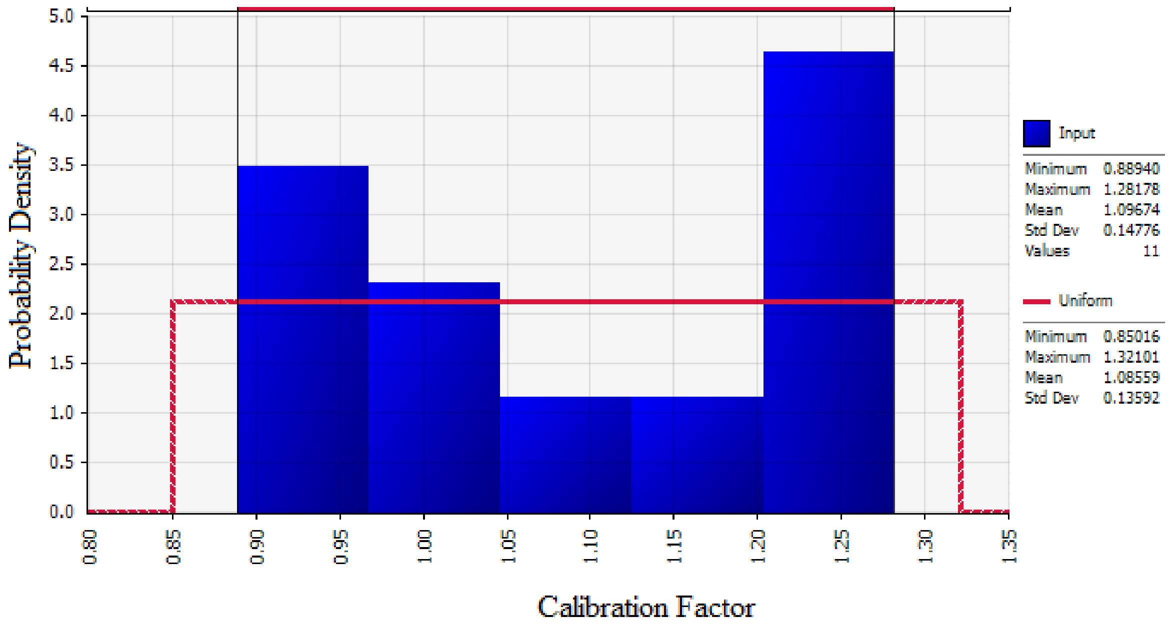

(a) Median CF1: 1.0857

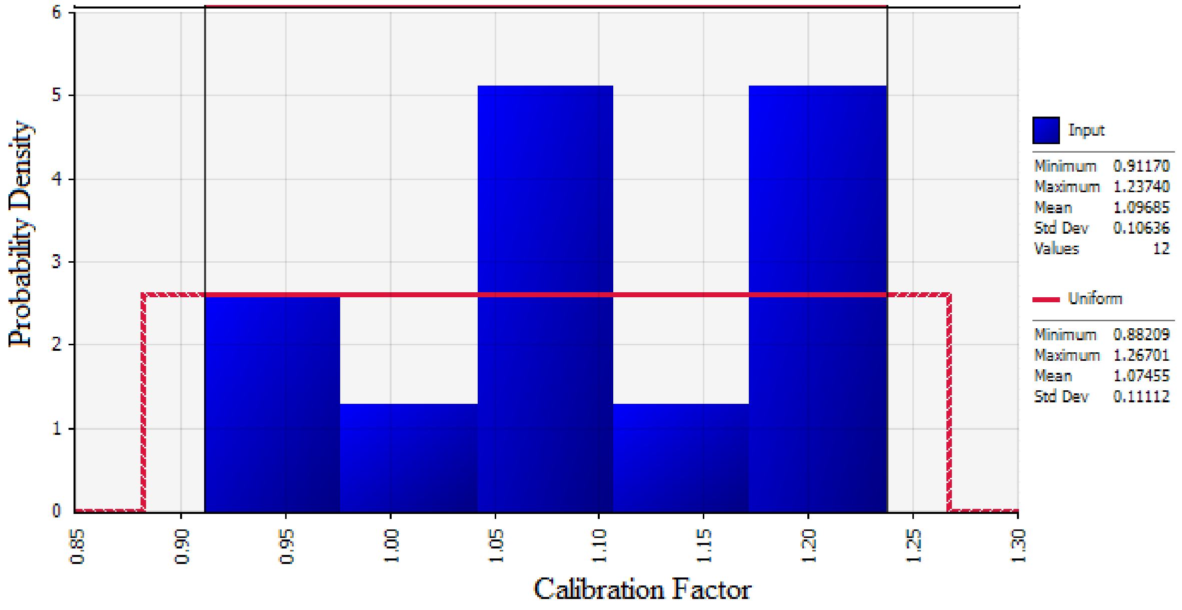

(b) Median CF2: 1.0928

Figure 6-3. The Distribution Fitted to The Calibration Factors of Two-Layer Pavements Generated Based on the (a) SOF (Using Deflection Data) (b) MOF (Deflection and Strain Data)

As mentioned before, the calibration process was conducted using 3D foundation model. However, to demonstrate the effect of using spring foundation, the calibration factors generated by incorporating Winkler foundation into RPAS calculations for the above example (two-layer pavement at NAPTF CC-2) will be shown here. The equivalent *k*-value as the initial input was found using the empirical results presented in ACPA (2020), which replaced the old correlation $k = M_r / 19.4$. Based on this reference, the initial subgrade resilient modulus of 13,467 psi is equivalent to 241 pci. After running the calibration process using Winkler foundation, the calibration factors presented in Table 6-6 and Figure 6-4 were produced. As can be seen, larger calibration factors are required when the spring model is utilized for the foundation layers. The median of the generated calibration factors (2.4652) is greater than twice that calculated using 3D foundation (1.0857). This comparison indicates that the results obtained using the 3D foundation are more accurate than those using the spring (Winkler) foundation, which was also demonstrated in Chapter 5.

Table 6-6. The Generated Calibration Factors for the Deflection (SOF) of Two-Layer Pavements at NAPTF CC-2 Utilizing Winkler Foundation

FWD Load, P (lb)	**Max. Deflection, D_0 (mil)**	**Given *k*-value of Soil† (pci)**	**Calibrated *k*-value of Soil (psi)**	**Calibration Factor, CF‡**
12207	3.4	241	556	2.3081
24149	7.2	241	490	2.0320
36438	9.3	241	671	2.7833
36341	10.5	241	522	2.1649
36475	9.3	241	672	2.7868
36414	9.6	241	628	2.6052
24303	6.3	241	650	2.6961
12130	3.6	241	489	2.0287
12235	3.3	241	594	2.4652
24262	6.3	241	647	2.6854
12037	3.7	241	454	1.8854
			Median:	2.4652

† Adapted from ACPA (2020)

‡ The ratio of calibrated *k*-value of soil to the correlated one.

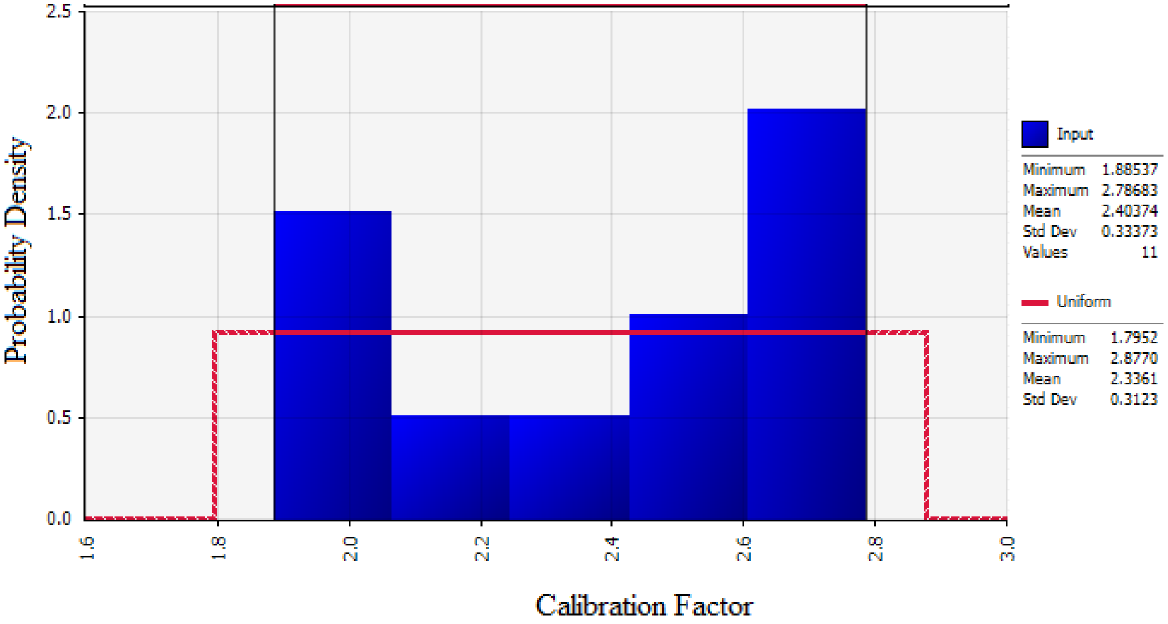

Median CF: 2.4652

Figure 6-4. The Distribution Fitted to The Calibration Factors of Two-Layer Pavements Generated Based on the SOF (Using Deflection Data) Utilizing Spring (Winkler) Foundation

Another example of the outcome of the calibration process for a three-layer concrete pavement at MnROAD Cell 32 using 3D foundation is presented here. Tables 6-7 and 6-8 list a portion of data (10%) from Cell 32 that was randomly selected from the database and the generated calibration factors from SOF (from deflection data) and MOF (from deflection and strain data), respectively. A plot of the calibration factors in Figures 6-5 and 6-6 show that there are higher discrepancies between these factors when a more complicated pavement structure is analyzed.

Table 6-7. The Generated Calibration Factors for the Deflection (SOF) of Three-Layer Pavements at MnROAD Cell 32

FWD Load, P (lb)	**Max. Deflection, D_0 (mil)**	**Given Modulus of Base (psi)**	**Given Modulus of Subgrade (psi)**	**Calibrated Modulus of Base (psi)**	**Calibrated Modulus of Subgrade (psi)**	**Calibration Factor of Base, CF1**	**Calibration Factor of Subgrade, CF2**
9,136	5.7	16,500	10,400	23,084	8,434	1.399	0.811
8,739	24.7	16,500	10,400	18,414	13,385	1.116	1.287
14,782	29.8	16,500	10,400	21,714	10,598	1.316	1.019
6,106	4.8	16,500	10,400	18,480	12,532	1.120	1.205
6,106	4.5	16,500	10,400	16,517	8,330	1.001	0.801
14,623	35.5	16,500	10,400	20,345	13,239	1.233	1.273
5,773	13.7	16,500	10,400	18,447	11,970	1.118	1.151
14,925	23.4	16,500	10,400	16,154	12,480	0.979	1.200
14,893	56.2	16,500	10,400	17,325	14,300	1.050	1.375
14,925	31.3	16,500	10,400	14,157	8,694	0.858	0.836
5,837	10.2	16,500	10,400	15,692	12,917	0.951	1.242
15,512	12.5	16,500	10,400	18,579	12,324	1.126	1.185
14,386	46.6	16,500	10,400	15,560	9,433	0.943	0.907
14,544	41.3	16,500	10,400	22,044	13,822	1.336	1.329
5,742	13.7	16,500	10,400	18,431	10,327	1.117	0.993
					Median:	1.1170	1.1850

Table 6-8. The Data of Deflection and (b) Strain at the Bottom of Slab Used for Generating the Calibration Factors using MOF for Three-Layer Pavements at MnROAD Cell 32

(a)

FWD Load, P (lb)	**Max. Deflection, D_0 (mil)**	**Given Modulus of Base (psi)**	**Given Modulus of Subgrade (psi)**	**Calibrated Modulus of Base (psi)**	**Calibrated Modulus of Subgrade (psi)**	**Calibration Factor of Base, CF1**	**Calibration Factor of Subgrade, CF2**
5,710	17.9	16,500	10,400	18,893	13,853	1.145	1.332
6,122	4.6	16,500	10,400	15,329	13,229	0.929	1.272
14,782	29.8	16,500	10,400	14,025	12,272	0.850	1.180
5,805	12.3	16,500	10,400	15,824	13,021	0.959	1.252
15,337	12.9	16,500	10,400	22,985	13,822	1.393	1.329
8,993	14.4	16,500	10,400	16,599	9,578	1.006	0.921
5,837	10.2	16,500	10,400	14,223	10,774	0.862	1.036
8,771	21.5	16,500	10,400	21,120	10,764	1.280	1.035
9,215	6.3	16,500	10,400	14,157	10,868	0.858	1.045
14,275	45.4	16,500	10,400	22,275	10,244	1.350	0.985
8,152	36.2	16,500	10,400	20,906	12,386	1.267	1.191
9,009	12.9	16,500	10,400	14,702	11,305	0.891	1.087
8,882	17.5	16,500	10,400	16,517	8,580	1.001	0.825
14,719	35.4	16,500	10,400	20,675	13,822	1.253	1.329
14,893	30.2	16,500	10,400	18,051	14,144	1.094	1.360
					Median:	1.0060	1.1800

(b)

Truck Load (kips)	**Strain in Slab ($\mu\varepsilon$)‡**
12.0	34.2
16.9	34.4
16.6	33.8
15.6	39.3
18.4	38.5

‡ Dynamic strain due to truck loading measured beneath the tire

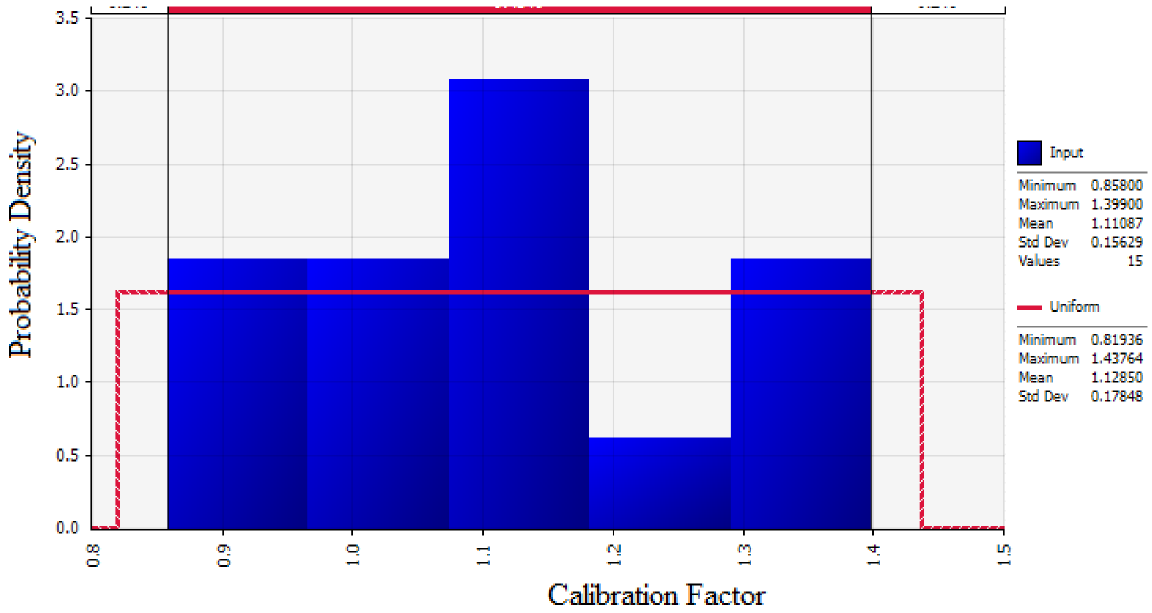

(a) Median CF1: 1.1170

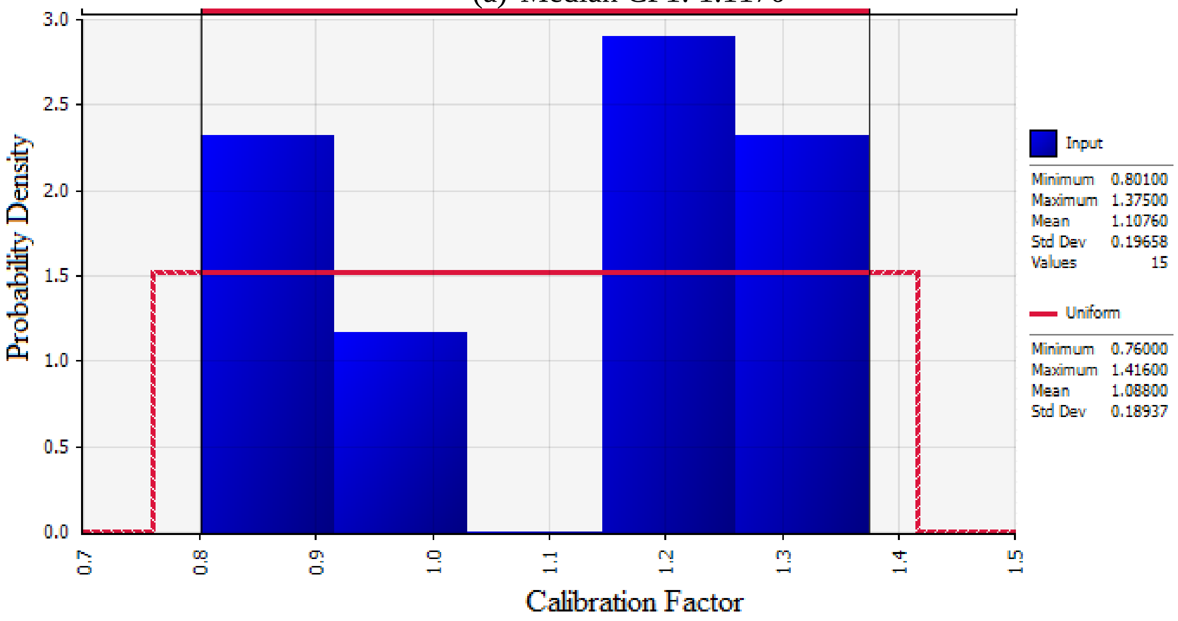

(b) Median CF2: 1.1850

Figure 6-5. The Distribution Fitted to The Calibration Factors of Three-Layer Pavements at MnROAD Cell 32 Generated Based on SOF (By Incorporating the Deflection Data) (a) CF1 for Base Layer (b) CF2 for Subgrade Layer

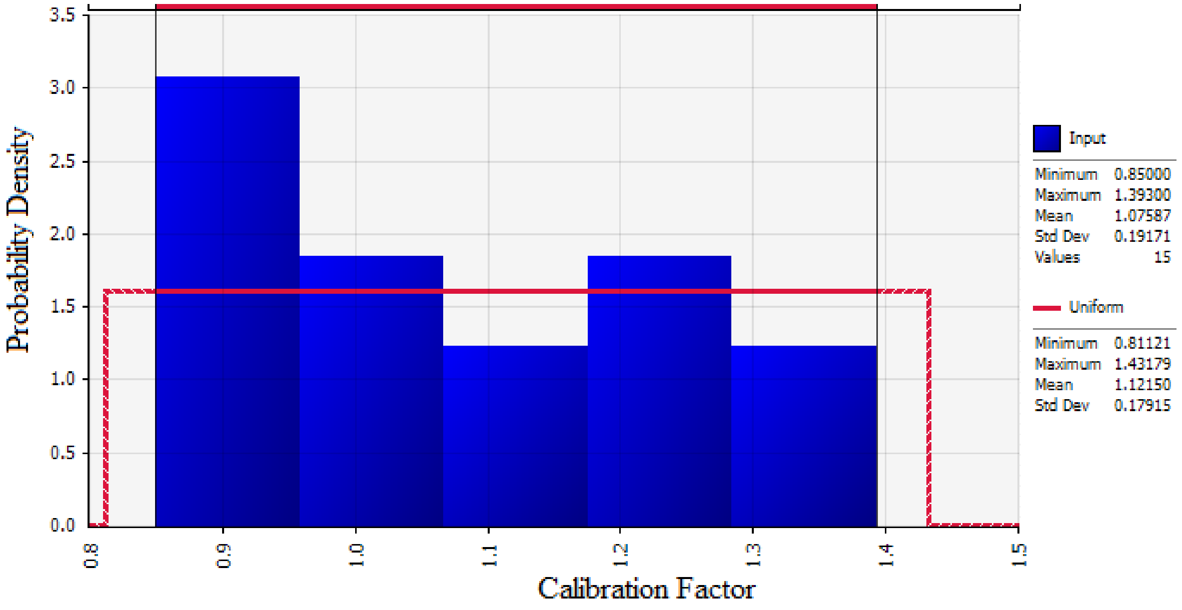

(a) Median CF1: 1.0060

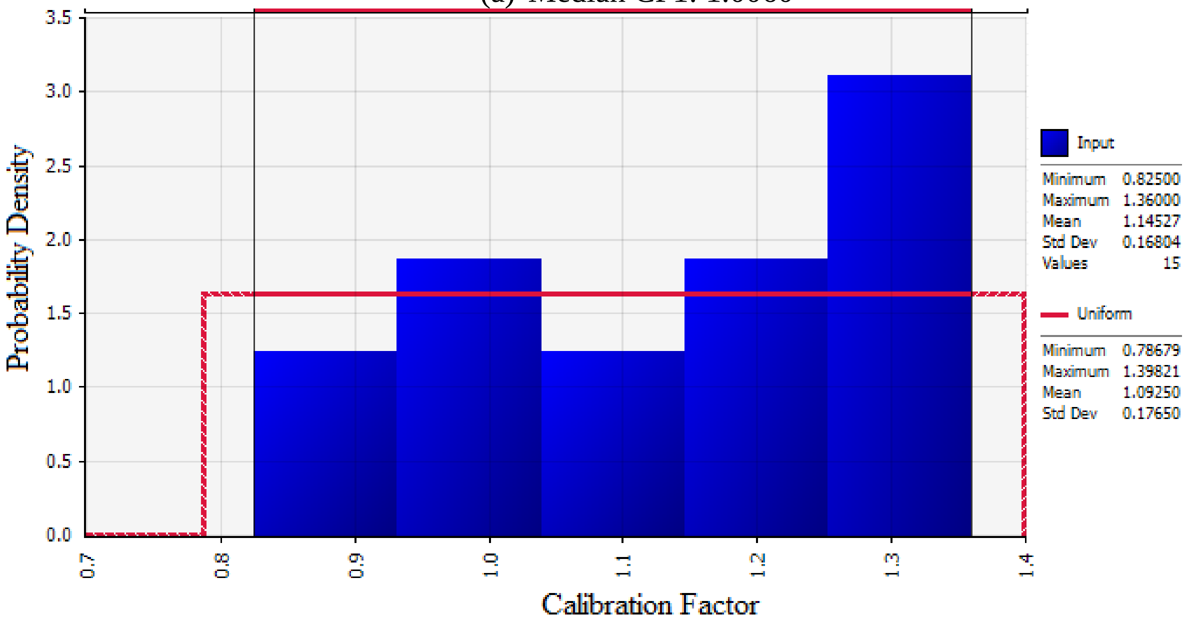

(b) Median CF2: 1.1800

Figure 6-6. The Distribution Fitted to The Calibration Factors of Three-Layer Pavements at MnROAD Cell 32 Generated Based on MOF (By Incorporating the Deflection and Strain Data) (a) CF1 For Base Layer (b) CF2 For Subgrade Layer

Tables A-1 through A-4 (and Figures A-1 through A-4) in Appendix A list the calibration factors for three-, and four-layer concrete pavements.

An important outcome of the calibration results shown here and in appendix A is that even for the complex pavement structures, the calibration factors range between 0.75 and 1.60. Since the analysis for three- and four-layer pavements were performed for the test sections at different locations and different properties, this range of calibration factors indicates the capability of RPAS in making accurate prediction of pavement responses and calibration will improve this accuracy. This was confirmed by the several studies conducted in Chapters 4 and 5 on the pre-validation and bench-marking of RPAS, where small errors between the predictions and measured responses were observed. Upon availability of more data, the calibration can be even further improved.

7. Validation

This chapter provides the results of the validation of RPAS using a set of field data randomly selected for this purpose. Different validation metrics are reviewed, and the reliability of the program (utilizing 3D foundation) based on the provided test data in the calibration and validation stages will be assessed.

7.1. Validation Metrics

As described in section 6.2, the field test dataset was divided into a calibration dataset and a validation dataset. The calibration dataset was used in Chapter 6 above to calculate calibration factors and in this Chapter the validation dataset will be used to assess the calibration process and the resulting calibration factors. This process is called model validation and it is important to highlight that it is conducted with a dataset that was excluded from the calibration process. Researchers have been developing different types of validation metrics that express the accuracy of a computational model through comparison with experimental data. Available approaches for quantitative model validation are based on statistical confidence intervals (Oberkampf and Barone 2006), computing distance between the model prediction and experimental data by computing the area metric (Roy and Oberkampf 2011, Ferson et al. 2008), normalizing residuals (Hills and Leslie 2003), classical statistics-based hypothesis testing (Urbina et al. 2003), Bayesian hypothesis testing (Gelfand and Dey 1994, Geweke 2007, Mahadevan and Rebba 2005), and reliability analysis-based techniques (Thacker and Paez 2014). Liu et al. (2011) and Ling and Mahadevan (2013) investigated several of these validation approaches in detail and discussed their practical implications in engineering. While some of these approaches compute validation metrics, some other approaches focus on directly estimating the so-called model form error (Rebba et al. 2006) as the difference between the model prediction and the underlying physical phenomenon the model seeks to represent.

Another important issue related to model validation is the topic of extrapolating the model to application conditions under which experiments may not have been performed. Typically, there are two types of extrapolation. The first type is where the model is validated at certain input values, but prediction needs to be performed at other input values that are not contained in the validation domain. The second type of extrapolation is where validation is performed using a simplified system (with restricted features, physics, etc.) and the desired prediction is of the original system. While regression-based techniques have been developed for the first type of extrapolation (Roy and Oberkampf 2011); model extrapolation, in general, is still a challenging issue and researchers are currently studying this problem.

In this study, a reliability analysis-based technique was used in which a model reliability metric (r) is calculated. This reliability metric that computes the probability that the model is valid and will be described here. Suppose a set of experimental data Y that can be expressed in general form of $Y = \left\{ \left\{ y_1, y_2, ..., y_{m_1} \right\}_1, \left\{ y_1, y_2, ..., y_{m_2} \right\}_2, ..., \left\{ y_1, y_2, ..., y_{m_k} \right\}_n \right\}$, in which each subset *1* through *n* indicates the replicates experimental data for the same input, i.e., same test spot and loading condition on pavement in the field. The numerical analysis (from RPAS) will return the prediction $\theta = \left\{ \theta_1, \theta_2, ...\theta_n \right\}$ from that shows a single prediction corresponding to each test case. Let's define *D* as the percent absolute difference between the experimental data (considering the average of each case, all the data, or any other statistical measure of data) and the model predictions. A small number ε_v (in percent) denotes the validation accuracy requirement, which will be set by the user (e.g., engineer, practitioner) as a target metric of model validation. The reliability metric r can be defined as $r = P(-\varepsilon_v < D < \varepsilon_v)$, indicating the probability that the difference between the experimental data and model predictions fall within the tolerance interval of validation accuracy requirement. A plot of experimental (measured) data against model predictions are presented before and after calibration. The correlation between these two variables as well as the prediction limits can be also used to somewhat evaluate the validity of the calibrated model.

7.2. Reliability Assessment Results

Once the calibration factor is generated from the calibration process explained in Chapter 6 and the median of **CF** is calculated, it will be applied to unseen data for validation. An example of the application of the proposed calibration and validity assessment on the three-layer pavement sections from MnRAOD Cells 32 and 52, as well as NAPTF CC-2 using the single-objective function (SOF) is shown in Figure 7-1. Like in the previous chapter, not all the utilized data were shown in this graph for brevity. The data used for this figure are listed in Table A-1 of Appendix A.

As can be seen in Figure 7-1, even though the equations showing the correlations in both graphs are very similar, the residuals for the fitted data before calibration are much higher ($R^2 = 0.77$) than those in the calibrated model ($R^2 = 0.99$). These larger residuals indicate a lower reliability of the model.

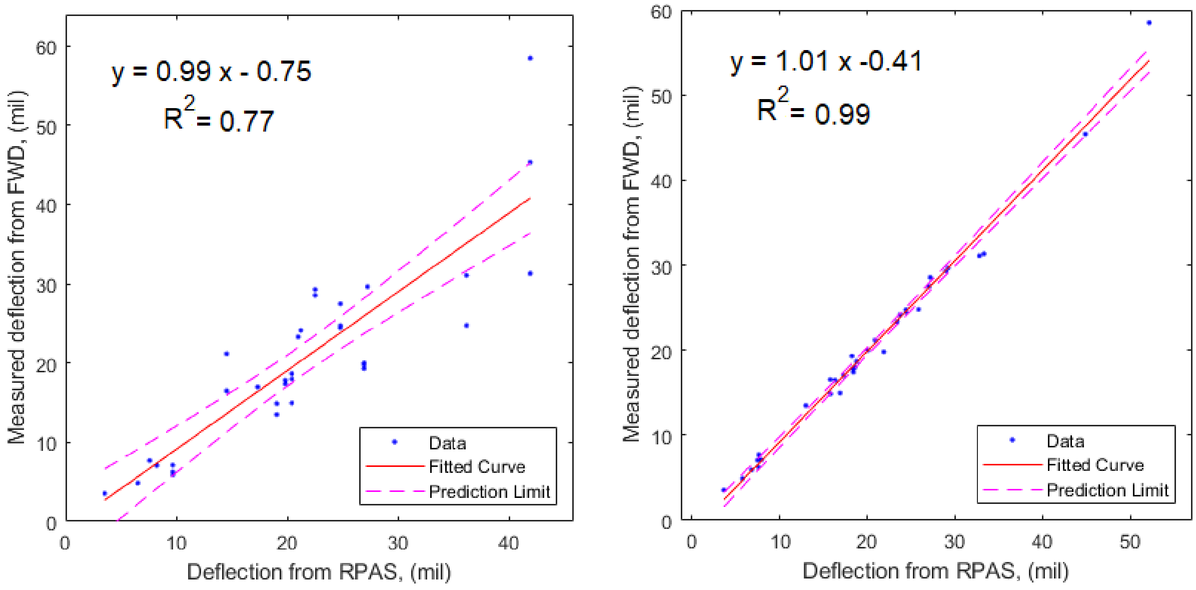

(a) (b)

Figure 7-1. Validity Assessment of RPAS for Three-Layer Pavement Systems (a) Correlation Before Calibration (b) Correlation After Calibration Using SOF

By utilizing the multi-objective function (MOF) for the calibration of three-layer pavement systems, the validity of the calibration process was assessed in Figure 7-2a for deflection and Figure 7-2b for strain responses. Again, note that only a portion of the entire data are visualized here. As can be seen, an improvement in deflection (R^2 increased from 0.90 to 0.99) and strain (R^2 increased from 0.98 to 0.99) response was observed after calibrating RPAS and the prediction limit became narrower.

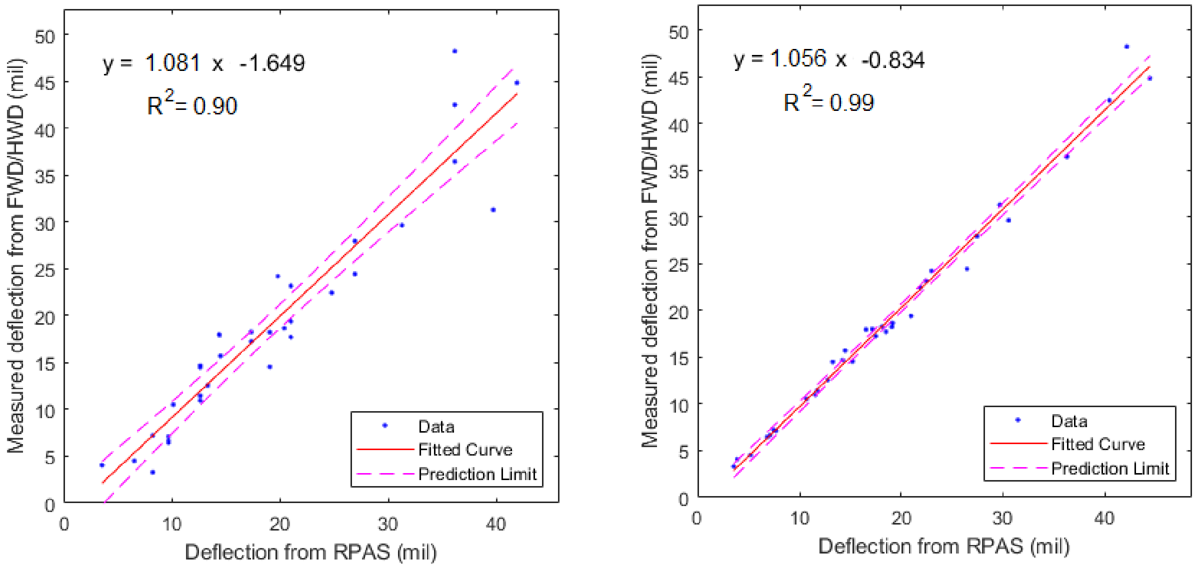

Before Calibration

After Calibration

(a)

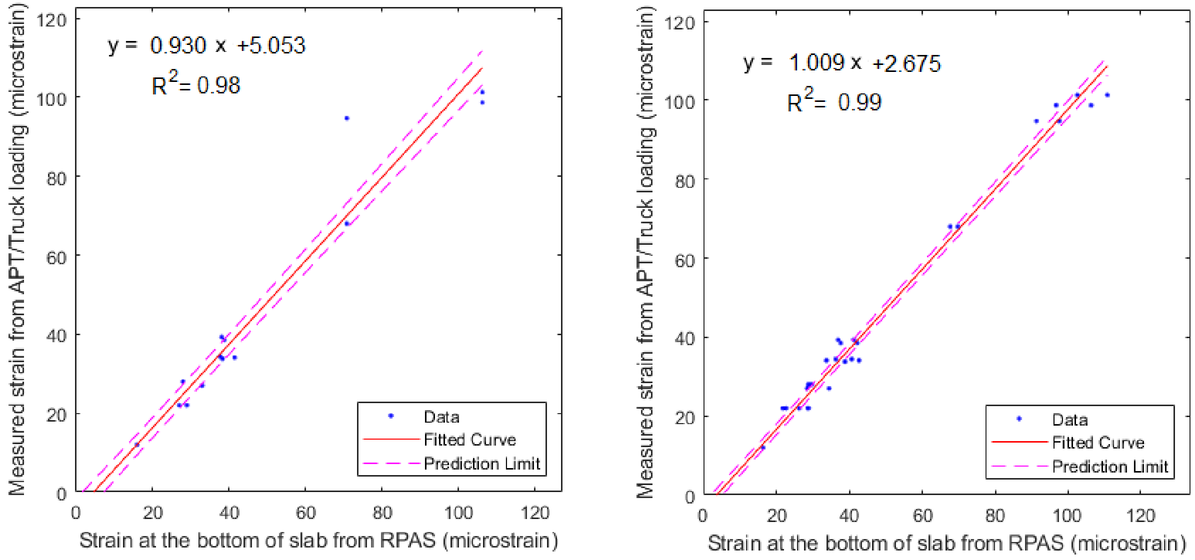

Before Calibration

After Calibration

(b)

Figure 7-2. Validity Assessment of RPAS for Three-Layer Pavement Systems (a) Correlation Before Calibration (b) Correlation After Calibration Using MOF

The calibrated model can also be assessed for the level of validity in terms of the reliability metric r. Figures 7-3 and 7-4 show the distribution of D as the percent absolute difference between the experimental data and RPAS predictions associated with the data used in Figures 7-1 and 7-2, respectively, using SOF and MOF. The summary of RPAS reliability results based on the difference *D* shown these figures are presented in Tables 7-1 and 7-2.

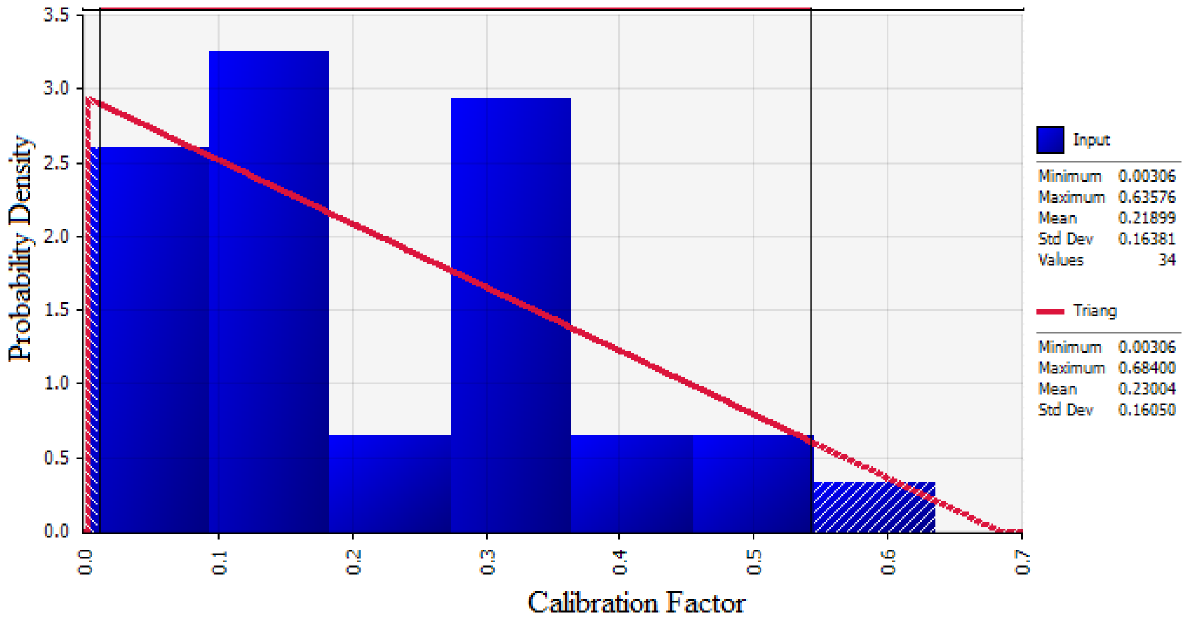

(a)

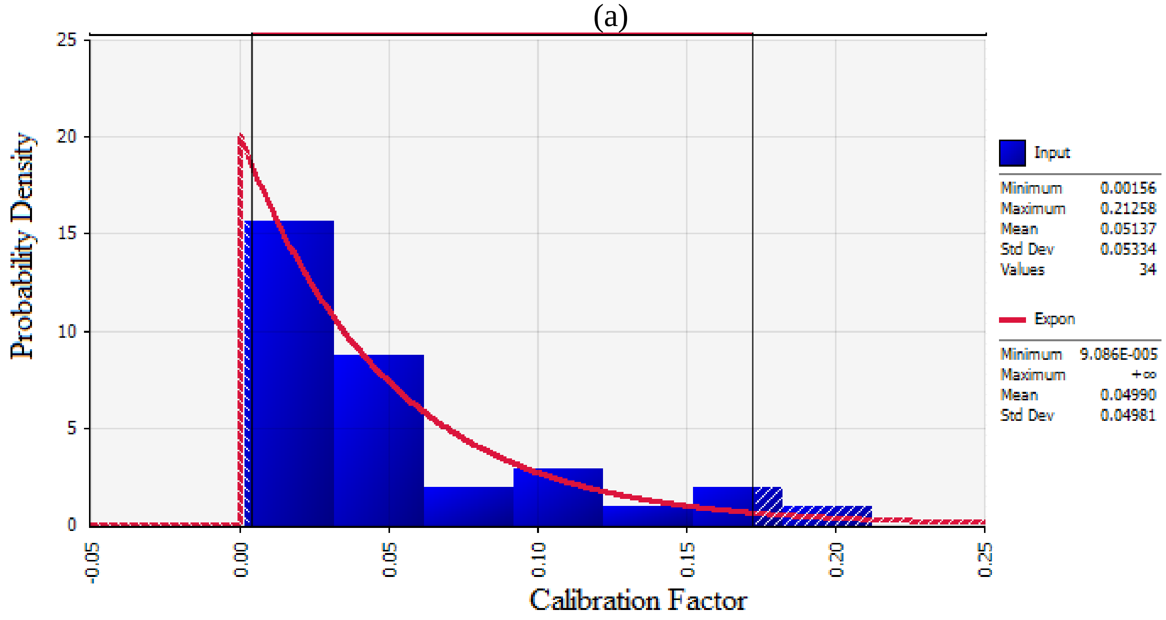

(b)

Figure 7-3. The Distribution of the Percent Absolute Difference Between the Deflections From Experimental and RPAS Predictions (*D*) For Three-Layer Pavements Using (a) Not Calibrated Model (b) Calibrated Model Utilizing SOF

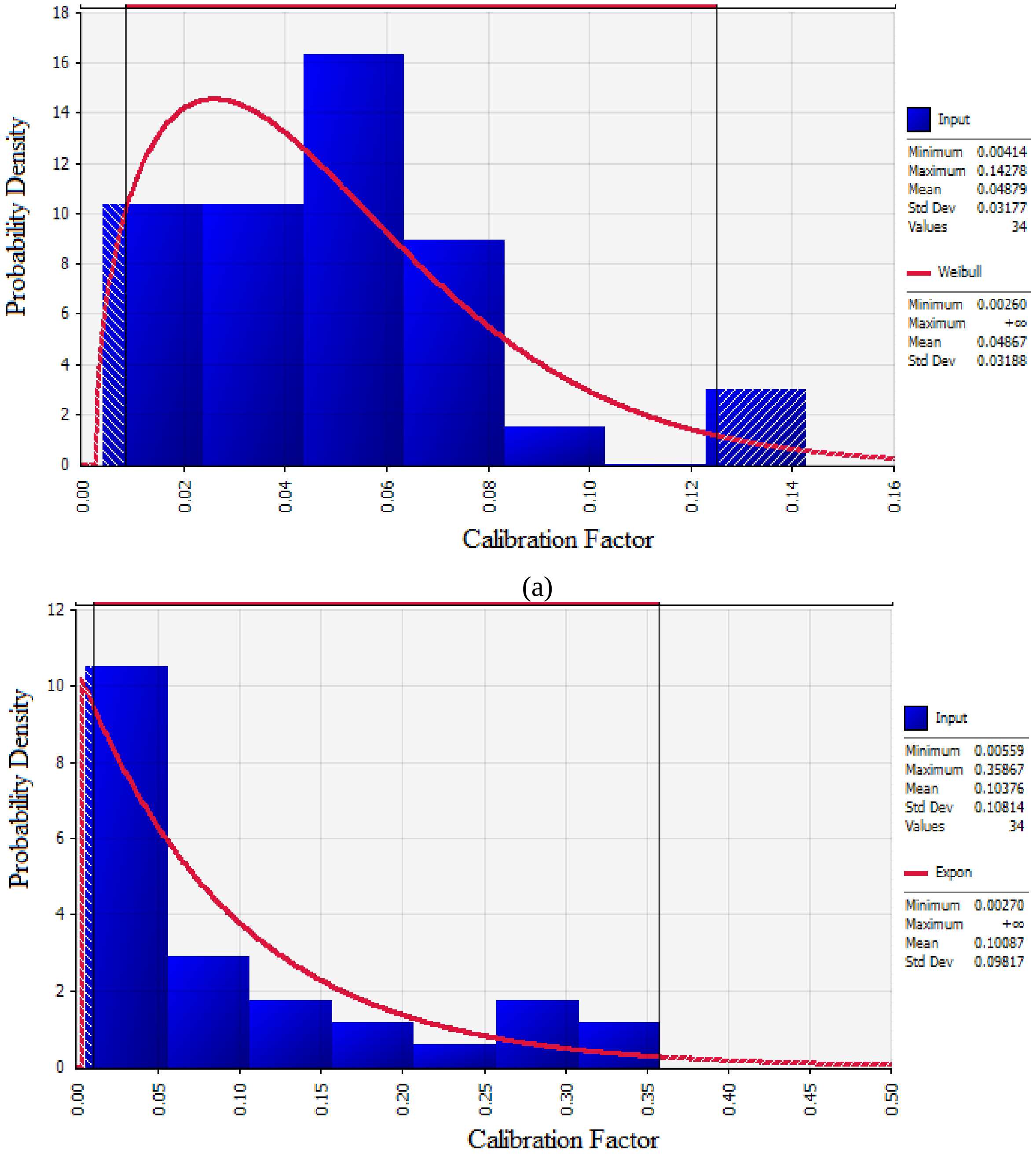

(a)

(b)

Figure 7-4. The Distribution of the Percent Absolute Difference Between the Experimental and RPAS Predictions (*D*) For Three-Layer Pavements For (a) Deflections (b) Strain Response Using MOF

Table 7-1. Reliability Metric r for Different Validation Accuracy Requirements ε_v for Three-Layer Pavements by Utilizing SOF

Accuracy Requirements, ε_v (%)	**Reliability Metric, r**	
	N/C†	**C‡**
1	0.05	0.19
5	0.13	0.64
10	0.25	0.86
15	0.50	0.96

† N/C: Not-Calibrated Model ; ‡C: Calibrated Model

Table 7-2. Reliability Metric r for Different Validation Accuracy Requirements ε_v for Three-Layer Pavements by Utilizing MOF

Accuracy Requirements, ε_v (%)	**Reliability Metric, r**			
	Deflection response		Strain response	
	N/C†	**C‡**	**N/C†**	**C‡**
1	0.03	0.05	0.05	0.08
5	0.19	0.60	0.25	0.38
10	0.40	0.95	0.45	0.65
15	0.58	0.99	0.60	0.78

† N/C: Not-Calibrated Model ; ‡C: Calibrated Model

As shown above, the level of reliability significantly increases after calibration. At a certain ε_v, it can be seen that the corresponding reliability metrics for calibrated models (for both deflections and strains) are higher than those from non-calibrated models. As can be seen in Table 7-1, when using the calibrated model, if the pavement design engineer decides to set the accuracy requirement at 1%, there will be only 19% probability that the predicted pavement responses from RPAS are within ±1% difference from measured responses. By increasing the accuracy requirement to 5%, the reliability of the pavement responses will greatly increase to 64%. In a typical design, the designer targets the accuracy requirement of 10%, from which the predictions from the calibrated model in RPAS are 86% in agreement with the field measurements listed above. In other words, in this set of validity analysis, 86% of the predictions from RPAS fall within ±10% difference with the field data. The same conclusions can be drawn for the reliability metrics obtained by utilizing MOF in Table 7-2.

As observed from the trend of the change of reliability metric of calibrated model with the respect to the accuracy requirement, there is a drastic increase in the reliability if the accuracy requirement is increased from 1 to 10%. This conclusion confirms the typical threshold value of 10% for the difference between the measured and calculated responses in the analysis of pavements. This trend was not observed for non-calibrated model and, if achievable, reaching the reliability of 70 to 80% needs using a wide range of accuracy requirement that may not be acceptable to pavement designer or transportation agencies.

7.3. Numerical Example

To better understand the effect of implementing the results from the sensitivity analysis into the calibration process of RPAS, an example was designed based upon the analysis of a pavement section in MnROAD Cell 32. In this example, two separate analyses were performed in RPAS using two different foundation models. For case I, the properties of the pavement foundation layers were assumed according to the recommended values in AASHTO (1993) and were entered into RPAS using a spring foundation model. Case II consisted of running RPAS utilizing a 3D solid foundation model by using the measured or back-calculated moduli of the foundation layers obtained from laboratory and field testing of the pavement section. A comparison between the responses obtained from these two models and the responses measured in field was made before and after applying the calibration factor to evaluate the importance of the implementation of GSA in the calibration process.

The pavement section studied in this example was described in Chapter 4; however, a brief description of this test section is presented here. This pavement consists of a 5-inch concrete slab placed on a 6-inch gravel base and a clay subgrade (R=12). The concrete slabs were 10 ft long and 12 ft wide. MnROAD Cell 32 was instrumented with static sensors (vibrating wire sensors and thermocouples) measuring the moisture and temperature distribution within the pavement depth as well as dynamics sensors measuring the responses under an 80-kip semi-trailer truck loading and falling weight deflectometer (FWD) tests.

The modulus and Poisson’s ratio of the concrete layer were defined as 4,445 ksi and 0.155, respectively. These values were measured from testing of cylinder specimens in the laboratory and were used for both cases I and II because they are also close to typical design values. The stiffness of the foundation layer for case I was determined from the typical values for fair to good subgrade in AASHTO (1993), i.e. 400 pci, whereas for case II, the moduli of 26,000 and 10,000 ksi were used for base and subgrade layers, respectively, according to back-calculation results. Further details on the back-calculated material properties and pavement configuration can be found in TaghaviGhalesari et al. (2020a). It should be noted that the effect of temperature loading has not been included in this study to achieve a similar comparison for both cases I and II.

Figure 7-5 illustrates the comparison of deflection and strain responses of the studied pavement section using cases I and II analyses. The percent difference between the results from case I or II and those from field measurements are shown below each location of pavement that was tested. As expected, there is a significant difference between responses predicted with spring model and 3D foundation (cases I and II, respectively), which had been shown in previous studies by Aguirre et al. (2019) and Luo et al. (2017). Modeling the supporting layers using the 3D solid foundation (case II) results in better agreement between the pavement deflections at different locations (16-29% difference) as compared to those using traditional method (case I) by utilizing the spring foundation (19-73% difference). The strains at the bottom of the concrete slab in dynamic sensor CE 120 in MnROAD Cell 32 that are shown in Figure 7-5b are also more consistent (less than 19% difference) with the RPAS modeling with 3D foundation that using a spring model (up to 70% difference). Therefore, the accurate modeling of the properties of the foundation layers using RPAS 3D foundation model will significantly improve the prediction of the pavement responses and, subsequently, will lead to more efficient pavement designs.

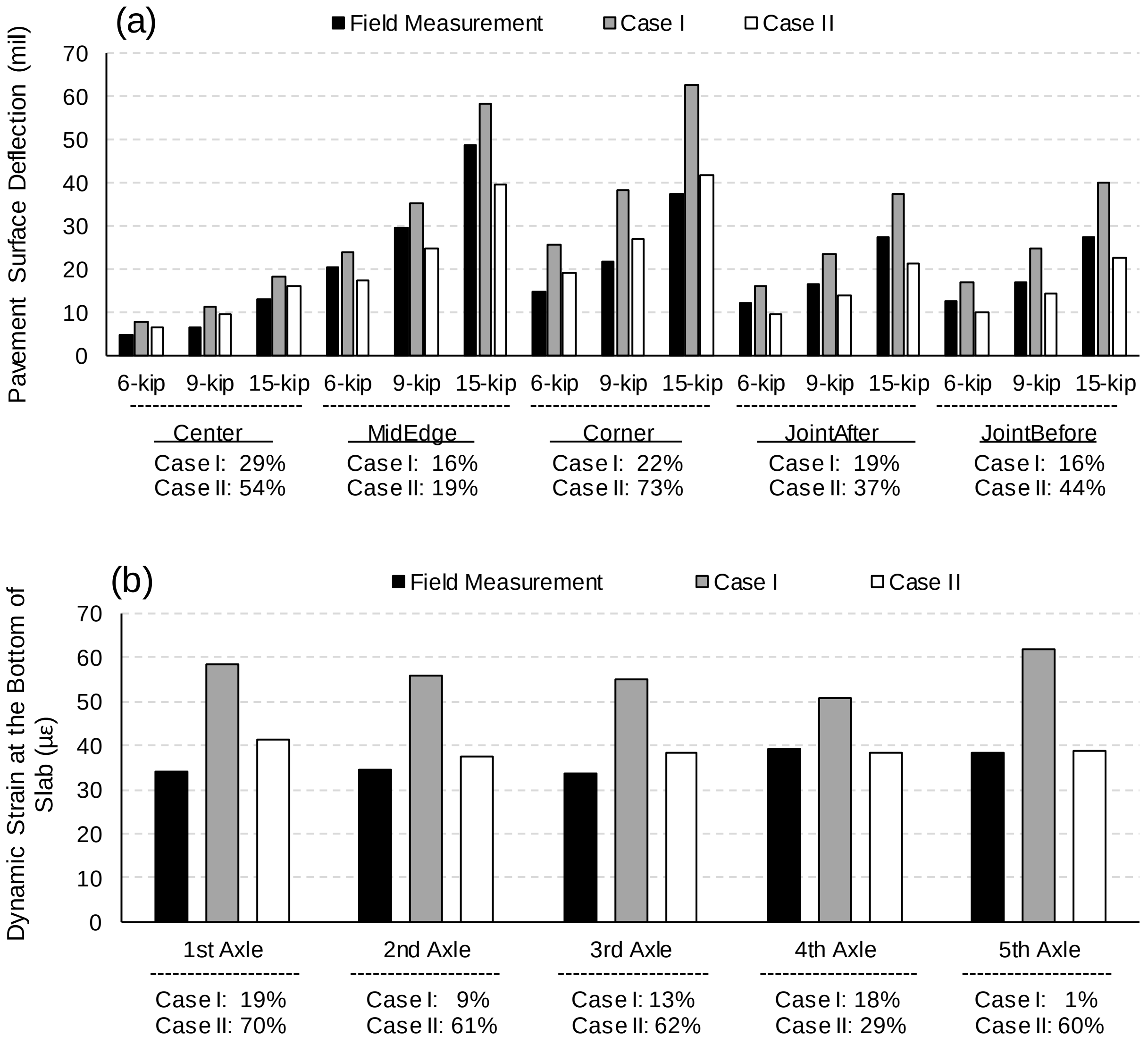

Figure 7-5. (a) Comparison of the Three-Layer Pavement Response from Field Measurements and Modeling With 3D And Spring Foundation (a) Pavement Surface Deflection Under FWD Test (b) Longitudinal Strain at The Bottom of Concrete Slab at MnROAD Cell 32.

An efficient way of calibration is to use a more comprehensive test dataset for calibration and running the calibration process using multi-objective minimization of the error function, which has been implemented earlier in this chapter. These calibration factors can be adjusted based on the GSA results. A simple type of this approach was employed in this section in a way that 70%

of data were used in the comparative study in Figure 7-5 and the remained 30% of field data were used for comparison against the 3D modeling results (case II) after application of the calibration factors derived from Pareto optimal front of error values. Figure 7-6 shows the deflection responses after calibration using the GSA results. As seen, the magnitudes of error have decreased from 29% to less than 6%. This high improvement in the perdition of pavement responses makes RPAS a reliable tool to be used by pavement design engineers and transportation agencies (TaghaviGhalesari et al. 2020c).

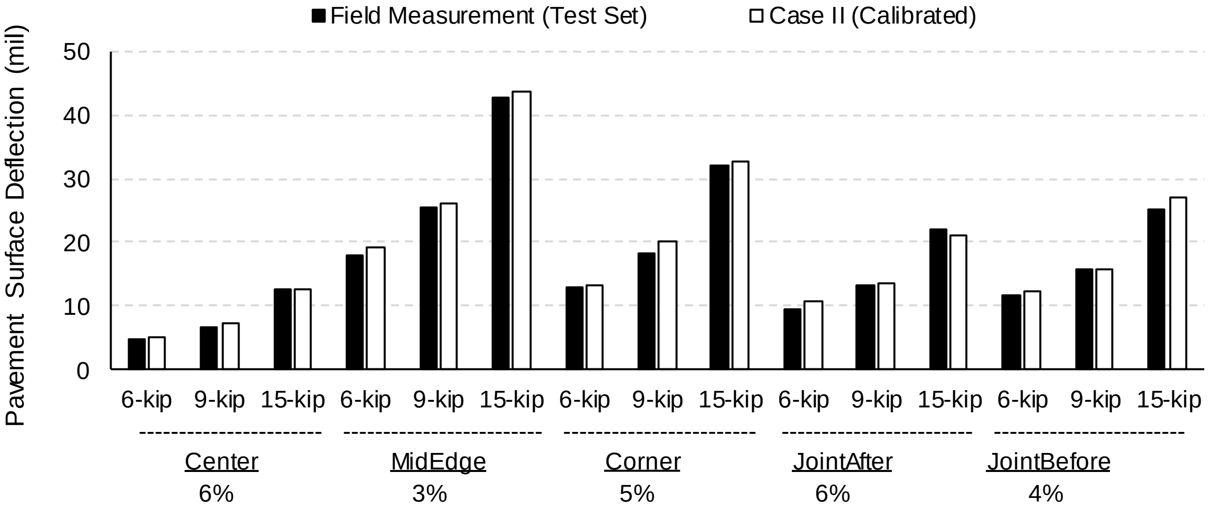

Figure 7-6. Comparison of Three-Layer Pavement Surface Deflection from FWD Measurements at MnROAD Cell 32 and Finite Element Simulation Using Calibrated RPAS Model.

8. Summary and Conclusions

Several analysis tools have been developed to predict the thermo-mechanical response of concrete pavements. Most of these tools use the finite element method to calculate bending stresses, strains and deflections in the concrete slabs caused by self-weight, tire loading, and thermal curling. RPAS is a software developed at the University of Texas at El Paso to model the behavior of concrete pavements and improve over the accuracy and capabilities of the previously developed tools. However, prior to the work presented in this dissertation there were only a limited number of studies conducted on the verification and validation of RPAS against analytical solutions and experimental data. To improve on the reliability of RPAS, a framework integrating a verification, calibration and validation process was proposed and implemented in this study.

8.1. Summary

A review of different types of concrete pavements, key factors influencing pavement response, modeling techniques and tools was conducted to understand the load transfer and interaction mechanisms of concrete pavements. Since the main focus of this study was the improvement of the reliability of RPAS using experimental data thorough a review of field and laboratory test methods, data collection and processing was conducted. The approaches and statistical metrics for the verification, calibration and validation of RPAS were presented.

As the initial step toward RPAS model validation, the data collected from pavement tests sections at MnROAD and NAPTF test facilities were processed and catalogued. The pavement structure and test condition were modeled in RPAS for the initial comparison called pre-validation. This step was performed to assess the performance of RPAS in modeling the pavement response before applying the calibration process.

Verification of RPAS consisted of two stages consisting of calculation verification and bench-marking. For the first stage, a stress convergence study was performed to find the error introduced to the model caused by the discretization, which is called solution approximation error. For the second stage a multi-level bench-marking was implemented, in which the comparison of

RPAS predictions with the analytical solutions was performed from a simplified problem (a plate under distributed load) and then was expanded to a more complicated 3D model created in other finite element tools.

Before the calibration was conducted a global sensitivity analysis using random decision forests was conducted to find the relative importance of the various input parameters on the calculation of the critical responses of concrete pavements. The results of this sensitivity analysis indicated that pavement moduli were among the most influential parameters. This coincided with the fact that foundation moduli have a large variability as observed in the field data and thus it was the reason that the moduli was selected for calibration. The calibration process consisted then of calibrating/correcting the moduli of the pavement foundation layers to find a reasonable agreement between the model predictions and field measurements. This calibration process used a multi-objective optimization to minimize the error of predictions while considering both the deflection and strain response of the test and model pavements. The Pareto Optimal Front algorithm was used for this multi-objective optimization. The calibration factors were generated as the ratio of the calibrated to the original moduli of foundation layers from laboratory tests or back-calculation.

Finally, by applying the calibration factors to the models, a validation of the predictions from RPAS was conducted. For this purpose, a reliability metric was proposed that calculates the probability of the differences between the RPAS results and the field data being within an acceptable range.

8.2. Conclusions

Based on the mathematical and statistical analyses conducted in this study utilizing the empirical data, the following conclusions were drawn:

1. In general, uncalibrated RPAS results show a reasonable agreement with deflections measured in the field. However, the stresses and strains calculated at the top and bottom of the concrete slab can, in certain cases, result in discrepancies of up to 50% between

RPAS and field measurements indicating the need for the calibration process presented here.

2. The results of global sensitivity analysis showed the significance of the contribution of pavement foundation layers on the critical responses of concrete pavements. This conclusion not only identified the foundation moduli as a parameter to focus on during the calibration process, but also highlights the issue of design guides such as MEPDG that assume a low importance for the properties of the foundation layers.
3. The first part of the verification of RPAS was calculation verification, that was based on finding the numerical error due to discretization of the foundation layers. The results indicated that to minimize this error, the first soil layer beneath the concrete slab must be discretized into elements with a vertical dimension of 1 in. Once this step was completed, the verified (corrected) model was used for bench-marking. This multi-level process showed a great agreement (r-square>0.9) between various analytical solutions and RPAS calculations for simple problems as the lowest level of bench-marking. The following higher levels included more complicated problems of pavement modeling using other advanced numerical tools in which RPAS results showed a good agreement with discrepancies of up to 11% for the longitudinal stress in slabs.
4. The calibration process included a multi-objective optimization that was used to calibrate the moduli of the foundation layers to minimize the difference between the field and numerical results. The calibration factors were generated for two-, three-, and four-layer pavement systems. The statistical distribution of these calibration factors was obtained and the median was selected to define the calibrated moduli to be used in RPAS. The range of calibration factors were between 0.75 and 1.60 with most being close to 1.00. After applying these calibration factors, the validation process was conducted.

5. One of the methods used to validate the responses of the calibrated RPAS model was to plot the correlations plots of measured and predicted response of different pavement structures before and after calibration. These graphs included the prediction limits as well as the discrepancy (r-square) of the data points. The results indicated narrow prediction confidence limits and a high accuracy ($r^2=0.99$) of the calibrated model. In addition to these plots, a reliability metric *r* that represents the probability of the differences between RPAS results and field data being within an acceptable range. This metric was calculated for the model before and after calibration. The values of the reliability metric were shown to significantly improve after calibration. For example, by assuming the accuracy requirement of 15%, the reliability of three-layer pavements increased from 50% to 96%.
6. The results shown in this dissertation demonstrate that the verification, calibration and validation method implemented here have resulted in a calibrated RPAS model that produces reliable concrete pavement responses.

8.3. Recommendations for Future Research

While the extensive effort to complete the work presented in this dissertation resulted in a significantly improved RPAS model, there are still many areas for potential improvement. The following recommendations are made for future research:

1. An improvement to the concrete pavement model would be to use three-dimensional hexahedron elements to discretize the slab. With this improvement, the steel reinforcement and its interaction with the surrounding concrete can be properly modeled. In addition, using these elements would allow for the modeling of the dowel bar looseness or misalignment that can have a prominent effect on dowel's mechanical performance due to its modified effective length. These improvements could also lead to the capability of modeling crack propagation, if the ultimate goal is to expand this

analysis tool to a design tool. Although the implementation of these three-dimensional elements could lead to additional capabilities, they would have to be weighed against the significant increase in required computational power.

2. The warping caused moisture intrusion into the pavement layers can significantly impact the development of bending stresses in concrete slab and can also have a negative impact on the mechanical properties of the foundation layers. Adding a model for moisture intrusion would also improve RPAS capabilities.
3. During the process to collect data to be used for calibration and validation purposes, a significant effort was made to gather as much data as possible from different types of pavement structures, tire loading, environmental conditions and material properties. However, the data available was limited to two pavement test facilities. It is recommended that more data be gathered from laboratories, test facilities and field tests across the nation to be implemented in the calibration process. This effort could then lead to various calibrated versions of RPAS specific to a particular district or state. As mentioned in Chapter 6, the framework presented here can be used for re-calibration additional data becomes available.
4. During the verification, benchmarking, calibration and validation process numerous statistical and data analysis algorithms were utilized. These algorithms were selected based on their wide-spread use for similar applications. However, the field of machine learning and statistical analysis in general is always expanding and new algorithms are being developed. For future work it is recommended to assess the performance of other algorithms to further improve on the calibrated version of RPAS.

References

AASHTO. 1993. Guide for Design of Pavement Structures. American Association of State Highway and Transportation Officials, Washington, D.C.

ACPA (2020): http://www.apps.acpa.org/apps/kvalue.aspx

Aguirre, N. 2020. Development of A Numerical Simulation Tool for Continuously Reinforced Concrete Pavements. PhD Dissertation, University of Texas at El Paso, El Paso, TX.

Aguirre, N., TaghaviGhalesari, A., Carrasco, C. 2019. A Comparison of Concrete Pavement Responses using Finite Element Method with Foundation Springs and 3-D Solid Elements, International Airfield and Highway Pavements Conference, Chicago, IL.

Aguirre, N., TaghaviGhalesari, A., Rogers, R., Carrasco, C., Nazarian, S. 2020. Influence of Foundation Layer Properties in a Concrete Pavement System Subjected to Heavy Vehicle Loads, International Conference on Transportation Geotechnics, Chicago, IL.

Anderson, M. P., Woessner, W. W., Hunt, R. J. (2015). Applied Groundwater Modeling: Simulation of Flow and Advective Transport. 2nd Edition, Academic press, San Diego, CA.

ASME, (2006). Guide for Verification and Validation in Computational Solid Mechanics, The American Society of Mechanical Engineers, ASME V&V 10-2006.

AIAA (American Institute of Aeronautics and Astronautics) 1998. Guide for the Verification and Validation of Computational Fluid Dynamics Simulations, AIAA-G-077-1998, Reston, VA, American Institute of Aeronautics and Astronautics.

Aure, T. W., Ioannides, A. M. 2010. Simulation of Crack Propagation in Concrete Beams with Cohesive Elements In ABAQUS. Transportation research record, 2154(1), 12-21.

Babuška I., Rheinboldt WC. (1978). A-Posteriori Error Estimates for The Finite Element Method. Int J Numer Methods Eng, 12(10): 1597–615.

Barbosa, R. S. 2011. Vehicle Dynamic Response Due to Pavement Roughness. Journal of the Brazilian Society of Mechanical Sciences and Engineering, 33(3), 302-307.

Beckemeyer, C., Khazanovich, L., Thomas Yu, H. 2002. Determining Amount of Built-in Curling in Jointed Plain Concrete Pavement: Case study of Pennsylvania I-80. Transportation Research Record, 1809(1), 85-92.

Bhatti, M. A. 2006. Advanced Topics in Finite Element Analysis of Structures: with Mathematica and MATLAB Computations. New York: John Wiley.

Bradbury, R. D. 1938. Reinforced Concrete Pavements, Wire Reinforcement Institute, Washington, D.C.

Breiman, L. 2001. Random forests. Machine learning, 45(1), 5-32.

Brill, D. R., Hayhoe, G. F., Ricalde, L. 2005. Analysis of CC2 Rigid Pavement Test Data from the FAA's National Airport Pavement Test Facility. In Proc. 7th International Conference on the Bearing Capacity of Roads, Railways, and Airfields, Trondheim, Norway.

Burmister, D. M. 1943. The Theory of Stresses and Displacements in Layered Systems and Applications to the Design of Airport Runways, Highway Research Board 23, 126-144.

Burmister, D. M. 1945. The General Theory of Stresses and Displacements in Layered Soil Systems, Journal of Applied Physics, 16, 84-94,126-127, 296-302.

Burnham, T. R. 2002. Construction Report for Mn/ROAD PCC Testcells 32, 52, and 52. Report No. MN/RC 2002-04. Minnesota Department of Transportation, Research Services Section, St. Paul, MN, USA.

Burnham, T. R., Tewfik, A., Srirangarajan, S. 2007. Development of A Computer Program for Selecting Peak Dynamic Sensor Responses from Pavement Testing (No. MN/RD-2007-49). Minnesota. Dept. of Transportation.

Carrasco, C., Limouee, M., Celaya, M., Abdallah, I. Nazarian, S. (2009). NYSLAB: A Software for Analysis of Jointed Pavements. Final Report. Report Number: FHWA-RD-07-1008-01.

Carrasco, C., Limouee, M., Tirado, C., Nazarian, S., and Bendaña, J. 2011. Development of NYSLAB: Improved Analysis Tool for Jointed Pavement. Transportation Research Record: Journal of the Transportation Research Board, (2227), 107-115.

Ceylan, H., Gopalakrishnan, K., Kim, S., Schwartz, C. W., Li, R. 2013. Global Sensitivity Analysis of Jointed Plain Concrete Pavement Mechanistic–Empirical Performance Predictions. Transportation Research Record, 2367(1), 113-122.

Chen, L., Feng, D., Quan, L. 2014. Inclusion of Built-In Curling Temperature Profile in Curling-Stress Determination for Rigid Pavement. Journal of Transportation Engineering, 141(4), 06014003.

Cheung, Y. K., Zinkiewicz, O. C. 1965. Plates and Tanks on Elastic Foundations - An Application of Finite Element Method. International Journal of Solids and structures, 1(4), 451-461.

Chou, Y. T. 1981. Structural Analysis Computer Programs for Rigid Multicomponent Pavement Structures with Discontinuities—WESLIQID and WESLAYER. Report 2, Manual for the WESLIQID finite element program, Tech. Report GL-81-6, Vicksburg, MS: U.S. Army Waterways Experiment Station.

Choubane, B. and M. Tia. 1992. Nonlinear Temperature Gradient Effect on Maximum Warping Stresses in Rigid Pavements. Transportation Research Record No. 1370. Washington, DC: Transportation Research Board, National Research Council, pp. 11–19.

Davids, W. G., G. M. Turkiyyah, J. P. Mahoney. 1998. EverFE: Rigid Pavement Three-Dimensional Finite Element Analysis Tool. Transportation Research Record: Journal of the Transportation Research Board, 1629 (1): 41-49.

Davids, W., Wang, Z., Turkiyyah, G., Mahoney, J., Bush, D. 2003. Three-dimensional finite element analysis of jointed plain concrete pavement with EverFE 2.2. Transportation Research Record: Journal of the Transportation Research Board 1853, 92-99.

De Jong, D. L. Peatz M. G. F, Korswagen, A. R. 1973. Computer Program BISAR Layered Systems Under Normal and Tangential Loads, External Report AMSR .0006 .73; Konin Klijke Shell-Laboratorium, Amsterdam.

Eymard, R., Guerrier, F., Jacob, B. 1990. Dynamic Behavior of Bridge under Full Traffic. In Bridge Evaluation, Repair and Rehabilitation (pp. 293-306). Springer, Dordrecht.

Ferson, S., Oberkampf, W.L., Ginzburg, L. 2008. Model Validation and Predictive Capability for The Thermal Challenge Problem. Comput Methods Appl Mech Eng, 197(29), 2408–30.

FHWA 2019. Concrete Pavement Joints, Technical Advisory T 5040.30. Federal Highway Administration. Washington, D.C. https://www.fhwa.dot.gov/pavement/ta504030.pdf.

Friberg, B. F. 1940. Design of Dowels in Transverse Joints of Concrete Pavements, Transactions, ASCE, 105, 1076–1095.

Gamez, A., Hernandez, J. A., Ozer, H., Al-Qadi, I. L. 2018. Development of Domain Analysis for Determining Potential Pavement Damage. Journal of Transportation Engineering, Part B: Pavements, 144(3), 04018030.

Gelfand, A. E., Dey, D. K. Bayesian Model Choice: Asymptotics And Exact Calculations. J R Stat Soc Ser B (Methodol) 1994:501–14.

Geweke, J. 2007. Bayesian Model Comparison and Validation. Am Econ Rev, 97(2), 60–4.

Gjorv, O. E., Baerland, T., Ronning, H. R. 1990. Abrasion Resistance of High Strength Concrete Pavements. Concrete International, 12(1), 45-48.

Grater, S. F., McCullough, B. F. 1994. Analysis of Jointed Concrete Pavement. Report FHWA/TX-95-1244-10, Center for Transportation Research, The University of Texas at Austin.

Guclu, A., Ceylan, H., Gopalakrishnan, K., Kim, S. 2009. Sensitivity Analysis of Rigid Pavement Systems Using the Mechanistic-Empirical Design Guide Software. Journal of Transportation Engineering, 135(8), 555-562.

Ha, S., Yeon, J., Choi, B., Jung, Y., Zollinger, D. G., Wimsatt, A., Won, M. C. 2011. Develop Mechanistic-Empirical Design for CRCP (No. FHWA/TX-11-0-5832-1), Texas Tech Univ., Lubbock, TX.

Hall, K. D., Beam, S. 2005. Estimating the Sensitivity of Design Input Variables for Rigid Pavement Analysis with A Mechanistic–Empirical Design Guide. Transportation Research Record, 1919(1), 65-73.

Hamim, A., Yusoff, N. I. M., Ceylan, H., Rosyidi, S. A. P., El-Shafie, A. 2018. Comparative Study on Using Static and Dynamic Finite Element Models to Develop FWD Measurement on Flexible Pavement Structures. Construction and Building Materials, 176, 583-592.

Hammons, M. I., Ioannides, A. M. 1997. Mechanistic Design and Analysis Procedure for Doweled Joints in Concrete Pavements. International Purdue Conference on Concrete Pavement Design and Materials for High Performance, Vol. 3, Indianapolis, Indiana, USA.

Han, W., Yuan, Y., Huang, P., Wu, J., Wang, T., Liu, H. 2017. Dynamic Impact of Heavy Traffic Load On Typical T-Beam Bridges Based on WIM Data. Journal of Performance of Constructed Facilities, 31(3), 04017001.

Hansen, W., Y. Wei, D. L. Smiley, Y. Peng, and E. A. Jensen. (2006). Effects of Paving Conditions on Built-in Curling and Pavement Performance. International Journal of Pavement Engineering, 7 (4): 291-296.

Hastie, T., Friedman, J., Tibshirani, R. 2017. The Elements of Statistical Learning, New York: Springer series in statistics.

Hiller, J. E., Roesler, J. R. 2009. Simplified Nonlinear Temperature Curling Analysis for Jointed Concrete Pavements. Journal of Transportation Engineering, 136(7), 654-663.

Hills, R. G., Leslie, I.H. 2003. Statistical Validation of Engineering and Scientific Models: Validation Experiments to Application. Technical report. Albuquerque, NM, USA; Livermore, CA, USA: Sandia National Labs.

Huang, K., Zollinger, D. G., Shi, X., Sun, P. 2017. A Developed Method of Analyzing Temperature and Moisture Profiles in Rigid Pavement Slabs. Construction and Building Materials, 151, 782-788.

Huang, Y. H., 1967. Stresses and Displacements in Viscoelastic Layered Systems Under Circular Loaded Areas, Proceedings, 2nd International Conference on the Structural Design of Asphalt Pavements, pp. 225–244.

Huang, Y. H. 1993. Pavement Analysis and Design. Englewood Cliffs, NJ: Prentice Hall.

Hwang, C. L., Masud, A. S. M. 2012. Multiple Objective Decision Making Methods And Applications: A State-Of-The-Art Survey, Vol. 164, Springer Science & Business Media, New York, U.S.

Ioannides, A. M., Khazanovich, L. 1998. Nonlinear Temperature Effects on Multilayered Concrete Pavements. Journal of Transportation Engineering, 124(2), 128-136.

Ioannides, A. M., Davis, C. M., Weber, C. M. 1999. Westergaard Curling Solution Reconsidered. Transportation Research Record, 1684(1), 61-70.

Joshaghani, A., Zollinger, D. G. 2019. Assessment of Concrete Pavement Set Gradient Based on Analysis of Slab Behavior and Field Test Data. Transportation Research Record, 0361198119849900.

Kannekanti, V. N., Harvey, J. T. 2005. Sensitivity Analysis of 2002 Design Guide Rigid Pavement Distress Prediction Models, Report No UCPRC-DG-2006-01, California Department of Transportation, Office of Roadway Research, Sacramento, CA, USA.

Kennedy, M. C., O'Hagan, A. 2001. Bayesian Calibration of Computer Models. Journal of the Royal Statistical Society: Series B (Statistical Methodology), 63(3), 425-464.

Khazanovich, L. 1994. Structural Analysis of Multi-Layered Concrete Pavement Systems. PhD Dissertation. University of Illinois at Urbana-Champaign.

Khazanovich, L. and A. M. Loannides. 1994. Structural Analysis of Unbonded Concrete Overlays Under Wheel And Environmental Loading, Transportation Research Record No. 1449. Washington, DC: Transportation Research Board.

Khazanovich, L., H. Yu, S. Rao, K. Galasova, E. Shats, R. Jones. 2000. ISLAB2000-Finite Element Analysis Program for Rigid and Composite Pavements. User's Guide. Champaign, IL: ERES Consultants.

Kim, S. M., Won, M., McCullough, B. F. 2001. CRCP-10 Computer Program User's Guide (No. FHWA/TX-0-1831-4,). Center for Transportation Research, Bureau of Engineering Research, The University of Texas at Austin.

Kok, A. W. M. 1990. A PC Program for The Analysis of Rectangular Pavements Structures. Proceedings, Second International Workshop on the Design and Rehabilitation of Concrete Pavements, Sigüenza, Spain, pp. 113–120.

Kramer, S. 1996. Geotechnical Earthquake Engineering. Prentice-Hall, Inc. New Jersey, 348-422.

Li, W., Pour-Ghaz, M., Castro, J., Weiss, J. 2011. Water Absorption and Critical Degree of Saturation Relating to Freeze-Thaw Damage in Concrete Pavement Joints. Journal of Materials in Civil Engineering, 24(3), 299-307.

Ling, Y., Mahadevan, S. 2013. Quantitative Model Validation Techniques: New insights. Reliabil Eng Syst Saf, 111, 217–31.

Liu, Y, Chen, W, Arendt, P, Huang, HZ. Toward A Better Understanding of Model Validation Metrics. Trans ASME J Mech Des 2011;133(7):071005.

Loh, W. Y., Shih, Y. S. 1997. Split Selection Methods for Classification Trees. Statistica sinica, 815-840.

Luo, X., Gu, F., Zhang, Y., Lytton, R. L., Zollinger, D. 2017. Mechanistic-Empirical Models for Better Consideration of Subgrade and Unbound Layers Influence on Pavement Performance. Transportation Geotechnics, 13, 52-68.

Mahadevan, S, Rebba, R. Validation of Reliability Computational Models Using Bayes Networks. Reliab Eng Syst Saf 2005;87(2):223–32.

Mallick, R.B., El-Korchi, T. 2018. Pavement Engineering, Principles and Practice, Third Edition, CRC Press, Boca Raton, FL.

McQueen, R. D., Hayhoe, G. F. 2014. Construction Cycle 6 (CC-6) Revisited: Fatigue Analysis and Economic and Design Implications, FAA Worldwide Airport Technology Transfer Conference, Galloway, New Jersey, USA.

Miettinen, K. 2012. Nonlinear Multiobjective Optimization, Vol. 12, Springer Science & Business Media, New York, U.S.

Misaghi, S. M. 2011. Impact of Truck Suspension and Road Roughness on Loads Exerted to Pavements. MSc Thesis, The University of Texas at El Paso.

MnROAD Data Library 2019: http://www.dot.state.mn.us/mnroad/data/index.html

Mohamed, A., Hansen, W. 1997. Effect of Nonlinear Temperature Gradient on Curling Stress in Concrete Pavements. Transportation Research Record: Journal of the Transportation Research Board, 65-71.

NAPTF Data Library 2019: https://www.airporttech.tc.faa.gov/Airport-Pavement/National-Airport-Pavement-Test-Facility/NAPTV.

Nash, J. E., Sutcliffe, J. V. 1970. River Flow Forecasting Through Conceptual Models Part I—A Discussion of Principles. Journal of hydrology, 10(3), 282-290.

NCHRP 1-37A. 2004. Guide for Mechanistic–Empirical Design of New and Rehabilitated Pavement Structures. Final Report, TRB, National Research Council, Washington, D.C.

Oberkampf, W. L., Barone, M. F. 2006. Measures of Agreement Between Computation and Experiment: Validation Metrics. J Comput Phys, 217(1), 5–36.

Ong, C. L., Newcomb, D. E., Siddharthan, R. 1991. Comparison of Dynamic and Static Backcalculation Moduli for Three-Layer Pavements. Transportation Research Record, 1293, 86-92.

Oreskes, N., Shrader-Frechette, K., Belitz, K. (1994). Verification, Validation, and Confirmation of Numerical Models In The Earth Sciences. Science, 263(5147), 641-646.

Pickett, G. and G. K. Ray. (1951). Influence Charts for Rigid Pavements. American Society of Civil
Engineers Transactions.

Prażnowski, K., Mamala, J. 2016. Classification of The Road Surface Condition on The Basis Of Vibrations Of The Sprung Mass In A Passenger Car. In IOP Conference Series: Materials Science and Engineering 148(1): 012022. IOP Publishing Press.

Rangavajhala S, Sura V, Hombal V, Mahadevan S. 2011. Discretization Error Estimation in Multidisciplinary Simulations. AIAA J, 49(12): 2673–712.

Rao, C., Titus-Glover, L., Bhattacharya, B. B., Darter, M. I., Stanley, M., Von Quintus, H. L. 2012. Estimation of Key PCC, Base, Subbase, and Pavement Engineering Properties from Routine Tests and Physical Characteristics, Report No. FHWA-HRT-12-030, FHWA Office of Infrastructure Research and Development, McLean, VA.

Rao, S., Roesler, J. R. (2005). Characterizing Effective Built-In Curling from Concrete Pavement Field Measurements. Journal of Transportation Engineering, 131(4), 320-327.

Rebba, R., Mahadevan, S., Huang, S. 2006. Validation and Error Estimation of Computational Models. Reliab Eng Syst Saf, 91(10), 1390–7

Reddy, J. N. 2004. Mechanics of Laminated Composite Plates and Shells: Theory and Analysis. CRC

Ricalde, L., Daiutolo, H. 2005. New Rigid Pavement Construction and Testing at the FAA National Airport Pavement Test Facility (NAPTF). In Proc. of the Fifth International Conference on Road and Airfield Pavement Technology, Seoul, Korea.

Rogers, R., Plei, M., Aguirre, N., Taghavi Ghalesari, A. 2017. Optimizing Structural Design for Overlaying HMA Pavements with A Concrete Pavement Using Critical Stresses/Strains. In Proc., TRB 11th University Transportation Center (UTC) Spotlight Conference: Rebuilding and Retrofitting the Transportation Infrastructure, Washington, DC.

Roy, C. J., Oberkampf, W. L. 2011. A Comprehensive Framework for Verification, Validation, And Uncertainty Quantification in Scientific Computing. Comput Methods Appl Mech Eng, 200(25–28), 2131–44.

Saltelli, A., Ratto, M., Andres, T., Campolongo, F., Cariboni, J., Gatelli, D., Saisana, M., Tarantola, S. 2008. Global Sensitivity Analysis: The Primer. John Wiley & Sons.

Sankararaman, S., Mahadevan, S. 2015. Integration of Model Verification, Validation, And Calibration for Uncertainty Quantification in Engineering Systems. Reliability Engineering & System Safety, 138, 194-209.

Schwer, L.E., 2006. Guide for Verification and Validation in Computational Solid Mechanics, ASME 20th International Conference on Structural Mechanics in Reactor Technology, Espoo, Finland.

SIMULIA. 2016. ABAQUS 6.16 Documentation. Dassault Systèmes, Simulia Corporation, Providence, RI.

Stoffels, S., Lopez, M., Yeh, L., Jeong, Y., Barzegari, S., Kermani, B. 2014. Fracture Characterization and SEM Examination of NAPTF CC6 Concrete Mixes, FAA Worldwide Airport Technology Transfer Conference, Galloway, New Jersey, USA.

Stoffels, S., Morian, D., Ioannides, A., Wu, S., Sadasivam, S., Yeh, L., Yin, H. 2008. Improved Overlay Design Parameters for Concrete Airfield Pavements. Innovative Pavement Research Foundation Report FAA-01-G-002-04-2, Conneaut Lake, PA.

Tabatabaie, A. M., Barenberg, E. J. 1980. Structural Analysis of Concrete Pavement Systems. Transportation Engineering Journal, 106 (5): 493-506.

TaghaviGhalesari, A., Aguirre, N., Carrasco, C., Vrtis, M., Garg, N. 2020a. Evaluation of the Response from the Rigid Pavement Analysis System (RPAS) Program for the Characterization of Jointed Concrete Pavements, Road Material and Pavement Design, https://doi.org/10.1080/14680629.2020.1747522.

TaghaviGhalesari, A., Aguirre, N., Carrasco, C., Vrtis, M., Garg, N. 2020b. Verification and Validation of the Response of a 3-D Finite Element Model for the Characterization of Jointed Concrete Pavements, TRB 99th Annual Meeting, Washington D.C.

TaghaviGhalesari, A., Aguirre, N., Carrasco. 2020c. Application of Sensitivity Analysis in The Calibration Process of a Concrete Pavement Analysis Software. International Conference on Transportation and Development, Seattle, WA.

TaghaviGhalesari, A., Aguirre, N., Carrasco. 2020d. Verification Process of Rigid Pavement Analysis System, Journal of Transportation Engineering, Part A: Pavements, Submitted.

Tayabji, S. D., Colley, B. E. 1986. Analysis of Jointed Concrete Pavements. Report FHWA/RD-86-041, Federal Highway Administration, Office of Engineering and Highway Operations, VA.

Texas Department of Transportation 2019. TxDOT Pavement Manual, Austin, TX.

Thacker, B. H., Paez, T.L. 2014. A simple Probabilistic Validation Metric for The Comparison of Uncertain Model and Test Results. In: The 16th AIAA non-deterministic approaches conference.

U.S. Department of Energy. 2000. Advanced Simulation and Computing (ASCI) Program Plan, 01-ASCI-Prog-01, Sandia National Laboratories, Albuquerque, New Mexico.

Uddin, W., Hackett, R. M., Joseph, A., Pan, Z., Crawley, A. B. 1995. Three-Dimensional Finite-Element Analysis of Jointed Concrete Pavement with Discontinuities. Transportation Research Record, 1482, 26-32.

Urbina, A., Paez, T. L., Hasselman, T., Wathugala, W., Yap, K. 2003. Assessment of Model Accuracy Relative to Stochastic System Behavior. In: The 44th AIAA/ASME/ASCE/AHS/ASC structures, structural dynamics, and materials conference.

Vallabhan, C. G. and Y. Das. (1988). Parametric Study of Beams on Elastic Foundations. Journal of Engineering Mechanics, 114 (12): 2072-2082.

Van Deusen, D. A., Burnham, T. R., Dai, S., Geib, J., Hanson, C., Izevbekhai, B. I., Johnson, E., Palek, L., Siekmeier, J., Vrtis, M., Worel, B. (2018). Report on 2017 MnROAD Construction Activities, Report No. MN/RC 2018-16, Minnesota. Dept. of Transportation. Research Services & Library.

Van Veldhuizen, D. A., Lamont, G. B. 2000. On Measuring Multiobjective Evolutionary Algorithm Performance. In Proc. 2000 Congress on Evolutionary Computation, IEEE 2000, 1, 204-211.

Vinson, J. R. 1999. The Behavior of Sandwich Structures of Isotropic and Composite Materials. CRC Press.

Wang, H., Li, M. 2015. Evaluation of Effects of Variations in Aggregate Base Layer Properties on Flexible Pavement Performance. Transportation Research Record, 2524(1), 119-129.

Westergaard, H. M. 1926. Stresses in Concrete Pavements Computed by Theoretical Analysis. Public Roads, 7(2), 25-35.

Westergaard, H. M. 1927. Theory of Concrete Pavement Design. Proceedings, Highway Research Board, Part 1(7), 175–181.

Westergaard, H. M. 1939. Stresses in Concrete Runways of Airports, Highway Research Board 19, 197–202.

Ye, Z., Lu, Y., Wang, L. (2018). Investigating the Pavement Vibration Response for Roadway Service Condition Evaluation. Advances in Civil Engineering, 2018.

Yuan, X., Chen, Z., Yuan, Y., Huang, Y., Zhang, X. (2015). A Strength Pareto Gravitational Search Algorithm for Multi-Objective Optimization Problems. International Journal of Pattern Recognition and Artificial Intelligence, 29(06), 1559010.

Zhou, W. 2013. Effect of Pavement Support Condition on CRCP Behavior and Performance, PhD Dissertation, Texas Tech University, Lubbock, TX, USA.

Zokaei-Ashtiani, M. A. (2014). Enhanced Finite Element Modeling of The Thermo-Mechanical Responses of Jointed PCC Pavements Under Environmental and Traffic Loads. PhD Dissertation, University of Texas at El Paso, El Paso, TX.

Zokaei-Ashtiani, M. A., Carrasco, C., Nazarian, S. 2014. Finite Element Modeling of Slab–Foundation Interaction on Rigid Pavement Applications. Computers and Geotechnics, 62, 118-127.

Zollinger, D. G., Barenberg, E. J. 1989. A Mechanistic Based Design Procedure for Jointed Concrete Pavements. Proceedings, 4th International Conference on Concrete Pavement Design and Rehabilitation, Purdue University, Report No: FHWA-RD-89-208.

Appendix A

This appendix lists the calibration factors generated from the process explained in Chapter 6. Similar to Chapter 6, the results in this appendix are listed in the following order for three-layer and four-layer pavements:

1. A list of calibration factors from utilizing the FWD/HWD deflection data (single variable optimization)
2. A list of calibration factors from simultaneous utilization of the FWD/HWD deflection data and dynamic strain data from either accelerated or truck loading.
3. Figures plotting the trend of the obtained calibration factors against a variable such as impact stiffness.

A-1. Three-Layer Pavement

The data used for obtaining the calibration factors for the three-layer pavement systems were collected from MnROAD Cells 32 and 52 as well as NAPTF CC-2. Although the entire dataset used for three-layer movement included a higher number of data (see Section 6.4 in Chapter 6), only a portion (15 percent) of the data utilized in calibration are shown here for brevity.

Tables A-1 through A-2 as well as Figures A-1 through A-2 show the generated calibration factors for the three-layer pavements.

Table A-1. The Generated Calibration Factors for the Deflection (Using SOF) of Three-Layer Pavements

FWD Load, P (lb)	**Max. Deflection, D_0 (mil)**	**Given Modulus of Base (psi)**	**Given Modulus of Subgrade (psi)**	**Calibrated Modulus of Base (psi)**	**Calibrated Modulus of Subgrade (psi)**	**Calibration Factor of Base, CF1**	**Calibration Factor of Subgrade, CF2**
5,932	4.88	16,500	10,400	18,522	11,951	1.1225	1.1492
14,988	31.30	16,500	10,400	20,862	13,027	1.2644	1.2526
14,814	29.29	16,500	10,400	12,228	8,454	0.7411	0.8128
9,215	6.26	16,500	10,400	19,775	14,006	1.1985	1.3468
24,141	7.70	16,045	13,467	14,284	14,652	0.8903	1.0880
14,322	29.65	27,560	27,000	29,310	21,652	1.0635	0.8019
14,703	28.54	16,500	10,400	12,534	9,305	0.7597	0.8947
14,719	14.96	27,560	27,000	34,682	31,242	1.2584	1.1571
8,739	24.72	16,500	10,400	16,716	10,606	1.0131	1.0198
14,909	58.46	16,500	10,400	12,470	8,868	0.7558	0.8527
9,247	5.91	16,500	10,400	24,851	13,818	1.5061	1.3286
9,231	7.13	16,500	10,400	19,097	13,286	1.1574	1.2775
5,995	16.46	27,560	27,000	24,621	23,841	0.8933	0.8830
14,750	17.99	27,560	27,000	34,103	25,814	1.2374	0.9561
5,916	7.09	27,560	27,000	32,274	27,461	1.1710	1.0171
8,882	19.29	16,500	10,400	26,819	13,840	1.6254	1.3308
8,850	19.80	16,500	10,400	25,320	9,641	1.5345	0.9270
9,025	17.83	27,560	27,000	33,599	25,408	1.2191	0.9410
9,009	17.40	27,560	27,000	32,560	26,217	1.1814	0.9710
14,211	31.06	27,560	27,000	34,902	25,381	1.2664	0.9400
14,687	18.66	27,560	27,000	33,085	26,301	1.2005	0.9741
14,275	45.35	16,500	10,400	13,753	10,774	0.8335	1.0360
8,882	23.31	27,560	27,000	25,007	23,949	0.9074	0.8870
5,757	14.88	16,500	10,400	19,869	12,530	1.2042	1.2048

Table A-1. Continued.

FWD Load, P (lb)	Max. Deflection, D_0 (mil)	Given Modulus of Base (psi)	Given Modulus of Subgrade (psi)	Calibrated Modulus of Base (psi)	Calibrated Modulus of Subgrade (psi)	Calibration Factor of Base, CF1	Calibration Factor of Subgrade, CF2
8,787	20.00	16,500	10,400	24,959	12,183	1.5126	1.1715
8,485	27.48	16,500	10,400	15,731	9,152	0.9534	0.8800
14,512	24.76	27,560	27,000	41,014	35,432	1.4882	1.3123
5,710	13.50	16,500	10,400	25,858	14,171	1.5672	1.3626
8,739	24.45	16,500	10,400	18,912	9,211	1.1462	0.8857
6,011	21.18	27,560	27,000	21,060	16,813	0.7642	0.6227
6,122	3.54	27,560	27,000	26,869	25,840	0.9749	0.9570
15,020	24.13	16,500	10,400	15,405	8,902	0.9336	0.8560
5,995	16.54	27,560	27,000	24,598	25,542	0.8925	0.9460
5,710	17.01	16,500	10,400	18,869	8,944	1.1436	0.8600

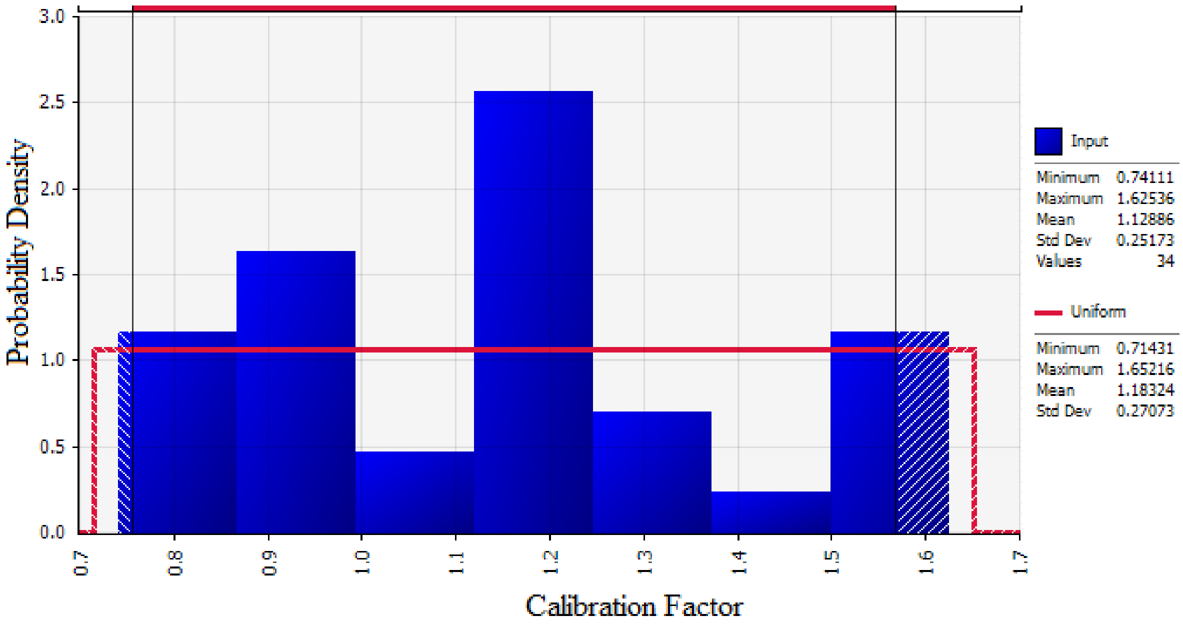

(a) Median CF1: 1.1518

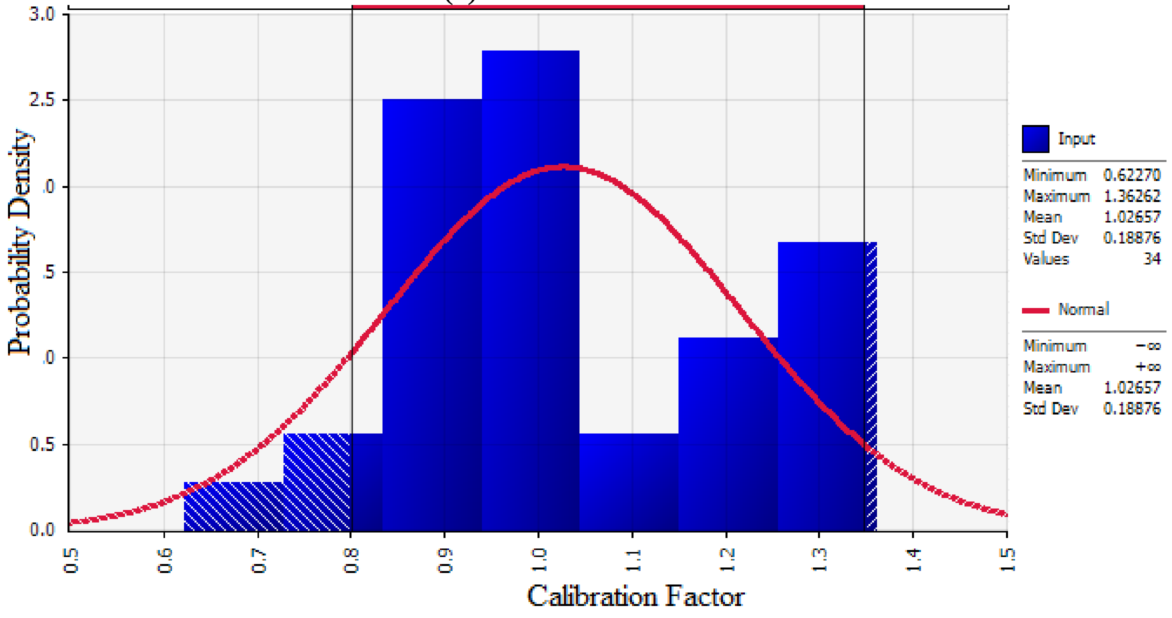

(b) Median CF2: 0.9640

Figure A-1. The Distribution Fitted to The Calibration Factors of Three-Layer Pavements Generated Based on SOF (By Incorporating the Deflection Data) (a) CF1 for Base Layer (b) CF2 for Subgrade Layer

Table A-2. The Generated Calibration Factors for the Deflection and Strain in Slab (Using MOF) of Three-Layer Pavements

(a)

FWD Load, P (lb)	Max. Deflection, D_0 (mil)	Given Modulus of Base (psi)	Given Modulus of Subgrade (psi)	Calibrated Modulus of Base (psi)	Calibrated Modulus of Subgrade (psi)	Calibration Factor of Base, CF1	Calibration Factor of Subgrade, CF2
6,249	3.31	27,560	27,000	34,753	34,371	1.2610	1.2730
9,072	11.46	27,560	27,000	25,024	33,615	0.9080	1.2450
14,084	36.46	27,560	27,000	34,863	28,836	1.2650	1.0680
9,278	14.69	27,560	27,000	24,914	25,650	0.9040	0.9500
14,322	29.65	27,560	27,000	27,064	29,133	0.9820	1.0790
9,231	6.65	16,500	10,400	17,754	11,669	1.0760	1.1220
8,882	24.21	27,560	27,000	32,190	29,916	1.1680	1.1080
5,710	14.53	16,500	10,400	14,768	13,499	0.8950	1.2980
6,027	12.56	27,560	27,000	30,536	34,398	1.1080	1.2740
5,567	18.27	16,500	10,400	16,121	10,109	0.9770	0.9720
5,995	4.53	16,500	10,400	20,130	10,088	1.2200	0.9700
14,322	44.84	16,500	10,400	19,239	13,364	1.1660	1.2850
8,628	27.95	16,500	10,400	19,833	12,262	1.2020	1.1790
6,154	4.06	27,560	27,000	24,143	24,408	0.8760	0.9040
8,787	23.19	27,560	27,000	28,304	32,697	1.0270	1.2110
9,183	7.13	16,500	10,400	15,378	9,994	0.9320	0.9610
9,056	10.94	27,560	27,000	23,591	31,779	0.8560	1.1770
5,599	18.23	16,500	10,400	17,606	9,568	1.0670	0.9200
8,961	17.99	16,500	10,400	15,048	9,162	0.9120	0.8810
9,263	6.46	16,500	10,400	19,289	13,198	1.1690	1.2690
8,993	17.72	27,560	27,000	30,261	23,085	1.0980	0.8550
9,247	14.49	27,560	27,000	35,194	33,831	1.2770	1.2530
8,818	22.44	16,500	10,400	14,784	11,804	0.8960	1.1350
5,900	10.51	16,500	10,400	20,576	10,535	1.2470	1.0130
14,671	18.66	27,560	27,000	24,363	29,997	0.8840	1.1110

Table A-2. Continued.

FWD Load, P (lb)	**Max. Deflection, D_0 (mil)**	**Given Modulus of Base (psi)**	**Given Modulus of Subgrade (psi)**	**Calibrated Modulus of Base (psi)**	**Calibrated Modulus of Subgrade (psi)**	**Calibration Factor of Base, CF1**	**Calibration Factor of Subgrade, CF2**
14,179	42.48	27,560	27,000	33,100	30,051	1.2010	1.1130
5,805	15.71	27,560	27,000	23,674	23,166	0.8590	0.8580
8,961	19.41	27,560	27,000	28,304	27,837	1.0270	1.0310
8,930	17.95	16,500	10,400	14,042	10,972	0.8510	1.0550
14,290	48.23	27,560	27,000	34,092	35,019	1.2370	1.2970
5,995	7.20	27,560	27,000	32,411	27,918	1.1760	1.0340
8,739	24.45	16,500	10,400	15,626	10,296	0.9470	0.9900
5,710	17.24	16,500	10,400	15,048	11,846	0.9120	1.1390
14,988	31.30	16,500	10,400	16,731	11,773	1.0140	1.1320

(b)

APT Load (kips)	**Strain in Slab ($\mu\varepsilon$)**
12.0	34.2
16.9	34.4
16.6	33.8
15.6	39.3
18.4	38.5
12.4	12.0
21.4	28.0
23.4	22.0
22.1	22.0
23.1	27.0
55.0	L: -114.7
55.0	L: 101.3
55.0	L: -110.7
55.0	L: 98.7
55.0	T: 94.7
55.0	T: 68.0

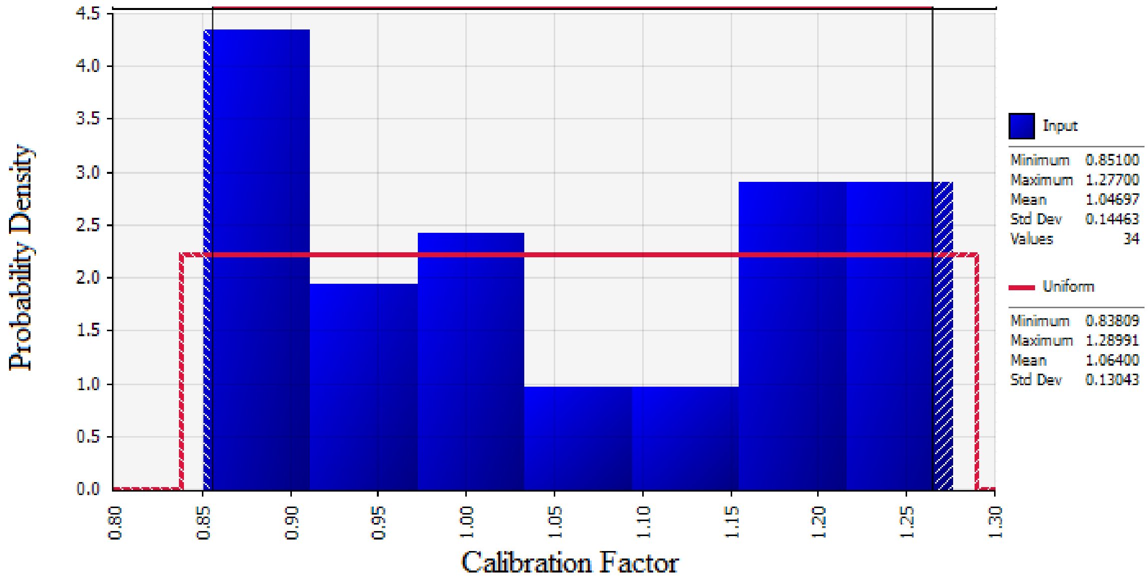

(a) Median CF1: 1.0270

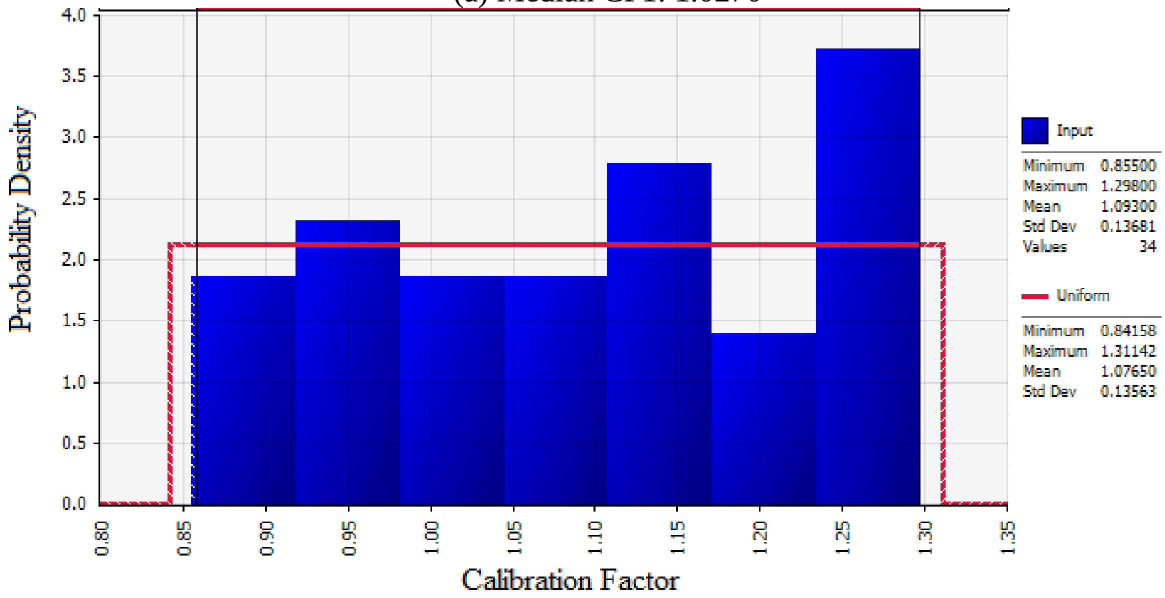

(b) Median CF2: 1.1095

Figure A-2. The Distribution Fitted to The Calibration Factors of Three-Layer Pavements Generated Based on MOF (By Incorporating the Deflection and Strain Data) (a) CF1 For Base Layer (b) CF2 For Subgrade Layer

A-2. Four-Layer Pavement

The data used for obtaining the calibration factors for the four-layer pavement systems were collected from MnROAD Cells 613 as well as NAPTF CC-2 and CC-6. The difference between these test sections and the conventional pavement sections is the existence of an additional base layer above the granular base layer. This additional base layer is another granular layer while CC-2 and CC-6 include a cement-stabilized or an asphalt-treated base layer. This dataset shows the variety of the test data used in the calibration to assess the performance of the developed calibration procedure.

Although the entire dataset used for four-layer movement included a higher number of data (see Section 6.4 in Chapter 6), only a portion (20 percent) of the data utilized in calibration are shown here for brevity. Tables A-3 through A-4 as well as Figures A-3 through A-4 show the generated calibration factors for the three-layer pavements.

Table A-3. The Generated Calibration Factors for the Deflection (Using SOF) of Four-Layer Pavements

FWD Load, P (lb)	Max. Deflection D_0 (mil)	Given Modulus of Base 1 (psi)	Given Modulus of Base 2 (psi)	Given Modulus of Subgrade (psi)	Calibrated Modulus of Base 1 (psi)	Calibrated Modulus of Base 2 (psi)	Calibrated Modulus of Subgrade (psi)	Calibration Factor of Base 1, CF1	Calibration Factor of Base 2, CF2	Calibration Factor of Subgrade, CF3
9,147	25.18	20,040	20,580	16,860	25,170	25,046	14,533	1.2560	1.2170	0.8620
6,573	3.19	20,040	20,580	16,860	23,126	24,490	16,826	1.1540	1.1900	0.9980
9,739	5.01	20,040	20,580	16,860	27,916	19,407	15,697	1.3930	0.9430	0.9310
11,918	30.22	20,040	20,580	16,860	24,810	21,835	15,073	1.2380	1.0610	0.8940
12,380	6.57	60,000	24,200	11,600	74,760	29,088	10,022	1.2460	1.2020	0.8640
12,422	7.31	20,040	20,580	16,860	27,996	18,152	16,894	1.3970	0.8820	1.0020
6,551	3.70	20,040	20,580	16,860	23,507	25,252	20,552	1.1730	1.2270	1.2190
12,320	4.11	1,432,000	25,500	12,300	1,158,488	20,961	11,156	0.8090	0.8220	0.9070
9,016	26.67	20,040	20,580	16,860	15,611	17,452	19,676	0.7790	0.8480	1.1670
24,181	5.30	72,000	16,045	13,467	84,528	17,152	11,959	1.1740	1.0690	0.8880
11,846	2.60	72,000	16,045	13,467	60,624	13,975	10,854	0.8420	0.8710	0.8060
6,145	15.10	20,040	20,580	16,860	18,958	23,338	18,023	0.9460	1.1340	1.0690
12,335	6.04	20,040	20,580	16,860	26,433	24,037	13,859	1.3190	1.1680	0.8220
6,452	9.75	20,040	20,580	16,860	21,563	25,087	15,359	1.0760	1.2190	0.9110
6,376	8.83	20,040	20,580	16,860	17,836	21,197	18,833	0.8900	1.0300	1.1170
12,291	6.48	20,040	20,580	16,860	24,128	23,770	17,888	1.2040	1.1550	1.0610
36,244	8.80	72,000	16,045	13,467	73,368	14,328	12,147	1.0190	0.8930	0.9020
36,472	18.69	60,000	24,200	11,600	83,760	24,781	12,458	1.3960	1.0240	1.0740
6,518	8.08	20,040	20,580	16,860	15,551	22,247	17,568	0.7760	1.0810	1.0420

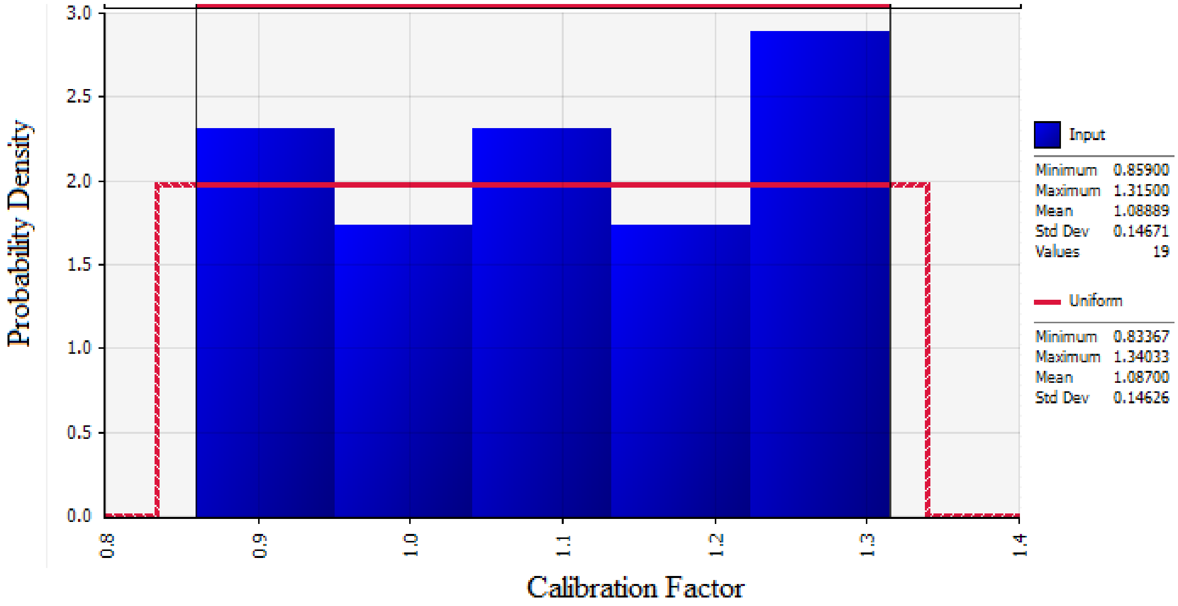

(a) Median CF1: 1.1730

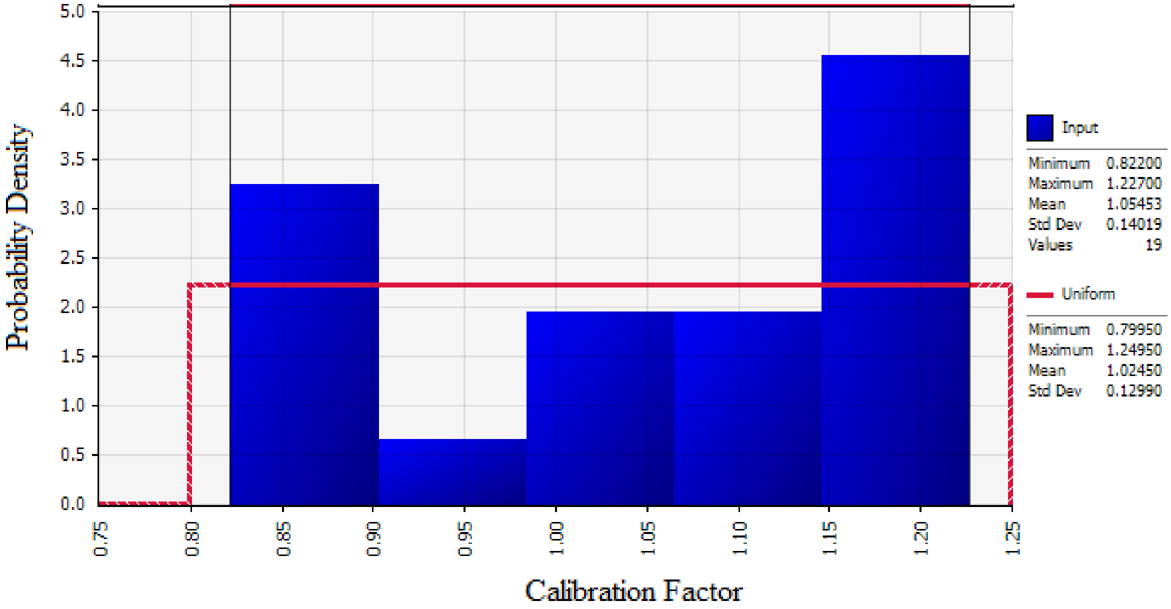

(b) Median CF2: 1.0690

Figure A-3. The Distribution Fitted to The Calibration Factors of Four-Layer Pavements Generated Based on SOF (By Incorporating the Deflection) (a) CF1 For Base 1 Layer (b) CF2 For Base 2 Layer (C) CF3 For Subgrade Layer

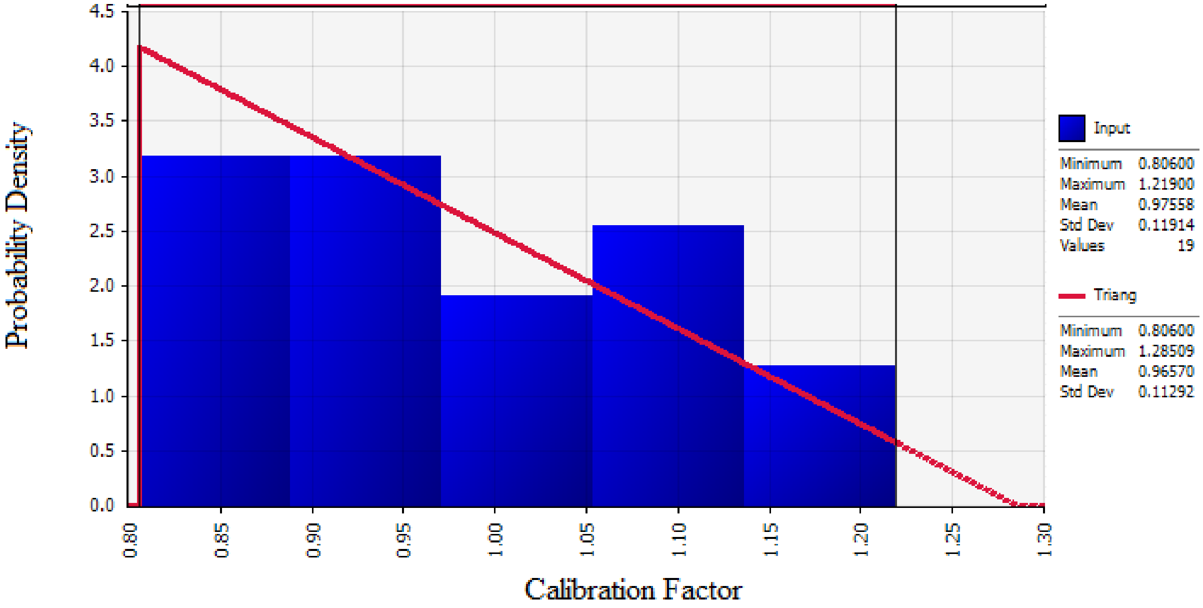

(c) Median CF3: 09310

Figure A-3. Continued.

Table A-4. The Generated Calibration Factors for the Deflection and Strain in Slab (Using MOF) of Four-Layer Pavements

(a)

FWD Load, P (lb)	Max. Deflection D_0 (mil)	Given Modulus of Base 1 (psi)	Given Modulus of Base 2 (psi)	Given Modulus of Subgrade (psi)	Calibrated Modulus of Base 1 (psi)	Calibrated Modulus of Base 2 (psi)	Calibrated Modulus of Subgrade (psi)	Calibration Factor of Base 1, CF1	Calibration Factor of Base 2, CF2	Calibration Factor of Subgrade, CF3
36,472	18.69	60,000	24,200	11,600	78,420	22,675	9,698	1.3070	0.9370	0.8360
9,728	5.63	20,040	20,580	16,860	18,056	28,730	15,208	0.9010	1.3960	0.9020
12,329	4.23	1,432,000	25,500	12,300	1,493,576	33,227	12,755	1.0430	1.3030	1.0370
9,519	14.72	20,040	20,580	16,860	21,122	23,770	15,090	1.0540	1.1550	0.8950
11,875	25.98	20,040	20,580	16,860	15,210	28,380	14,297	0.7590	1.3790	0.8480
12,039	17.99	20,040	20,580	16,860	21,142	22,165	16,658	1.0550	1.0770	0.9880
11,975	4.95	1,432,000	25,500	12,300	1,784,272	28,892	13,149	1.2460	1.1330	1.0690
6,397	10.72	20,040	20,580	16,860	26,633	20,415	12,982	1.3290	0.9920	0.7700
24,181	5.50	72,000	16,045	13,467	64,800	14,088	14,706	0.9000	0.8780	1.0920
12,427	6.50	60,000	24,200	11,600	45,960	31,605	15,289	0.7660	1.3060	1.3180
12,380	6.57	60,000	24,200	11,600	60,900	21,465	15,254	1.0150	0.8870	1.3150
36,639	9.55	1,432,000	25,500	12,300	1,958,976	33,278	10,369	1.3680	1.3050	0.8430
11,864	28.48	20,040	20,580	16,860	24,709	17,966	22,120	1.2330	0.8730	1.3120
11,776	30.60	20,040	20,580	16,860	16,272	21,732	22,120	0.8120	1.0560	1.3120
12,211	2.80	72,000	16,045	13,467	85,464	15,836	17,453	1.1870	0.9870	1.2960
11,590	35.23	20,040	20,580	16,860	16,272	18,028	14,044	0.8120	0.8760	0.8330
24,285	9.98	1,432,000	25,500	12,300	1,147,032	35,675	11,820	0.8010	1.3990	0.9610
9,487	14.48	20,040	20,580	16,860	27,495	17,740	13,303	1.3720	0.8620	0.7890
9,224	23.80	20,040	20,580	16,860	15,511	24,058	21,851	0.7740	1.1690	1.2960

Table A-4. Continued.

(b)

APT Load (kips)	**Strain in Slab ($\mu\varepsilon$)**
11.7	21.8
17.7	24.3
16.5	24.2
16.8	25.1
17.1	24.5
55.0	L1:-104
55.0	L2:126.7
55.0	L3:110.7
55.0	L4:77.3
55.0	T1:54.7
55.0	T2:73.3
50.0	L5:-82.4
50.0	L6:72.5

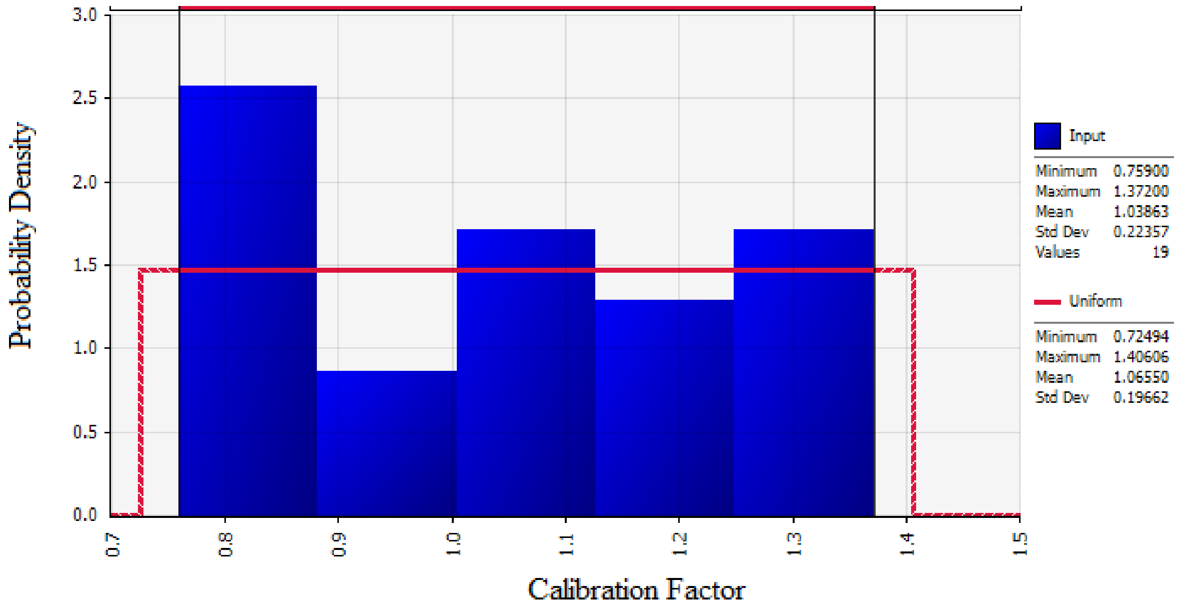

(a) Median CF1: 1.0430

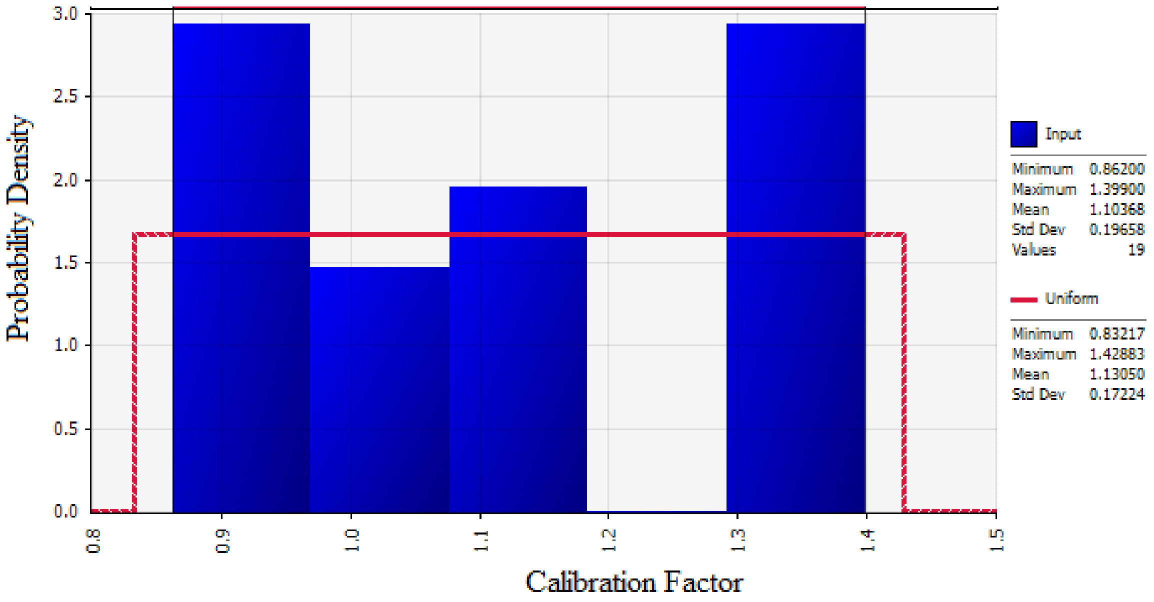

(b) Median CF2: 1.0770

Figure A-4. The Distribution Fitted to The Calibration Factors of Four-Layer Pavements Generated Based on MOF (By Incorporating the Deflection and Strain in Slab) (a) CF1 For Base 1 Layer (b) CF2 For Base 2 Layer (C) CF3 For Subgrade Layer

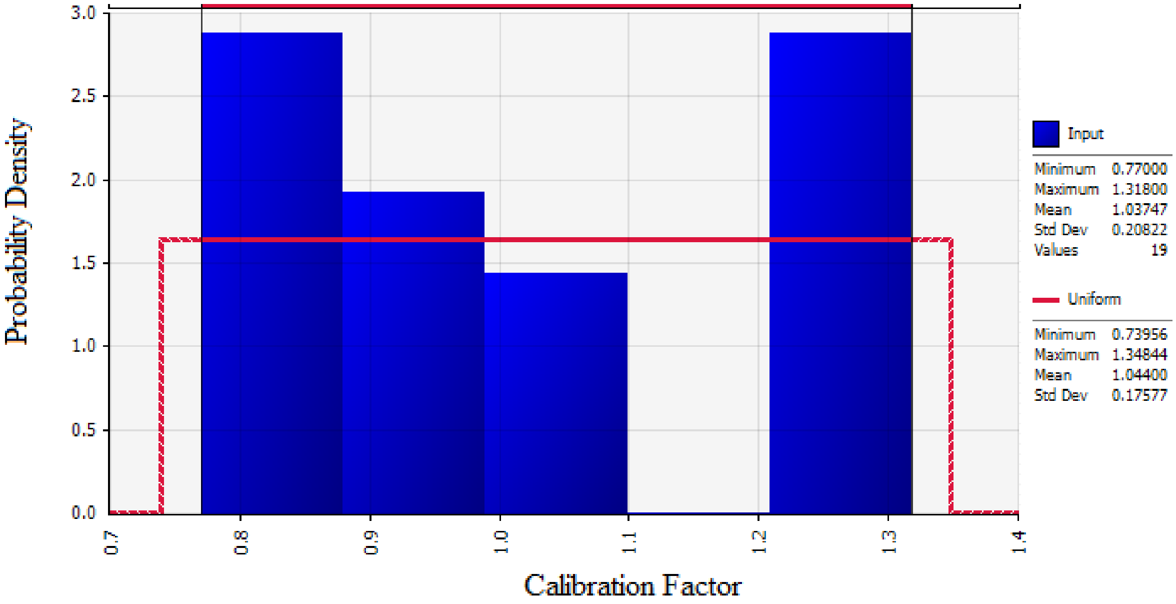

(c) Median CF3: 0.988

Figure A-4. Continued.

Curriculum Vitae

Mr. Abbasali TaghaviGhalesari, M.Sc., E.I.T., obtained his B.Sc. in Civil Engineering in 2010 and his M.Sc. in Geotechnical Engineering in 2013. His M.Sc. thesis was on the development of a numerical model for the analysis and optimum design of piled raft foundations based on field test data. He later extended his research to the analysis of offshore foundations and fiber-reinforced soil. After four years of professional work as a geotechnical engineer and technical manager in several building, railway and highway projects, he started his Ph.D. at The University of Texas at El Paso in 2017. His research at Center for Transportation Infrastructure Systems (CTIS) was focused on the development and calibration of RPAS, an analysis tool for concrete pavements through successful completion of SPTC14.1-94 research project. During his Ph.D. studies, he received Frank B. Cotton Trust Scholarship and Graduate School Grant. He also served as an Assistant Instructor at the Department of Civil Engineering at The University of Texas at El Paso. Mr. TaghaviGhalesari is currently working as a Project Manager at The Transtec Group Inc., working on several research projects funded by state and federal transportation agencies.